

# University of St Andrews



Full metadata for this thesis is available in  
St Andrews Research Repository  
at:

<http://research-repository.st-andrews.ac.uk/>

This thesis is protected by original copyright

**Magnetism and superconductivity in  
amorphous alloys**



**A Thesis submitted for the degree of Doctor of Philosophy**

**By**

**Pascal MANUEL**

**December 2001**



to E114

# Abstract

In this thesis, the magnetic and superconducting properties of various amorphous alloys will be investigated using a combination of in-house techniques such as ac susceptibility, Vibrating Sample Magnetometry, Mössbauer spectroscopy and work at international facilities on neutron or muon instruments (ISIS in Didcot, Oxfordshire and ILL in Grenoble, France). The samples have all been made by melt-spinning in St Andrews and neutron diffraction confirms that the ribbons are amorphous.

The first problem this thesis addresses is the dynamics of  $\alpha$ -RE<sub>7</sub>TM<sub>3</sub> by a combination of ac susceptibility and neutron spin echo. The results will be discussed according to the current theories on Random Anisotropy systems, differences with spin glass dynamics will be discussed and parallels with structural glasses will be drawn.

Then, this work will focus on the fabrication of novel crystalline phases. Indeed, using the latest development in high intensity neutron diffraction such as the D20 spectrometer at the ILL, a new route, where the crystallisation of amorphous alloys is watched directly in a neutron beam while collecting data (kinetic neutron diffraction), has been pioneered and a previously unreported binary alloy has been seen in at least two systems.

At last, the nature of the Flux Line Lattice in amorphous superconducting Zr<sub>76</sub>TM<sub>24</sub> (where TM = Fe, Cu, Ni, Rh and Co) will be investigated in the final chapter of this work. The data suggest a quasi-perfect FLL on the length scale of the muon. The pinning in these superconductors will also be studied by introducing random pins in the materials by heat treatment at low temperatures.



I, Pascal Manuel, hereby certify that this thesis, which is approximately 40,000 words in length, has been written by me, that it is a record of work carried out by me and that it has not been submitted in any previous application for a higher degree.

date.....19...DEC...2001... signature of candidate... .....

I was admitted as a research student in December 1996 and as a candidate for the degree of Doctor of Philosophy in December 1996; the higher study for which this is a record was carried out in the University of St Andrews between 1997 and 2000.

date...19...DEC...2001... signature of candidate ..

I hereby certify that the candidate has fulfilled the conditions of the Resolution and Regulations appropriate for the degree of Doctor of Philosophy in the University of St Andrews and that the candidate is qualified to submit this thesis in application for that degree.

date.....15/2/02... signature of supervisor..... .....

In submitting this thesis to the University of St Andrews I understand that I am giving permission for it to be made available for use in accordance with the regulations of the University Library for the time being in force, subject to any copyright vested in the work not being affected thereby. I also understand that the title and abstract will be published, and that a copy of the work may be made and supplied to any bona fide library or research worker.

date...19...DEC...2001... signature of candidate..

# Acknowledgements

It is a pleasure to thank my supervisor Prof. R. Cywinski for his stimulating remarks throughout this thesis. No matter how busy Bob was, he always found some time to discuss physics and keep me on the right track. I would also like to express my gratitude towards Ian Campbell from the Laboratoire de Physique des Solides, Orsay, France. Without Ian's contacts with Bob, I would never had the opportunity to come to Britain for my PhD. I wish to thank the EPSRC and the MENESR (French Ministry of Research and Education) for their financial support. I am very grateful to Drs. Sue Kilcoyne, Adrian Hillier and Rob Bewley for their invaluable help during experiments. Since a good-humoured environment is very important to work in good conditions, I would like to thank all the other past members of the Magnetism and Superconductivity Group at St Andrews: Mark Telling, Jude Dann, Judith Preston and Phil Bentley. I would also like to thank the technicians at St Andrews that have helped me set up some of the equipment I have used (especially Reg Gavine).

A good part of this thesis relies on experiments done at international facilities (ISIS at the Rutherford Laboratory, Didcot, Oxfordshire and the Institut Laue Langevin, Grenoble, France) where I have been helped by many local contacts. These "travailleurs de l'ombre" that don't hesitate to come in during the evenings or at the week-end to make sure the experiment is running fine deserve all the users' respect. These wonderful people include (with the hope of not forgetting anybody who has helped me during these neutron or muon experiments) : Ken Anderson, Amir Murani, Clemens Ritter, Pierre Convert, Thomas Hansen, Bob Cubbitt, Bela Farago and Paul Schleger at the ILL; Chris Scott, Philip King, Steve Cottrell, James Lord, Alex Hannon, Ron Smith, Richard Ibberson and Jimmy Chauhan at ISIS.

The Squid measurements were performed at the Laboratoire SPEC at Saclay, France where Eric Vincent showed me how to use the equipment and I would like to thank him for his help. Similarly, the heat capacity measurements were undertaken at Oxford Instruments Superconductivity in Oxfordshire where Rod Bateman and Paul Rivitt have helped me with the experimental setup.

At least but not last, I would like to thank my parents, my little brother and Eli. Their constant encouragement helped me keep the necessary courage to go through a PhD thesis.

# Contents

## I. Introduction

## II. Sample preparation and characterisation

II.1. Introduction

II.2. Definitions

II.3. Amorphous sample preparation techniques

II.3.a. glass-forming ability

II.3.b. techniques using the solid phase as starting material

II.3.c. techniques using the gaseous phase as starting material

II.3.d. techniques using the liquid phase as starting material

II.4. The art of melt-spinning

II.4.a. preparing the alloys

II.4.b. the melt-spinning method

II.5. Characterisation by neutron scattering

II.5.a. Introduction

II.5.b. properties of the neutron

II.5.c. scattering cross-sections

*II.5.d.1. definitions*

*II.5.d.2. partial differential cross-section in the general case*

*II.5.d.3. coherent and incoherent scattering*

*II.5.d.4. scattering law for amorphous materials*

*II.5.d.5. scattering law for crystalline materials*

*II.5.d.6. magnetic scattering*

II.6. Vibrating Sample Magnetometry

II.7. AC susceptibility

II.8. Heat capacity measurements

II.9. Mössbauer spectroscopy

References for Chapter II

### **III. Muon Spin Rotation and Relaxation**

#### III.1. Introduction

#### III.2. properties, production and decay of the muon

##### III.2.a. properties

##### III.2.b. production of a spin polarised beam

##### III.2.c. thermalisation of the muon

##### III.2.d. decay of the muon and emission of a positron

#### III.3. Muon spectroscopy at ISIS

##### III.3.a. the muon beam lines at ISIS

##### III.3.b. the MuSR spectrometer

###### *III.3.c.1. general overview*

###### *III.3.c.2. sample mounting*

#### III.4. Muon Spin Rotation Technique

##### III.4.a. First principles

##### III.4.b. data analysis

###### *III.4.b.1. experimental parameters*

###### *III.4.b.2. detectors grouping*

###### *III.4.b.3. frequency domain analysis : maximum entropy method*

#### III.5. Muon Spin Relaxation

##### III.5.a. Sample mounting and detectors grouping

##### III.5.b. Muon depolarisation functions

###### *III.5.b.1. static fields*

###### *III.5.b.2. dynamic spin systems*

#### References for Chapter III

## IV. AC susceptibility and Neutron Spin Echo study of Random Anisotropy Magnets

### IV.1. Introduction

### IV.2. Rare Earth Magnetism

#### IV.2.a. localised magnetism

#### IV.2.b. paramagnetism of Rare Earth elements

#### IV.2.c. origins of the interactions in Rare-Earths

#### IV.2.d. the HPZ Hamiltonian

### IV.3. AC susceptibility

#### IV.3.a. sample preparation and structural characterisation

#### IV.3.b. experimental procedure

#### IV.3.c. transition temperatures for $\alpha$ -Er<sub>67</sub>Fe<sub>33</sub> and $\alpha$ -Er<sub>67</sub>Ni<sub>33</sub>

#### IV.3.d. frequency dependence as a probe for sample dynamics

##### *IV.3.d.1. Lundgren's $\pi/2$ law*

##### *IV.3.d.2. Cole Cole analysis*

##### *IV.3.d.3. distribution of relaxation times*

##### *IV.3.d.4. frequency dependence of $T_g$*

### IV.4. Magnetic Diffuse Scattering

### IV.5. Neutron Spin Echo measurements

#### IV.5.a. NSE results

#### IV.5.b. previous NSE work and related theories on Spin Glasses

#### IV.5.c. NSE measurements on Random Anisotropy Magnets

### IV.6. Conclusion and perspectives

### References for Chapter IV

**V. Synthesis and characterisation of novel Rare Earth - Transition Metal by crystallisation of amorphous alloys**

V.1. Introduction

V.2. the D20 and the D2B spectrometers at the ILL

V.3. crystallisation of  $\alpha$ -  $Y_{67}Fe_{33}$  : a novel YFe phase

V.3.a. previous studies on the YFe system

V.3.b. neutron study of crystallisation processes in  $\alpha$ -  $Y_{67}Fe_{33}$

*V.3.b.1. low angle region*

*V.3.b.2. formation and evolution of the Y phase*

*V.3.b.3. intermediate phase*

*V.3.b.4. final phases : Y and  $YFe_2$*

V.3.c. magnetic study of the new intermediate YFe alloy

*V.3.c.1. DC and AC magnetisation measurements*

*V.3.c.2. Mössbauer results*

*V.3.c.3. Muon Spin Relaxation*

*V.3.c.4. Neutron Scattering result*

V.4. crystallisation study of other RE-TM amorphous alloys

V.5. Conclusions and further work

References for Chapter V

## **VI. Study of the superconducting properties of amorphous Zr-TM**

VI.1. Introduction

VI.2. A brief review of superconductivity

VI.2.a. Meissner effect and the two types of superconductivity

VI.2.b. The two fluid model

VI.2.c. Pinning and the critical state

VI.2.d. Ginzburg-Landau equations and London model

VI.2.e. Microscopic theory of Bardeen, Cooper and Schrieffer

VI.2.f. Local pairing superconductivity and Uemura classification

VI.3. Superconducting properties of  $\alpha$ -Zr-TM (TM = Co, Fe, Ni, Rh and Cu) by conventional methods

VI.3.a. Structural characterisation

VI.3.b. DC magnetisation measurements

VI.3.c. Heat capacity measurements

VI.4.  $\mu$ SR study of  $\alpha$ -Zr<sub>76</sub>TM<sub>24</sub>

VI.5. Conclusions and further work

References for Chapter VI

## **VII. Conclusions and perspectives**

# Chapter I : Introduction

Since their discovery, metallic glasses have attracted a great deal of interest in the condensed matter community. Indeed, not only do they provide the opportunity to make samples over a wide range of composition unlike in the crystalline case where only specific compositions corresponding to crystallographic phases can be made but they possess attractive electronic properties. For example, as a result of the Fermi surface being smoothed in an amorphous metal, the electrical and magnetic properties can be quite different than their crystalline analogues.

The ease with which an element can be substituted by another and/or the composition changed offers the opportunity to study phenomena as diverse as the random anisotropy problem, the spin glass state, superconductivity... For instance, in the random anisotropy systems, it becomes possible to change both the exchange  $J$  and the anisotropy  $D$  by substituting a non  $s$ -state ion by Gd (or Y) or changing Fe by Ni without significantly affecting the morphology of the sample. The spin glass and the random anisotropy behaviours are very similar in the sense that, for instance, both exhibit a frequency dependent peak in the ac susceptibility. However, based on an analysis of critical exponents, some authors<sup>1</sup> have claimed that random anisotropy magnets are representative of a completely different universality class. Theorists believe that the key to the glass and spin glass problem lies in the dynamics and clearly more information is needed on the dynamics of random anisotropy systems. The only direct way of probing the spin autocorrelation function in magnetic systems is the Neutron Spin Echo technique. Such a NSE experiment and its combination with good quality ac susceptibility data enable one to study the dynamics at very different frequencies. In Chapter IV such a NSE study on a typical RAM will be undertaken. To my knowledge, this is the first time it has been tried on RAM systems.

The very good homogeneity of the amorphous alloys ensures an intimate mixing of the constituents. This offers the opportunity to study metastable phases by heat-treating the amorphous samples. Chapter V will show that this in-situ crystallisation technique can lead to the formation of previously unreported crystalline phases. The magnetic properties of one of these new phases (YFe) are then investigated by a combination of neutron diffraction,  $\mu$ SR, VSM, Mössbauer, and ac susceptibility. The results from the magnetic data will be discussed in the light of recent LTMO



calculations on the Fe moment of binary alloys as it expands the concentration range previously available.

At last, the superconductivity in amorphous  $Zr_{76}Fe_{24}$  alloys will be examined with conventional laboratory instruments and with muon spin rotation. It will be shown that  $\mu$ SR reveals the existence of an almost perfect flux line lattice, which to my knowledge has not been reported anywhere. The results will also be analysed within the framework of the Uemura classification scheme<sup>ii</sup> for conventional and exotic superconductors.

---

<sup>i</sup> B. Dieny and B. Barbara, Phys. Rev. Letters **57** (1986) 1169

<sup>ii</sup> Y.J. Uemura, Hyperfine Int.**105** (1997) 35

# Chapter II. Sample preparation and characterisation

## II.1. Introduction

Although amorphous alloys such as window- or stained- glasses (silica based) have been manufactured by men for over hundreds of years, it is still very difficult to predict whether an alloy will be an easy glass-former or not. After defining what is meant by amorphous, this chapter will try to pin down some common features observed in metallic glasses and then mention the amorphous sample preparation techniques concentrating on the one used to produce the samples studied throughout this thesis (melt-spinning). Then, this chapter will focus on the structure of the obtained amorphous ribbons. Finally, the in-house techniques used throughout the other chapters, such as AC susceptibility, Mössbauer spectroscopy, Vibrating Sample Magnetometry will be reviewed.

## II.2. Definitions

The terms amorphous, non-crystalline and glassy are often regarded as synonyms throughout the literature<sup>1</sup>. Strictly speaking, amorphous and non-crystalline can be considered as interchangeable since they both refer to materials lacking the long-range translational order (periodicity) characteristic of crystals. The term glassy is more specific : a glass is an amorphous solid which exhibits a glass transition. As any phase transition (leaving the special spin glass case apart), the glass transition occurs at the temperature at which a discontinuity in the derivatives of the thermodynamic potential (e.g. specific heat) is observed. Looking more carefully at the above definitions of amorphous and non-crystalline solids, one notices that they could also be applied to a liquid. To differentiate the amorphous from the liquid state, it is necessary to introduce the key concept of viscosity, or the property by virtue of which the liquids offer resistance to flow. It then becomes obvious that the amorphous state has a much greater shear viscosity than the liquid state. As a convention, a material is a solid when its shear viscosity exceeds  $10^{13.6}$  N.m<sup>2</sup>s, value corresponding to a deformation of 0.02mm if a force of 100N is applied to 1cm<sup>3</sup> of material for one day.

## II.3. Amorphous sample preparation techniques

### II.3.a. Glass- forming ability

The characteristic that seems common to most of the amorphous alloys obtained so far is the presence of a deep eutectic in the phase diagram in the composition range where these alloys can form. To illustrate this, the phase diagram of one of the binary alloy that will be studied later in this thesis (Y-Fe)<sup>2</sup> is plotted in *Figure II- 1* along with its glass forming composition range. It has also been suggested that the relative size of the atomic radii of a binary alloy must differ by at least 10% for this alloy to form a metallic glass. Moreover, since quenching from the melt can be regarded as a rapid increase in viscosity therefore alloys having high viscosities in the liquid state are generally easy glass-formers.

The first metallic alloy (Au<sub>75</sub>Si<sub>25</sub>) was obtained in 1959 by W. Klement, R.H. Willens and P. Duwez<sup>3</sup> by quenching from the molten state (splat-cooling). Since then, all three phases of matter (solid, liquid, gaseous) have been used as starting materials to produce amorphous samples<sup>1</sup>.

### II.3.b. Techniques using the solid phase as a starting material

Solid crystalline materials can be rendered amorphous by :

- simple irradiation<sup>4</sup> : the alloy is bombarded by a beam of particles (neutrons, or electrons) creating enough structural damage to turn the material amorphous.
- ion beam mixing<sup>5</sup> : a multilayered structure is bombarded by Ar<sup>+</sup> or Xe<sup>+</sup> and amorphous mixing of the components of the multilayer occurs.
- ion implantation<sup>6</sup> : a substrate A (e.g. Fe, Ni, Co, Cu...) is bombarded by ions B ( e.g. B<sup>+</sup>, P<sup>+</sup>, Si<sup>+</sup>, Ge<sup>+</sup>, Ca<sup>+</sup> ...). These ions implant in the substrate and the process is stopped when the desired AB composition is reached. This process produces very clean samples but unfortunately is limited to the surface of the multilayered structure.
- solid state diffusion<sup>7</sup> : alternate layer of crystalline films interdiffuse under isothermal conditions (a few hundreds degrees).
- ball milling<sup>8</sup> : a mixture of crystalline powders is placed in a steel enclosure with a steel ball constantly agitated.

A few amorphous materials (e.g. NiP) can also be obtained by electrolytic deposition<sup>9</sup>.

### **II.3.c. Techniques using the gaseous phase as a starting material**

Amorphous materials can also be produced by rapidly cooling the gaseous phase:

- thermal evaporation<sup>10</sup> : the material is heated at a high temperature so that it vaporises before being collected on a cold substrate.
- sputtering (diode, RF or triode)<sup>11</sup> : a gas (e.g. Ar) is ionised by applying a tension between two electrodes. The target (cathode) is bombarded by positive ions and its atoms are therefore sputtered onto a substrate (anode).
- Glow Discharge Decomposition<sup>12</sup> and Chemical Vapor Decomposition<sup>13</sup> : a plasma of the alloy to produce in the amorphous state is created and deposition takes place on a substrate.

### **II.3.d. Techniques using the liquid phase as a starting material**

Rapid quenching can also produce amorphous alloys. It is evident that the cooling must be sufficiently fast to prevent nucleation and crystal growth. The techniques involved are :

- high local pressure<sup>14</sup> : a shock-wave is sent through a crystalline sample. Some parts of the sample melt and if they cool rapidly enough the amorphous state results.
- laser glazing<sup>15</sup> : a laser beam melts a film that is rapidly cooled on a moving substrate.
- splat-cooling<sup>16</sup> (e.g. piston and anvil method) : the passage of a droplet of molten alloy triggers a piston that squeezes the droplet on an anvil.
- melt-spinning<sup>17</sup> and related techniques : this will be discussed in detail in the next section.

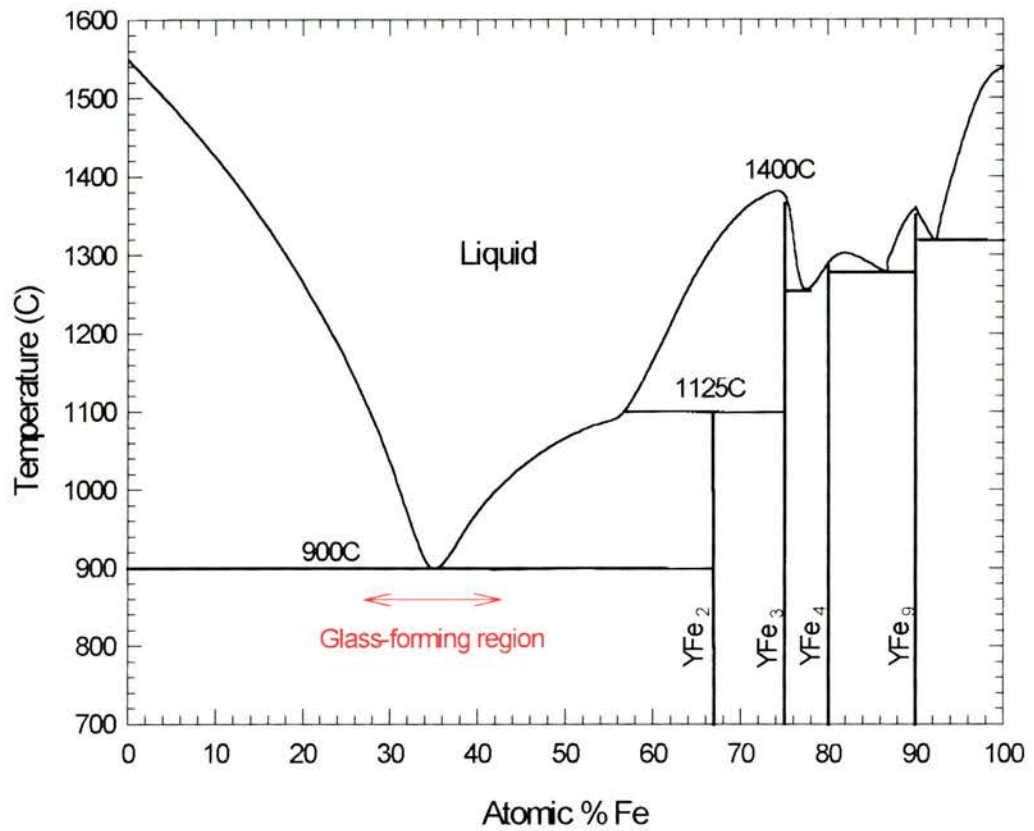


Figure II- 1 : Y-Fe phase diagram. Note the deep eutectic in the glass-forming region.

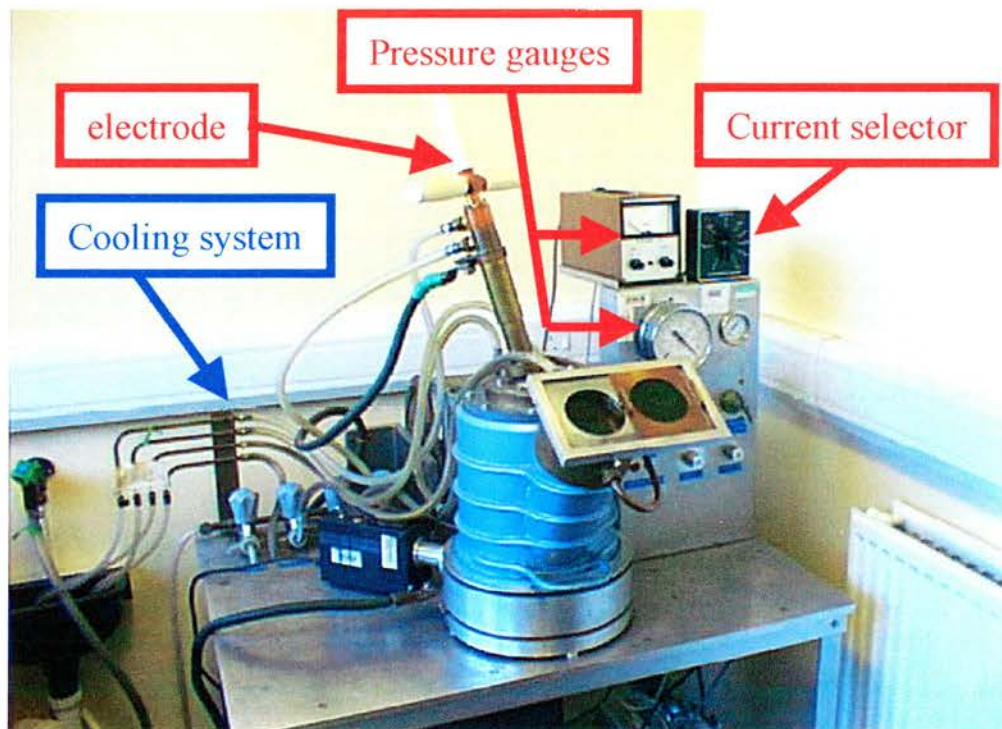


Figure II- 2 : the argon arc furnace

## **II.4. The art of melt-spinning**

### **II.4.a. Preparing the alloys**

All the initial polycrystalline ingots were prepared by melting together the appropriate quantities of pure elements in the argon arc furnace (see *Figure II- 2*) in our own sample preparation laboratory. The purity of each constituent varied from 99.9% (for samples containing yttrium) to reactor grade (samples containing zirconium). The elements were placed in a high purity argon atmosphere from which any gaseous impurities were removed by melting a titanium “getter”. By slowly increasing the current (up to 300A), the electric arc passing between the electrode and the water cooled Copper earth enables temperatures of about 3000°C (if necessary) to be reached within the sample. To ensure homogeneity, the ingots were melted several times and their masses were limited to 10g. Maximum weight losses were of the order of 0.05%.

### **II.4.b. The melt-spinning process**

Once the polycrystalline ingots were made, they were broken into pieces of about 0.7-1.2g so that they fit into a quartz tube. These pieces were then melted in the quartz tube by an r.f. heating coil and the melt was forced onto a rapidly rotating copper disk by an argon blast (see *Figure II- 3*).

The wheel was made by the workshop using an identical design to the one used at Reading University for previous work on amorphous ribbons<sup>18</sup>. Briefly, a copper band (7mm thick) has been grown, by electrolysis, on a 230 mm diameter aluminium disk by Waveform Electroforming Ltd (Norwich). Copper was chosen for its high thermal conductivity in order to conduct the heat away from the sample as fast as possible. Holes were drilled in the aluminium part to further reduce the weight of the wheel (see *Figure II- 3*), thereby increasing the maximum speed obtainable and the cooling rate. The resulting wheel was carefully balanced in order to prevent vibrations at high speeds. Variants of this method, the melt-drag and laminar flow techniques, use a rectangular nozzle (instead of circular) held very close to the wheel, thereby producing larger ribbons, and are therefore used to produce amorphous samples in semi-industrial quantities.



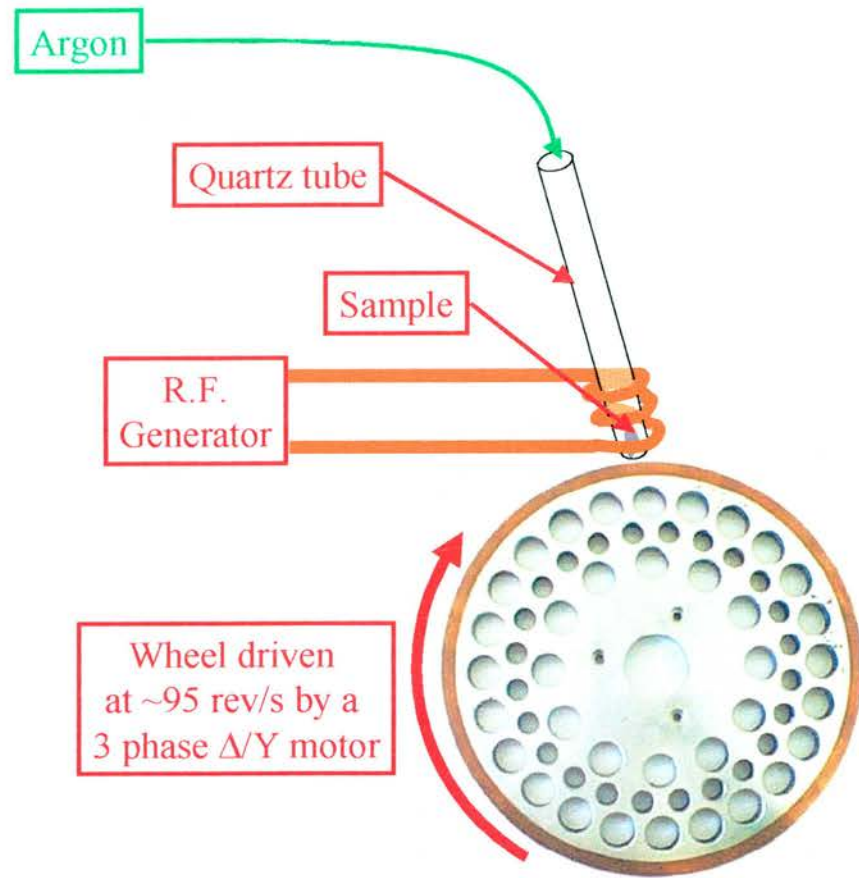


Figure II- 3 : the melt-spinning process

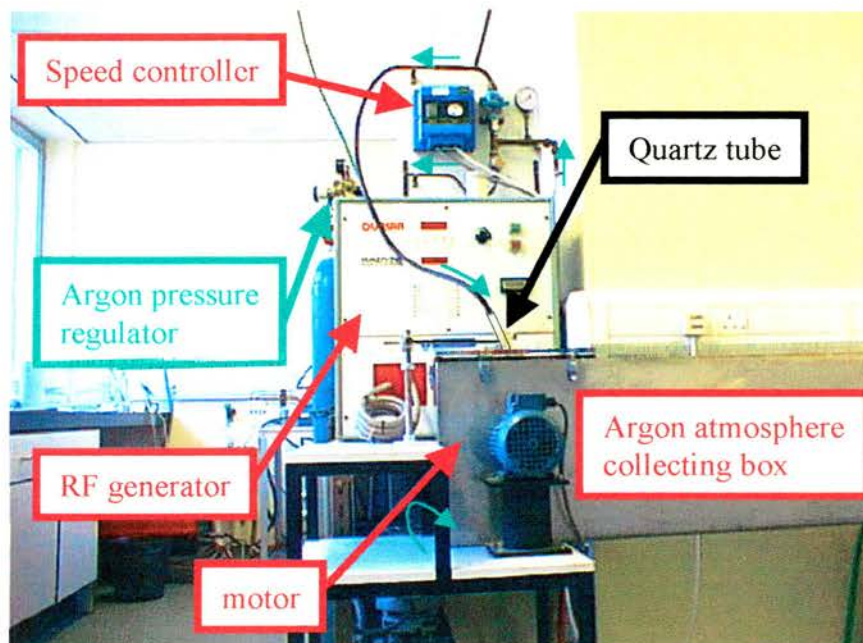


Figure II- 4 : the melt spinner

The resulting ribbons were collected in a box, also made by the workshop, specifically designed to ensure a pure argon atmosphere. A photograph of the whole apparatus can be seen on *Figure II- 4*. This is very important as some of the alloys prepared were extremely sensitive to oxidation and if sufficient care was not taken, the ribbons would end up blue or even burnt in the box. The ratio of the mass of the amorphous ribbons produced over the mass of the polycrystalline ingot inserted in the quartz tube was very sample dependent. For instance, a 95% yield could be achieved in the melt-spinning process for samples such as  $\alpha$ -Dy<sub>7</sub>Ni<sub>3</sub>, whereas a mere 5-10% could only be obtained on other samples such as some  $\alpha$ -ZrFe. For each specific sample, a long time was spent in optimising the parameters controlling the quality and yield of the ribbons.

Indeed, the melt-spinning method is known to be hard to tune<sup>19, 20, 21</sup> but it allows large quantities of samples to be produced which is crucial for some experiments, such as neutron scattering. The production of amorphous ribbons by the melt-spinning technique is dependent on numerous parameters : the viscosity of the liquid, the angle of inclination  $\alpha$  between the tube and the wheel, the size and shape of the nozzle, the pressure of the argon blast influencing the flow rate  $d$  of the molten jet, the speed of the wheel, the surface of the wheel. The difficulty lies in the control of the melt puddle<sup>19</sup> that forms when as an intermediate state between the molten jet and the solidified ribbon. Intuitively, it is easy to see that the longer the length  $L$  of the melt puddle is, the higher the cooling rate will be.  $L$  can be increased by increasing  $\alpha$  but then the thickness of the ribbon will also increase and the ribbon will cease to be amorphous above a certain critical thickness. Alternatively,  $d$  may be increased but that requires the speed of the wheel to increase or the cooling rate will be slower and this unfortunately reduces  $L$ . It is easy to see that the production of amorphous ribbons is therefore a compromise between all the parameters. If the speed and the surface of the wheel were generally kept constant (highest possible speed and polishing with a fine emery cloth followed by an acetone wash between each spin to ensure maximum smoothness), the pressure of the argon blast, the nozzle size and shape and  $\alpha$  had to be varied for each sample to obtain sufficient yields.



## II.5. Characterisation by neutron scattering

### II.5.a. Introduction

The amorphicity of the samples can be checked by either X-ray or neutron diffraction. The relative cheapness of the X-rays is counterbalanced by the fact that X-rays can only probe the surface of the ribbons where small crystalline impurities are more likely to occur, especially on the surface away from the copper wheel. Previous work<sup>18</sup> on amorphous alloys prepared by the melt-spinning technique has indeed shown some crystalline impurity peaks on the surface by X-ray scattering whereas the bulk, probed by neutron scattering was perfectly amorphous. The following discussion, largely based on references<sup>22, 23, 24</sup>, will therefore be restricted to neutron scattering.

### II.5.b. Properties of the neutron

The enormous amount of information made available by neutron scattering on the structure and dynamics of solids has recently been under the spotlight. Indeed, in 1994, C.G Shull and B.N. Brockhouse were awarded the Physics Nobel Prize<sup>25</sup> for their pioneering work on the use of the neutron as a probe for condensed matter. The uniqueness of the neutron as a probe of solid state lies in its basic properties listed in *Table II-1*.

Mass	$1.675 \times 10^{-27}$ kg
Charge	0
Spin	$\frac{1}{2}$
Magnetic dipole moment	$-1.913 \mu_N$

*Table II- 1 : Properties of the neutron*

A neutron, being an uncharged particle, can penetrate deeply into the sample where it is scattered by nuclear forces. Since its De Broglie wavelength is of the order of atomic spacing ( $\sim \text{\AA}$ ), interference effects occur and structural informations can be extracted. Furthermore, the wavelength of thermal neutrons is much bigger than the range of the nuclear forces causing the scattering ( $\sim \text{fm}$ ) rendering the scattering s-wave i.e. spherically symmetric.

Since the neutron also possesses a magnetic moment, it interacts with the unpaired electrons in magnetic atoms and magnetic information can be extracted from neutron scattering as well as structural information.

The energy  $E$  of a neutron of wavevector  $\mathbf{k}$ , wavelength  $\lambda$  and velocity  $\mathbf{v}$  is given

$$\text{by :} \quad E = \frac{\hbar^2 k^2}{2m} = \frac{1}{2}mv^2 = \frac{h^2}{2m\lambda^2} \quad \text{Eq. II- 1}$$

Hence, a neutron of velocity  $v = 2200 \text{ m.s}^{-1}$  (conventional value for thermal neutron) has a corresponding energy of 25 meV. The inelastic neutron scattering where the neutron exchanges a part of its energy with the scattering system will therefore be an extremely useful tool since the energy range of the excitations, either structural (e.g. phonons) or magnetic (e.g. magnons) is  $10^{-6}$ - $10^{-2}$  eV. For comparison, X-rays of similar  $\lambda$  have an energy of several keVs and inelastic study would require an energy resolution of  $10^{-6}$ - $10^{-2} / 10^3$  !

### II.5.c. Scattering cross-sections

#### II.5.c.1. Definitions

In a scattering process, an incoming neutron beam of flux  $\phi$  and wavevector  $\mathbf{k}$  is incident on a target. The outgoing neutrons, after having interacted with the scattering system, are analysed by a detector sustaining a solid angle  $d\Omega$  (see *Figure II- 5*). Any neutron experiment measures the number of neutrons scattered per second into that solid angle  $d\Omega$ . However, one can differentiate between experiments where the energy of the scattered neutrons is analysed and those where all the neutron are counted, regardless of their energies. Consequently, there are two quantities of interest in a neutron scattering experiment : the partial differential cross-section  $d^2\sigma/d\Omega dE'$  and the differential cross-section  $d\sigma/d\Omega$ . Their definitions are given by the following equations :

$$\frac{d^2\sigma}{d\Omega dE'} = \frac{N^0 \text{ of neutrons scatt./s into } d\Omega \text{ with final energy between } E' \text{ and } E'+dE'}{\phi \text{ } d\Omega \text{ } dE'}$$

$$\frac{d\sigma}{d\Omega} = \frac{N^0 \text{ of neutrons scatt./s into } d\Omega}{\phi \text{ } d\Omega} = \int_0^{\infty} \frac{d^2\sigma}{d\Omega dE'} dE' \quad \text{Eq. II- 2}$$

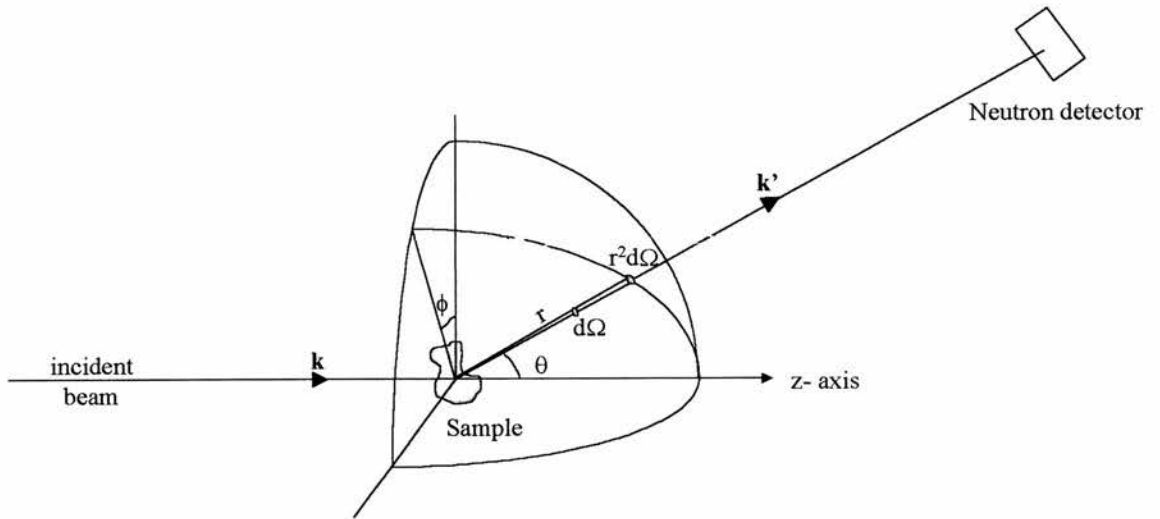


Figure II- 5 : Geometry of the scattering problem

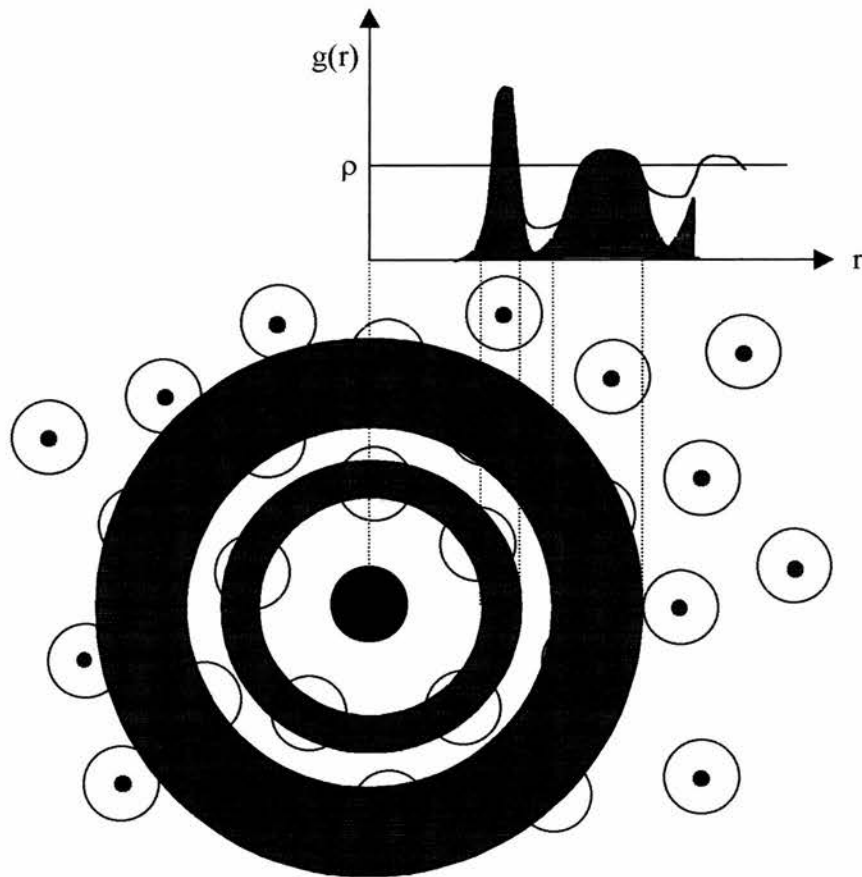


Figure II- 6 : representation of a pair distribution function in an amorphous solid.

### II.5.c.2. Partial differential cross-section in the general case

A more accurate description of the scattering system and the neutron is now required to derive an expression for the differential cross-section. Ignoring the spin of the neutron, the state of the neutron before being scattered (respectively after) is entirely described by its wavevector  $\mathbf{k}$  (resp  $\mathbf{k}'$ ) and consequently its wavefunction  $\psi_{\mathbf{k}}$  (resp.  $\psi_{\mathbf{k}'}$ ). Similarly, the initial (resp. final) state of the scattering system can be characterised by an index  $\lambda$  (resp  $\lambda'$ ) or a wavefunction  $\chi_{\lambda}$  (resp.  $\chi_{\lambda'}$ ). The origin of the scattering system being arbitrarily set up, it is possible to ascribe the position of the  $j$ -th nucleus to be  $\mathbf{R}_j$  ( $j = 1 \dots N$ ) and  $\mathbf{r}$  that of the neutron and to define  $\mathbf{x}_j = \mathbf{r} - \mathbf{R}_j$ . The differential cross-section is then given by :

$$\left(\frac{d\sigma}{d\Omega}\right)_{\lambda \rightarrow \lambda'} = \frac{1}{\phi} \frac{1}{d\Omega} \sum_{\mathbf{k}' \text{ in } d\Omega} W_{\mathbf{k},\lambda \rightarrow \mathbf{k}',\lambda'} \quad \text{Eq. II- 3}$$

In Eq. II- 3,  $W_{\mathbf{k},\lambda \rightarrow \mathbf{k}',\lambda'}$  is the number of transitions per second from the state ( $\mathbf{k}$ ,  $\lambda$ ) to the state ( $\mathbf{k}'$ ,  $\lambda'$ ) and is given by the Fermi golden rule :

$$\sum_{\mathbf{k}' \text{ in } d\Omega} W_{\mathbf{k},\lambda \rightarrow \mathbf{k}',\lambda'} = \frac{2\pi}{\hbar} \rho_{\mathbf{k}'} \left| \langle \mathbf{k}'\lambda' | V | \mathbf{k}\lambda \rangle \right|^2 \quad \text{Eq. II- 4}$$

$V$  is the interaction potential of the neutron/scattering system, and  $\rho_{\mathbf{k}'}$ , the number of momentum states in  $d\Omega$  per unit energy range for neutrons in the state  $\mathbf{k}'$ . Using the usual box normalisation of volume  $V$ , one obtains:

$$\rho_{\mathbf{k}'} = \frac{V}{(2\pi)^3} k' \frac{m}{\hbar} d\Omega \quad \text{Eq. II- 5}$$

The wavefunction of the neutron is a plane wave is :  $\psi_{\mathbf{k}} = \langle \mathbf{r} | \mathbf{k} \rangle = \frac{1}{\sqrt{V}} e^{i\mathbf{k}\cdot\mathbf{r}}$ ,

therefore :

$$\langle \mathbf{k}'\lambda' | V | \mathbf{k}\lambda \rangle = \frac{1}{V} \int e^{-i\mathbf{k}'\cdot\mathbf{r}} \chi_{\lambda'}^* V \chi_{\lambda} e^{i\mathbf{k}\cdot\mathbf{r}} d\mathbf{r} \quad \text{Eq. II- 6}$$

Using Eq. II- 5, Eq. II- 3 becomes :

$$\left(\frac{d\sigma}{d\Omega}\right)_{\lambda \rightarrow \lambda'} = V \frac{k'}{k} \left(\frac{m}{2\pi\hbar^2}\right)^2 \left| \langle \mathbf{k}' \lambda' | V | \mathbf{k} \lambda \rangle \right|^2 .$$

It can be seen, from Eq. II- 6 that the volume V of the normalisation will disappear as required. To obtain the differential cross-section, we must take the conservation of energy  $E + E_\lambda = E' + E_{\lambda'}$ , where E and  $E_\lambda$  (resp.  $E'$  and  $E_{\lambda'}$ ) are the initial (resp. final) energies of the neutron and the scattering system into consideration. Thus,

$$\left(\frac{d^2\sigma}{d\Omega dE'}\right)_{\lambda \rightarrow \lambda'} = V \frac{k}{k'} \left(\frac{m}{2\pi\hbar^2}\right)^2 \left| \langle \mathbf{k}' \lambda' | V | \mathbf{k} \lambda \rangle \right|^2 \delta(E + E_\lambda - E' - E_{\lambda'}) . \quad \text{Eq. II- 7}$$

The potential V of the whole system is  $V = \sum_j V_j(\mathbf{r} - \mathbf{R}_j) = \sum_j V_j(\mathbf{x}_j)$  inserted in Eq.

II- 6 gives  $\langle \mathbf{k}' \lambda' | V | \mathbf{k} \lambda \rangle = \frac{1}{V} \sum_j V_j(\boldsymbol{\kappa}) \langle \lambda' | \exp(i\boldsymbol{\kappa} \cdot \mathbf{R}_j) | \lambda \rangle$  where  $\boldsymbol{\kappa} = \mathbf{k} - \mathbf{k}'$  is the scattering

vector,  $V_j(\mathbf{k}) = \int V_j(\mathbf{x}_j) e^{i\mathbf{k} \cdot \mathbf{x}_j} d\mathbf{x}_j$  is the Fourier transform of the potential function

for the j-th nucleus and  $\langle \lambda' | \exp(i\boldsymbol{\kappa} \cdot \mathbf{R}_j) | \lambda \rangle = \int \chi_{\lambda'}^* \exp(i\boldsymbol{\kappa} \cdot \mathbf{R}_j) \chi_\lambda d\mathbf{R}$ .

Introducing the well-known Fermi pseudo-potential<sup>22, 23, 24</sup> for the j-th nucleus having a scattering length  $b_j$ :  $V_j(\mathbf{x}_j) = \frac{2\pi\hbar^2}{m} b_j \delta(\mathbf{x}_j)$  gives :

$$\left(\frac{d^2\sigma}{d\Omega dE'}\right)_{\lambda \rightarrow \lambda'} = \frac{k}{k'} \left| \sum_j b_j \langle \lambda' | e^{i\boldsymbol{\kappa} \cdot \mathbf{R}_j} | \lambda \rangle \right|^2 \delta(E + E_\lambda - E' - E_{\lambda'}) .$$

Let H be the hamiltonian of the scattering system such that  $H | \lambda \rangle = E_\lambda | \lambda \rangle$ , one can rearrange the above expression to obtain, posing  $\hbar\omega = E - E'$  :

$$\left(\frac{d^2\sigma}{d\Omega dE'}\right)_{\lambda \rightarrow \lambda'} = \frac{k}{k'} \sum_{j, j'} b_j b_{j'} \int_{-\infty}^{+\infty} \langle \lambda | \exp(-i\boldsymbol{\kappa} \cdot \mathbf{R}_{j'}) | \lambda' \rangle \times \\ \langle \lambda' | \exp(i\mathbf{H}t / \hbar) \exp(i\boldsymbol{\kappa} \cdot \mathbf{R}_j) \exp(-i\mathbf{H}t / \hbar) | \lambda \rangle \exp(-i\omega t)$$

Summing over all possible final states  $\lambda'$  and averaging over  $\lambda$  gives :

$$\left( \frac{d^2\sigma}{d\Omega dE'} \right) = \frac{k}{k'} \frac{1}{2\pi\hbar} \sum_{j,j'} b_j b_{j'} \int_{-\infty}^{+\infty} \langle \exp(-i\mathbf{k}\cdot\mathbf{R}_{j'}(0)) \exp(i\mathbf{k}\cdot\mathbf{R}_j(t)) \rangle \exp(-i\omega t) dt \quad \text{Eq. II- 8}$$

where the Heisenberg representation  $A(t) = \exp(iHt/\hbar) A \exp(-iHt/\hbar)$  and the definition

$$\langle B \rangle = \sum_{\lambda} \rho_{\lambda} \langle \lambda | B | \lambda \rangle$$

### II.5.c.3. coherent and incoherent scattering

Due to the presence of spin or isotopes, the scattering lengths  $b_j$ 's vary from one nucleus to another. The  $b_j$ 's can be distributed in many ways inside the system. Using a stochastic argument, one can replace  $b_j b_{j'}$  in Eq. II- 8 by  $\overline{b_j b_{j'}}$ . Assuming that there is no correlation between  $b_j$ 's gives :  $\overline{b_j b_{j'}} = (\overline{b})^2$  for  $j' \neq j$  and  $\overline{b_j b_{j'}} = \overline{b^2}$  for  $j'=j$ . Therefore, Eq. II- 8 can be separated in two parts :

$$\left( \frac{d^2\sigma}{d\Omega dE'} \right)_{\text{coh}} = \frac{\sigma_{\text{coh}}}{4\pi} \frac{k}{k'} \frac{1}{2\pi\hbar} \sum_{j,j'} \int_{-\infty}^{+\infty} \langle \exp(-i\mathbf{k}\cdot\mathbf{R}_{j'}(0)) \exp(i\mathbf{k}\cdot\mathbf{R}_j(t)) \rangle \exp(-i\omega t) dt \quad \text{Eq. II- 9}$$

$$\left( \frac{d^2\sigma}{d\Omega dE'} \right)_{\text{incoh}} = \frac{\sigma_{\text{incoh}}}{4\pi} \frac{k}{k'} \frac{1}{2\pi\hbar} \sum_j \int_{-\infty}^{+\infty} \langle \exp(-i\mathbf{k}\cdot\mathbf{R}_j(0)) \exp(i\mathbf{k}\cdot\mathbf{R}_j(t)) \rangle \exp(-i\omega t) dt \quad \text{Eq. II- 10}$$

$$\text{where } \sigma_{\text{coh}} = 4\pi (\overline{b})^2 \text{ and } \sigma_{\text{incoh}} = 4\pi (\overline{b^2} - (\overline{b})^2).$$

Eq. II- 9 can be rewritten as  $\left( \frac{d^2\sigma}{d\Omega dE'} \right)_{\text{coh}} = \frac{\sigma_{\text{coh}}}{4\pi} \frac{k}{k'} N S(\kappa, \omega)$  with  $S(\kappa, \omega)$  known as the scattering function of the system. Its Fourier Transforms of use are termed, the intermediate  $I(\kappa, t) = \text{FT}_{\text{time}} S(\kappa, \omega)$  and the time dependent correlation functions  $G(\mathbf{r}, t) = \text{FT}_{\text{time and space}} S(\kappa, \omega)$ .

### II.5.c.4. the scattering law for amorphous materials

The problem now is to determine the average  $\langle \exp(-i\mathbf{k}\cdot\mathbf{R}_{j'}(0)) \exp(i\mathbf{k}\cdot\mathbf{R}_j(t)) \rangle$  in Eq. II- 8 for an amorphous material. For a crystal, the  $\mathbf{R}_j$ 's are located on lattice points (neglecting displacements from atomic position, i.e. considering only elastic scattering)

and the sum over  $j$  gives :  $\sum_{\tau} \delta(\kappa - \tau)$  where  $\tau$  is a reciprocal lattice vector. This will be developed in more detail in the next section.

For an amorphous solid, however, there is not such a thing as a lattice and one is reduced to consider some kind of average distances between the atoms. The static pair correlation function (see *Figure II- 6*) is the most widely used tool to describe amorphous solid. It is zero for distances less than the first nearest neighbours separation, tends towards the mean density  $\rho$  and displays peaks at the average interatomic distances. In the static approximation (where a relaxed energy resolution is assumed and the incident neutron energy is much greater than the energy of the responding states such that  $E_{\lambda} - E_{\lambda'} = 0$ ), the coherent scattering due to a monoatomic amorphous solid is given by :

$$S(\kappa) = 1 + \int (g(r) - \rho) \sin(\kappa \cdot r) dr \quad \text{with} \quad g(\mathbf{r}) = \sum_{j \neq 0} \langle \delta(\mathbf{r} - \mathbf{R}_j + \mathbf{R}_0) \rangle$$

is the static pair distribution function. Since  $g(\mathbf{r}) = g(|\mathbf{r}|)$ , one obtains,

$$S(\kappa) = 1 + \frac{4\pi}{\kappa} \int (g(r) - \rho) \sin(\kappa r) r dr \quad \text{Eq. II- 11}$$

From *Eq. II- 11*, it can be seen that when  $\kappa r \gg 1$ ,  $S(\kappa)$  tends towards unity as required and for  $\kappa r = 0$ ,  $S(\kappa) = 1 + \int (g(r) - \rho) dr$  is related to the density fluctuations in the material.

For a binary system AB, it is possible to define three partial pair distribution functions  $g_{AA}$ ,  $g_{AB}$  and  $g_{BB}$  and generalise the results obtained above. The relation between the coherent differential cross-section and the scattering function becomes more complicated. If  $x_A$  and  $x_B$  are the atomic fraction of elements A and B, *Eq. II- 11* is still valid but  $g(r)$  is replaced by :

$$g(r) = W_{AA} g_{AA}(r) / x_A + W_{BB} g_{BB}(r) / x_B + 2 W_{AB} g_{AB}(r) / x_A x_B$$

with  $W_{AA} = x_A^2 b_A^2 / (x_A b_A^2 + x_B b_B^2)$ ,  $W_{BB} = x_B^2 b_B^2 / (x_A b_A^2 + x_B b_B^2)$  and

$$W_{AB} = x_A x_B b_A b_B / (x_A b_A^2 + x_B b_B^2).$$

This is known as the Faber-Ziman formalism but the most used expressions are those given by Bathia and Thornton<sup>26</sup>. The partial correlation functions are replaced by the number-number  $S_{NN}(\kappa)$ , the concentration-concentration  $S_{CC}(\kappa)$  and the number

concentration  $S_{NC}(\kappa)$  functions which represent the topological short range order, the chemical short-range order and a measure of the randomisation of the mixture.

The great advantage of neutron scattering is that the neutron scattering lengths  $b$  of each elements varies from element to element and even from isotope to isotope. This implies that the weighting factor  $W_{ij}$  can be varied. When one of the constituents of the amorphous alloy has a scattering length that changes sign for different isotope (eg. Ni or Dy), it becomes possible to set the scattering length of that constituent to zero by appropriately choosing the isotope proportions. By investigating three samples  ${}^N A^N B$ ,  ${}^0 A^N B$ ,  ${}^N A^0 B$  where superscript  $N$  denotes the natural element and  $O$  the isotopic composition resulting in zero scattering length, the separation of the three partial pair distribution functions can be unambiguously achieved. Indeed, if  $b_A = 0$ ,  $g_{BB}(r)$  is readily obtained and vice versa. This is an extremely powerful technique<sup>27</sup> but unfortunately very expensive due to the price of the isotopes and the poor yield achieved in the preparation of amorphous ribbons and was therefore not used in the remainder of this thesis. However, several samples were checked for amorphicity and an example, obtained on D1B with a wavelength of 2.52Å, can be found in *Figure II- 7*.

### II.5.c.5. Scattering from crystalline materials

As part of this thesis is devoted to the study of the crystallisation processes in  $\alpha$ -RE-TM where crystalline phases appear if the sample is heated to sufficient temperatures, it seems appropriate to include the scattering law for crystalline materials. As mentioned in the previous paragraph, in a crystal, the atoms are located on lattice positions given by the crystal symmetry. In the ideal case,  $\mathbf{R}_j = \mathbf{l}$  where  $\mathbf{l}$  is a lattice vector. If thermal motion is taken into account,  $\mathbf{R}_j = \mathbf{l} + \mathbf{u}_j$  where  $\mathbf{u}_j$  is the displacement from equilibrium position . If the scattering is elastic ( $k'=k$ ), *Eq. II- 9* becomes :

$$\left( \frac{d^2 \sigma}{d\Omega dE'} \right)_{\text{coh}} = \frac{\sigma_{\text{coh}}}{4\pi} N \frac{(2\pi)^3}{V_0} \exp(-2W) \sum_{\tau} \delta(\mathbf{k} - \tau) \quad \text{Eq II- 12}$$

where  $V_0$  is the volume of the unit cell,  $\tau$  is a reciprocal lattice vector and  $2W$  is the Debye-Waller factor which can be expressed in terms of phonon modes if the theory is further refined. *Eq. II- 12* is equivalent to the well-known Bragg's law. Indeed, the reciprocal lattice vector  $\tau$  is, by definition, perpendicular to a set of crystal planes and its magnitude is  $\tau = 2 \pi / d$  where  $d$  is the spacing of the planes. As illustrated by



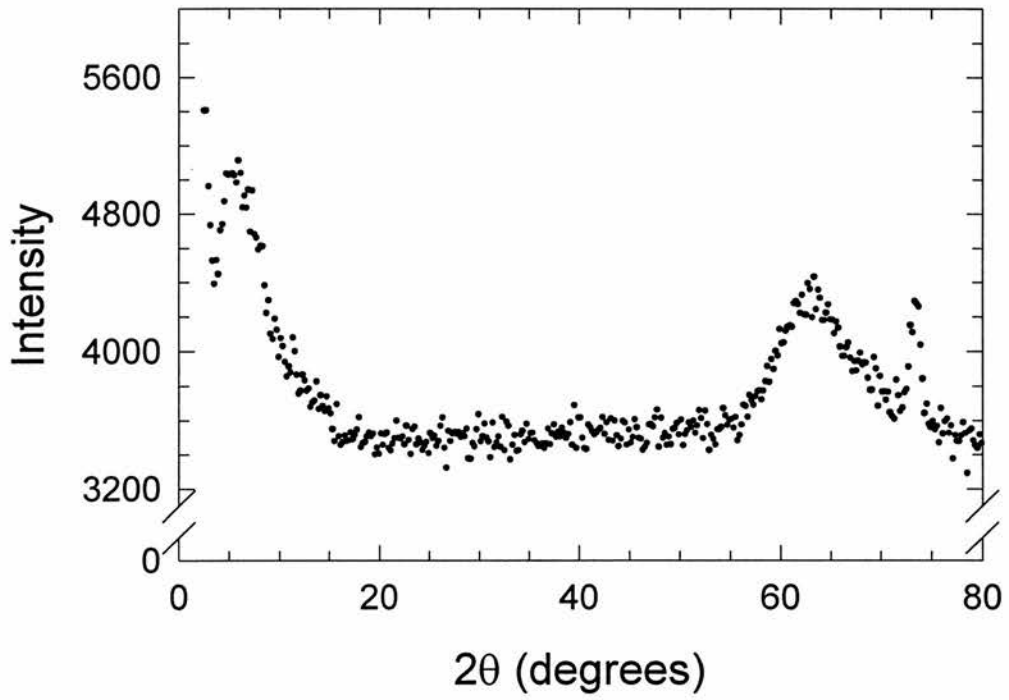


Figure II- 7 : diffraction pattern of  $\alpha\text{-Zr}_{76}\text{Ni}_{24}$  obtained on D1B.

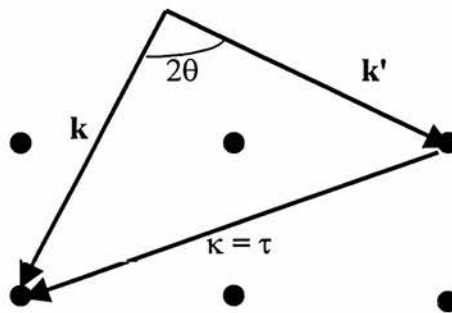


Figure II- 8 : Bragg's law ( $k = k'$ )

Figure II- 8,  $\tau$  is also given by  $\tau = 2k \sin (\theta)$ . Recalling,  $k = 2\pi / \lambda$  where  $\lambda$  is the neutron wavelength, we obtain the famous Bragg's law :

$$2d \sin (\theta) = \lambda$$

In this thesis, we will be concerned with powder diffraction for which many crystals have random orientations. For each incident wave-vector  $\mathbf{k}$ , there are many  $\mathbf{k}'$  such that the scattering vector  $\kappa = \mathbf{k} - \mathbf{k}'$  is a reciprocal lattice vector  $\tau$  but they will all lie on a cone, called the Debye-Scherrer cone.

If the crystal possesses more than one atom per unit cell, the position of the atom  $d$  in the unit cell  $l$  is now :  $\mathbf{R}_{ld} = \mathbf{l} + \mathbf{d} + \mathbf{u}(\mathbf{l}, \mathbf{d})$ . Eq II- 12 is transformed into :

$$\left( \frac{d^2\sigma}{d\Omega dE'} \right)_{\text{coh}} = N \frac{(2\pi)^3}{V_0} \sum_{\tau} \delta(\kappa - \tau) |F_N(\kappa)|^2 \quad \text{where} \quad F_N(\kappa) = \sum_{\mathbf{d}} \overline{b_{\mathbf{d}}} \exp(i\kappa \cdot \mathbf{d}) \exp(-W_{\mathbf{d}})$$

is called the nuclear unit-cell structure factor.

### II.5.c.6. *Magnetic scattering*

Finally, neutron scattering from magnetic materials should be mentioned here as it will be used during a part of this work. The calculations for magnetic neutron scattering are rather lengthy and can be found in the original papers by Bloch<sup>28</sup> and Schwinger<sup>29</sup> or by Halpern and Johnson<sup>30</sup> in more detail or in any good textbooks<sup>22,23,24</sup>. Therefore, only the main results will be presented in this paragraph. The magnetic scattering is due to the interaction of the magnetic dipolar moment of the neutron with the magnetic fields in the sample (of both spin and orbital origin). The general expression for the magnetic scattering cross-section is :

$$\left( \frac{d^2\sigma}{d\Omega dE'} \right)_{\sigma\lambda \rightarrow \sigma'\lambda'} = (\gamma r_0)^2 \frac{k}{k'} \left| \langle \sigma' \lambda' | \boldsymbol{\sigma} \cdot \mathbf{Q}_{\perp} | \sigma \lambda \rangle \right|^2 \delta(E_{\lambda} - E_{\lambda'} + \hbar\omega) \quad \text{Eq. II 13}$$

Where  $\gamma$  is the magnetic dipole moment of the neutron,  $r_0$  the classical radius of the electron ( $\mu_0 e^2 / 4\pi m_e = 2.818$  fm),  $\sigma$  the spin Pauli operator for the neutron and

$$\mathbf{Q}_{\perp} = \sum_{\mathbf{i}} \exp(i\kappa \cdot \mathbf{r}_{\mathbf{i}}) \left\{ \hat{\mathbf{x}} \times (\mathbf{s}_{\mathbf{i}} \times \hat{\mathbf{x}}) + \frac{i}{\hbar\kappa} (\mathbf{p}_{\mathbf{i}} \times \hat{\mathbf{x}}) \right\} \quad \text{Eq II- 14}$$

$\mathbf{s}_i$  and  $\mathbf{r}_i$  are respectively the spin and the position of the  $i$ -th electron. The first term in Eq. II- 14 is the contribution due to the spin of the electron whereas the second term arises from the orbital motion of the electrons. It can be shown that the operator  $\mathbf{Q}$  is the Fourier transform of the magnetisation :

$$\mathbf{Q} = \mathbf{Q}_S + \mathbf{Q}_L = -\frac{1}{2\mu_B} \mathbf{M}(\kappa)$$

Geometrically,  $\mathbf{Q}_\perp$  is the projection of  $\mathbf{Q}$  onto the plane perpendicular to  $\hat{\kappa}$  .

The analysis can be pushed further and the elastic magnetic cross-section is :

$$\left(\frac{d\sigma}{d\Omega}\right)_{el} = (\gamma r_0)^2 N \left(\frac{1}{2} g F(\kappa)\right)^2 \exp(-2W) \sum_{\alpha\beta} (\delta_{\alpha\beta} - \kappa_\alpha \kappa_\beta) \sum_l \exp(i\kappa \cdot \mathbf{l}) \langle S_0^\alpha \rangle \langle S_l^\beta \rangle$$

Where  $F(\kappa)$  is the magnetic form factor. For a ferromagnet aligned in the  $z$ -direction, the average spin values will be both equal to  $\langle S^z \rangle$  and the exponential sum will be non zero for  $\kappa = \tau$ , a reciprocal vector ie the signal from the magnetic scattering will add some intensities to the already existing nuclear peaks. For an antiferromagnet, the *magnetic* unit cell has to be considered and extra peaks, at different  $d$ -spacings than the nuclear peaks appear.

## II.6. Vibrating sample magnetometry

For DC magnetic measurements, an Oxford Instruments 3001 Vibrating Sample Magnetometer (VSM) with a 12 T superconducting magnet was used. The material under investigation is mounted in a delrin sample holder, chosen for its low diamagnetic background and ease to machine, at the end of a carbon fibre rod and inserted into an Oxford Instruments CF1200 continuous flow Helium Cryostat. The end of the cryostat lies inside a conventional NbSn superconducting magnet whose 10V-120A power supply can achieve fields up to 12T. Once a DC field is applied, the sample is vibrated at a constant frequency of 66 Hz with an amplitude of about 1.5mm along the vertical axis in a uniform applied field. Two pickup coils, placed above and below the sample, experience a change of the magnetic flux due to the motion of the sample and, according to Faraday's law, an emf, proportional to the rate of that change of flux, is therefore

induced in the two pickup coils. The induced emf, also proportional to the magnetic susceptibility of the sample, passes through a two-stage amplification process and is monitored by the VSM electronics and recorded on a computer via a standard RS232 connection. A schematic of the VSM is presented on *Figure II- 9*.

The VSM is calibrated by adjusting the gain of the second amplifier stage while measuring the saturation magnetisation of a Ni sphere (demagnetising factor of 1/3) of known mass. When possible, the Ni standard used had a similar magnetic dipole moment to the sample so that the primary stage amplifier gain remained the same. The value for Ni magnetic dipole moment per unit mass used for the calibration was that given by Aldred<sup>31</sup> (54.85 emug<sup>-1</sup> at 300K). The centre of vibration of the sample can be positioned at the exact centre of the sense coil arrangement, to within an accuracy of  $\pm 10\mu\text{m}$ , in order to achieve the maximum output signal.

The sample temperature is measured by a AuFe/Chromel thermocouple in direct contact with a copper heat exchanger situated below the sample. The temperature control (temperature range : 3.6 - 320 K) is achieved by an Oxford Instruments ITC4 temperature controller. A picture of the whole apparatus can be found on *Figure II- 10*.

## **II.7. AC susceptibility**

AC susceptibility is a simple method of probing both the static and dynamic magnetic and superconducting properties of materials. Its use for determining superconducting transition temperatures and critical current densities since the 60's<sup>32</sup> made the AC susceptometer an indispensable tool for the study of high TC's cuprates<sup>33</sup> in the late 80's. The interest in the dynamics of spin glass systems in the 70's and 80's also contributed to the popularity of the AC susceptometer in magnetics laboratories<sup>34</sup>. In the 90's, AC susceptibility measurements have been progressively superseded by SQUID and/or torque measurements with which better sensitivities can be achieved allowing the study of smaller samples or samples with weaker magnetic signals. If it is true that the sensitivity of the AC susceptometer is a drawback compared with newer techniques, it is however unrivalled for the study of dynamical processes as the frequency of the applied field can be varied over several decades. Compared with dc techniques, the ac susceptibility is also the only technique where the actual

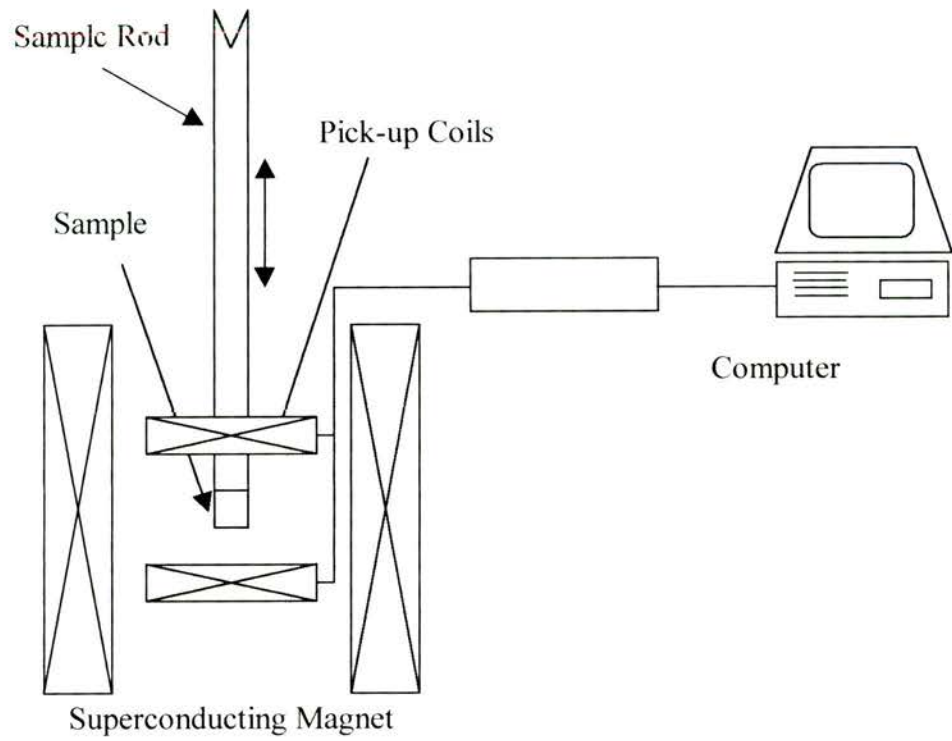


*Figure II- 9 : Schematic of the 12T Oxford Instruments VSM*



*Figure II- 10 : The Oxford Instruments VSM*

susceptibility ( $dM/dH$ ) is measured directly instead of measuring the gradient of the initial magnetisation curve. At last, the magnitude of the applied field is usually smaller with ac susceptometer than with dc techniques and the state probed by ac susceptibility is therefore much closer to the ground state, which can be crucial in the study of spin glasses.

The measurement of the ac susceptibility relies on the change of the mutual inductance of a set of two coil or the self-inductance of a single coil if a magnetic sample is inserted. Experimentally, the ac susceptometer operates as a modified Hartshorn bridge network : a primary coil produces a small ac field and the resulting emf, directly proportional to the derivative of the magnetisation of the sample, induced in the secondary (pick-up) coil wound around the sample is analysed. The in-phase and out-of-phase components (w.r.t. the driving current of the primary coil) of the out-of-balance voltage are proportional to the real  $\chi'$  and imaginary  $\chi''$  components of the susceptibility. A schematic of an ac susceptometer is given on *Figure II- 11*. It should be noted that the harmonics of the signal can also be detected for looking at non-linear effects such as those induced by intergrain couplings in HTc's superconductors.

In this study, the ac susceptibility measurements were made on the AC probe of the Oxford Instruments MagLab<sup>EXA</sup>. The design adopted by Oxford Instruments is similar to that of C. Rillo et al<sup>35</sup> where the sample moves between the two secondary coils. This setup does not give the best results for an ac susceptometer but it is more versatile as it can also be used for measuring the magnetisation of the sample by the extraction method (the sample is pulled from one of the secondary coils to the other in a time  $\Delta t$  and the magnetisation is simply proportional to the time integral of the emf over  $\Delta t$ ). Calibrations of the susceptibility are obtained by running a superconducting sample (Nb) with a known demagnetising factor (eg. a sphere for which  $D=1/3$ ) below the transition temperature for which  $\chi' = -1$ . As for a superconductor below  $T_c$ ,  $\chi'' = 0$ , this procedure also allows the phases (one for each frequency) between the pick-up voltage and the reference signal to be set correctly.

## II.8. Heat capacity measurements

The heat capacity of a solid is defined by :

$$C_v = \frac{\partial u}{\partial T}$$

where  $u$  is the thermal energy density and  $T$  the temperature.

The results are often given in terms of the specific heat which is the heat capacity per kg or per mole. It should be noted here that there is a difference between the heat capacity at constant volume  $C_v$  and at constant pressure  $C_p$  but that it is in general ignored for solids (whereas it cannot be ignored for gases where the ratio  $C_p/C_v$  is  $1 + 2/p$ ,  $p$  being the number of degrees of freedom).

Heat capacity measurements provide useful information on the nature of transitions in solids. For instance, its measure allows the order of the transition to be determined in the Ehrenfest-Landau classification of phase transitions scheme (a transition is of the  $n$ th order if all the derivatives of the thermodynamic potential of order  $n-1$  are continuous but one of the derivatives of the order  $n$  is discontinuous). A good illustration of this point is given by the superconducting transition in niobium where a jump in the specific heat at the transition is seen and the superconducting transition is therefore of the second order<sup>36</sup>.

Experimentally, the heat capacity is measured as the change of heat input divided by the temperature change :

$$C = \frac{\Delta Q}{\Delta T}$$

According to the first law of thermodynamics,  $\Delta U = \Delta Q + \Delta W$  where  $\Delta Q$  is the heat given to the system and  $\Delta W$  is the work done on the system and as no work is done on the system, it is easy to see that the experimental  $C$  equates to the theoretical  $C_v$ . During the experiment, the resulting changes are very small and the temperature needs to be known in one part in  $10^5$  which involves the use of a bridge<sup>37</sup>. A schematic of a heat capacity set-up is shown on *Figure II- 12*.

The microcalorimeter used for this study is the heat capacity probe of a MagLab<sup>EXA</sup>. For measurements above 2K, the magnet and cryostat used were the same



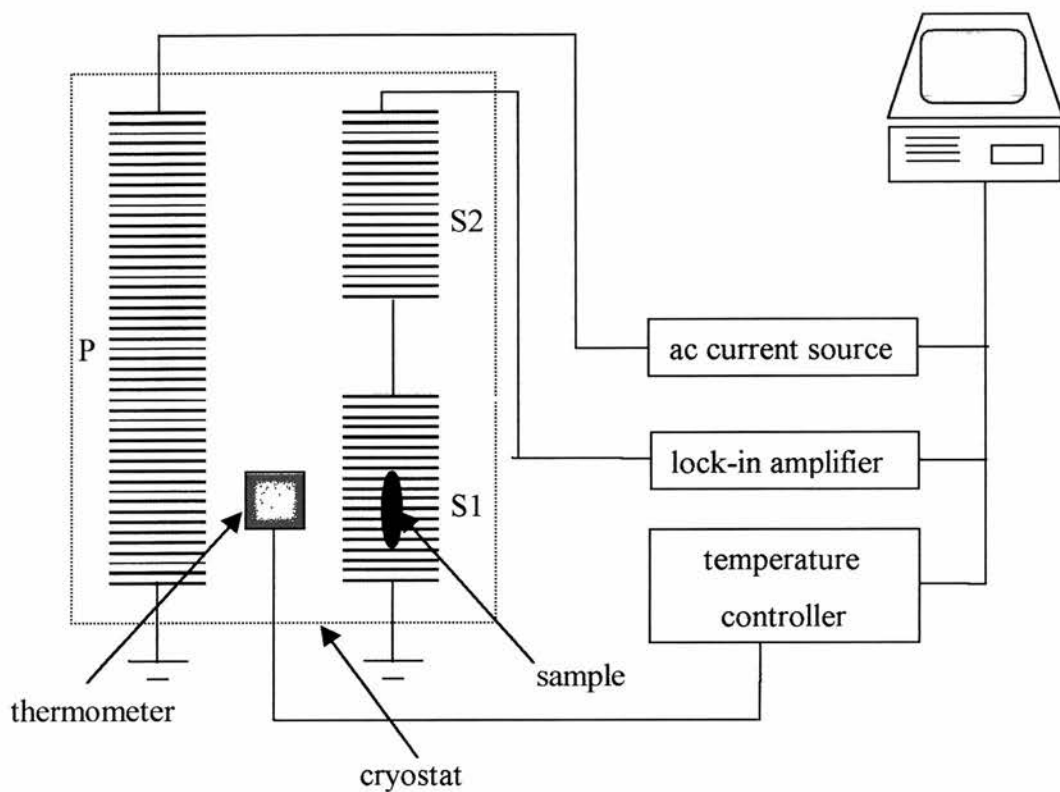


Figure II- 11 : Diagram of an ac susceptometer.  $P$  is the primary coil,  $S1$  and  $S2$  are the secondary coils (counter-wound).

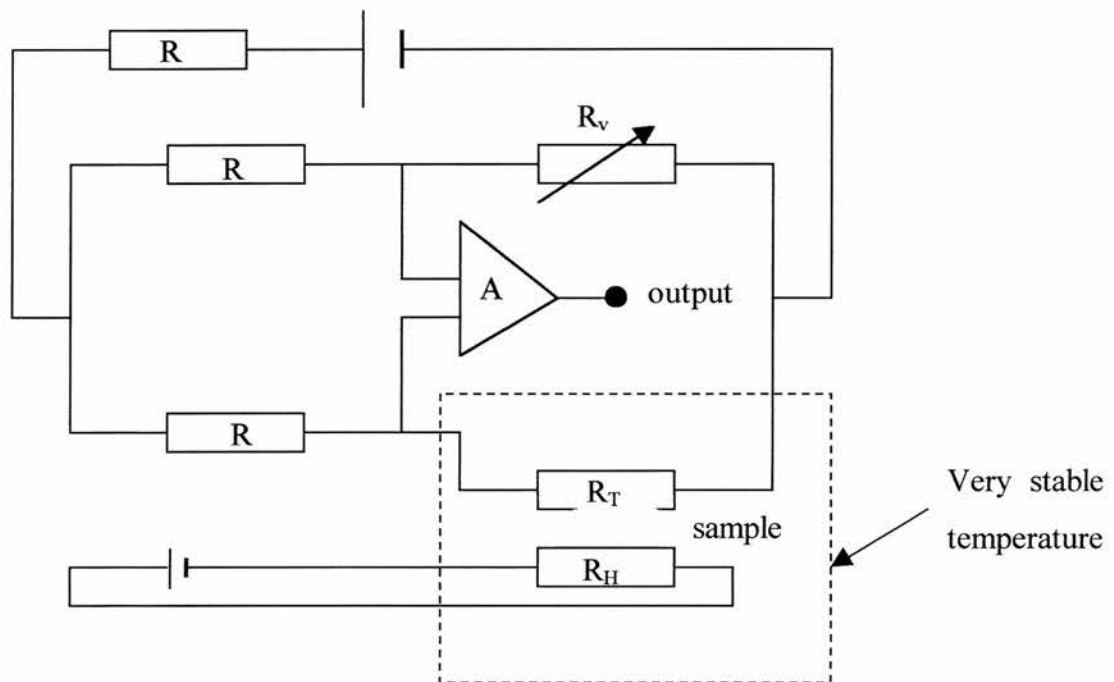


Figure II- 12 : schematic diagram of a microcalorimeter.  $R$  are standard resistances,  $R_v$  is a variable resistance for balancing the bridge,  $R_T$  and  $R_H$  are the Thermometer and Heater resistances respectively. The power supply to the heater resistance has been simplified for clarity.



as for the ac susceptometer. The measurements done below 2K were performed at Oxford Instruments factory in Tubney, Oxfordshire, using a prototype  $^3\text{He}$  insert.

To lower the vapor pressure above the liquid  $^3\text{He}$  and thereby reduce the boiling temperature of the  $^3\text{He}$ , the  $^3\text{He}$  bath was pumped on by a sorption pump placed in the sample space of the MagLab and kept at around 1.5 K (base temperature obtained by pumping on the  $^4\text{He}$  bath).

Samples were mounted on a sapphire chip where a serpentine metallic heater was evaporated ( $R_H$ ) and the temperature was monitored by a Cernox temperature sensor. The only assembly is shown<sup>38</sup> on *Figure II- 13*. The procedure for mounting the sample involves sticking a polished surface of a sample (for ribbons, the surface is sufficiently flat to directly mount it) onto the back of the heater with highly conductive Wakefield grease. The contribution of the assembly sapphire platform + Cernox to the specific heat is very small and taken into account by performing a measurement with no sample on. As the Cernox displays magnetoresistance effects, this calibration involves measurements at different fields. Each chip was also tested with a "typical" sample, such as a piece of copper. The contribution from the grease is reduced by using as little grease as possible and accounted for by carefully weighing the sample and the sample with the grease on (the contribution from the grease is known). Once thermal equilibrium is reached for a given temperature, a power step is applied to the sample and the resistance of the Thermometer as a function of time is measured and converted into temperature. As the decay towards new equilibrium temperature is exponential ( $1 - \exp(-t/\tau)$ ), the temperature evolution is fitted and the time constant  $\tau$ , directly proportional to the heat capacity, can be extracted from the data. A typical measurement usually involves only one transient pair (see *Figure II- 14*) for the power but can be repeated as many times as is necessary to improve the statistics.

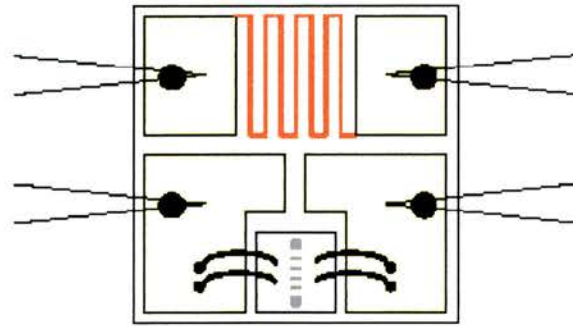


Figure II- 13 : the microcalorimeter "chip" showing the heater on the top part and the Cernox at the bottom

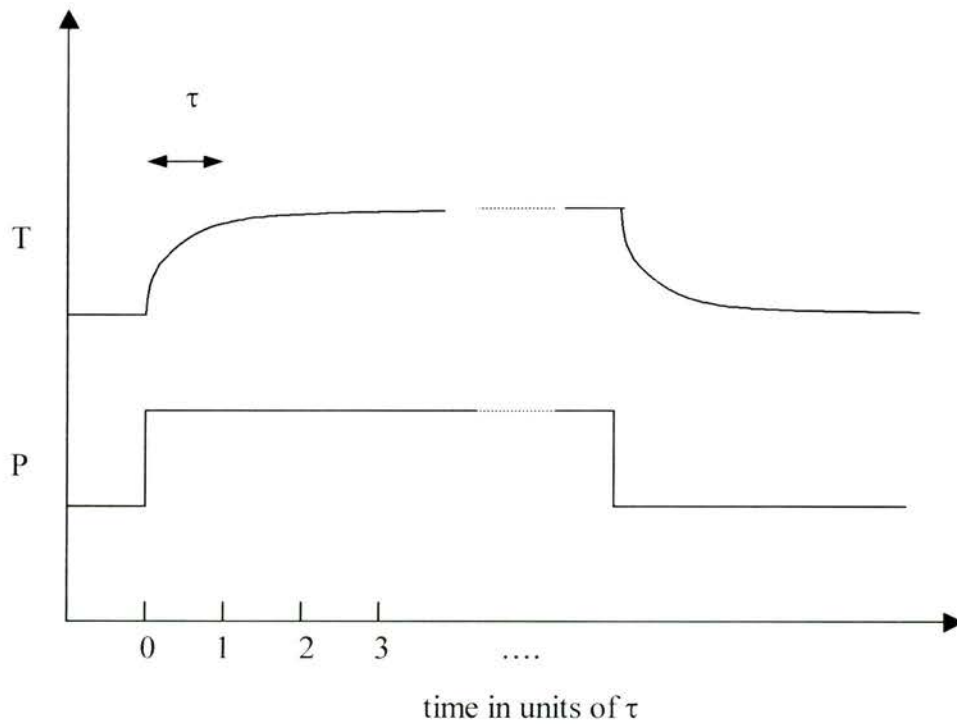


Figure II- 14 : Power and temperature for a transient pair.

## II.9. Mössbauer spectroscopy

The principle behind Mössbauer spectroscopy is the emission and resonant absorption of  $\gamma$  rays related to transitions between nuclear levels, more specifically between the fundamental and the excited Mössbauer levels<sup>39</sup> observed for Mössbauer isotopes such as  $^{57}\text{Fe}$ ,  $^{61}\text{Ni}$ ,  $^{119}\text{Sn}$ ,  $^{67}\text{Zn}$ ,  $^{155}\text{Gd}$ ,  $^{161}\text{Dy}$ ,  $^{170}\text{Yb}$ ,  $^{153}\text{Eu}$  and  $^{197}\text{Au}$ . For this study, only  $^{57}\text{Fe}$  was used.

For free atoms, the conservation laws of energy and angular momentum imply that the energy of a photon emitted by a transition between nuclear levels is too small to be able to excite this same transition again due to the recoil energy; in other words, the resonance phenomenon is forbidden. However, for atoms embedded in a solid, the nucleus cannot recoil arbitrarily and there is a finite probability  $P$  that the photon is emitted without exciting any phonons<sup>40</sup>. The probability  $P$  is bigger for smaller  $\gamma$  rays energies and increases when the temperature of the crystal decreases. This is the reason why experiments on  $^{57}\text{Fe}$  ( $\gamma$  energy : 14.4 keV) use a source at room temperature whereas those on, for instance,  $^{155}\text{Gd}$  ( $\gamma$  energy : 86.6 keV) use a source maintained at a low temperature (generally 4.2K). Mössbauer spectroscopy compares the displacement of the Mössbauer and fundamental nuclear levels of a probe nucleus placed in an absorber (sample) with the same levels for the same nucleus in a source.

Experimentally, the emission of monochromatic  $\gamma$  rays is achieved by placing the emitter in a solid (source). The source used for this study was a 50mCi  $^{57}\text{Co}$  source in a Rh matrix. In order to see the transitions between levels in the sample, the energies must be scanned. Usually, the source is moved backwards and forwards and the resulting change in the photon energy by Doppler effect is sufficient to induce the transitions. A schematic of the apparatus is shown on *Figure II- 15*. There are several ways of varying the velocity of the drive<sup>41</sup> and the constant acceleration mode was chosen for this study. The  $\gamma$  are detected with an argon/methane proportional counter. Data are acquired in 512 velocity channels using a PC fitted with an MCA interface card and the experimental setup is a modified Harwell spectrometer. The sample is placed in an Oxford Instruments blue cryostat where two thin mylar windows in the tail let the  $\gamma$  through. The He bath can be pumped through a capillary by a rotary pump. The temperature is regulated by an Oxford Instruments Temperature Controller ITC4 and the typical operating range is 1.5- 320 K.

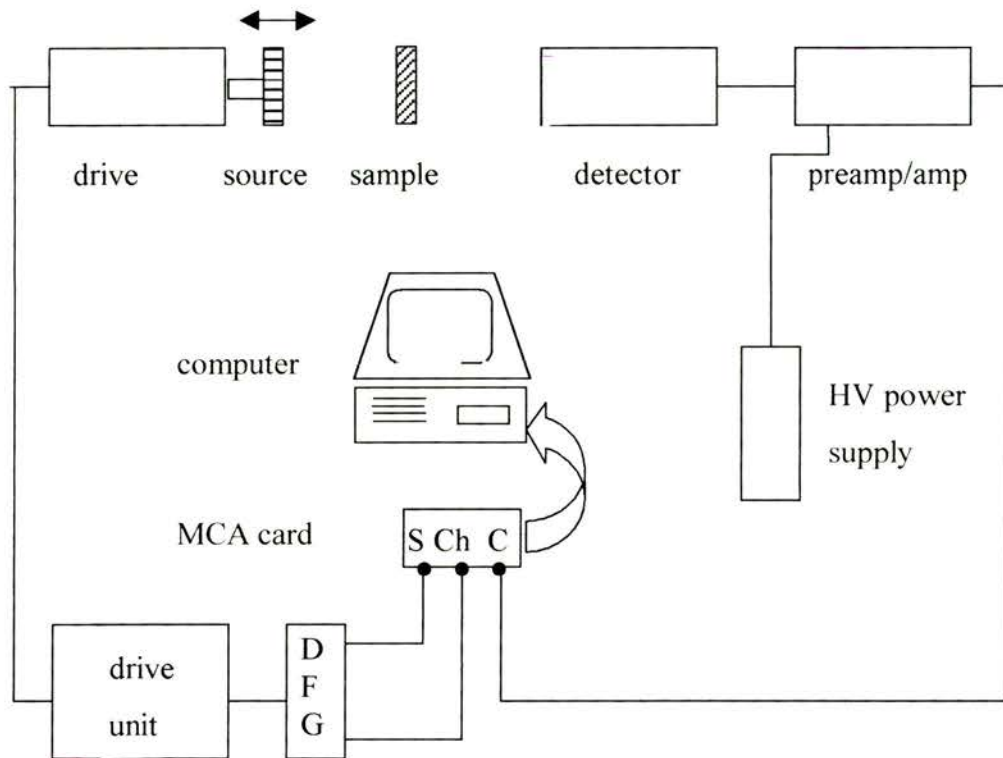


Figure II- 15 : Schematic of a Mössbauer spectrometer. The S, Ch, C and DFG represent Start, Channel, Count and Digital function Generator.



Figure II- 16 : The Mössbauer spectrometer used for this study.

The ensemble source, sample and detector is placed in a lead-lined cabinet to minimise radiation. A picture of the whole experimental assembly can be seen on *Figure II- 16*.

For a nucleus in a sample, these energy shifts are due to the electric and magnetic hyperfine interactions between the nucleus and its environment and will be described below. A schematic diagram of the energy levels for  $^{57}\text{Fe}$  and the corresponding Mössbauer spectra can be found on *Figure II- 17*.

- The *isomer shift* arises from the fact that the nucleus is not point-like but has a finite size and a positive electric charge. There is a finite probability to find s- electrons at the nucleus and the interaction between electronic and nuclear charges induces a shift between the Mössbauer and the fundamental levels. As the electronic configuration and the atomic environment is different between the source and the absorber, Mössbauer spectroscopy allows the difference of the electronic densities between the source and the absorber to be measured. The resulting Mössbauer spectrum is shifted by  $\delta$ .
- The *quadrupole splitting* is the consequence of the non-spherical distribution of the nuclear charge. Indeed, a non-spherical nucleus has a quadrupolar moment which interacts with the electric field gradient in the sample and this quadrupolar electric interaction partially lifts the degeneracy of the nuclear levels. Consequently, two lines separated by  $\Delta$  appear in the Mössbauer spectrum.
- The *magnetic Zeeman* interaction is the most interesting of the three interactions for the study of the magnetic properties of solids. The effective magnetic field completely removes the degeneracy of the nuclear levels. Selection rules impose  $\Delta_m = 0$  or  $\pm 1$ . For  $^{57}\text{Fe}$ , this generates six lines on the Mössbauer spectrum, the separation between the first and the sixth line is called the hyperfine field splitting (H).

The real spectra are a combination of these effects and are non-linearly fitted with the Recoil software package<sup>42</sup>.

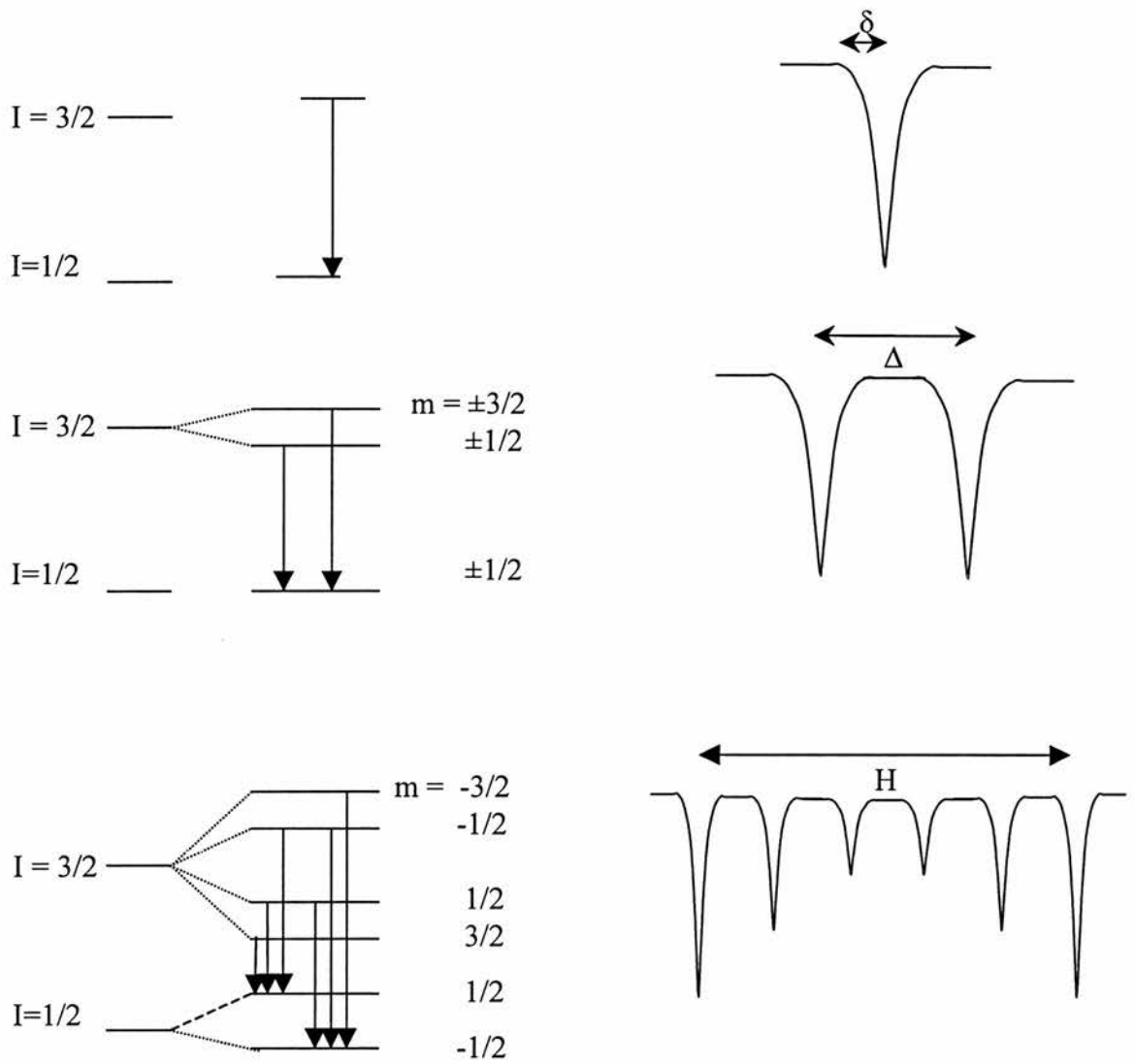


Figure II- 17 (left) : schematic diagram of the energy levels and the allowed transition (arrows) for  $^{57}\text{Fe}$  due to (a) the isomer shift (top), (b) the quadrupole splitting (middle) and (c) the magnetic Zeeman splitting (bottom).

(right) the corresponding Mössbauer spectra.



## References for Chapter II

---

- <sup>1</sup> S.R Elliott, Physics of amorphous materials (1990, second edition)
- <sup>2</sup> Smithells metals reference book Oxford : Butterworth-Heinemann, 1998, 7th ed. ; edited by E.A. Brandes and G.B. Brook
- <sup>3</sup> W. Klement, R.H. Villens, P. Duwez, Nature, **187** (1960) 869
- <sup>4</sup> W.L. Johnson, Prog. Mat. Sci. **30** (1986) 81
- <sup>5</sup> J. W. Mayer et al, Nucl. Instr. Methods **182/183** (1981) 1
- <sup>6</sup> A. Ali, W. Grant and P. J. Grundy, Philos. Mag. B **37** (1978) 353
- <sup>7</sup> R.B. Schwartz and W.L. Johnson, Phys. Rev. Lett. **51** (1983) 415
- <sup>8</sup> C.C. Koch et al, Appl. Phys. Lett. **43** (1983) 1017
- <sup>9</sup> J. Flechon et al, Bull. Soc. Chim. de France **7-8** (1982) 1257
- <sup>10</sup> G. Marchal, P. Mangin and C. Janot, Philos. Mag. **32** (1975) 1007
- <sup>11</sup> Y. Shimada and H. Kojima, J. Appl. Phys **50** (1979) 1541 and *ibid*, **53** (1982) 3156
- <sup>12</sup> A. Donnadieu et al, J. de Phys. **C4 Suppl. N° 10 T42** (1981) 755
- <sup>13</sup> J. Bessot, Surfaces **124-128** 3
- <sup>14</sup> P.S. DiCarli and J.C. Jamieson, J. Chem. Phys. **31** (1959) 1675
- <sup>15</sup> O.V. Abramov et al, Poverkhn. **11** (1982) 149
- <sup>16</sup> P. Duwez, R.H. Willens, W. Klement, J. Appl. Phys. **31** (1960) 1136
- <sup>17</sup> J.R. Bedell, US Patent n° 3862.658 (1975)
- <sup>18</sup> R.I. Bewley, PhD thesis, University of Reading (1994)
- <sup>19</sup> H. Hillman and H.R. Hilzenger , Rapidly Quenched metals III, Vol. I, The metal Society London (1978), 22
- <sup>20</sup> H.H. Liebermann, *ibid*, 34
- <sup>21</sup> P. Cremer, Ecole d' Hiver sur les Amorphes Métalliques, 63
- <sup>22</sup> G.L. Squires, Introduction to the theory of thermal neutron scattering, Cambridge University Press (1978)
- <sup>23</sup> S.W. Lovesey, Theory of neutron scattering from condensed matter, Clarendon Press - Oxford (1984)
- <sup>24</sup> Hercules Courses, 1992
- <sup>25</sup> The Nobel prize speech can be found in Les Prix Nobel, Ed. by Tore Frängsmyr
- <sup>26</sup> A.B. Bathia and D.E. Thornton, Phys. Rev. B **2** (1970) 3004
- <sup>27</sup> G.W. Neilson and J.E. Enderby, Proc. Roy. Soc. **A390** (1983) 353
- <sup>28</sup> F. Bloch, Phys. Rev. **50** (1936) 259 and *ibid* **51** (1937) 994
- <sup>29</sup> J. Schwinger, Phys. Rev. **51** (1937) 544
- <sup>30</sup> O. Halpern and M.H. Johnson, Phys. Rev. **55** (1939) 898
- <sup>31</sup> A.T. Aldred, Phys. Rev. B **11** (1975) 2597
- <sup>32</sup> E. Maxwell and M. Strogin, Phys. Rev. Lett. **10** (1963) 212
- <sup>33</sup> T. Ishida and R.B. Goldfarb, Phys. Rev. B **41** (1990) 8937
- <sup>34</sup> V. Cannella, J.A. Mydosh and J.I. Budnick, J. Appl. Phys. **42** (1971) 1689
- <sup>35</sup> C. Rillo et al, in Magnetic Susceptibility of Superconductors and other spin systems, Ed. R.A. Hein et al, Plenum press, New York, 1991, p 1.
- <sup>36</sup> N.E. Philips, Phys. Rev. **134** (1964) 385
- <sup>37</sup> M. de Podesta, Understanding Properties of matter, London UCL Press, 1996.
- <sup>38</sup> Heat Capacity Relaxation Probe, Oxford Instruments, July 2000.
- <sup>39</sup> R.L. Mössbauer, Z. Phys. **151**(1958) 124
- <sup>40</sup> A. Abragam, L' effet Mössbauer, Gordon and Bleach Science Publishers, New York, 1964
- <sup>41</sup> Mössbauer spectroscopy applied to inorganic chemistry, ed. by G.J. Long, Plenum Press, New York, 1987
- <sup>42</sup> 'Recoil' Mössbauer spectral analysis for Windows v1.0, K. Lagrec and D.G. Rancourt, University of Ottawa (1998)

# Chapter III : Muon Spin Rotation and Relaxation

## III.1 Introduction

The purpose of this chapter is to introduce the techniques of  $\mu$ SR and their extreme sensitivity to the static and dynamic local field environment around the implanted muons. The acronym  $\mu$ SR is widely used throughout the literature where it means either muon spin rotation, muon spin relaxation or muon spin resonance. The difference between these techniques is associated with the different possible geometries with which a  $\mu$ SR experiment can be performed. When a field is applied perpendicularly to the muon beam direction, an implanted muon precesses at a frequency dependent on the internal field it is sensing and the technique is referred to as muon spin rotation (also transverse geometry). Muon spin relaxation, also known as longitudinal geometry, corresponds to an applied field parallel to the muon momentum although in many cases, this field is zero. In this case, the spin of the muon does not precess but relaxes away from its initial direction. The third technique, muon spin resonance, is still in its infancy but is very similar to pulsed NMR : a static field is applied parallel to the initial muon spin polarisation (z) and an RF pulse is applied perpendicular to the z-direction.  $\mu$ SR has given some unique insights into the study of an exceptionally wide range of materials from magnets<sup>1</sup>, superconductors<sup>2</sup> and semiconductors<sup>3</sup> to biological systems<sup>4</sup>.

In the remainder of this chapter, the rotation and the relaxation techniques will be discussed since they are the only ones relevant in throughout this thesis for the study of superconductors (rotation) and magnetism (relaxation).

## III.2 Properties, production and decay of the muon

### III.2.a Properties of the muon

The muon, first identified in 1937 by Neddermeyer and Anderson<sup>5</sup> who were studying cosmic rays, belongs, along with the electron, to the lepton family. A summary of the properties of the muon can be found in *Table III- 1*.

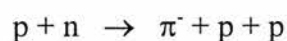
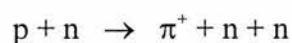
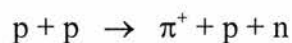


It can be seen that muons exist with either a positive ( $\mu^+$ ) or a negative charge ( $\mu^-$ ). The most common technique, and the one used for this work, involves  $\mu^+$  and therefore, in this thesis we shall ignore the  $\mu^-$  technique.

As a spin  $\frac{1}{2}$  particle, the muon does not sense the electric quadrupolar interaction and interacts only with the local magnetic field and this makes  $\mu$ SR a useful tool to probe the magnetic field distribution inside a sample.

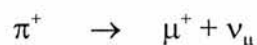
### III.2.b Production of a spin polarised beam

The muons are obtained from pion ( $\pi$ ) decay.  $\pi$  are produced by the interaction of a proton beam and a Graphite or Beryllium target via the elementary reactions :



Proton production at ISIS is achieved by accelerating  $H^+$  ions in a linear accelerator (linac), to an energy of 70 MeV. The electrons are then stripped from the  $H^+$  ions by a very thin alumina foil. The protons are further accelerated to 800MeV in a 52m diameter synchrotron ring, before they are extracted and sent to the target. At ISIS (Rutherford Laboratory, Chilton, Didcot, Oxfordshire) the muon target used is a 7mm thick water-cooled graphite plate. The ISIS synchrotron produces a *double* pulsed beam of protons with a frequency of 50 Hz. Indeed, each pulse contains *two* proton bunches each with a width of approximately 80 ns and a separation of 300 ns. Therefore, the muon beam will reflect this double pulse structure.

Once  $\pi^+$  have been produced when the protons hit the target, the positive muons  $\mu^+$  are subsequently obtained from the decay of positive pions  $\pi^+$  (the average lifetime of the  $\pi$  is 26ns) :



To understand how it is possible to obtain a polarised beam, it is useful to consider *Figure II- 1* where  $S_\mu$  (resp.  $S_\pi$  and  $S_\nu$ ) describes the spin of the muon (resp. pion and neutrino) and  $P_\mu$  (resp.  $P_\nu$ ) the momentum of the muon (resp. neutrino). As the spin of the pion is  $S_\pi = 0$ , the conservation of the angular momentum requires that the  $\mu^+$  and the  $\nu_\mu$  all together are in a  $S = 0$  state. The helicity of the  $\nu_\mu$  is -1 therefore its spin has to be antiparallel to its momentum. Hence it becomes evident from the conservation of momentum that the spin of the  $\mu^+$  is also antiparallel to its momentum and that the muons emerging from a particular direction will be 100% spin polarised. At the surface of the target, the pion decay occurs at rest and the muons emerge with a unique momentum of 29.8 MeV/c.

This is referred to as 'surface muon beam'. The production of muons from pions decaying in flight will not be discussed here since the experiments at ISIS were carried out on the MuSR spectrometer using a surface muon beam. The advantages of surface muons lie in the fact that they are 100% spin polarised and that their kinetic energies (4.12 MeV) are small which implies that they will be stopped by relatively thin samples (about 150 mg.cm<sup>-2</sup> corresponding to a few millimetres of sample). However, the drawbacks of surface muons are also due to this small kinetic energy since it implies that a transverse field of the order of a tenth of a Tesla strongly deviates the beam. Moreover, it requires the whole muon path must be evacuated as 1m of air is sufficient to stop the beam completely.

It should be noted that surface beams cannot contain any negative muons as any negative pions created at rest in the target will be immediately captured by target nuclei before they can decay into negative muons.

### **III.2.c Thermalisation of the muon**

Once the muons are produced, they are guided onto a sample . Several important concerns for the experimentalist then arise : how does the implantation of the muons take place ? How long does it take ? And more importantly : is the polarisation of the muons affected ?

The implantation and thermalisation of the muon is achieved in several successive steps and the whole process takes between 0.1ns and 1ns<sup>6</sup>. Firstly, the  $\mu^+$  is slowed down in the sample by ionisation of the atoms and scattering with electrons until

Mass	$105.6 \text{ MeV}/c^2$
Lifetime	$2.197 \mu\text{s}$
Charge	$\pm e$
Spin	$\frac{1}{2}$
Magnetic moment	$3.183 \mu_p$
Gyromagnetic ratio	$8.5161 \cdot 10^8 \text{ rad}\cdot\text{s}^{-1}\cdot\text{T}^{-1}$ or $13.55 \text{ kHz}\cdot\text{G}^{-1}$

Table III- 1 : fundamental properties of the muon.

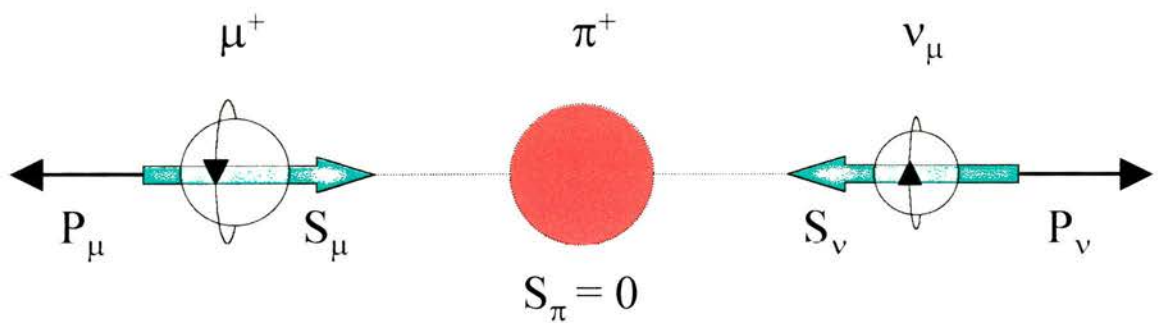


Figure III- 1 : decay of a pion into a muon and a neutrino.

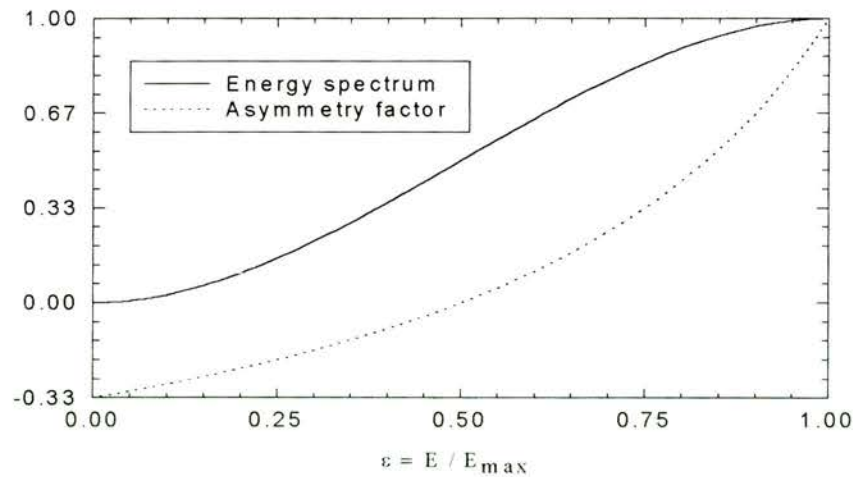
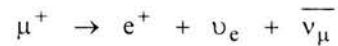


Figure III- 2 : Energy spectrum of the emitted positrons during a muon decay and energy dependence of the asymmetry factor  $A$ .

its energy falls to about a few keV. At this stage, the muons can capture an electron to form muonium. Then, successive captures and losses of electrons and inelastic collisions muonium-atoms slow the muonium. The loss of polarisation is inhibited by relativistic effects. Lastly, dissociation of the thermalised muonium occurs to leave a free thermal muon. Given the gyromagnetic ratio of the muon, these processes occur over too short a period of time for the spin of the muon to start a precession significant enough to induce a noticeable deviation from the initial polarisation.

### III.2.d Decay of the muon and emission of the positron

After being thermalised in the sample over a time of the order of 0.1 to 1 ns, the positive muon, of lifetime  $\tau_\mu = 2.197 \mu\text{s}$  decays via the following process :



The emitted positron,  $e^+$ , is then detected. As the decay is a three-body process, the kinetic energy of the  $e^+$  varies from zero (the antiparallel neutrinos carry away all the

available kinetic energy) and  $E_{\text{max}} = \frac{(m_\mu - m_e)^2}{2m_\mu} c^2$  when the two neutrinos travel together and antiparallel to the positron .

The energy spectrum of the emitted positrons is given<sup>7</sup> by  $(3-2\varepsilon)\varepsilon^2$ , where  $\varepsilon = E/E_{\text{max}}$  is the normalised positron energy, and is shown in *Figure III- 2*. The emission of the positron is anisotropic and the probability that a positron is emitted along a direction forming an angle  $\theta$  with the spin of the muon is given by

$$1 + A \cos(\theta) \tag{Eq. III- 1}$$

where the so-called asymmetry factor  $A = (2\varepsilon-1)/(3-2\varepsilon)$  is plotted in *Figure III- 2*. *Figure III- 3* represents the angular distribution of the emitted positrons given by for  $A=1$  (only the positrons having the maximum energy are collected) on the left hand-side and  $A=1/3$  (all the positrons are accepted) on the right hand-side. This positron emission anisotropy is the key feature of  $\mu\text{SR}$  since it implies that the direction of the muon spin at the time of decay can be derived from the positron count-rate. *Figure III- 3* clearly shows that the anisotropy increases with  $A$ . Hence, it is common to place a degrader in front of the detectors to reinforce  $A$  by selecting the most energetic positrons.

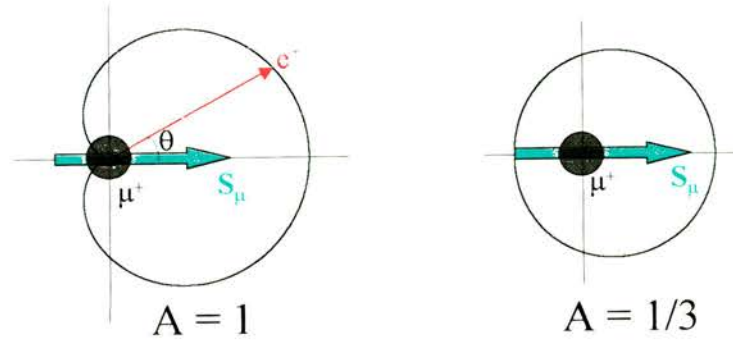


Figure III- 3 : angular distribution of the emitted positrons when only maximum energy positrons are accepted (left) and when all positrons are collected (right).

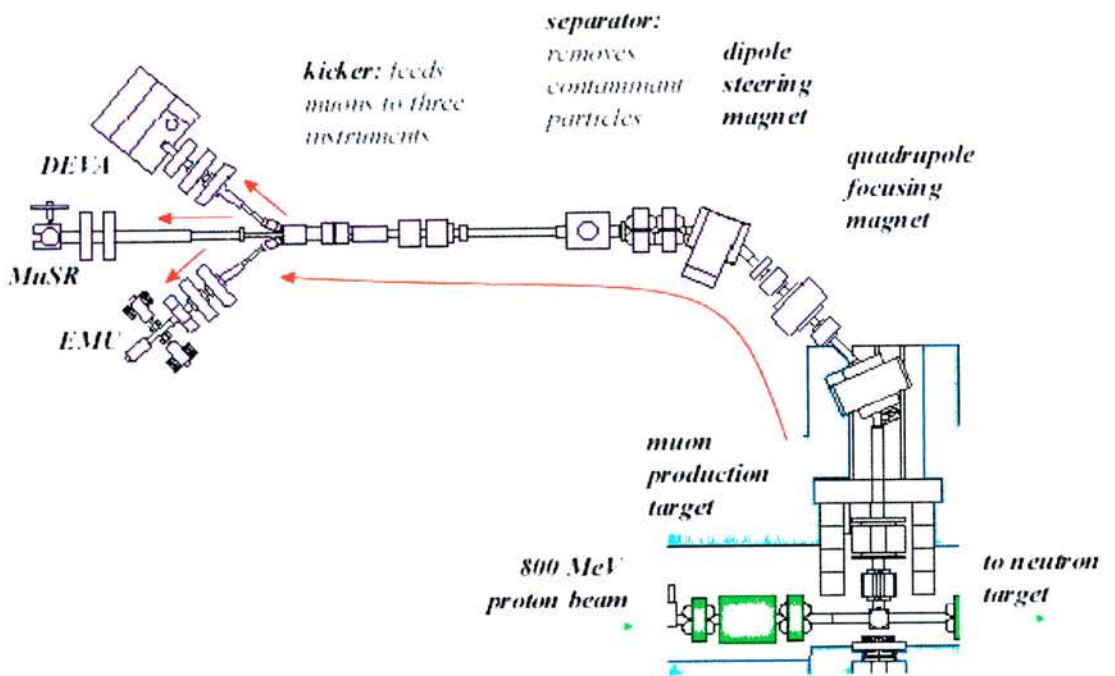


Figure III- 4 : The ISIS south side muon beamlines



### III.3 Muon spectroscopy at ISIS

#### III.3.a The muon beam lines at ISIS

At ISIS, there are three independent spectrometers at the end of the EC muon beamline : MuSR, EMU and DEVa (see *Figure III-4*)<sup>8</sup>. Once produced, the positive muons are led into the experimental area by a series of quadrupole and bending magnets, a separator and an electrostatic kicker. The role of the bending magnets is to select the required particle momentum 26.5 MeV/c. In order to eliminate any contaminant particles (for instance, some muons will decay into positrons during their flight from the target to the spectrometers), the electrostatic separator will select the velocity of the particles to be the proper one for the 26.5 MeV muons (0.24c). A 6° deflection of the spin of the muon with respect to the muon momentum will result and has to be taken into account when analysing data. The kicker allows the two pulses to be separated : the first pulse is split into EMU and DEVa whereas the second pulse goes straight into MuSR. A photograph showing the electrostatic kicker separating the muon beam into the three muon instruments can be found in *Figure III- 5*.

#### III.3.b The MuSR spectrometer

##### III.3.b.1 general overview

There are three instruments available for use on the EC muon beamlines : EMU, MuSR and DEVa. EMU can only be used in longitudinal geometry and DEVa is a test beam. As this thesis is concerned mainly with Muon Spin Rotation, only the MuSR spectrometer will be discussed in the remainder of this paragraph. However, for esthetical purpose, a general picture of the three instruments is shown on *Figure III- 5*.

A picture of the MuSR spectrometer in transverse configuration can be found in *Figure III- 6*. As already mentioned in § III.2.3, the muons,  $\mu^+$ , implanted in the sample decay into positrons,  $e^+$ , and the fact that this decay occurs preferentially along the  $\mu^+$  spin direction is the essence of  $\mu$ SR. On MuSR, the emitted  $e^+$  are detected via the following process : as the  $e^+$  passes through a scintillator, it emits light which is transmitted to a photomultiplier tube via an acrylic light-guide<sup>8</sup>. The photomultiplier then converts light into an electrical signal subsequently collected by a TDC which

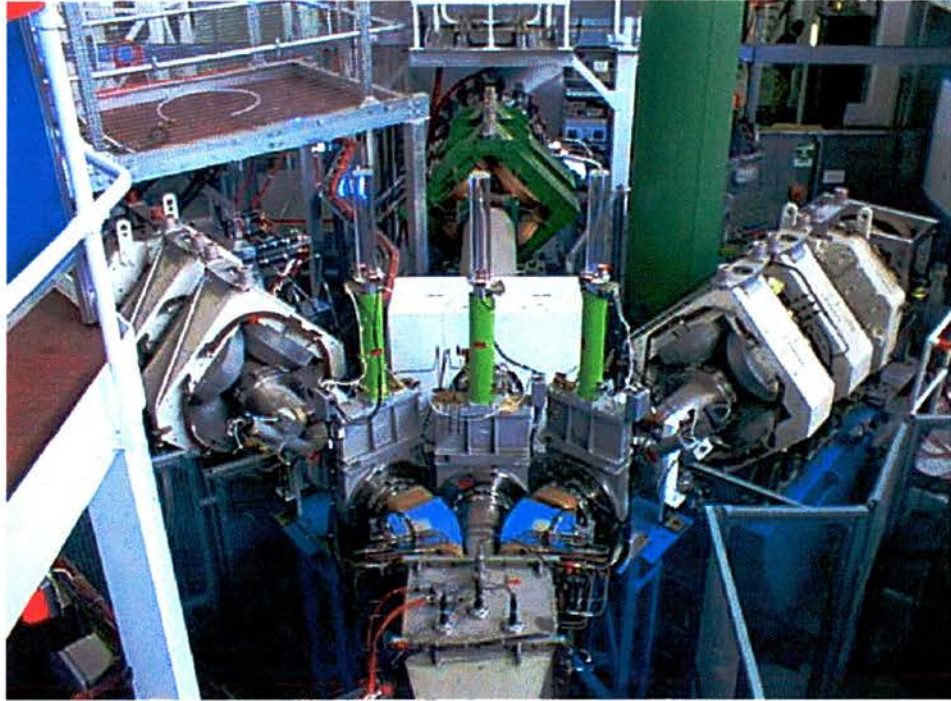


*Figure III- 5 : the three ISIS instruments (from left to right : EMU, MuSR and DEVA).*

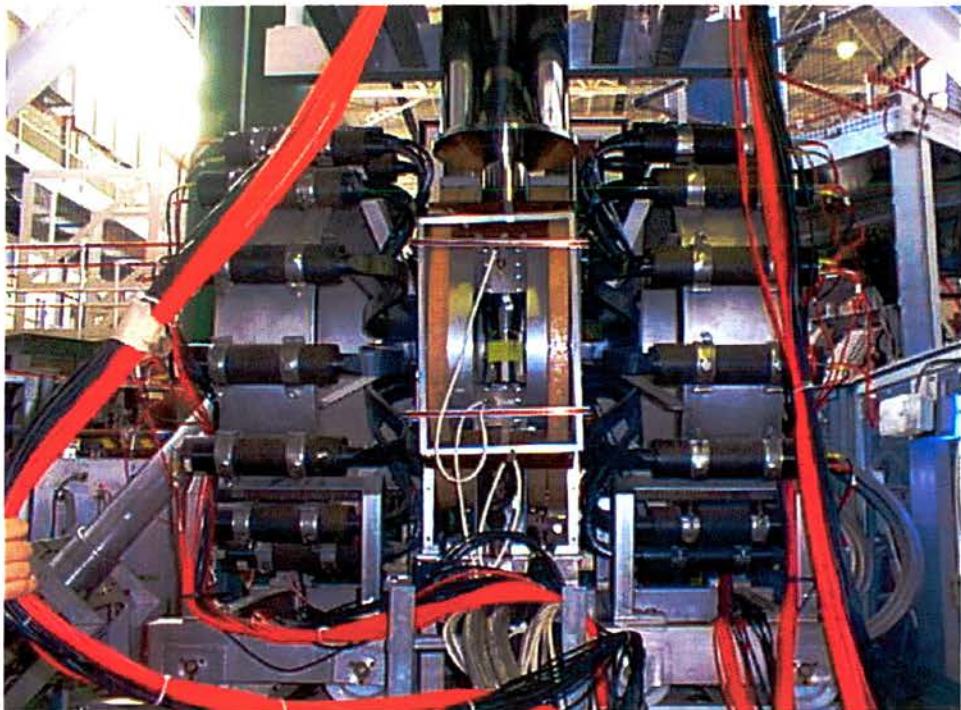


*Figure III- 6 : The MuSR spectrometer in transverse geometry with the dilution refrigerator inserted. This picture is taken looking back along the muon beamline.*



builds up the histogram of the emitted  $e^+$  (the time  $t=0$  is known from a Cerenkov detector placed near the production target). MuSR has 32 such detectors mounted on two circles together with a set of Helmholtz coils. The whole ensemble (detectors and magnets) can be easily rotated through  $90^\circ$  in about 45 minutes allowing the MuSR spectrometer to be used in both transverse and longitudinal geometries.

The Helmholtz coils can produce fields which are sufficiently homogeneous for the  $\mu$ SR technique with a maximum field of 0.2T. In addition, there is a set of compensating coils with which zero field can be obtained within a precision of  $3\mu\text{T}$ . However, due to the finite muon pulse width, the maximum useable field in transverse configuration is about 600G (0.06T) : for higher fields, the initial asymmetry becomes too low. Indeed, as the field increases, the phase difference between the  $\mu^+$  starting their precessions at the beginning of the pulse and those starting theirs at the end of the pulse becomes more significant<sup>9</sup>. This effect and its consequences are clearly demonstrated on *Figure III- 7*.

On the sample environment point of view, a wide range of temperatures can be covered on MuSR since a dilution fridge (40mK-4.5K), a cryostat (1.5K-320K), a Closed Cycle Refrigerator (12K-350K) and a furnace (up to 1000K ) are made available for the users.

### *III.3.b.2 Sample mounting*

The amorphous superconductors studied in this thesis were mounted with extreme care (about 12-18 hours per sample depending on the width of the ribbons) as shown in *Figure III- 8*. The ribbons were mounted onto a 40mm\*40mm silver plate with GE varnish, used for its good thermal conducting properties at low temperatures. Nine to eleven layers of the amorphous ribbons were mounted on the top of each other, the preferential direction of the ribbons within each layer being orthogonal to the one of the layer above and below. This orientation of the ribbons is ideal since it implies a low demagnetising factor as the shortest dimension is perpendicular to the applied field direction.

We chose a silver sample holder since the damping of the oscillations from the muons implanting in Ag is negligible (see § III.4.1) and Ag does not superconduct down to the lowest obtainable temperature on the MuSR dilution fridge, unlike aluminium (used as a sample holder for samples having higher transition temperatures, its main



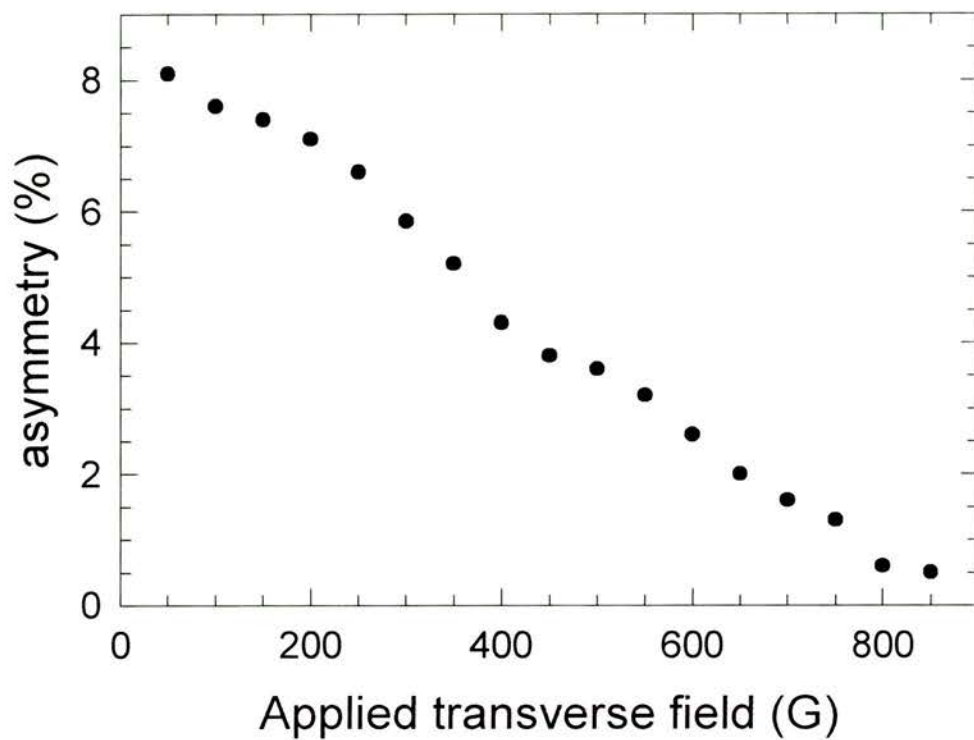


Figure III-7 : Frequency response of the MuSR spectrometer<sup>8</sup>.



Figure III- 8 : An amorphous sample mounted on the MuSR dilution fridge showing the orientation of the ribbons and the surrounding haematite mask.

advantage being obviously its cheapness compared to silver) which has a superconducting transition temperature of 1.1K. The surrounding edges of the silver plate are covered with haematite ( $\text{Fe}_2\text{O}_3$ ) mixed with Bostick glue. Having a high internal field (about  $210\text{MHz}^{10}$  i.e. far higher than that measurable on MuSR, see §III.3.2.a),  $\text{Fe}_2\text{O}_3$  will immediately depolarise any muons implanted in it and give a small incoherent background contribution over the time region of interest (1-16 $\mu\text{s}$ ). The silver plate and sample were inserted into the dilution refrigerator enabling a base temperature of 50mK and a maximum of 4.2K to be reached. In order to reduce the heat leak radiation through the muon window the sample was wrapped with a thin aluminium foil.

### III.4 Muon Spin Rotation technique

#### III.4.a First Principles

Ideally, the depolarisation function of the muon spins should be calculated by a full quantum mechanical treatment<sup>11</sup>. The quantity of interest, the depolarisation function of the muon along the direction  $\alpha$ , suitably chosen for longitudinal or transverse case, is given by  $P_\alpha(t) = \langle \Psi | \sigma_\alpha(t) | \Psi \rangle = \text{Tr}(\rho \sigma_\alpha(t))$ .

$|\Psi\rangle$  (respectively  $\rho$ ) is the wave-function (resp. density matrix) describing the initial state of the combined muon-system and  $\sigma_\alpha(t)$  is the spin of the muon at time  $t$ .

Recalling that the expression of the time-evolution of the muon spin,  $\sigma_\alpha(t)$ , is given, in Heisenberg representation, by  $\sigma_\alpha(t) = \exp(iHt/\hbar) \sigma_\alpha \exp(-iHt/\hbar)$ , where  $H$  is the Hamiltonian describing the interactions in the ensemble muon-system, it is easy to see that extremely valuable information can be obtained on the system in which the muons are implanted. Taking the example of a magnetic system,  $H$  contains the Zeeman term for the muon itself, the magnetic (sum of a dipolar and a contact term) and electric interactions\* between the muon and the system and, of course, the interactions within the system itself (both magnetic and electric) and the Zeeman term for the nuclear or electronic magnetic moments of the system. However, the time

---

\* As stated in §III.2.1, the  $\mu^+$  is a spin  $\frac{1}{2}$  particle. Its spin degeneracy is therefore not lifted by the electric interactions but its charge can disturb the system in which it is implanted.

evolution of the muon spin can be obtained by a much simpler classical treatment which gives the same results as the quantum mechanical treatment.

The evolution of a spin  $\mathbf{S}$  placed in a magnetic field  $\mathbf{B}$  is given by the Larmor equation

(see *Figure III- 9*) :

$$\frac{d\mathbf{S}}{dt} = \gamma_{\mu} \mathbf{S} \times \mathbf{B} .$$

The spins of the muons will then precess around  $\mathbf{B}$  at a frequency  $\omega = \gamma_{\mu} B$  . If all the muons sense the same field, perpendicular to their initial polarisation (transverse geometry), in a material having no magnetic moment, such as silver for instance, they all have the same phase at a chosen time and the resulting polarisation along the initial polarisation of the muons is a simple cosine.

However, if there is a distribution of local fields at the  $\mu^+$  sites, the  $\mu^+$  spins do not have all the same phase and, as a result, the oscillations will be damped.

In order to clarify this concept, let  $D(\mathbf{B},t)$  be the distribution of the local magnetic field at the muon sites, the depolarisation function along the  $\alpha$  direction is given by :

$$P_{\alpha}(t) = \int \frac{S_{\alpha}(\mathbf{B},t)}{S} D(\mathbf{B},t) d\mathbf{B} \quad \text{Eq. III- 2}$$

It becomes easy to see that the distribution of the magnetic field inside a sample can be extracted from the muon depolarisation and then compared to theoretical models such as those describe in Chapter VI.

Useful distributions to be considered as examples include a Dirac peak centred on  $B_{\text{ext}}$  giving a simple cosine form for the depolarisation (e.g. Ag), a gaussian giving a gaussian envelope function for the depolarisation function or a lorentzian resulting in an exponential damping of the oscillations. In a superconductor,  $D(\mathbf{B},t)$  is not as simple as the three distributions just mentioned and is dependent on the magnetic penetration depth  $\lambda$ , the coherence length  $\xi$  and the Flux Line Lattice structure itself (3D hexagonal, square, “pancake”, presence of melting).  $\mu\text{SR}$  has given unique insights of the nature of the FLL in high  $T_{\text{cs}}$ <sup>12, 13</sup>.



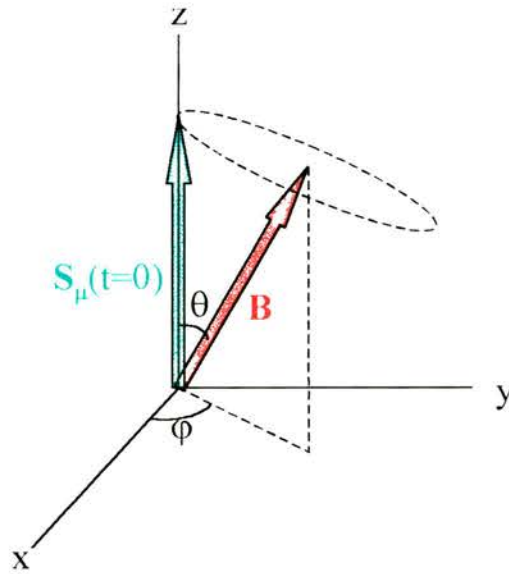


Figure III- 9 : Larmor precession of the muon spin induced by the field at the muon site.

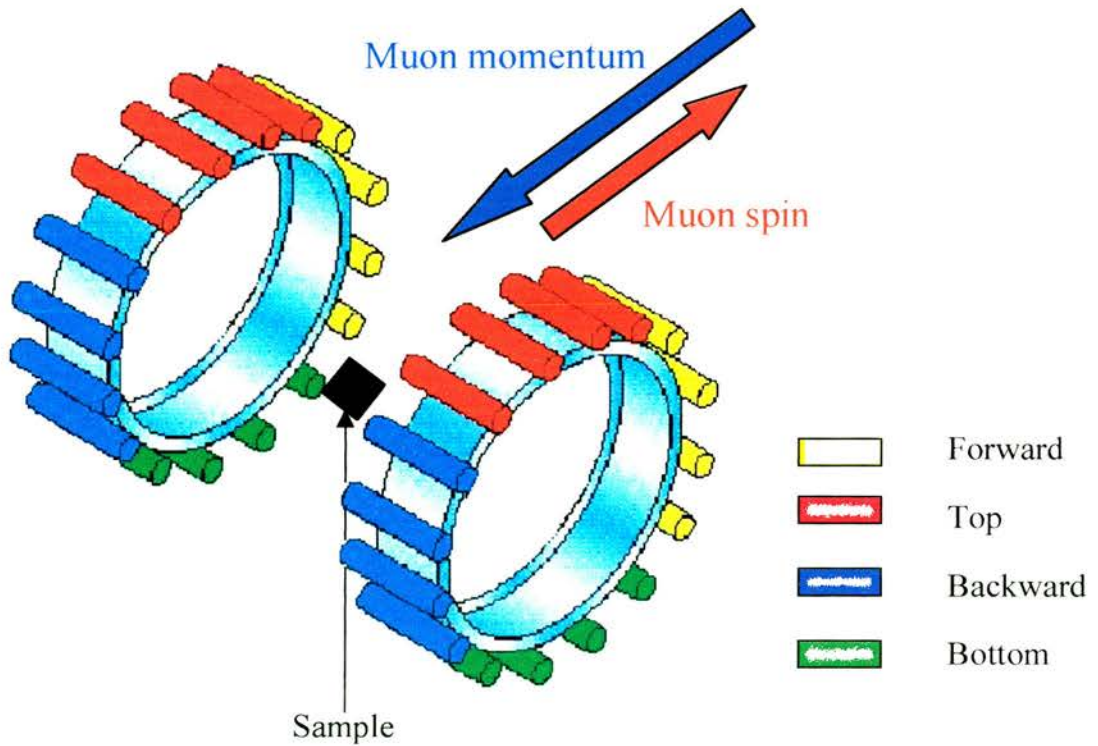


Figure III- 10 : A schematic of the MuSR instrument in transverse geometry with the grouping of the detectors.

### III.4.b Data analysis

#### III.4.b.1 Experimental parameters

For a detector positioned at an angle  $\phi$  with respect to initial spin direction of implanted muons, the number of emitted positrons counted by this detector at time  $t$  is :

$$N^{e^+}(t) = N_0 \exp(-t/\tau_\mu) (1 + a \cos(\phi)) \quad \text{Eq. III- 3}$$

$N_0$  and  $a$  are effective parameters related to the number of muons implanted at time  $t = 0$  and the solid angle covered by the detector (about 0.01 steradian for a MuSR detector). This equation (Eq. III- 3) is valid only if all the spins of the muons make the same angle with the detector. However, when the spins interact with the local magnetic field inside the sample, this expression should be modified.

Using the same notation as in III.4.2,  $P_\alpha(t)$ , the polarisation of the beam along the direction  $\alpha$  of the detector at time  $t$ , given by Eq. III- 2, is related to the number of detected positrons by :

$$N_\alpha^{e^+}(t) = N_0 \exp(-t/\tau_\mu) (1 + a P_\alpha(t)) \quad \text{Eq. III- 4}$$

Rewriting the expression of  $P_\alpha(t)$  (Eq. III- 2) specifically for the transverse configuration, the number of detected positrons in a detector  $j$  is<sup>14</sup> :

$$C_j(t_n) = N_j^0 \Delta t e^{-t_n/\tau_\mu} \left[ 1 + A_j D_j(t_n) \right]$$

$$\text{with } D_j(t_n) = \int_0^\infty D(\omega) \cos(\omega t_n - \phi_j) d\omega \quad \text{Eq. III- 5}$$

where  $\phi_j$  is the phase of the detector  $j$ . The determination of the phases can be achieved by collecting spectra from a material with a slowly depolarising function\*. For the study of superconductors, it is therefore convenient to use the  $\mu$ SR spectrum of the superconducting material itself, above its transition temperature.

Another instrumental parameter needed for the data analysis is the dead time,  $\tau_d$ , of the detectors. Two events occurring very close to each other are counted as one single event due to electronic limitation.

---

\* It is of course possible to use a silver run, for which  $D(\omega)$  is a Dirac peak centred on the applied field,  $B_{ext}$ , giving  $D_j(t_n) = \cos(\omega_{ext} t_n - \phi_j)$ . If the Ag run is performed for different transverse fields, it also allows the start time, which should be the same for all the detectors, to be determined.

Obviously, this is particularly important at short times when the number of events is high. Due to dead time, the number of recorded events  $N_{\text{rec}}$  is modified from the number of “ideal” events  $N_{\text{true}}$  via the expression :

$$N_{\text{true}} = \frac{N_{\text{rec}}}{1 - N_{\text{rec}} \tau_d}$$

By plotting  $1/N_{\text{rec}}$  of a high statistics Zero Field silver run, versus  $(1/N_0)\exp(-t/\tau_d)$ , a straight line is obtained whose intercept is  $\tau_d$ . It is again possible to use the superconducting material itself, above its transition temperature.

#### III.4.b.2 Detector grouping

Instead of plotting the data as 32 different histograms, one can choose to group the detectors for clarity. On MuSR, this is done according to *Figure III- 10* in 4 groups at roughly  $90^\circ$  from one another (the approximate phase of each group is given in brackets) : top ( $\sim 75^\circ$ ), bottom( $270^\circ$ ), forward( $\sim -15^\circ$ ) and backward( $\sim 165^\circ$ ). This grouping is particularly interesting for polycrystalline superconducting samples, where the field distribution can be approximated by a gaussian<sup>15</sup>. In this case, the second moment associated with the superconductivity can be simply corrected from the dipolar and instrumental broadening\* :

$$\sigma_{\text{super}}^{\text{corr}} = \sqrt{(\sigma_{\text{super}}^{\text{raw}})^2 - (\sigma_{\text{normal}}^{\text{raw}})^2}$$

The temperature dependence of the corrected moment can be fitted to the N-fluid model ( $\sigma = \sigma_0 (1-(T/T_C)^N)$ ) and its  $T=0$  value,  $\sigma_0$  is directly related to the magnetic penetration depth of the sample,  $\lambda$ , by  $\sigma_0 = 0.0609 \gamma_\mu \phi_0 / \lambda^2$  (where  $\phi_0$  is the flux quantum) for hexagonal lattice in the high  $\kappa$  limit. However, fitting the time domain data in this way assumes a predetermined form for the field distribution and should be avoided when dealing with non polycrystalline samples since it implies throwing away information on the structure of the FLL (as can be seen in chapter VI, the London model for a FLL gives a field distribution which is very different from a symmetric gaussian). It seems therefore useful at this point to introduce the field-domain analysis.

---

\* In the general case the instrumental and dipolar broadening, seen above the transition temperature of the superconductor,  $T_C$ , should be deconvolved from the data obtained below  $T_C$ , to obtain the signal arising purely from the mixed state. By using gaussians, the deconvolution can be done analytically.



### III.4.b.3 Frequency domain analysis : maximum entropy method

The equations III-5 suggest that the field distribution inside a sample can be directly obtained from the data : the polarisation of the muon beam is simply given by the Fourier Transform (recalling that the frequency is linearly related to the field by the gyromagnetic ratio of the muon) of the field distribution. It is crucial to understand that the dimensions of the FLL, at the fields used on MuSR, are far greater than those of a "random" unit cell of a glassy network. The muons will therefore sense all the possible values of the internal fields and thus probe the field distribution. However, standard Fourier Transform (FT) methods applied on  $\mu$ SR can lead to substantial noise due to relatively poor statistics at several muon lifetimes and also the finite time window. The alternative is to use an apodising function<sup>16</sup> but it implies throwing away part of the data. A program, initially written by Brian Rainford and Geoff. Daniell<sup>17</sup> and modified by Ted Forgan and Bob Cubitt<sup>18</sup> has been developed to give a model independent field profile from  $\mu$ SR data and been used throughout this thesis.

This program relies upon the maximum entropy method. The basic idea of this method is to maximise  $S - \lambda\chi^2$  where  $\lambda$  is a Lagrange multiplier,  $\chi^2$  the usual "chi-squared function" and  $S$  the entropy of the distribution, given by :

$$S = - \sum_k (p_k / b_k) \ln(p_k / b_k).$$
 The  $\{p_k\}$  are the heights of the frequency spectrum and the  $\{b_k\}$  are scale factors (usually, they are independent of  $k$  to start off with). The method has been successfully tested in areas as diverse as astronomy, imaging (an impressive image reconstruction of a blurred photograph can be found in page 142 of reference 19) and has been used to study the field profile of, for instance, high  $T_C$  materials<sup>13</sup>. The power of the Maximum Entropy method in  $\mu$ SR is beautifully shown in the classic picture of a "silver run" (*Figure III- 11*).

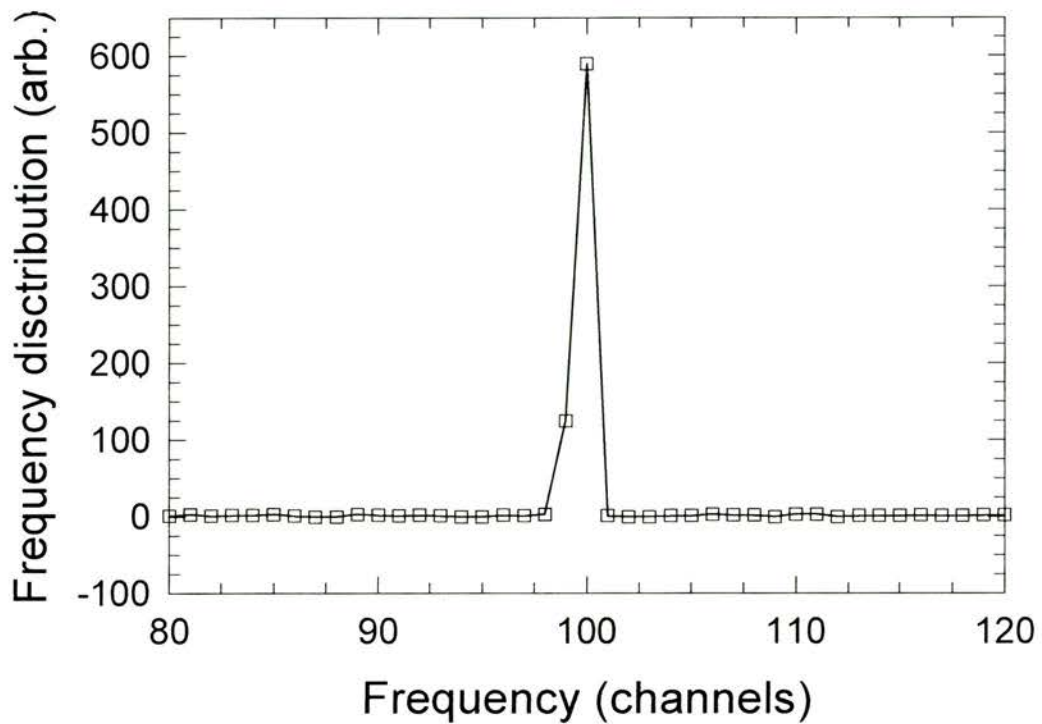


Figure III- 11 : Maximum Entropy signal of a "silver run". As required, the frequency distribution is very close to a delta function<sup>14</sup>.

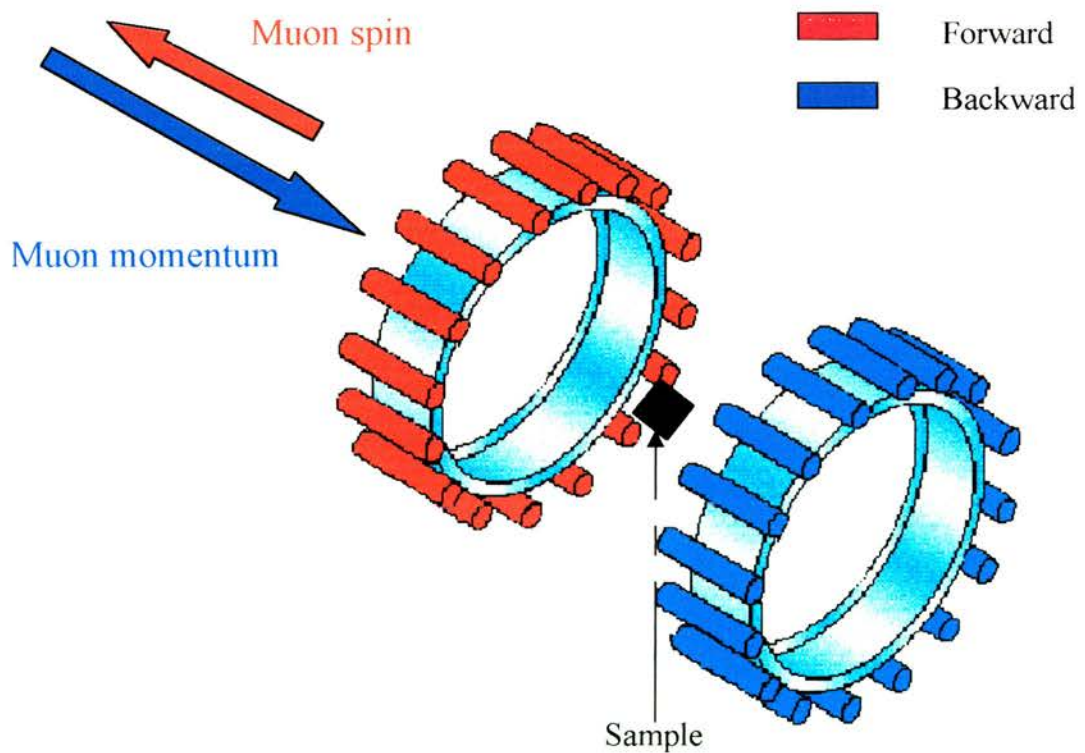


Figure III- 12 : A schematic of the MuSR instrument in longitudinal geometry with the grouping of the detectors.



## III.5 Muon spin relaxation

### III.5.a Sample mounting and detectors grouping

In a muon spin relaxation experiment, the sample is generally mounted onto a silver sample holder or onto an aluminium sample holder surrounded by a silver mask. In longitudinal geometry, in contrast to the transverse case described above, the detectors are grouped in a forward and a backward bank (see *Figure III- 12*). The positron count in each bank is related to  $G_z(t)$ , the longitudinal muon spin relaxation function by :

$$N_{F,B}(t) = N_{F,B}(0) \exp(-t/\tau_\mu) [ 1 \pm G_z(t) ]$$

$G_z(t)$  is directly extracted from the data by taking the ratio :

$$R_z(t) = a_0 G_z(t) = \frac{N_F(t) - \alpha N_B(t)}{N_F(t) + \alpha N_B(t)}$$

where  $\alpha$  is a calibration constant depending on the relative efficiencies of the forward and backward detectors, the sample thickness, the sample environment, etc... and  $\alpha$  is determined for each sample by applying a 2mT transverse field. In such a field, the muon spin precesses at the Larmor frequency  $\omega = \gamma_\mu B$  and the resulting muon asymmetry plot is a oscillation at frequency  $\omega$  modulated by an depolarisation envelope  $G_x(t)$ . The value of  $\alpha$  is adjusted until the measured asymmetry oscillates around zero and is then kept constant for all the data collected in zero field or in any longitudinal field. If some muons land outside the sample area (in the sample holder or the silver mask), the spins of those muons will still precess at the Larmor frequency and therefore not affect the value of  $\alpha$  but merely contribute to another (small) term (the depolarisation envelope for silver is extremely flat).

### III.5.b Muon depolarisation functions

#### III.5.b.1 Static fields

Assuming that a muon implants in the sample at time  $t=0$  with its spin along the  $z$ -direction, the time evolution of the  $z$ -component of the muon spin  $S_z(t)$  is given by :

$$S_z(t) = \cos^2 \theta + \sin^2 \theta \cos(\gamma \mu B t)$$

where  $B$  is the magnitude of the field that the muon experiences and  $\theta$  is the angle between  $B$  and the  $z$ -axis (*Figure III- 9*). For the muon beam, the depolarisation function is given by a statistical average of  $S_z$ . Recalling *Eq. III-2* gives :

$$P_z(t) = G_z(t) = \iiint \frac{S_z(t)}{S} D(B_x) D(B_y) D(B_z) dB_x dB_y dB_z$$

In the case of nuclear dipoles static on the time scale of the muon lifetime for instance, a gaussian distribution *for each orthogonal components* ( $x,y,z$ ) can be assumed. Kubo and Toyabe<sup>20</sup> showed that for such a gaussian distribution, the depolarisation function is :

$$G_{GKT}(t) = \frac{1}{3} + \frac{2}{3} \left(1 - \sigma^2 t^2\right) e^{-\frac{\sigma^2 t^2}{2}}$$

This function is referred to as the Gaussian Kubo-Toyabe and shows a characteristic dip at  $\sigma t = \sqrt{3}$  and the asymmetry recovers the value of  $1/3$  at long times.

In the case of a more dilute system, a lorentzian distribution can be expected and the depolarisation is then given by the Lorentzian Kubo-Toyabe function<sup>21</sup> :

$$G_{LKT}(t) = \frac{1}{3} + \frac{2}{3} (1 - \lambda t) e^{-\lambda t}$$

This function also shows a dip for  $\lambda t = 2$  and a recovery of the  $1/3$  tail at long times.

Both the Gaussian and Lorentzian Kubo-Toyabe can be seen on *Figure III- 13*.

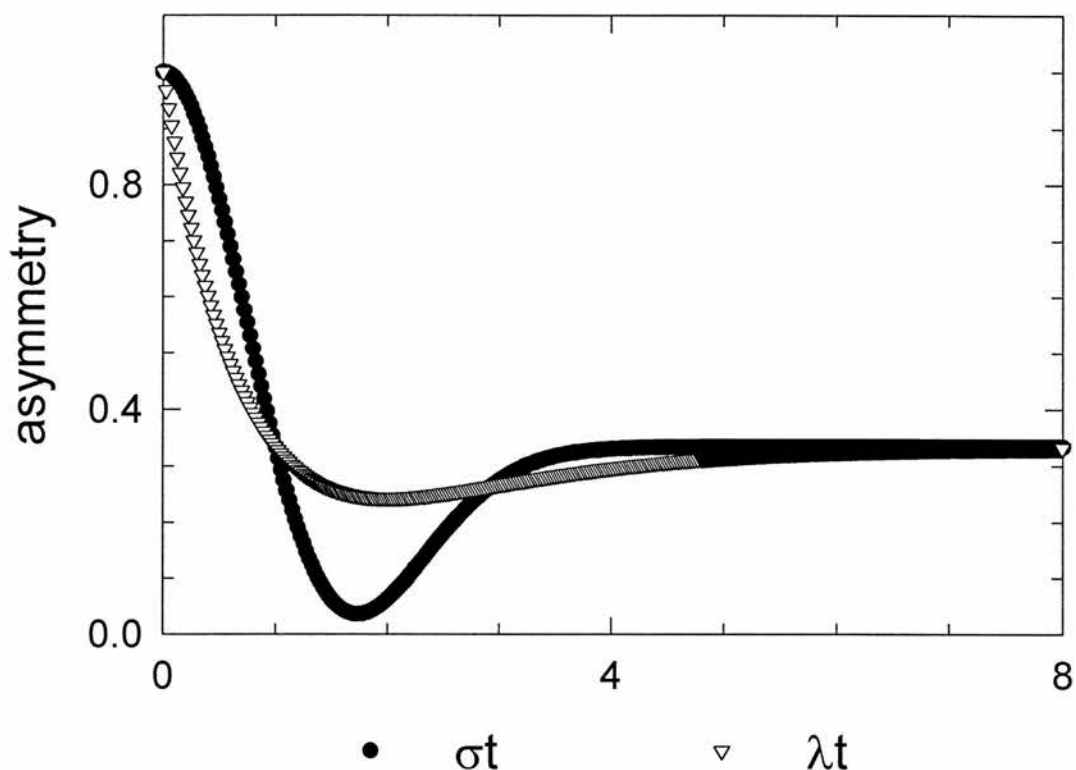


Figure III- 13 : The Gaussian (circles) and Lorentzian (triangles) Kubo-Toyabe functions as a function of reduced times.

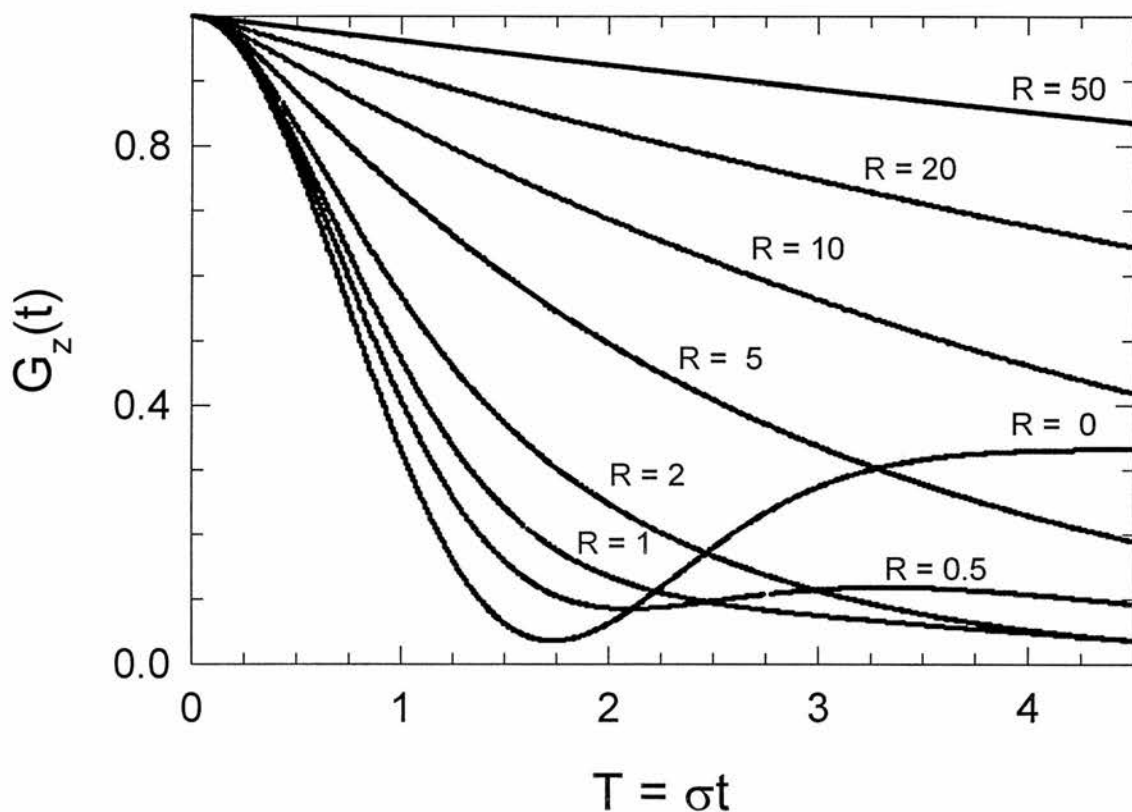


Figure III- 14 : Dynamic Gaussian Kubo-Toyabe as a function of reduced time  $T = \sigma t$  for different  $R = \nu/\sigma$  values.

### III.5.b.2 Dynamic spin systems

When the field at the muon site is time dependent, and in the limit of fast fluctuations, the well-known motional narrowing phenomenon occurs and the depolarisation function is described by an exponential. To further refine this intuitive description, let us follow the strong collision model described by Uemura et al<sup>22</sup>. At a time  $t$ , the local field changes direction (a "collision" occurs) with a probability distribution  $\rho(t)$  proportional to  $e^{-\nu t}$  and the new field is given by the field distribution  $D(B)$ , which can be a gaussian for instance. Until the first collision at  $t_1$ , the spin ensemble decays following the static depolarisation function  $g_z(t)$  whereas after the collision, it decays following the static form  $g_z(t)$  but with  $t_1$  as the initial time zero. By applying the same logic to successive collisions, the dynamic depolarisation function can be regarded as an envelope of static functions. Mathematically, this is expressed as :

$$G_z(t) = e^{-\nu t} \left[ g_z(t) + \nu \int_0^t g_z(t_1) g_z(t-t_1) dt_1 + \nu^2 \int_0^t \int_0^{t_1} g_z(t_1) g_z(t_2-t_1) g_z(t-t_2) dt_1 dt_2 + \dots \right]$$

Several ways to solve this equation have been used. It is possible to take the Laplace transform to obtain  $G_z(\omega)$  (the convolutions are then simple multiplications), and then use a numerical algorithm to inverse Laplace transform back to the time domain<sup>23</sup>. Alternatively, more direct numerical methods can be used but they require considerable time and computing power; hence the reason why they may be tabulated and fitted to the experimental data using a linear interpolation routine<sup>24</sup>. It should be noted that as  $\nu$  increases, the relaxation becomes slower up to a point where it becomes an exponential (motional narrowing). If the static depolarisation function is a Gaussian Kubo-Toyabe (GKT) characterised by a width  $\sigma$ , the threshold for the dynamic depolarisation to become exponential is  $\nu/\sigma > 5$ . This is well illustrated<sup>25</sup> by the GKT dynamic depolarisation functions for different  $\nu/\sigma$  ratios shown on *Figure III- 14*.

## References for chapter III

---

- <sup>1</sup> M.L.G. Foy et al, Phys. Rev. Letters, **30** (1973) 1064
- <sup>2</sup> Y. J. Uemura et al, Phys. Rev. Letters, **62** (1989) 2317
- <sup>3</sup> J. H. Brewer et al, Phys. Rev. Letters, **31** (1973) 143
- <sup>4</sup> see for instance : G. M. Pettigrew and G. R. Moor, CytochromeC, Springer-Verlag (1987)
- <sup>5</sup> S. H. Neddermeyer and C.D. Anderson, Phys. Rev. **51** (1937) 884
- <sup>6</sup> J.H. Brewer, K.M. Crowe, F. N. Gyax and A. Schenck, in "Muon Physics" Vol. III (1975), edited by V.W. Hugues and C. S. Wu, Academic Press, New York .
- <sup>7</sup> A. Schenck, Muon Spin Rotation Spectroscopy : Principles and Applications in Solid State Physics, Adam Hilger Ltd, Bristol (1985).
- <sup>8</sup> MuSR User Guide, <http://www.isis.rl.ac.uk/muons/musr%20manual/index.html>
- <sup>9</sup> G. H. Eaton et al, Nuclear Instr. and Methods in Phys. Research **A269** (1988) 483
- <sup>10</sup> K. Ruegg et al, Hyperfine Interactions **8** (1981) 547
- <sup>11</sup> T. McMullen and E. Zaremba, Phys. Rev. B, **18** (1978) 3026
- <sup>12</sup> D. Herlach et al, Hyperfine Interactions **63** (1990) 41
- <sup>13</sup> S.L. Lee et al, Phys. Rev. Letters **71** (1993) 3862
- <sup>14</sup> B.D. Rainford in Muon Science, Muons in Physics, Chemistry and Materials, (1999) NATO/SUSSP51 Summer School (Editors : S.L. Lee, S.H. Kilcoyne and R. Cywinski), Institute of Physics Publishing
- <sup>15</sup> B. Pumpkin et al, Phys. Rev. B **42** (1990) 8019
- <sup>16</sup> W. H. Press et al, numerical recipes in Fortran
- <sup>17</sup> B.D. Rainford and G.J. Daniell, Hyperfine Interactions **87** (1994) 1129
- <sup>18</sup> R. Cubbitt, PhD thesis, University of Birmingham (1994)
- <sup>19</sup> D.S. Sivia, Data Analysis, a Bayesian tutorial (1996), Clarendon Press, Oxford.
- <sup>20</sup> R. Kubo and T. Toyabe, Magnetic Resonance and Relaxation, (1967) North Holland
- <sup>21</sup> R. Kubo, Hyp. Int. **8** (1981) 731
- <sup>22</sup> Y.J. Uemura et al, Phys. Rev. B **31** (1985) 546
- <sup>23</sup> P. Dalmas de Réotier, PhD thesis, Grenoble, 1991
- <sup>24</sup> M.R. Crook and R. Cywinski, J. Phys. Cond. Mat. **9** (1997) 1149
- <sup>25</sup> R.S. Hayano et al, Phys. Rev. B **20** (1979) 850

## Chapter IV : AC susceptibility and Neutron Spin

### Echo study of Random Anisotropy Magnets.

#### IV.1 Introduction

In this chapter, after a brief theoretical review of the Random Anisotropy problem in magnetism, the temperature and frequency dependence of the real  $\chi'$  and imaginary  $\chi''$  components of the complex ac susceptibility are examined in detail in order to study the dynamics of the Random Anisotropy Magnets (RAM)  $\alpha$ -Er<sub>7</sub>Fe<sub>3</sub> and  $\alpha$ -Er<sub>7</sub>Ni<sub>3</sub>. The last part of this chapter will then be devoted to a Neutron Spin Echo (NSE) study of the same two samples. As shown in *Figure IV- 1*, the time window over which AC susceptibility probes the spin dynamics is beautifully complemented by the NSE technique.

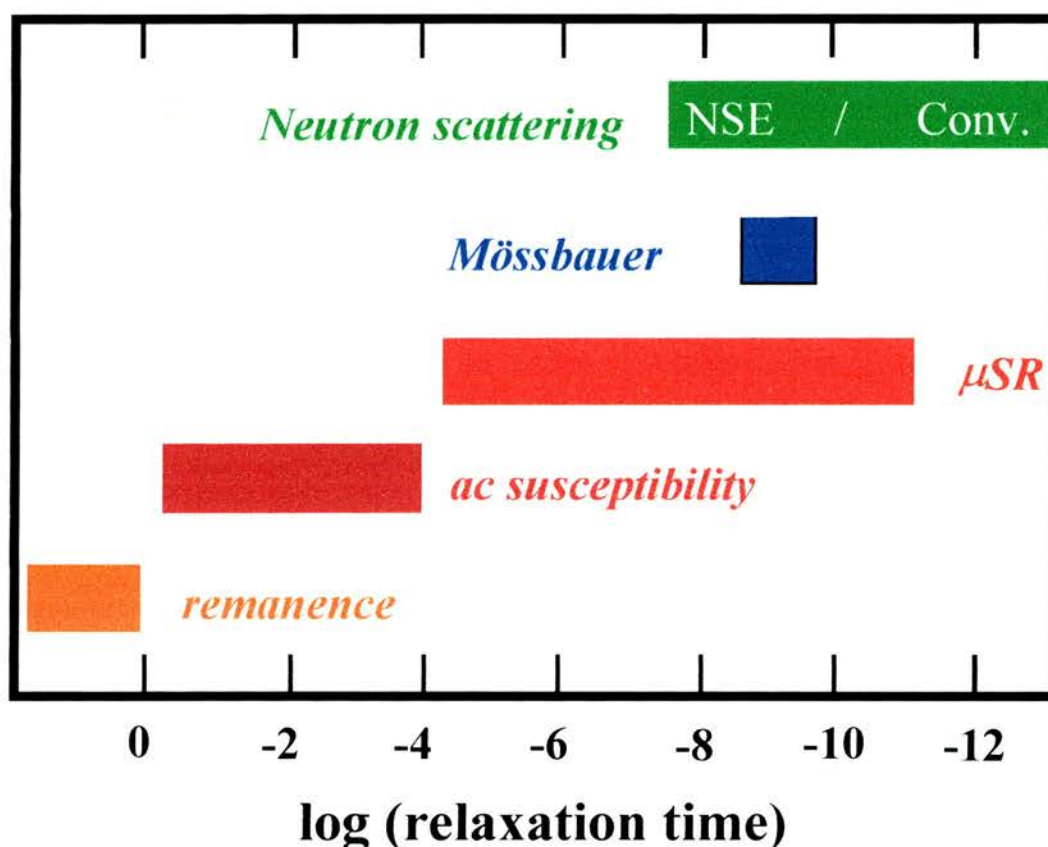


*Figure IV- 1 : range of relaxation times for various techniques used in magnetism.*

## IV.2 Rare Earth Magnetism

### IV.2.a Localised Magnetism

The magnetic properties of an ion are associated with the magnetic moments arising from the spin and orbital angular momentum of the electrons in an incomplete shell. For instance, the transition metal ions that have incomplete 3d shell or the rare-earth ions with incomplete 4f<sup>n</sup> shell exhibit magnetism. As the 4f<sup>n</sup> electrons are deep within the atom, they are screened from external influences by the 5s and 5p electrons and the magnetic moments associated with the 4f<sup>n</sup> shell can be regarded as localised. The crystal field has therefore only a small influence and can be treated as a perturbation (whereas for a 3d insulator, crystal fields have to be considered from the very beginning). The spin, S, and orbital, L, momentum quantum numbers of each rare-earth ion are those of the free ions and the state of lowest energy is obtained using Hund's rules<sup>1</sup> : the lowest energy state is that with 1) the highest spin value consistent with Pauli's exclusion principle, 2) for that value of S, the value of L should be as high as possible and 3) for electron shells less than half-full, the total momentum, J, is  $J = L - S$  and for electron shells more than half-full,  $J = L + S$ .

In the rare-earths, J is considered to be a good quantum number and, because the crystal field are usually small compared with the exchange, the Wigner-Eckart theorem can be used to project  $\underline{S}$  onto  $\underline{J}$ , namely :

$$\underline{S} = (g - 1)\underline{J} \qquad \text{Eq. IV-1}$$

where g is the Landé g-factor.

Standard quantum mechanics textbooks<sup>2</sup> state that the ground state, defined by its quantum number J, is (2J+1)-fold degenerate. Each degenerate state is characterised by  $J_z |J, M_J\rangle = M_J |J, M_J\rangle$  ( $J \geq M_J \geq -J$ ). However, as we shall see in the next paragraph, an external field (Zeeman splitting) or a crystal field can lift this degeneracy.

## IV.2.b Paramagnetism of the rare-earth elements

The presence of an applied field  $H_z$  splits the ground state into  $(2J+1)$  levels.

These energy levels are the eigenstates of the perturbing Hamiltonian :

$$H = -g \mu_B J_z H_z \quad \text{Eq. IV- 2}$$

where  $g$ , the Landé  $g$ - factor, is given by :

$$g = 1 + \frac{J(J+1) + S(S+1) - L(L+1)}{2J(J+1)} \quad \text{Eq. IV- 3}$$

At  $T=0$ , only the ground state is occupied and the magnetisation in the  $z$ - direction due to  $N$  atoms per unit volume is simply  $M = Ng\mu_B J$ . However, at a temperature  $T \neq 0$ , the thermal population of the excited states has to be considered. The probability  $p_i$  of the atom being in one of the possible  $(2J+1)$  states of energy  $E_i$  is, according to Boltzmann statistics :

$$p_i = \frac{\exp(-E_i / k_B T)}{\sum_i \exp(-E_i / k_B T)} \quad \text{Eq. IV- 4}$$

The value of the magnetisation at a finite temperature can therefore be written as:

$$\langle M \rangle_T = \sum_i p_i M_i = \frac{\sum_{M=-J}^{+J} g\mu_B M \exp(g\mu_B H_z M / k_B T)}{\sum_{M=-J}^{+J} \exp(g\mu_B H_z M / k_B T)} \quad \text{Eq. IV- 5}$$

After some manipulations, Eq. IV- 5 can be transformed into :

$$\langle M \rangle_T = Ng\mu_B JB(x) = Ng\mu_B J \left\{ \frac{2J+1}{2J} \coth\left(\frac{2J+1}{2J} x\right) - \frac{1}{2J} \coth\left(\frac{x}{2J}\right) \right\} \quad \text{Eq. IV- 6}$$

where  $B(x)$  is the Brillouin function,  $x = gJ\mu_B H_z / k_B T$  and  $M_0 = Ng\mu_B J$  is the saturation magnetisation at  $T=0$ .

At high temperatures or low fields ( $x \ll 1$ ), Eq. IV- 6 reduces to :

$$\langle M \rangle_T = \frac{N(J+1)}{3J} (g\mu_B J) \frac{g\mu_B J H}{k_B T} = C \frac{H}{T} \quad \text{Eq. IV- 7}$$



This is the well-known Curie law, valid for a system of non-interacting spins, and  $C$  is called the Curie constant.

The magnetic susceptibility is then given by :

$$\chi = \frac{d \langle M \rangle_T}{dH} = \frac{C}{T} \quad \text{Eq. IV- 8}$$

When interactions are present, the replacement of the applied field  $H_z$  by the sum of the applied field and a magnetic field created by the surrounding spins (molecular field approximation) gives an expression for  $\chi$  very similar to *Eq. IV- 8* :

$$\chi = \frac{C}{T - \theta_p} \quad \text{Eq. IV- 9}$$

This equation is called the Curie-Weiss law and  $\theta_p$  is termed the paramagnetic temperature. The sign of  $\theta_p$  is an indication of the nature of the interaction between the magnetic atoms : if it is positive, the moments tend to align themselves and the interaction is called ferromagnetic whereas if it is negative, the interaction is dominantly antiferromagnetic and the moments tend to lie antiparallel to one another.

#### IV.2.c Origins of the interactions in rare-earths

The fact that the  $4f^n$  shell is localised implies that there is negligible overlap of the  $4f$  electronic wavefunctions hence if a magnetic ordering is observed, the exchange mechanism involved must be indirect in nature. Ruderman, Kittel, Kasuya and Yosida<sup>3</sup> proposed an exchange via the conduction electrons. Their treatment requires second quantisation operators and will not be repeated here. The basic idea is the following : a spin  $\underline{S}_i$  localised at a position  $\underline{R}_i$  interacts with the conduction electrons to give a spin polarisation of the conduction band. This polarisation then interacts with another spin  $\underline{S}_j$  localised at another position  $\underline{R}_j$  thus resulting in an exchange, indirect in nature and mediated by the conduction electrons, between  $\underline{S}_i$  and  $\underline{S}_j$ .

The exchange Hamiltonian can be written as :

$$H = - \sum_{i,j \neq i} J(|\underline{\mathbf{R}}_i - \underline{\mathbf{R}}_j|) \underline{\mathbf{S}}_i \cdot \underline{\mathbf{S}}_j \quad \text{Eq. IV-10}$$

Using Eq. IV-1 and Eq. IV-10, it is easy to show that the strength of the exchange interaction in the rare-earths scales according to the de Gennes factor :

$$(g-1)^2 |\underline{\mathbf{J}}_i \cdot \underline{\mathbf{J}}_j| = (g-1)^2 J(J+1) \quad \text{Eq. IV-11}$$

Detailed calculations show that the polarisation is oscillating and therefore the interaction between spins is itself of variable sign (and long-distance), depending on the distance separating the two spins  $i$  and  $j$  considered. In other words,  $J(|\underline{\mathbf{R}}_i - \underline{\mathbf{R}}_j|) = J(R)$  is an oscillating function  $(J_{sf}^2 \cos(2k_F R) / E_F(2k_F R)^3)$  where  $J_{sf}$  is the exchange integral between the  $5s$  electrons and the  $f$  electrons and  $k_F$  and  $E_F$  are respectively the Fermi vector and energy) and can be either positive or negative, the exchange thus being ferromagnetic or antiferromagnetic. The RKKY interaction has proved invaluable for the understanding of the behaviour of dilute magnetic alloys. For instance, a spin  $A$  at a distance  $r_{AB}$  from a spin  $B$  such that  $J(r_{AB}) > 0$  and  $r_{AC}$  from a spin  $C$  such that  $J(r_{AC}) < 0$  can sense both a ferromagnetic and an antiferromagnetic exchange at the same time, this frustration has been invoked to explain the spin-glass character of these dilute magnetic alloys.

#### IV.2.d The HPZ Hamiltonian

Harris, Plischke and Zuckermann<sup>5</sup> pointed out that a Hamiltonian supposed to describe the features of a Random Anisotropy Magnet should at least contain an exchange term, an anisotropy term and, if one is to study its behaviour under the influence of a magnetic field, a Zeeman term. Let us describe these terms one by one.

The exchange Hamiltonian of the system can be written as :

$$H = - \sum_{i,j} J \underline{\mathbf{J}}_i \cdot \underline{\mathbf{J}}_j \quad \text{Eq. IV-12}$$

where  $\underline{\mathbf{J}}_i$  and  $\underline{\mathbf{J}}_j$  are the total angular momentum vectors of spins  $i$  and  $j$ , localised at  $\underline{\mathbf{R}}_i$  and  $\underline{\mathbf{R}}_j$  respectively.  $J$  is the nearest neighbour Heisenberg coupling constant.

Ions possessing a non-zero value of orbital momentum L (non S-state ions) will interact with the crystal fields. As already stated in §IV.2.a., crystal field is much smaller than the spin-orbit (LS) coupling for the rare-earths and will consequently remove degeneracy of the ground multiplet determined by LS coupling.

However, crystal field is of the same order of magnitude as the molecular field. It is this superposition of two interactions of comparable strength that is responsible for the richness of magnetic phases found in rare-earth compounds. Indeed, the exchange interaction (either positive or negative), favours a certain type of magnetic order whereas the anisotropy term tends to favour an alignment of the spins along the random anisotropy axes. As the temperature increases, the energy barrier associated with the anisotropy term becomes gradually easier to overcome and a subsequent progression of magnetic phases can be observed.

The crystal field Hamiltonian at the  $i$ -th rare-earth site is given by<sup>4</sup> :  $H_c^i = A_i(\underline{S}_{xi})^2 + B_i(\underline{S}_{yi})^2 + C_i(\underline{S}_{zi})^2$ . When  $C_i$  is larger than the other coefficients, the  $z_i$ -axis becomes the local easy axis. Replacing  $C_i$  by an average value  $-D'$  gives the simpler term  $H_c = -D' \sum_i (\underline{S}_{zi})^2$ .

Rewriting this term, using a unit vector  $\underline{n}_i$  along the  $z_i$  direction, and adding the exchange term and a Zeeman term in the presence of an external field gives the well-known Harris-Plischke-Zuckermann<sup>5</sup> Hamiltonian:

$$H = -D \sum_i (\underline{n}_i \cdot \underline{J}_i)^2 - J \sum_{i,j} \underline{J}_i \cdot \underline{J}_j - g\mu_B \sum_i \underline{H} \cdot \underline{J}_i \quad \text{Eq. IV-13}$$

where the applied field defines the  $z$ -axis and  $\underline{n}_i$  points in the direction of the local anisotropy i.e. is random from site to site.

A further refinement includes the possibility of fluctuations in the exchange interaction. The exchange  $J$  in Eq. IV-13 is then replaced by  $J_0 + \Delta J_{ij}$  where  $J_0$  is the average exchange and  $\Delta J_{ij}$  is the fluctuation varying from site to site. This Hamiltonian has been solved for zero applied field and a phase diagram was proposed<sup>6</sup>. A schematic phase diagram can be found on Figure IV- 2.

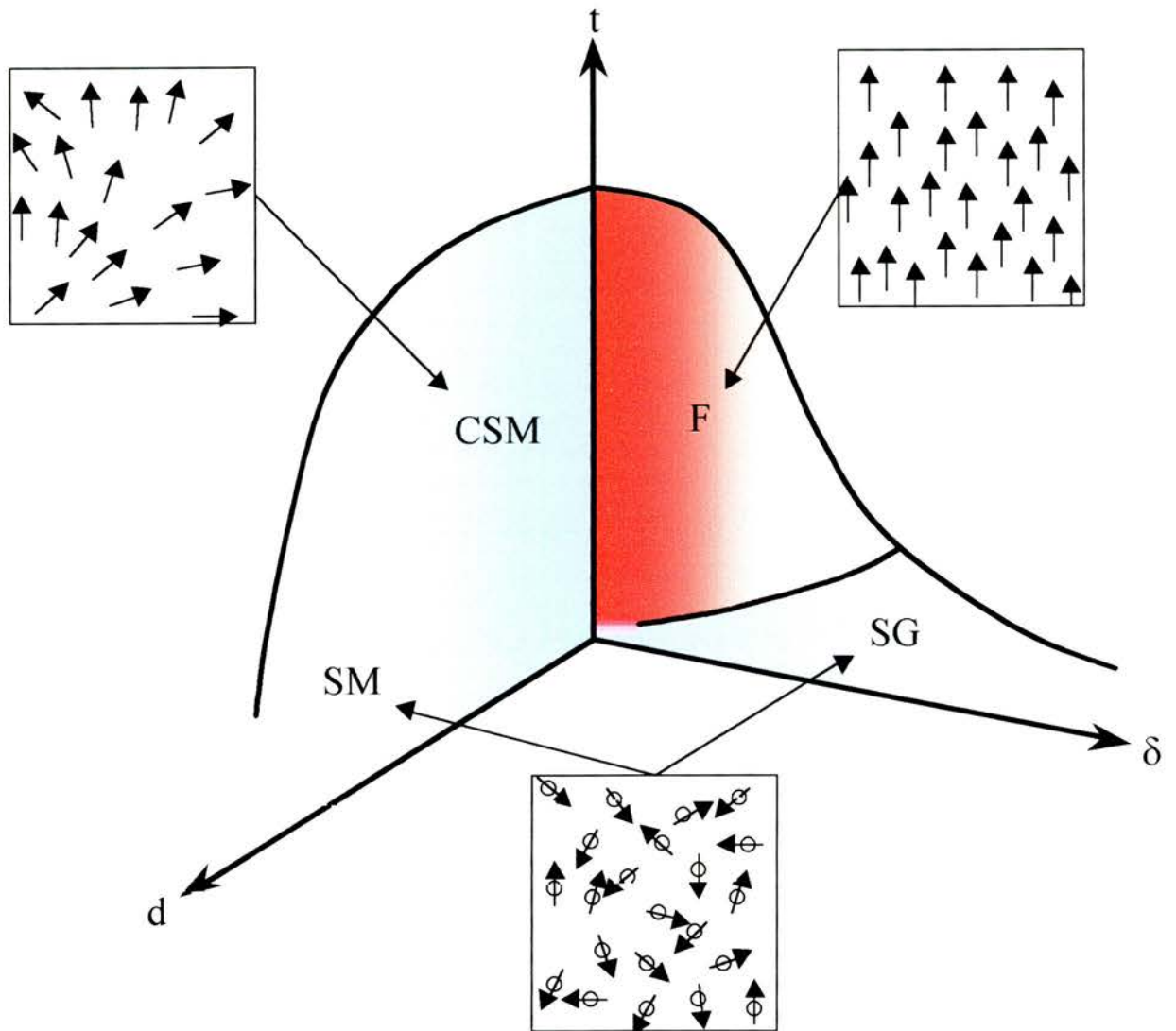


Figure IV- 2 : Schematic phase diagram for representing the possible magnetic states in presence of a Random Magnetic Anisotropy and exchange fluctuations.

Three important reduced parameters are needed to understand the phase diagram:  $t = k_B T / J_0$ ,  $d = D / J_0$  and  $\delta = \langle \Delta \rangle / J_0$ . When no random magnetic anisotropy (RMA) is present, ( $d=0$  plane) a ferromagnetic state is energetically favourable for low  $t$  and low  $\delta$ . For high  $\delta$  values, a spin glass (SG) state can exist. In the  $\delta=0$  plane, large values of  $d$  give rise to a speromagnet (SM) phase whereas small  $d$  values a correlated speromagnet exists in which a relatively long range magnetic order is present without the occurrence of a net spontaneous magnetisation.

The SM phase is similar to a SG state where the spins are frozen in a random direction from site to site but origin of the mechanism is different : for spin glasses the frustration in the interactions are responsible whereas in a speromagnet, the RMA is at the origin of the phenomenon. A common characteristic of both SG and SM state is the frequency dependent susceptibility cusp (see figure 14 from reference 14). The existence of a history dependent behaviour below a De Almeida-Thouless<sup>7</sup> irreversibility line is also observed in the SM and as well as in the SG state. Based on the fact that RAM can be analysed by the same scaling procedure used for SG, some authors claim that RMA systems undergo a SG like transition. However, for other authors<sup>8</sup>, RAM constitute an entirely new class.

### **IV.3 AC Susceptibility**

#### **IV.3.a Sample preparation and structural characterisation**

The samples ( $\alpha$ -Er<sub>7</sub>Fe<sub>3</sub> and  $\alpha$ -Er<sub>7</sub>Ni<sub>3</sub>) were prepared in St Andrews by the melt-spinning method described in chapter II. These samples were fairly easy to spin and they could be bent through a small radius of curvature without breaking which generally indicates a good amorphicity. In order to check that the samples were good amorphous ribbons, about 4g of each sample were placed into a vanadium can and a short neutron diffraction pattern was collected for each sample using the D1B diffractometer at the Institut Laue Langevin, Grenoble, France. The resulting diffraction patterns (see *Figure IV-3* and *IV-4*) are typical of amorphous alloys (see chapter II) and the only "Bragg" peak seen was associated with the can.

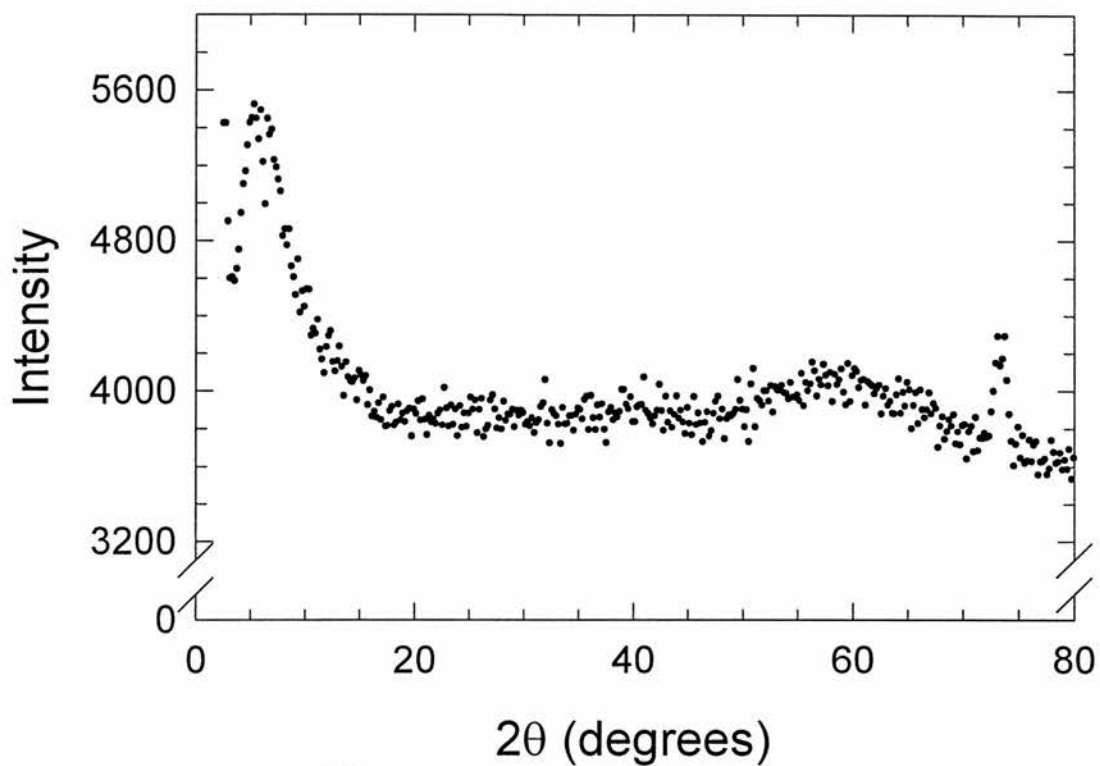


Figure IV- 3 :  $\alpha\text{-Er}_7\text{Ni}_3$  diffraction pattern measured on DIB.

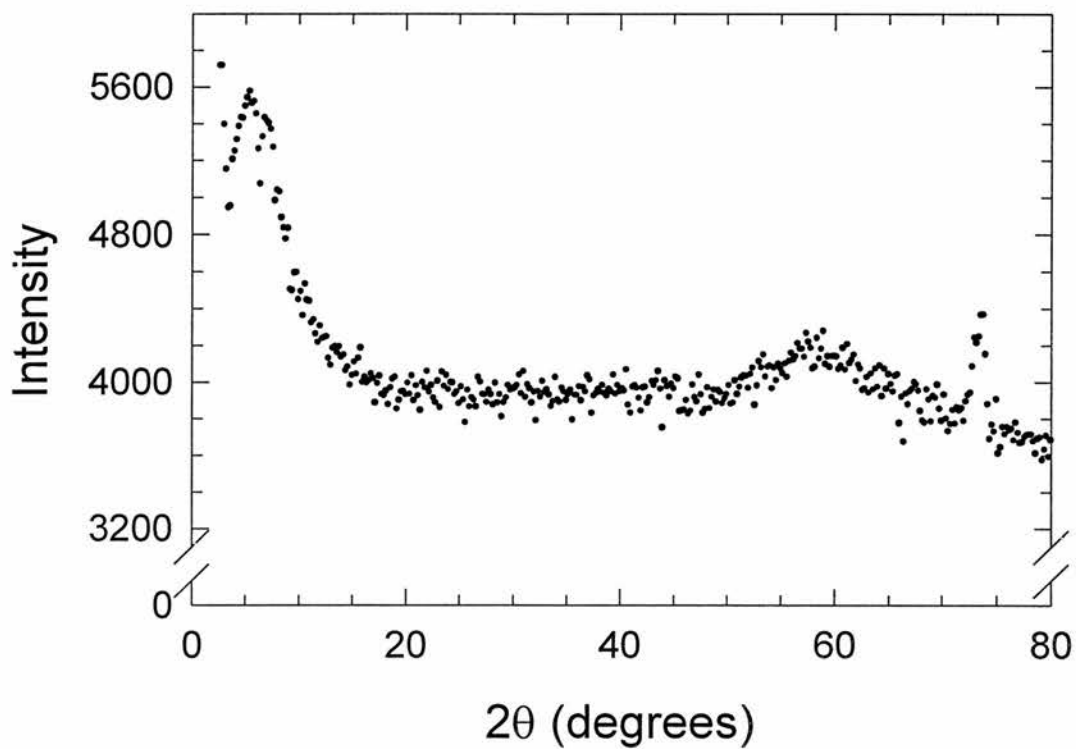


Figure IV- 4 :  $\alpha\text{-Er}_7\text{Fe}_3$  diffraction pattern measured on DIB.



### IV.3.b Experimental procedure

0.0248g of  $\alpha\text{-Er}_7\text{Fe}_3$  and 0.0184g of  $\alpha\text{-Er}_7\text{Ni}_3$  were placed in an Oxford Instrument MagLab<sup>EXA</sup> in AC susceptibility configuration (see chapter II for details). The samples consisted of fifteen to twenty pieces of ribbons stuck together with vacuum grease, wrapped in cotton wool and placed in a gelatine capsule. The sole purpose of the cotton wool is to prevent the sample from moving inside the capsule. Both cotton wool and vacuum grease give a very small diamagnetic contribution. This is accounted for in the data presented in this chapter by performing a background measurement that is subsequently subtracted from the raw data. The dimensions of each pieces of ribbon were approximately 1cm long, 1.5mm wide and 20 $\mu\text{m}$  thick. As the length of the sample is far greater than its other dimensions, the demagnetisation factor  $N$  is negligible<sup>9</sup>. This can be important as susceptibility in RAM can be very large ( $\chi_0 \sim (J/D)^4$ ), thereby reaching the demagnetising value of  $1/N$ . Hence, a correlated speromagnet could be easily mistaken with a ferromagnet if sufficient care is not taken.

The frequencies used for the AC susceptibility measurements were 11, 33, 77, 330, 567, 1054, 2110, 3330 and 5670 Hz, carefully avoiding any mains harmonics. The maximum frequency was low enough to avoid eddy currents. Zijlstra<sup>10</sup> showed that for the case of an infinitely long cylinder subject to a uniaxial ac applied field, the deviations between the applied and the internal field in both magnitude and phase are a function of the reduced radius  $a_0$ .

$$a_0 = \frac{d}{\delta\sqrt{2}} \quad \text{with} \quad \delta = \sqrt{\frac{\rho}{\pi f \mu}} \quad \text{Eq. IV-14}$$

where  $\delta$  is the skin depth of the sample,  $d$  the diameter of the cylinder in cm,  $\rho$  the resistivity of the sample in  $\mu\Omega\text{m}$ ,  $f$  the frequency of the applied field and  $\mu$  the sample permeability equal to the free space permeability  $\mu_0$  multiplied by  $(1+\chi)$ . It can be shown that the errors in  $\chi$  are less than 3% if  $a_0 < 0.9$  and negligible if  $a_0 < 0.2$ .

It can be seen from the expression of  $a_0$  that for a given sample, the only way to reduce the eddy current effects is to reduce the frequency. Fortunately for the samples under consideration, the skin depths are quite large due to their high resistivities. Indeed, the lack of atomic order in an amorphous material implies a short electron mean

free path and therefore a high value for the resistivity<sup>11</sup> (about 180 $\mu\Omega$ .cm for these samples). A quick calculation shows that even in the worse case scenario, i.e. d=1.5mm and f=5670Hz,  $a_0$  is still below 0.2.

### IV.3.c Transition temperatures for $\alpha$ -Er<sub>7</sub>Fe<sub>3</sub> and $\alpha$ -Er<sub>7</sub>Ni<sub>3</sub>

*Figure IV- 5* and *Figure IV- 7* show the temperature dependence of  $\chi'$  and  $\chi''$  for  $\alpha$ -Er<sub>7</sub>Fe<sub>3</sub> and  $\alpha$ -Er<sub>7</sub>Ni<sub>3</sub> respectively in an AC driving field of 1 Oe and 330 Hz. A sharp cusp, similar to that observed in spin glasses<sup>12</sup> can clearly be seen in both samples. The cusp temperatures are 26.2K and 9.8K for  $\alpha$ -Er<sub>7</sub>Fe<sub>3</sub> and  $\alpha$ -Er<sub>7</sub>Ni<sub>3</sub> respectively (see *Table IV- 1*). Sharp cusps have been observed in the past in amorphous RAM with large anisotropy to exchange ratio<sup>13, 14</sup>. A confirmation that the samples were good amorphous ribbons is also shown by the absence of a secondary peak sometimes observed in other RAM systems (eg  $\alpha$ -Dy<sub>7</sub>Ni<sub>3</sub>) and attributed to small crystallites is absent in both samples<sup>15</sup>.

At high temperatures, the real component of the susceptibility of  $\alpha$ -Er<sub>7</sub>Ni<sub>3</sub> clearly obeys the well-known Curie-Weiss law (*Eq. IV- 9*):

$$\chi = \frac{C}{T - \theta_P}$$

where C is the so-called Curie constant and  $\theta_P$  is the paramagnetic Curie temperature. Clearly, the best way to present the data is to linearise *Eq. IV- 9* which is achieved by plotting  $1/\chi'$  versus the temperature as on *Figure IV- 8*. Such a plot is commonly known as a Curie plot. *Eq. IV- 9* also holds for  $\alpha$ -Er<sub>7</sub>Fe<sub>3</sub> but there is a small deviation from linearity starting at a temperature much further from the freezing temperature than for the case of  $\alpha$ -Er<sub>7</sub>Ni<sub>3</sub>. The values for  $\theta_P$ , given by the intercept between the linearised inverse susceptibility and the x-axis from *Figure IV- 6* and *Figure IV- 8* are found to be 45.4K for  $\alpha$ -Er<sub>7</sub>Fe<sub>3</sub> and 11.3K for  $\alpha$ -Er<sub>7</sub>Ni<sub>3</sub> (see *Table IV- 1*).

It is instructive to see whether these temperatures, and thereby the strength of the exchange energy between the spins, scale with the de Gennes factor or not. Indeed, as discussed in the previous paragraph, de Gennes scaling holds very well for light rare-earths (RE) but discrepancies occur for the heavy RE for which spin-orbit coupling

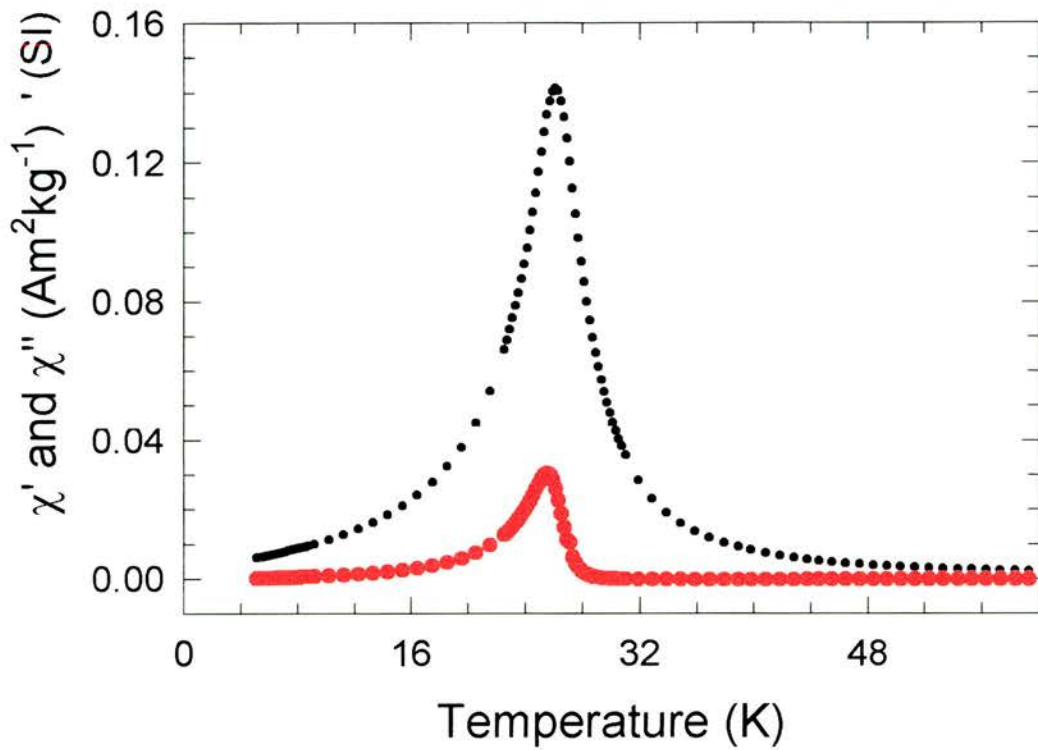


Figure IV- 5 : the real  $\chi'$  and imaginary  $\chi''$  component of the magnetic susceptibility for  $\alpha\text{-Er}_7\text{Fe}_3$  (AC field of 10e and 333Hz) as a function of temperature.

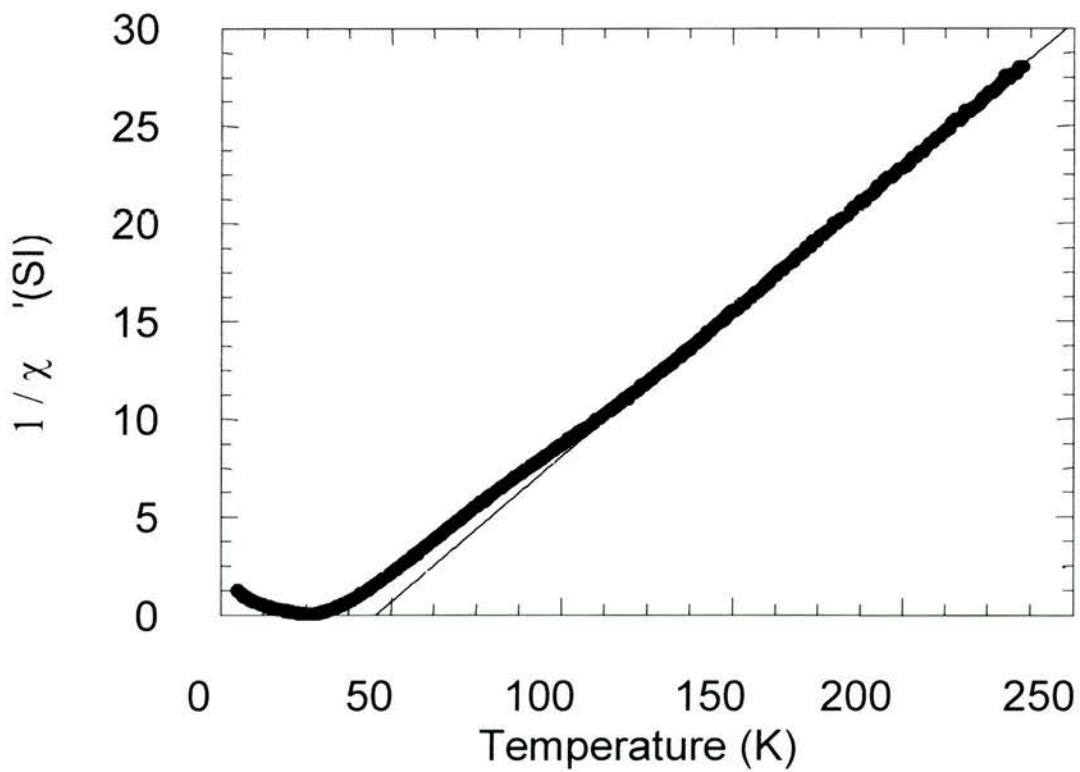


Figure IV- 6 :  $1/\chi'$  versus Temperature for  $\alpha\text{-Er}_7\text{Fe}_3$ . The line corresponds to the Curie-Weiss law.

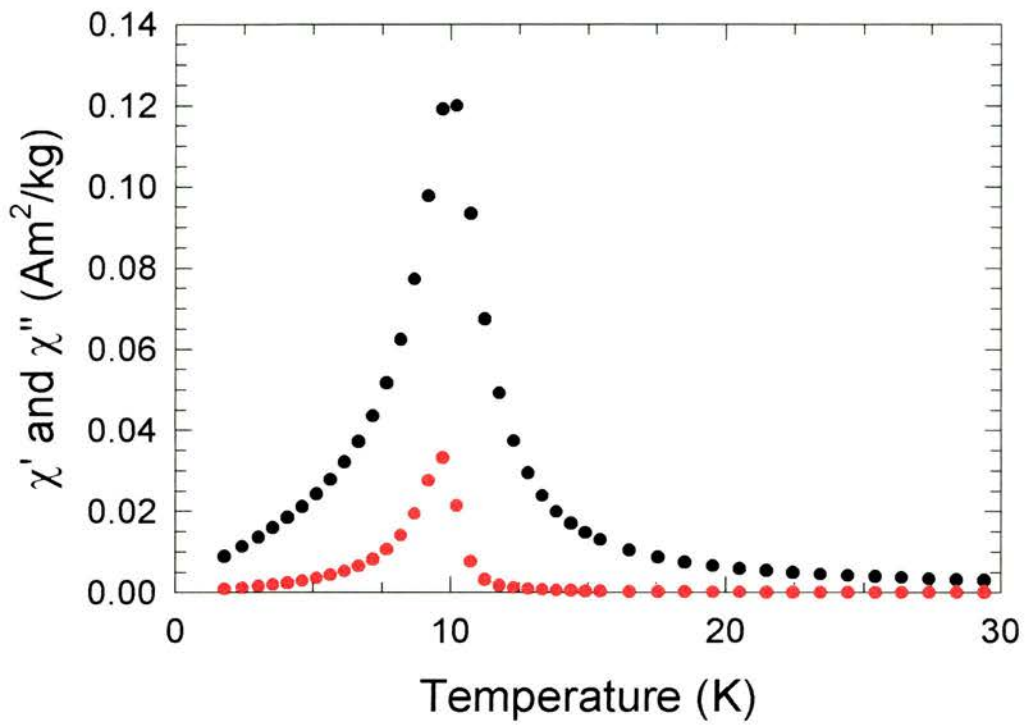


Figure IV- 7 : the real  $\chi'$  and imaginary  $\chi''$  component of the magnetic susceptibility for  $\alpha\text{-Er}_7\text{Ni}_3$  (AC field of 10e and 333Hz) as a function of temperature.

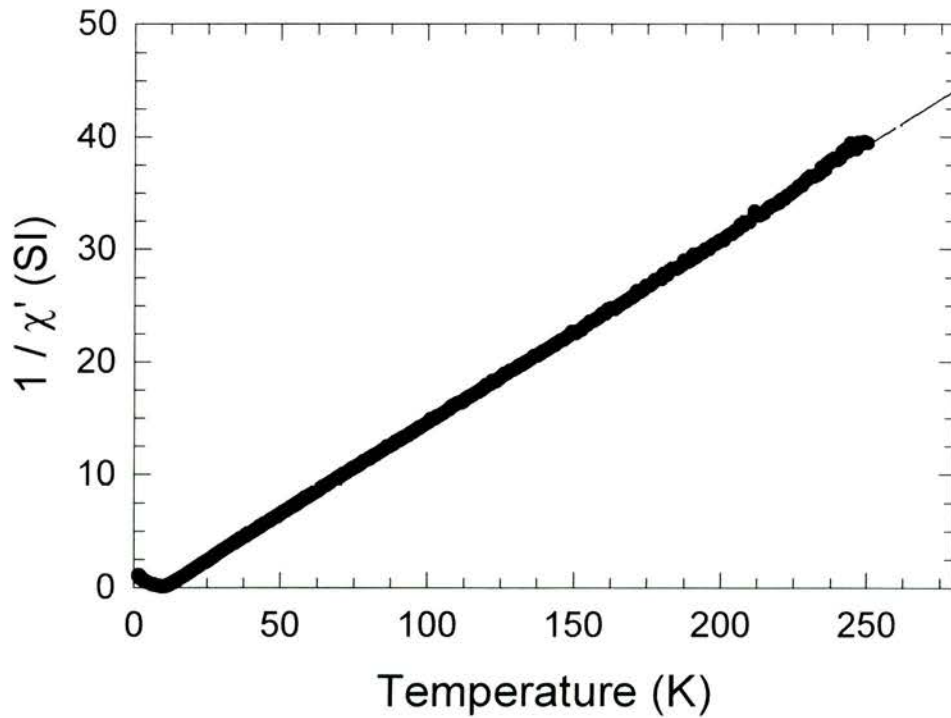


Figure IV- 8 :  $1/\chi'$  versus Temperature for  $\alpha\text{-Er}_7\text{Ni}_3$ . The line corresponds to the Curie-Weiss law.

starts to play a role<sup>16</sup>. Er classifies as “heavy” as it is after Gd in the periodic table. It is therefore anticipated that de Gennes scaling should not be accurately verified.

Recalling Eq. IV- 11,  $(g-1)^2 \left| \underline{\mathbf{J}}_i \cdot \underline{\mathbf{J}}_j \right| = (g-1)^2 J(J+1)$  gives 7.08 for Dy and 2.55 for Er. For  $\alpha$ -Dy<sub>7</sub>Ni<sub>3</sub>,  $\theta_P = 42.8\text{K}$ , as given by reference 15, this should give a value of 15.4K for  $\alpha$ -Er<sub>7</sub>Ni<sub>3</sub>, not too far off the experimental value (see Table IV- 1). I have not found any report for the value of  $\theta_P$  for  $\alpha$ -Dy<sub>7</sub>Fe<sub>3</sub> but  $T_f$  is about 85K which gives a theoretical value of 30.6 K; again the agreement is qualitatively correct.

The slope of the linearised inverse susceptibility, is simply the inverse of the Curie constant C. Recalling the Eq. IV- 7, the Curie constant is :

$$C = \frac{N\mu_0\mu_{\text{eff}}^2}{3k} \quad \text{Eq. IV-15}$$

The extracted values of  $\mu_{\text{eff}}$  are 9.4 $\mu_B$  and 9.5 $\mu_B$  for  $\alpha$ -Er<sub>7</sub>Ni<sub>3</sub> and  $\alpha$ -Er<sub>7</sub>Ni<sub>3</sub> respectively which are very close to the free Er ion value of 9.58  $\mu_B$  given by :

$$\mu_{\text{eff}} = g\sqrt{J(J+1)}\mu_B \quad \text{Eq. IV-16}$$

For comparison with the Er<sub>7</sub>Fe<sub>3</sub>, the parent compound  $\alpha$ -Y<sub>7</sub>Ni<sub>3</sub> was made and found to be Pauli paramagnetic in agreement with Reference <sup>17</sup>. Furthermore, magnetic<sup>18</sup> and neutron scattering<sup>19</sup> study of the strong RMA system Dy<sub>x</sub>Y<sub>7-x</sub>Ni<sub>3</sub> indicates that the Ni atoms do not support a significant local moment. These facts, combined with the absence of magnetic splitting in the Mössbauer spectra (see Figure IV- 9) of  $\alpha$ -Er<sub>7</sub>Fe<sub>3</sub> at temperatures above and below  $T_f$  indicate that the Fe atoms (and by extension the Ni atoms as Ni atoms substitute on the Fe sites) do not carry a significant moment, confirming the neutron measurements on the (DyY)<sub>7</sub>Ni<sub>3</sub> alloys.

Sample	T <sub>f</sub> (330 Hz)	$\theta_P$ (exp)	$\theta_P$ (theory)	$\mu_{\text{eff}}$ (exp)	$\mu_{\text{eff}}$ (theory)
$\alpha$ -Er <sub>7</sub> Fe <sub>3</sub>	26.2 K	45.4 K	15.4 K	9.5	9.58
$\alpha$ - Er <sub>7</sub> Ni <sub>3</sub>	9.8 K	11.3 K	-	9.4	9.58

Table IV- 1 : summary of the properties of  $\alpha$ -Er<sub>7</sub>Fe<sub>3</sub> and  $\alpha$ -Er<sub>7</sub>Ni<sub>3</sub>



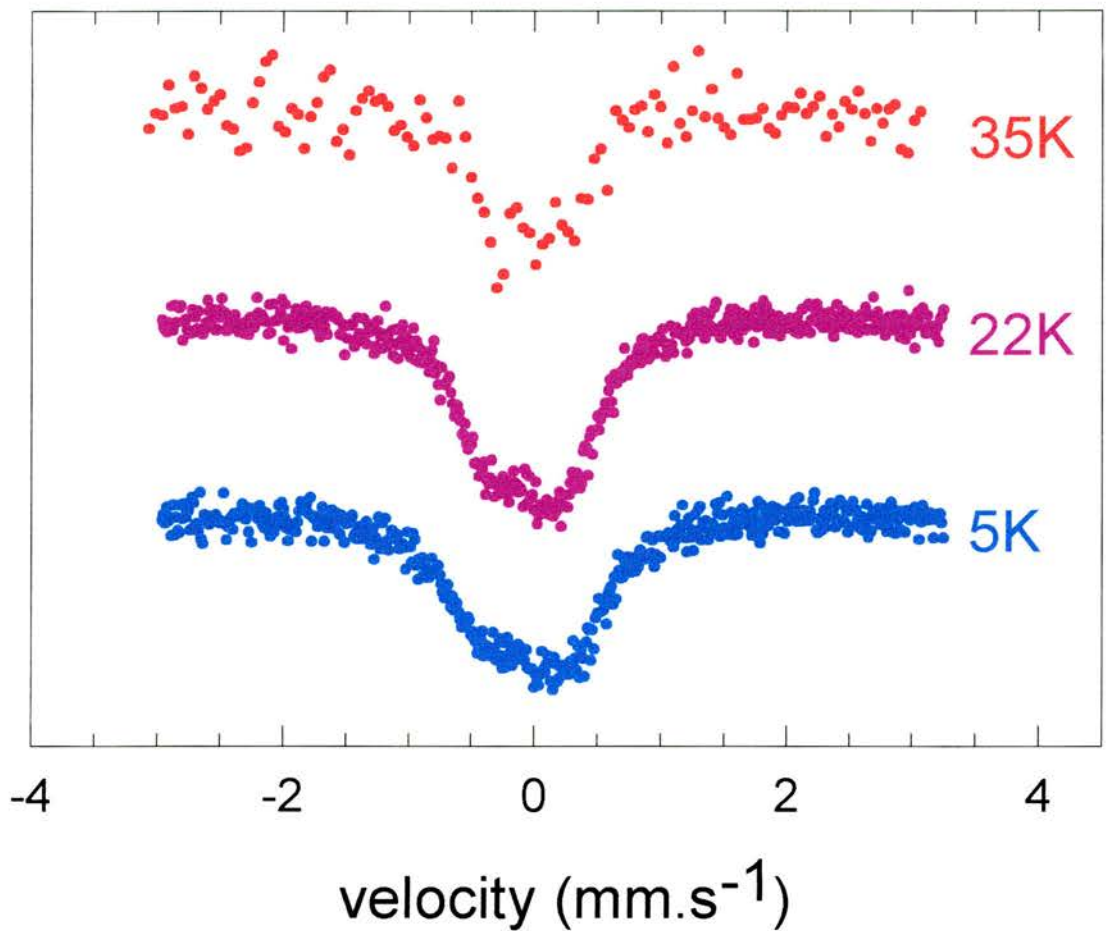


Figure IV- 9 : Mössbauer spectra for  $\alpha$ -  $\text{Er}_7\text{Fe}_3$  showing the absence of a magnetic sextet. Note : the difference in the number of points in the velocity range  $[-3\text{mm}\cdot\text{s}^{-1}, +3\text{mm}\cdot\text{s}^{-1}]$  between the 35K data and the 22K and 5K data is due to the fact that these datasets have been collected using a different velocity ramp.



### IV.3.d Frequency dependence as a probe for sample dynamics

The  $\alpha$ -Er<sub>7</sub>Fe<sub>3</sub> and  $\alpha$ -Er<sub>7</sub>Ni<sub>3</sub> samples were measured at 11 different frequencies : 11, 33, 77, 167, 333, 567, 767, 1054, 2110, 3330 and 5670 Hz thereby covering a time window of  $2 \times 10^{-4}$  s to 0.1s. Whilst the lower limit of the frequency range is limited by the signal size (the voltage across the secondary pick-up coil is proportional to the frequency, as discussed in chapter II). The upper limit of the frequency was determined such that eddy currents are negligible as discussed in §IV.2.a. The temperature dependence for these frequencies is shown on *Figure IV- 10* for  $\alpha$ -Er<sub>7</sub>Fe<sub>3</sub> and *Figure IV- 11* for  $\alpha$ - Er<sub>7</sub>Ni<sub>3</sub>.

The magnetic susceptibility shows a very sharp cusp for all the frequencies studied. The cusp temperatures change from 25.4K at 11 Hz to 26.5K at 5670Hz for  $\alpha$ -Er<sub>7</sub>Fe<sub>3</sub>. Frequency dependence of the cusp has been previously observed in spin glasses (SG) in the classic work by Cannella and Mydosh<sup>12</sup> and also by Tholence<sup>20</sup>. However, it can be seen from *Figure IV- 10* that the cusp susceptibility in our samples increases by a factor of nearly three over the frequency range studied; this dependence is much more pronounced than in “conventional” SG but is in accordance with observations on other strong RMA systems<sup>14</sup>. Large frequency dependencies have been observed in the 2D spin glass<sup>21</sup> Rb<sub>2</sub>Cu<sub>1-x</sub>Co<sub>x</sub>F<sub>4</sub> and also in superparamagnets, although for the latter case, the cusp is no longer sharp. It should be noted that in our samples, the time dependence effects are only observed around and below the freezing temperature  $T_f$  as for spin glass systems (and unlike superparamagnets<sup>22</sup>).

#### IV.3.d.1 Lundgren's $\pi/2$ law

Lundgren et al<sup>23</sup> proposed a simple relationship between  $\chi'$  and  $\chi''$  for systems in which a broad distribution of relaxation times is present. Without reinventing the wheel, their results will be briefly reviewed below. First, we consider a system with a unique relaxation time  $\tau$ , applicable for instance to a dilute paramagnet, for which the Debye relation<sup>24</sup> holds:

$$\chi^*(\omega) - \chi_\infty = \frac{\chi_s - \chi_\infty}{1 + i\omega\tau} \quad \text{Eq. IV-17}$$

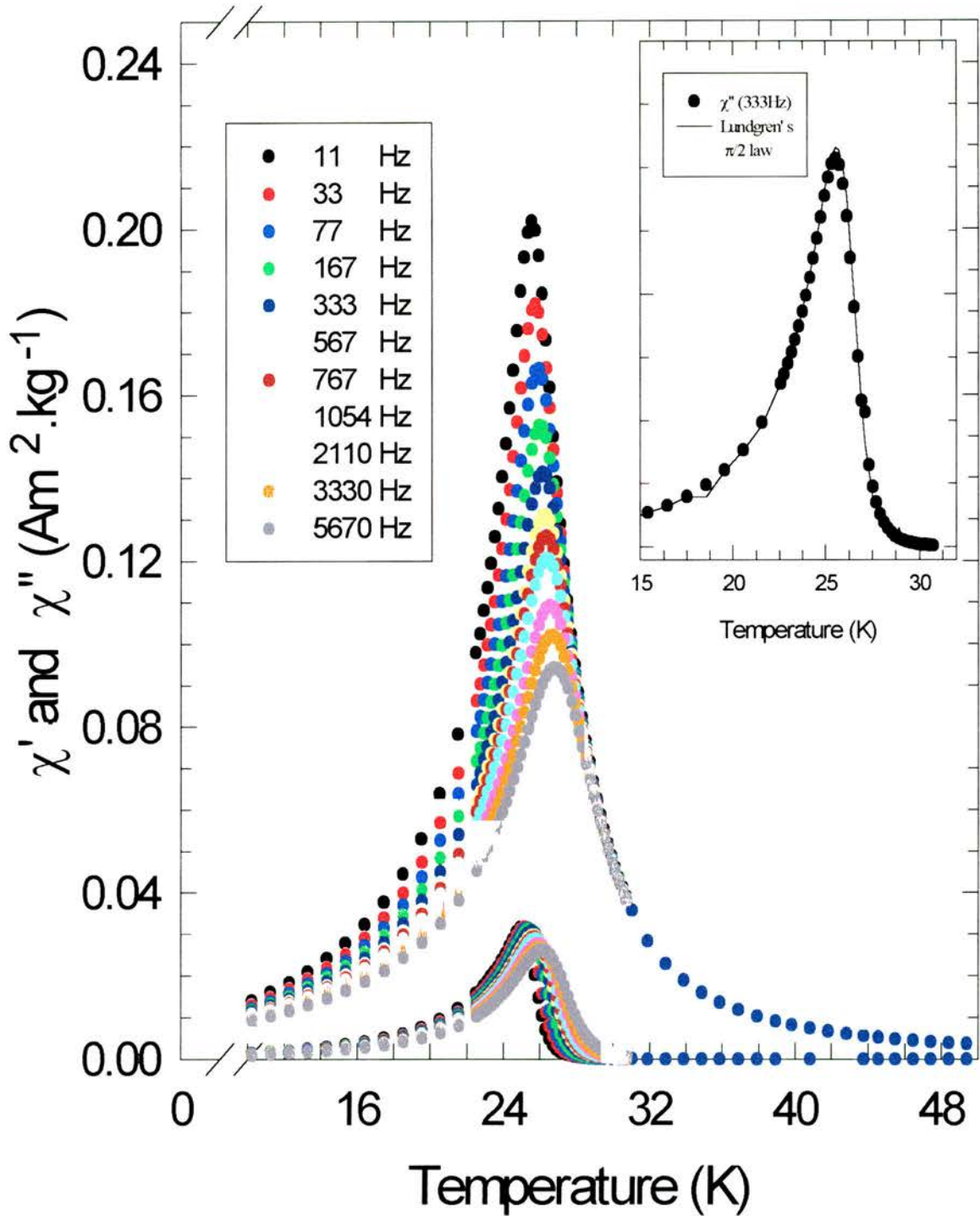


Figure IV- 10 : Temperature dependence of the magnetic susceptibility for  $\alpha\text{-Er}_7\text{Fe}_3$  for different frequencies. Insert :  $\pi/2$  Lundgren's law at 333 Hz.

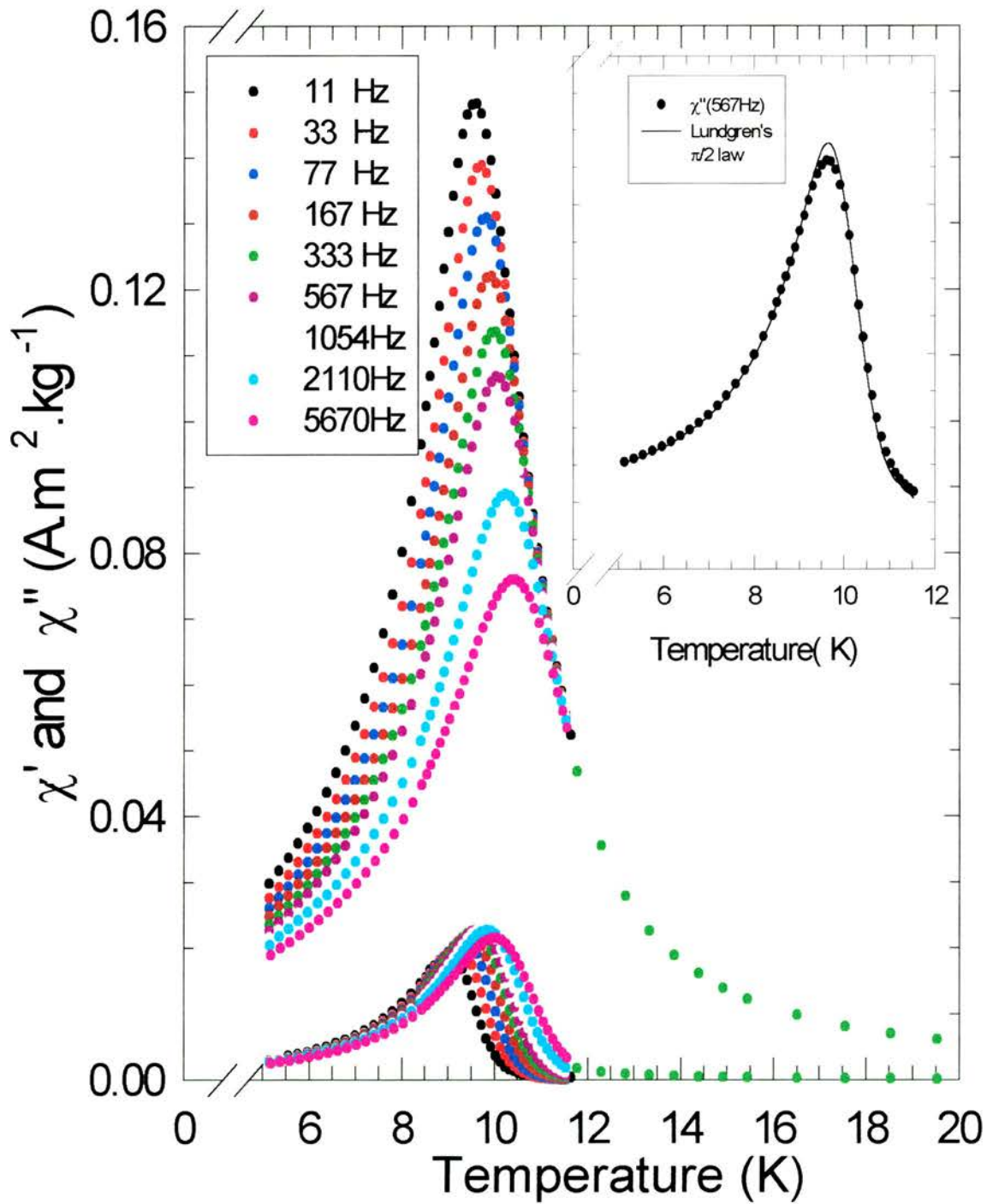


Figure IV- 11 : Temperature dependence of the magnetic susceptibility for  $\alpha\text{-E}_7\text{Ni}_3$  for different frequencies. Insert :  $\pi/2$  Lundgren's law at 567 Hz.

$\chi_s$  is the static (or isothermal) susceptibility and corresponds to the susceptibility as the time after the field was applied approaches infinity whereas  $\chi_\infty$  is the adiabatic susceptibility of the system and corresponds to the infinite frequency limit.

If we then extend that model to a system in which the probability distribution of relaxation times is no longer a delta function centered on  $\tau$  but a broader function  $g(\ln\tau)$ , Eq. IV-17 can be rewritten as :

$$\chi^*(\omega) - \chi_\infty = (\chi_s - \chi_\infty) \int_0^\infty \frac{g(\ln \tau)}{1 + i\omega\tau} d(\ln \tau) \quad \text{Eq. IV-18}$$

$g(\ln\tau)$  corresponds to the number of magnetic entities with relaxation times between  $\ln\tau$  and  $\ln(\tau)+d(\ln\tau)$  and, as every probability distribution is normalised :

$$\int_0^\infty g(\ln \tau) d(\ln \tau) = 1 \quad \text{Eq. IV-19}$$

Separating Eq. IV-18 into its real and imaginary component and taking  $\chi_\infty = 0$  gives :

$$\chi'(\omega) = \chi_s \int_{\tau_{\min}}^{\tau_{\max}} \frac{g(\ln \tau)}{1 + (\omega\tau)^2} d(\ln \tau) \quad \text{Eq. IV-20}$$

$$\chi''(\omega) = \chi_s \int_{\tau_{\min}}^{\tau_{\max}} \frac{\omega\tau g(\ln \tau)}{1 + (\omega\tau)^2} d(\ln \tau) \quad \text{Eq. IV-21}$$

where  $\tau_{\min}$  and  $\tau_{\max}$  are the minimum and maximum values of the relaxation times respectively. Within Lundgren's framework, the time associated with the measuring frequency  $\tau_m=1/\omega$  is such that  $\tau_m \ll \tau_{\max}$  for a paramagnet and  $\tau_{\min} \ll \tau_m \ll \tau_{\max}$  for a spin glass. Taking the partial derivative of Eq. IV-20 with respect to  $\ln\omega$  gives :

$$\frac{\partial \chi'}{\partial \ln \omega} = \chi_s \int_{\tau_{\min}}^{\tau_{\max}} \frac{2(\omega\tau)^2 g(\ln \tau)}{(1 + (\omega\tau)^2)^2} d(\ln \tau) \quad \text{Eq. IV-22}$$

The range of relaxation times contributing to that integral is only limited to approximately a decade centred around  $\tau_m$ . If the distribution  $g(\ln\tau)$  is slowly varying in

$\ln\tau$  over that range, it can be replaced by  $g(\ln\tau_m)$  and it becomes therefore possible to bring it out of the integral. Integration of Eq. IV-22 then leaves :

$$\frac{\partial\chi'}{\partial\ln\omega} = \chi_s g(\ln\tau_m) \left( \frac{1}{1+(\omega\tau_{\max})^2} - \frac{1}{1+(\omega\tau_{\min})^2} \right) \quad \text{Eq. IV-23}$$

Recalling  $\tau_{\min} \ll \tau_m \ll \tau_{\max}$ , Eq. IV-23 conveniently reduces to :

$$\frac{\partial\chi'(\omega)}{\partial\ln\omega} = -\chi_s g(\ln\tau_m) \quad \text{Eq. IV-24}$$

On the other hand, Eq. IV-21 for the imaginary component of the susceptibility can be integrated directly. Again, a slow varying distribution of relaxation times  $g(\ln\tau)$  can be replaced by its value at  $\tau_m$  and be brought out of the integral.

$$\chi''(\omega) = -\chi_s g(\ln\tau_m) (\arctan(\omega\tau_{\max}) - \arctan(\omega\tau_{\min})) \quad \text{Eq. IV-25}$$

which reduces for the spin glass case ( $\tau_{\min} \ll \tau_m \ll \tau_{\max}$ ) to :

$$\chi''(\omega) = -\frac{\pi}{2} \chi_s g(\ln\tau_m) \quad \text{Eq. IV-26}$$

Comparing Eq. IV-24 and Eq. IV-26 leads to the  $\pi/2$  Lundgren's law<sup>23</sup> :

$$\chi''(\omega) = \frac{\pi}{2} \frac{\partial\chi'(\omega)}{\partial\ln\omega} \quad \text{Eq. IV-27}$$

Eq. IV-27 has been checked for in the  $\alpha$ -Er<sub>7</sub>Fe<sub>3</sub> and  $\alpha$ -Er<sub>7</sub>Ni<sub>3</sub> RAM systems. For each temperature, the real component of the susceptibility  $\chi'$  was spline fitted to a polynomial of the third order  $ax^3+bx^2+cx+d$  ( $x=\ln(\omega)$ ) and then its derivative  $3ax^2+2bx+c$  was multiplied by  $\pi/2$  and compared with the imaginary component  $\chi''$ . The results (inserts of Figure IV- 10 and Figure IV- 11) show an impressive agreement suggesting a very broad distribution of relaxation times.

#### IV.3.d.2 Cole-Cole analysis.

The frequency dependence of the amorphous Er<sub>7</sub>Fe<sub>3</sub> and Er<sub>7</sub>Ni<sub>3</sub> alloys can be well accounted for using a simple phenomenological model, which has proved to hold in spin glass systems<sup>25</sup>, in which the susceptibility arises from two contributions. The



first contribution is a simple Debye model (Eq. IV-17) arising from the independent “free” spins. The relaxation time  $\tau_f$  associated with these single spin relaxation processes is of the order of  $10^{-9}$  s –  $10^{-13}$  s. Separating the complex susceptibility in Eq. IV-17 into its real and imaginary part and adopting  $\tau$  the subscript  $f$  (for “free”), gives :

$$\chi'_f = \chi_\infty^f + \frac{\chi_s^f - \chi_\infty^f}{1 + (\omega\tau_f)^2} \quad \text{Eq. IV-28}$$

$$\chi''_f = (\omega\tau_f) \frac{\chi_s^f - \chi_\infty^f}{1 + (\omega\tau_f)^2} \quad \text{Eq. IV-29}$$

The relaxation time  $\tau_f$  of the free spins being so small, even the highest frequency of the measurements  $\omega=35625$  rad.s<sup>-1</sup> multiplied by  $\tau_f$  gives a results that can be neglected when compared with unity. Under this  $\omega\tau_f \ll 1$  condition, it becomes evident that the free spins will not contribute at all to the imaginary component of the susceptibility but they will contribute an amount  $\chi_s^f$  (that for simplicity we shall rewrite as  $\chi_f$  from now on) to the real component.

Strongly correlated or clustered spins are responsible for the second contribution to the susceptibility. Using the successful phenomenological model of relaxation that Cole and Cole<sup>26</sup> first introduced, this second contribution can be written as :

$$\chi(\omega) - \chi_\infty^c = \frac{(\chi_s^c - \chi_\infty^c)}{1 + (i\omega\tau_c)^{(1-h)}} \quad \text{Eq. IV-30}$$

where the parameter  $h$  characterises the width of the distribution of relaxation times : for  $h \rightarrow 0$ , Eq. IV-30 reduces to the Debye expression for a single relaxation time and for  $h \rightarrow 1$ , the distribution is infinitely broad. An argand diagram in which  $\chi''$  is plotted against  $\chi'$  (i.e. a so-called Cole-Cole plot) can be used as evidence of the broadening of the distribution of relaxation times : as  $h$  increases from zero, the result ceases to be a semi-circle and starts to become an arc.

Carefully separating the real and imaginary components of Eq. IV-30 gives the results (with  $p=\ln(\omega\tau_0)$ ):

$$\chi'(\omega) = \chi_\infty^c + \frac{\chi_s^c - \chi_\infty^c}{2} \left( 1 - \frac{\sinh[(1-h)p]}{\cosh[(1-h)p] + \sin\left(\frac{\pi h}{2}\right)} \right) \quad \text{Eq. IV-31}$$



$$\chi''(\omega) = \frac{\chi_s^c - \chi_\infty^c}{2} \left( \frac{\cosh\left(\frac{\pi h}{2}\right)}{\cosh[(1-h)p] + \sin\left(\frac{\pi h}{2}\right)} \right) \quad \text{Eq. IV-32}$$

The plus sign in the denominator of Eq. IV-31 disagrees with reference 25 but the separation of a quantity that is complex because of its denominator  $z$  into a real and an imaginary part simply involves the multiplication of both the numerator and denominator by the complex conjugate of  $z$  and it is therefore easy to see that this will lead to the same denominator for both the real and imaginary part. Secondly, some of the authors of reference 25 published a later paper<sup>27</sup> in which they have corrected the mistake and thirdly, the dielectric analogy that can be found in Chelkowski's book<sup>28</sup> gives the same result as Eq. IV-31.

Neglecting the susceptibility  $\chi_\infty^c$  that is predicted to be small (and is indeed according to the Cole-Cole plots, Figures IV- 14 and IV- 15, in which the arc intercepts the origin), rewriting  $\chi_s^c$  as  $\chi_c$  for simplicity, and adopting  $A=N_f\chi_f$  and  $B=N_c\chi_c$  gives the final expressions :

$$\chi' = A + \frac{B}{2} \left( 1 - \frac{\sinh[(1-h)p]}{\cosh[(1-h)p] + \sin\left(\frac{\pi h}{2}\right)} \right) \quad \text{Eq. IV-33}$$

$$\chi'' = \frac{B}{2} \left( \frac{\cosh\left(\frac{\pi h}{2}\right)}{\cosh[(1-h)p] + \sin\left(\frac{\pi h}{2}\right)} \right) \quad \text{Eq. IV-34}$$

A simultaneous fit of Eq. IV-33 and Eq. IV-34 to the frequency dependent complex susceptibility data of the  $\alpha\text{-Er}_7\text{Fe}_3$  and  $\alpha\text{-Er}_7\text{Ni}_3$  samples has been performed for each temperature. The program used for the fitting was a modified version of our fitting program based on Bevington's book<sup>29</sup> : because of the few number of points, the fits were improved if the derivatives of the functions with respect to the parameters A, B, h and  $\ln\tau_c$  were given analytically rather than calculated numerically. The quality of

the fits can be seen for a few temperatures on *Figures IV- 12* for  $\alpha$ -Er<sub>7</sub>Fe<sub>3</sub> and *IV-13* for  $\alpha$ -Er<sub>7</sub>Ni<sub>3</sub>. *Tables IV- 2* and *IV- 3* show the resulting parameters A, B, h and ln( $\tau_0$ ) for these temperatures. Obviously, the fits are more accurate at temperatures for which ln( $\tau_0$ ) is included in the experimental frequency range (ie. near the transition). Indeed, ln( $\tau_0$ ) determines the position of the peak of  $\chi''$  (and h its width) and therefore, for temperatures well above or well below the transition, only the tail of  $\chi''$  is fitted.

*Figures IV-16* and *IV-17* show the evolution of the fitting parameters as a function of temperature for  $\alpha$ -Er<sub>7</sub>Fe<sub>3</sub> and  $\alpha$ -Er<sub>7</sub>Ni<sub>3</sub> respectively. Above the transition temperature, the values of both h and ln( $\tau_0$ ) increase rapidly as the temperature is reduced and they carry on increasing below T<sub>f</sub> but at a much slower rate, suggesting that they are reaching a plateau. This evolution is concordant with a previous study<sup>30</sup> on the insulating spin glass system Eu<sub>x</sub>Sr<sub>1-x</sub>S. This suggests that the growth of the clusters is very limited below T<sub>f</sub> and is in full accord with small angle neutron scattering results on Dy<sub>x</sub>Y<sub>1-x</sub>Ni<sub>3</sub> which show that below T<sub>g</sub>, the magnetic correlation length remains constant<sup>31</sup>. However, previous measurements by Filippi et al<sup>32</sup> on the a-Dy<sub>x</sub>Gd<sub>1-x</sub>Ni system have shown that below T<sub>f</sub>,  $\tau_0$  decreases slightly and then reaches a plateau but their analysis, based on a 1/ $\chi''$  vs 1/ $\chi'$  plot and using a different expression for the distribution of relaxation times, did not present any values for h. Another interesting property of the Cole-Cole analysis is that the total isothermal susceptibility  $\chi_T(0)$  can be extracted by simply adding the isothermal free spin (A) and clustered spin (B) contributions. The results are shown on the top of *Figures IV-16* and *IV-17*. Interestingly, the low temperature behaviour of this fitted isothermal (or "dc") is still very different from the experimental low-frequency (11Hz) data but the two converge at higher temperatures. The salient feature of  $\chi_T(0)$  is the presence of a peak at a finite temperature T<sub>g</sub>(0). This reinforces the already mentioned difference between a RAM and a superparamagnetic system for which a continuous Curie-like increase in  $\chi_T(0)$  is expected.

Temperature	A	B	$\ln(\tau_0)$	H
19.55 K	13.04	0.09	-1.40	0.854
24.54 K	34.66	0.02	-3.80	0.791
25.55 K	26.46	1.40	-7.03	0.706
25.94 K	18.98	3.33	-8.27	0.622

Table IV- 2 : parameters obtained for  $\alpha\text{-Er}_7\text{Fe}_3$  from fitting the data in Figure IV- 12.

Temperature	A	B	$\ln(\tau_0)$	h
8.91 K	21.57	0.12	-5.36	0.779
9.22 K	20.89	0.06	-6.78	0.748
9.42 K	16.99	1.55	-7.68	0.675
9.93 K	11.65	3.08	-9.32	0.524

Table IV- 3 : parameters obtained for  $\alpha\text{-Er}_7\text{Ni}_3$  from fitting the data in Figure IV- 13.

Finally, two Cole-Cole plots, one for each sample, are presented in Figures IV-14 and IV-15 . On such a plot, the horizontal axis is the real susceptibility due to the cluster term (ie.  $\chi' - \chi'_f$ ) and the vertical axis is the imaginary component of the complex magnetic susceptibility  $\chi''$ . One can see that the complex susceptibility is well represented by an arc of a circle. This arc flattens off as the temperature is reduced confirming the existence of a broad distribution of relaxation times. As the temperature is lowered, the data sweeps around the arc from the right hand side of the Cole-Cole plot (isothermal limit) to the left-hand side (adiabatic limit).

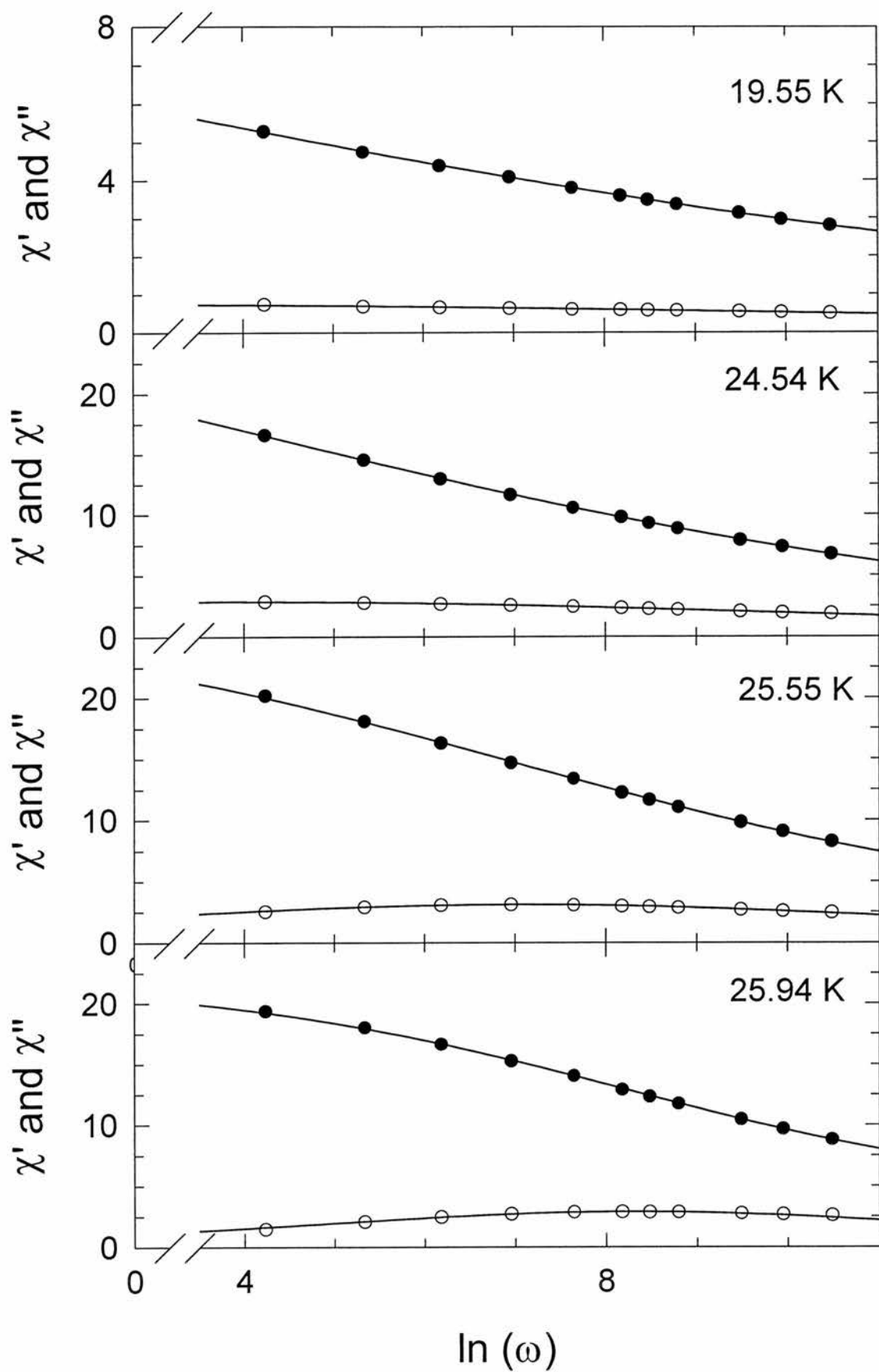


Figure IV- 12 : Data and fits to Eq. IV- 33 and IV- 34 for  $\alpha$ -Er<sub>7</sub>Fe<sub>3</sub> at different temperatures.

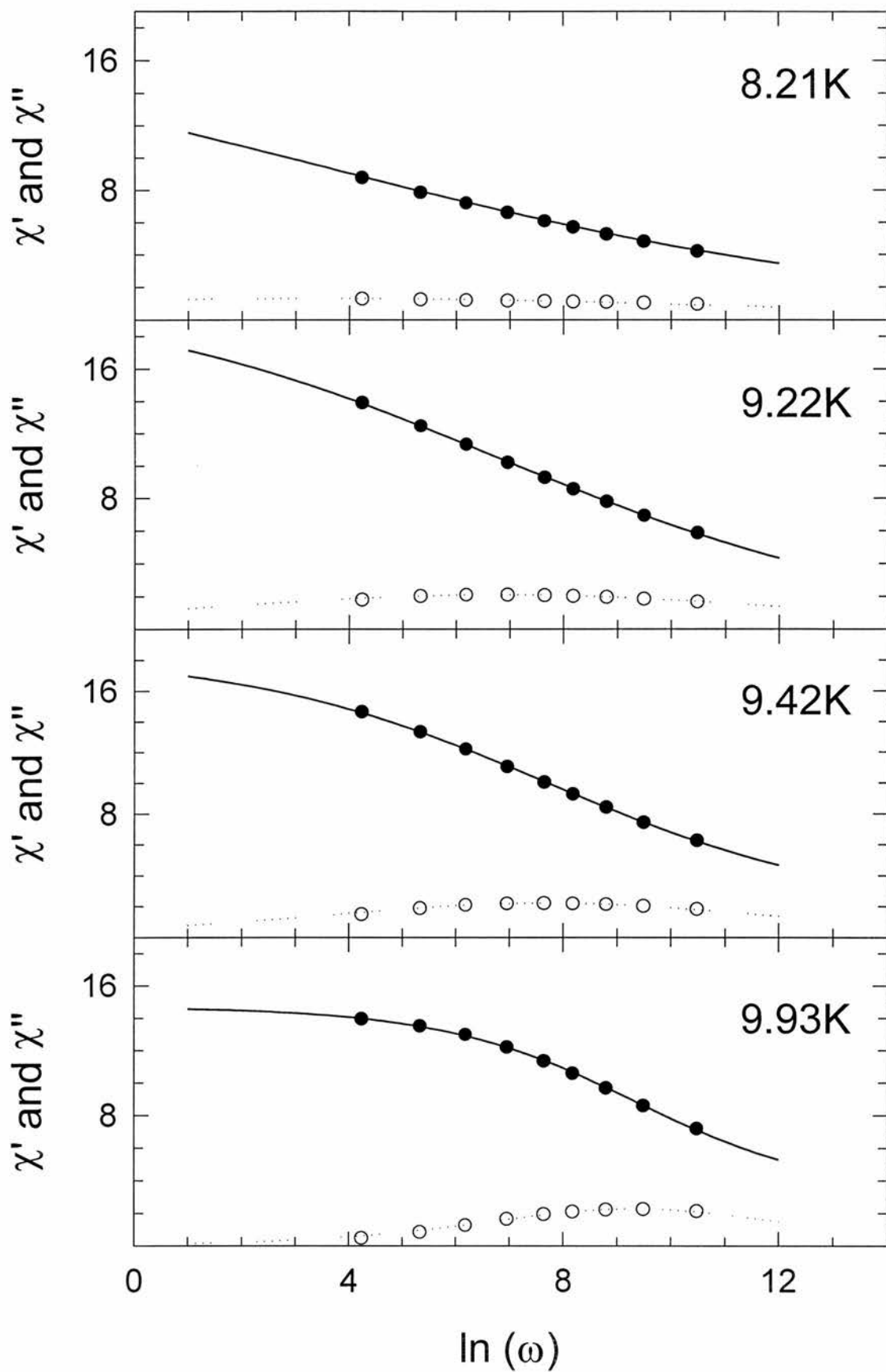


Figure IV- 13 : Data and fits to Eq. IV- 33 and IV- 34 for  $\alpha$ -Er<sub>7</sub>Ni<sub>3</sub> at different temperatures.

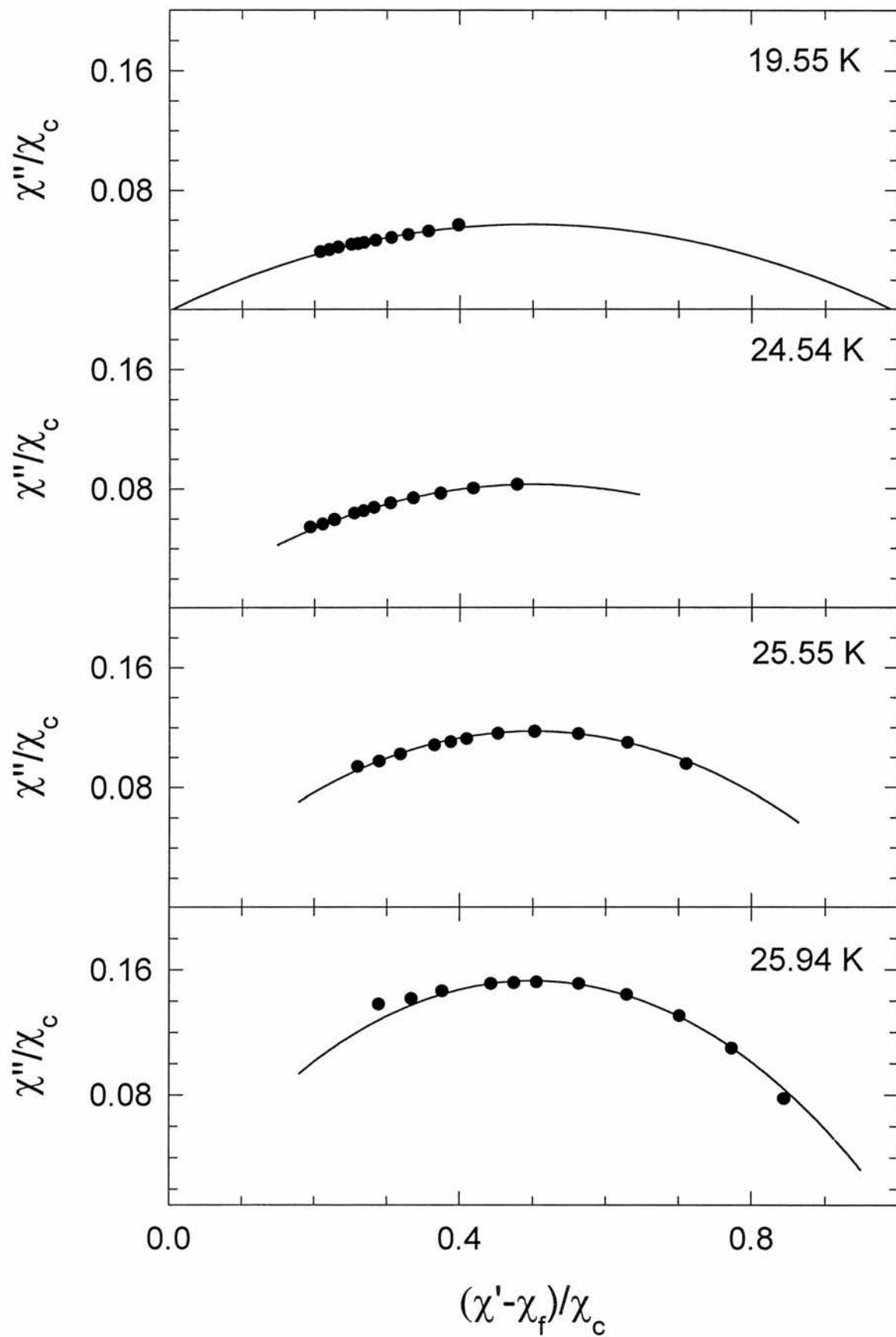


Figure IV- 14 : Cole-Cole plots for  $\alpha\text{-Er}_7\text{Fe}_3$  in the temperature range  $19.55\text{K} < T < 25.94\text{K}$ .



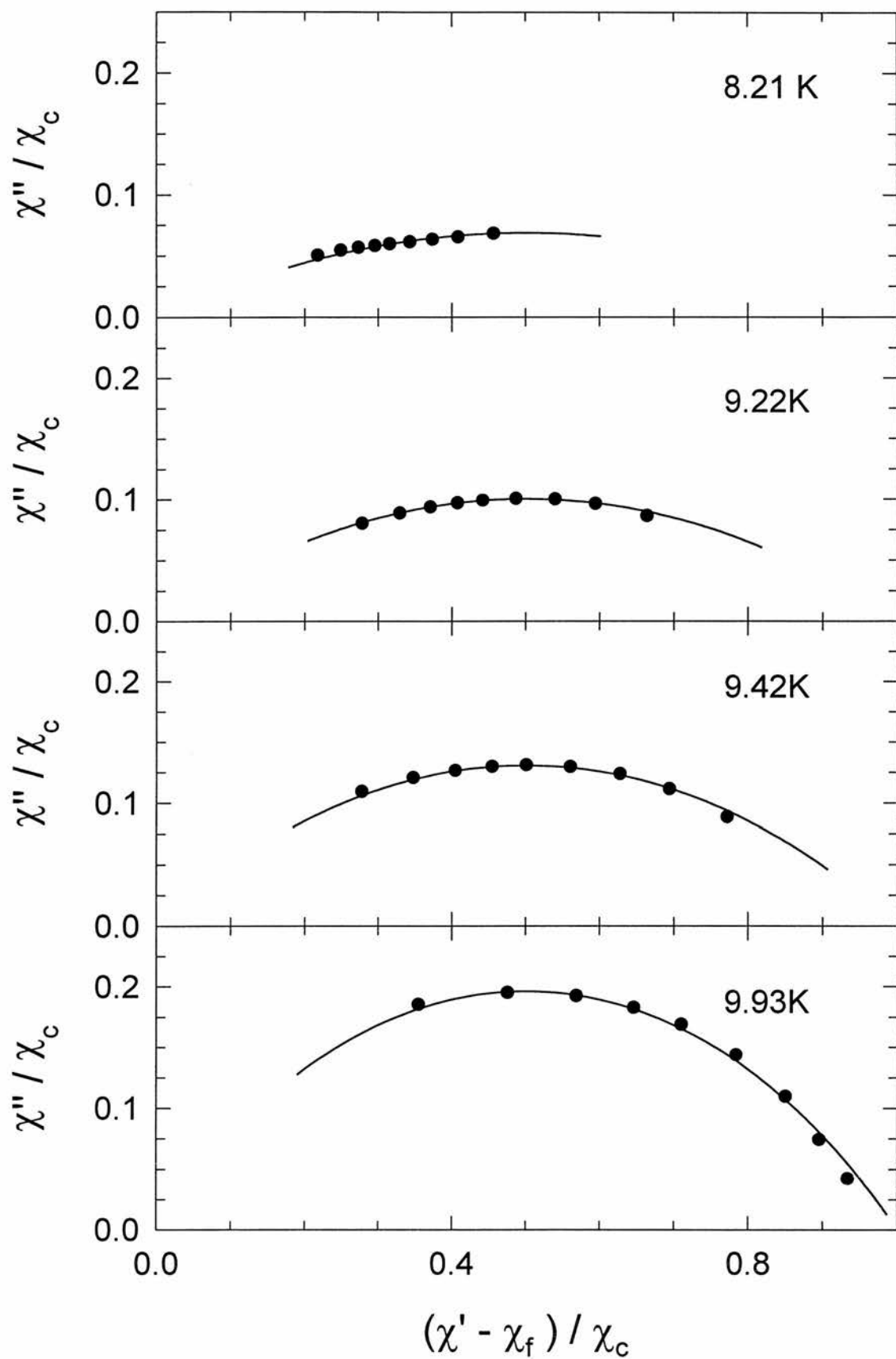


Figure IV- 15 : Cole-Cole plots for  $\alpha\text{-Er}_7\text{Ni}_3$  in the temperature range  $19.55\text{K} < T < 25.94\text{K}$ .

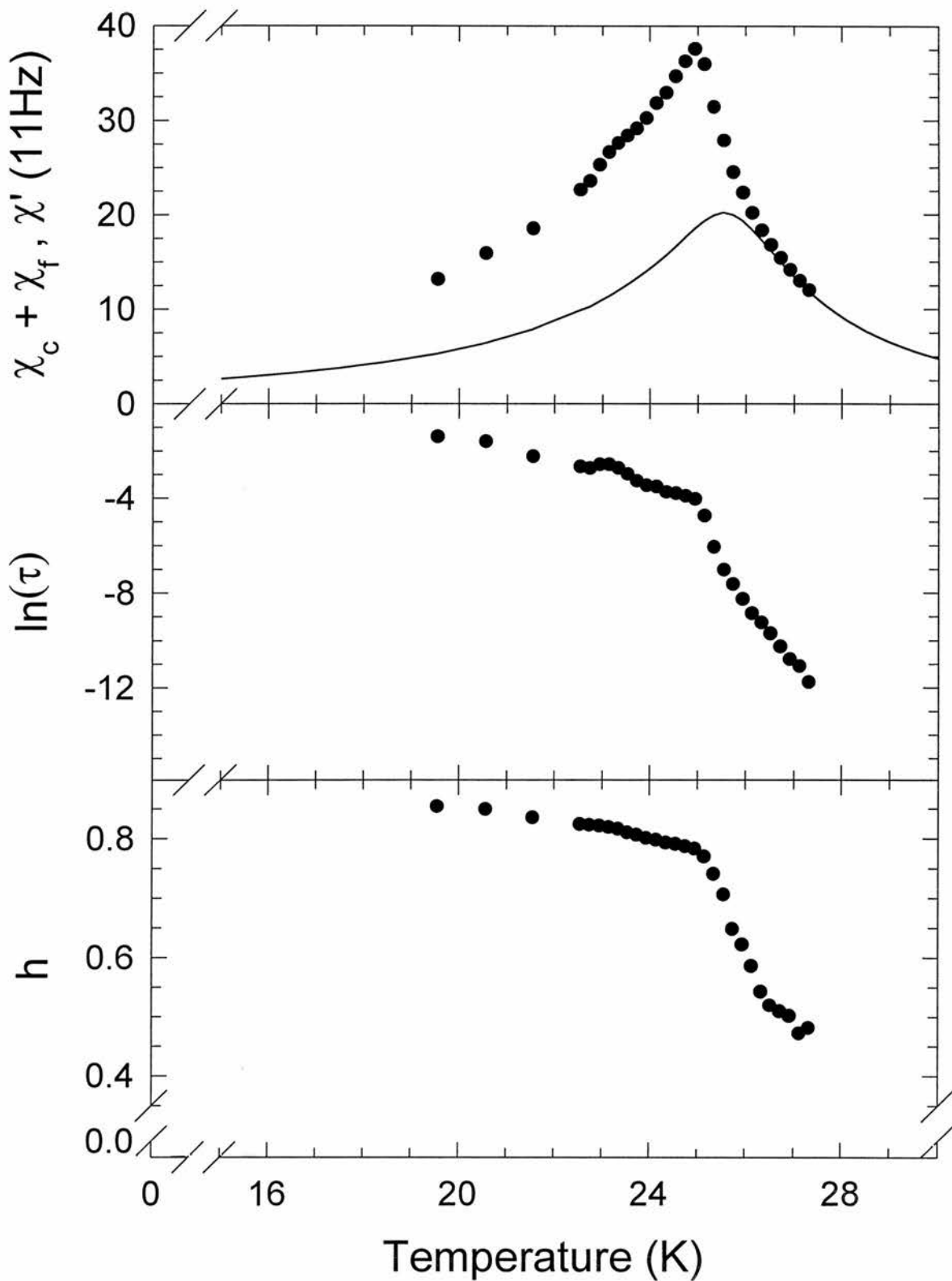


Figure IV- 16 : Evolution of the fitting parameters  $A+B$ ,  $h$  and  $\ln(\tau_0)$  as a function of temperature. The line plotted along the sum of the  $A$  and  $B$  parameters is the real susceptibility at the lowest frequency measured 11 Hz.

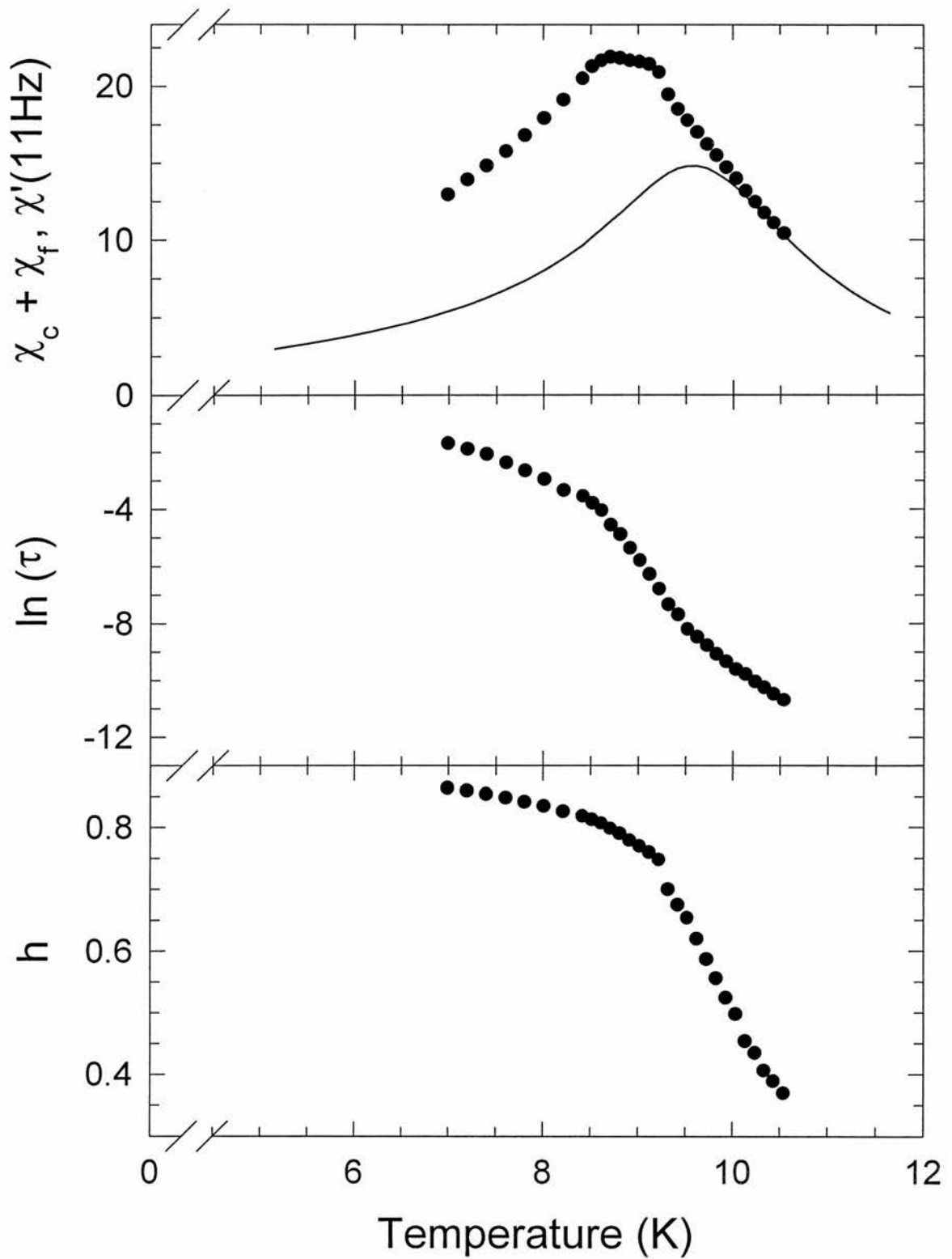


Figure IV- 17 : Evolution of the fitting parameters  $A+B$ ,  $h$  and  $\ln(\tau_0)$  as a function of temperature. The line plotted along the sum of the  $A$  and  $B$  parameters is the real susceptibility at the lowest frequency measured 11 Hz.

### IV.3.d.3 Distribution of relaxation times

Fuoss and Kirkwood<sup>33</sup> showed that the distribution of relaxation times can be directly obtained from the experimental frequency dependence of  $\chi''$ . Using their phenomenological expression for  $\chi(\omega)$  (Eq. IV-30), Cole and Cole<sup>26</sup> were able to demonstrate that the distribution is given by :

$$g(\ln \tau) = \frac{1}{2\pi} \frac{\sin(\pi h)}{\cosh[(1-h)\ln(\tau/\tau_c)] - \cos(\pi h)} \quad \text{Eq. IV-35}$$

This distribution is gaussian-like and centred around  $\ln(\tau_c)$ . A three dimensional plot of  $g(\ln\tau)$  is presented on *Figures IV- 18* and *IV- 19* and constitutes a nice visual way of illustrating the broadening of the distribution as the temperature decreases. The validity of the distribution obtained can be checked by transforming Eq. IV- 20 . If the relaxation frequency of the magnetic entities is much smaller than the measuring frequency, or in other words if  $\omega\tau \gg 1$ , the magnetic entities are effectively blocked and do not contribute to the magnetic susceptibility. This simply implies that the only contribution of the magnetic entities to the magnetic susceptibility  $\chi'$  arise from those entities with relaxation frequencies faster than the measuring frequencies. This can be written as :

$$\frac{\chi'(\omega)}{\chi_c} = \int_{\tau_{\min}}^{1/\omega} g(\ln \tau) d(\ln \tau) \quad \text{Eq. IV-36}$$

*Figures IV- 20* and *IV- 21* show  $(\chi'(\omega)-\chi_f)/\chi_c$  for  $\alpha\text{-Er}_7\text{Fe}_3$  and  $\alpha\text{-Er}_7\text{Ni}_3$  respectively at several temperatures alongside the integration of the corresponding distribution of relaxation times. The free spin component  $\chi_f$  had to be subtracted from  $\chi'(\omega)$  as only the cluster susceptibility is given by Eq. IV-20. The agreement between the data and the integral is remarkable and gives confidence in the fact that the distribution of relaxation times are well represented by *Figures IV-18* and *IV-19*.

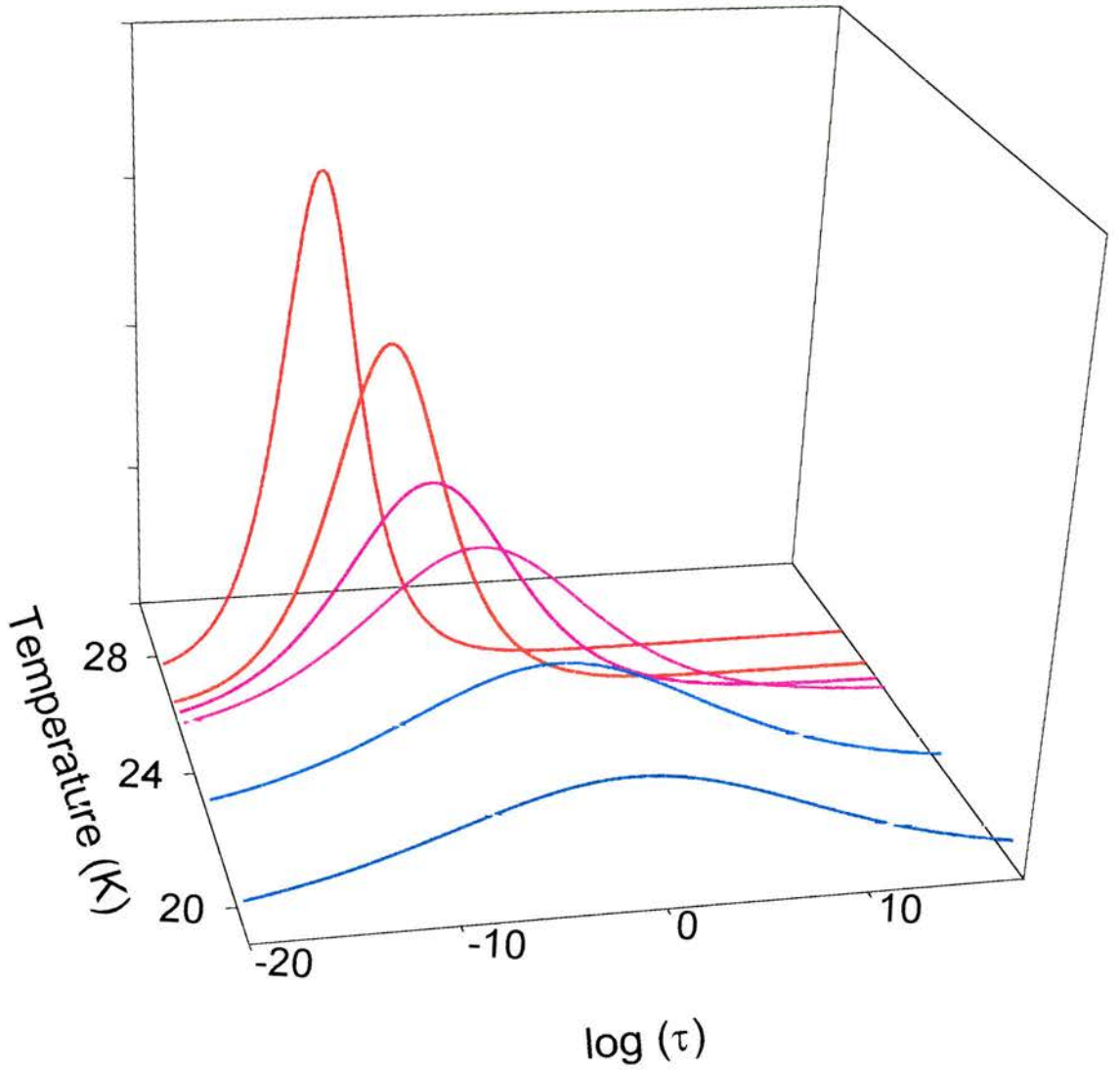


Figure IV- 18 : Distribution of relaxation times for  $\alpha$ -  $\text{Er}_7\text{Fe}_3$ .

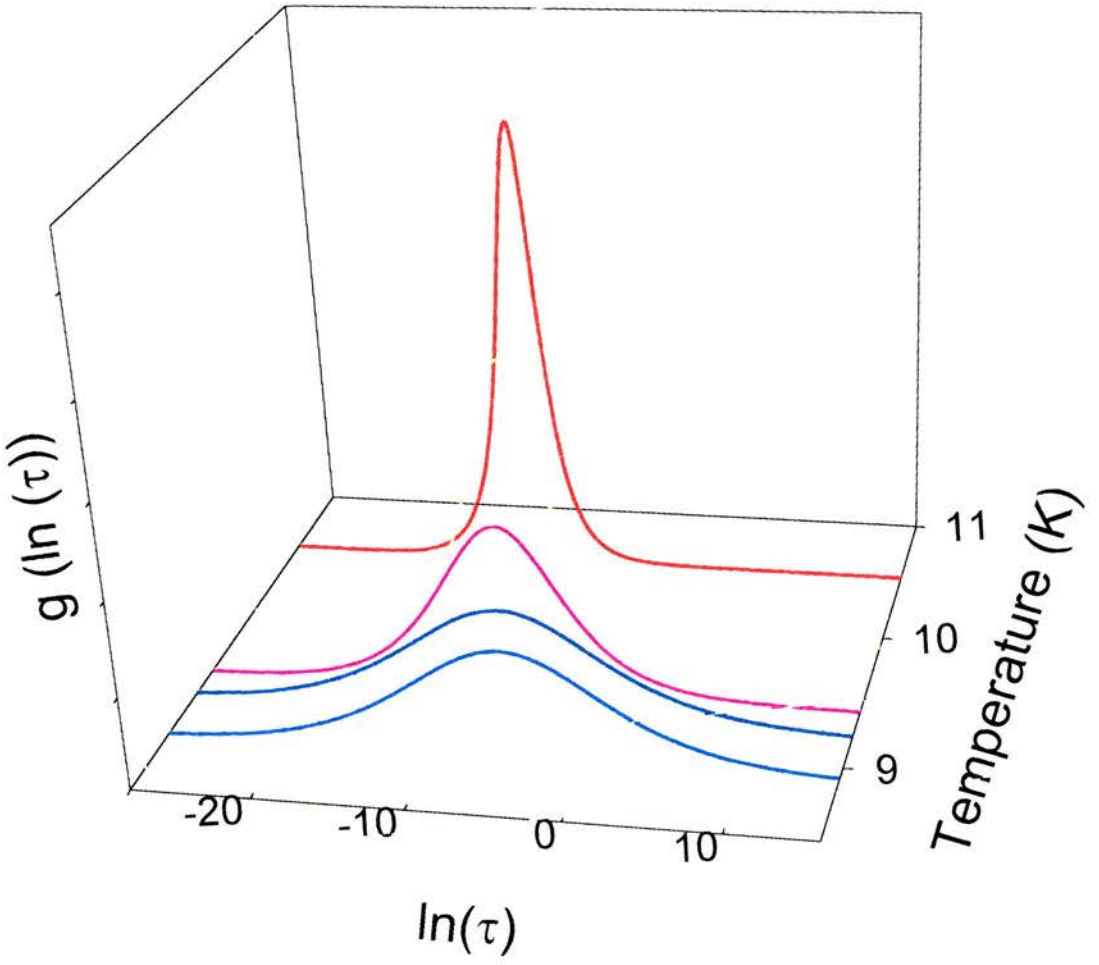


Figure IV- 19 : distribution of relaxation times for  $\alpha$ -  $\text{Er}_7\text{Ni}_3$ .



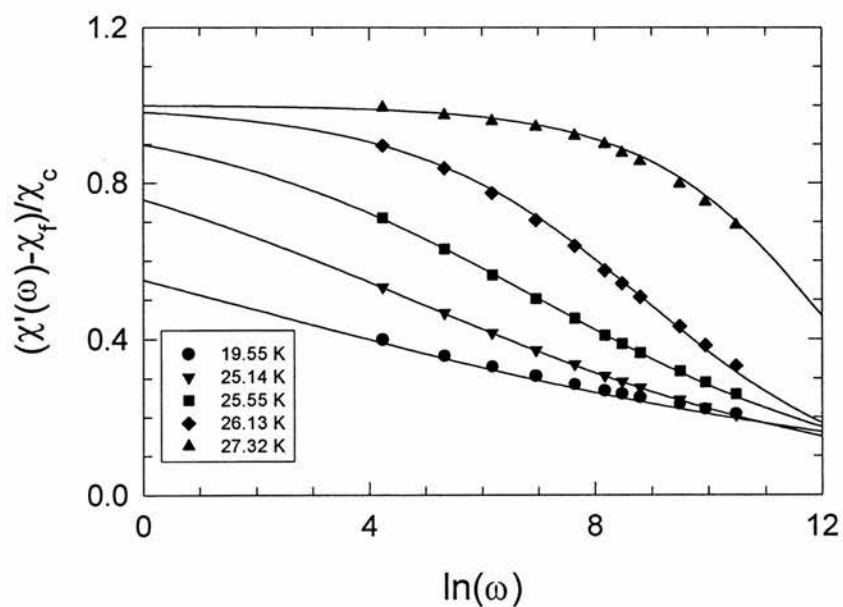


Figure IV - 20 : Cluster spin susceptibility of  $\alpha\text{-Er}_7\text{Fe}_3$ . See text for details.

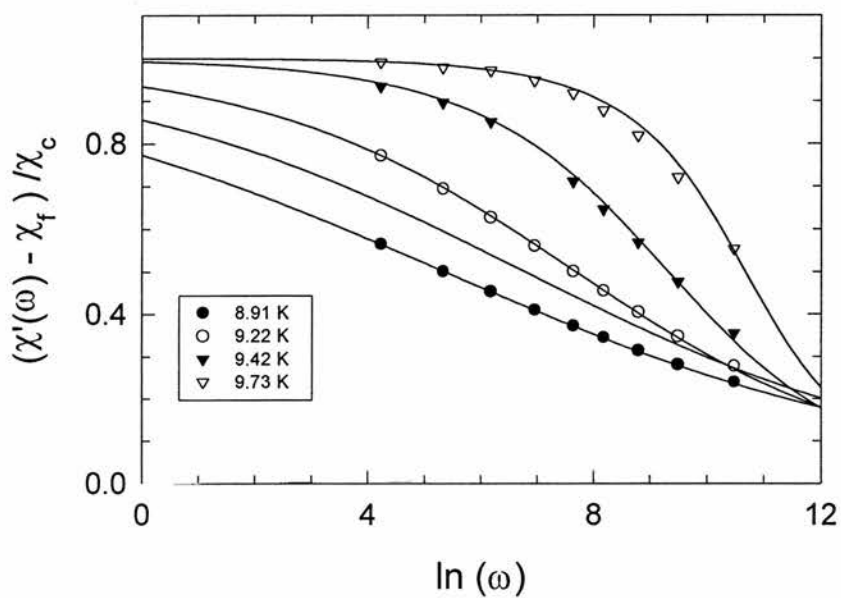


Figure IV- 21 : Cluster spin susceptibility of  $\alpha\text{-Er}_7\text{Ni}_3$ . See text for details.

#### IV.3.d.4 Frequency dependence of $T_g$ .

The frequency dependence of the freezing temperature in spin glasses has been the subject of many papers throughout the years<sup>34</sup>. If it is clear that the freezing temperature increases with the frequency of the measurement, the functional form of this increase is still open to debate. On that particular point, insulating spin glasses such as  $\text{Eu}_x\text{Sr}_{1-x}\text{S}$  have been particularly useful as the magnetic susceptibility measurements are not limited by eddy currents as is the case for metallic spin glasses<sup>35</sup>. The well-known Arrhenius law (see *Eq. IV-37*) gives totally unphysical values<sup>36</sup> for the activation energy  $E_A$  and the intrinsic relaxation time  $\tau_0$  ( $10^{-37}$ s for instance in  $\text{CuMn}$ ).

$$\tau = \tau_0 \exp(E_A / k_B T_f) \quad \text{Eq IV-37}$$

This is perhaps not too surprising as this expression implies that the mechanism involved is the simple overcoming of a barrier height and therefore excludes interactions between magnetic entities. It seems therefore logical that the Arrhenius law is found to be adequate for the description of superparamagnets without inter-cluster coupling.

Tholence<sup>20</sup> pointed out that the empirical Vogel-Fulcher<sup>37, 38</sup> law (*Eq. IV-38*) could be used to describe the frequency dependence of the blocking temperature.

$$\tau = \tau_0 \exp(E_A / k_B (T_f - T_0)) \quad \text{Eq. IV-38}$$

The physical significance of  $T_0$  remains obscure but an interpretation in terms of inter-cluster coupling has been proposed by Strickman and Wohlfarth<sup>39</sup>. In addition to its validity for spin glasses, this relation has been successfully applied to superparamagnets with inter-cluster interactions<sup>40</sup>. An interesting parallel exists with structural glasses : the behaviour of the inverse viscosity is well described by the Arrhenius law for "strong" glasses such as  $\text{SiO}_2$  or  $\text{GeO}_2$  , but the Vogel-Fulcher relation is required for "fragile" glass-forming systems such as o-terphenyl<sup>41</sup>. Again, the physical meaning of  $T_0$  is poorly understood.

For our random anisotropy samples, the Arrhenius law gives completely unphysical values for  $\tau_0$  and the frequency dependence of the freezing temperature is best described by the Vogel-Fulcher law. The fits obtained are quite good but the parameters can be varied over a fairly wide volume of parameter space without decreasing significantly the quality of the fits (the best fit for  $\alpha$ -Er<sub>7</sub>Fe<sub>3</sub> gives  $\tau_0 = 5.5 \times 10^{-11}$  s,  $E_A / k_B = 50$  and  $T_0 = 23$  K but  $\tau_0$  could be varied within the range  $10^{-13}$  s -  $10^{-10}$  s and  $E_A$  and  $T_0$  adjusted to obtain a decent fit). This is confirmed by the high value of the dependencies of the parameters which is the reason why these fits have not been shown.

#### IV.4 Magnetic diffuse scattering

Due to problems occurring during the experiment only two samples ( $\alpha$ -Er<sub>7</sub>Ni<sub>3</sub> and  $\alpha$ -Tb<sub>7</sub>Ni<sub>3</sub>) were examined on D7. The combination of a small amount of data and the need to keep the length of this chapter to a reasonable size, implies that this technique will be reviewed only briefly. D7 is a general purpose long wavelength diffuse scattering spectrometer. A general view of the instrument<sup>42</sup> is presented on *Figure IV-22*. Monochromatic neutrons travelling along the x-direction (imposing the direction of the incident wavevector  $\mathbf{k}$  to be along the x-direction) are polarised by a supermirror polariser and pass through a Mezei  $\pi$  spin flipper which is either on (for measuring spin flip events, SF) or off (for measuring non spin flip events, NSF). Neutrons then enter the spin turn coil (3 orthogonal Helmholtz coils) at the centre of which the sample is placed. The effect of these coils is to rotate by  $\pi/2$  the initial z-polarisation of the neutron onto either x- or y -as desired before the sample and rotate the scattered neutrons back by  $-\pi/2$ . At last, the neutrons enter the detector banks, placed in the (x,y) plane (therefore  $\mathbf{Q}=\mathbf{k}'-\mathbf{k}$  is in that plane and an angle  $\alpha$  between  $\mathbf{Q}$  and the x-axis can be defined), where they first pass through supermirror analysers and are subsequently detected by <sup>3</sup>He detector tubes. Therefore, the polarisation as well as the scattering angle of the neutrons can be determined, giving 6 possible cross-sections (x,y,z) for the axis along which the incident polarisation lies and (SF,NSF)<sup>43</sup>:



Figure IV- 22 : the D7 spectrometer at the ILL.

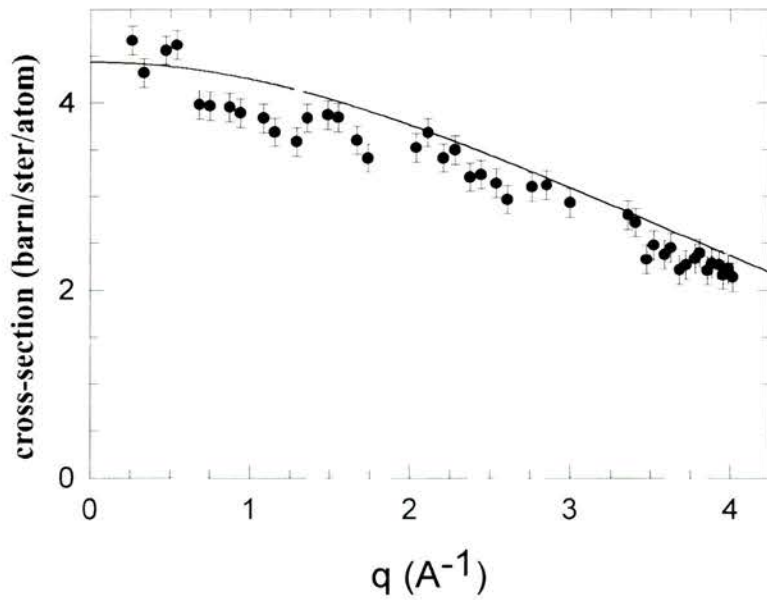


Figure IV- 23 : magnetic cross-section of  $\alpha$ -Er<sub>7</sub>Ni<sub>3</sub> at 60 K (about 6T<sub>g</sub>) . The line corresponds to the magnetic form factor for the Er<sub>3</sub> ions.

$$\left(\frac{d^2\sigma}{d\Omega d\omega}\right)_{SF}^x = \frac{2}{3}\left(\frac{d^2\sigma}{d\Omega d\omega}\right)_{SI} + (1 + \cos^2 \alpha)\frac{1}{2}\left(\frac{d^2\sigma}{d\Omega d\omega}\right)_{MAG}$$

$$\left(\frac{d^2\sigma}{d\Omega d\omega}\right)_{NSF}^x = \frac{1}{3}\left(\frac{d^2\sigma}{d\Omega d\omega}\right)_{SI} + (\sin^2 \alpha)\frac{1}{2}\left(\frac{d^2\sigma}{d\Omega d\omega}\right)_{MAG} + \left(\frac{d^2\sigma}{d\Omega d\omega}\right)_{NUC} + \left(\frac{d^2\sigma}{d\Omega d\omega}\right)_{II}$$

$$\left(\frac{d^2\sigma}{d\Omega d\omega}\right)_{SF}^y = \frac{2}{3}\left(\frac{d^2\sigma}{d\Omega d\omega}\right)_{SI} + (1 + \sin^2 \alpha)\frac{1}{2}\left(\frac{d^2\sigma}{d\Omega d\omega}\right)_{MAG}$$

$$\left(\frac{d^2\sigma}{d\Omega d\omega}\right)_{NSF}^y = \frac{1}{3}\left(\frac{d^2\sigma}{d\Omega d\omega}\right)_{SI} + (\cos^2 \alpha)\frac{1}{2}\left(\frac{d^2\sigma}{d\Omega d\omega}\right)_{MAG} + \left(\frac{d^2\sigma}{d\Omega d\omega}\right)_{NUC} + \left(\frac{d^2\sigma}{d\Omega d\omega}\right)_{II}$$

$$\left(\frac{d^2\sigma}{d\Omega d\omega}\right)_{SF}^z = \frac{2}{3}\left(\frac{d^2\sigma}{d\Omega d\omega}\right)_{SI} + \frac{1}{2}\left(\frac{d^2\sigma}{d\Omega d\omega}\right)_{MAG} \quad Eqs. IV-39$$

$$\left(\frac{d^2\sigma}{d\Omega d\omega}\right)_{NSF}^z = \frac{1}{3}\left(\frac{d^2\sigma}{d\Omega d\omega}\right)_{SI} + \frac{1}{2}\left(\frac{d^2\sigma}{d\Omega d\omega}\right)_{MAG} + \left(\frac{d^2\sigma}{d\Omega d\omega}\right)_{NUC} + \left(\frac{d^2\sigma}{d\Omega d\omega}\right)_{II}$$

By combining these six equations, it is possible to isolate each component (the isotope incoherent scattering II is often omitted as its contribution is small). Furthermore, if the spin incoherent (SI) cross-section is known or negligible, D7 can be operated in the zSF-zNSF configuration to separate the nuclear (NUC) from the magnetic (MAG) contribution, reducing the data collection time by a factor of 2.

We used the latter configuration with neutrons of wavelength 8.31Å. About 5g of sample were placed in a cylindrical aluminium can. All the usual corrections (running a quartz sample to check the SF-NSF ratio as it does not flip neutrons, running a vanadium sample to correct for multiple scattering and running the sample with a cadmium foil with a slit to work out the transmission) were performed to the data.

The resulting magnetic scattering for  $\alpha$ -Er<sub>7</sub>Ni<sub>3</sub> above T<sub>g</sub> (at 60K) is shown on *Figure IV-23*. The line through the data is obtained using the formalism (ref. 44) :

$$\frac{d\sigma}{d\Omega} = \left(\frac{1}{2} r_0 \gamma\right)^2 g^2 |F(q)|^2 \frac{2}{3} J(J+1) \quad \text{with } (r_0 \gamma)^2 = 0.29 \times 10^{-28} \text{ m}^2.$$

where

$$F(q) = \langle j_0(q) \rangle + (1 - 2/g) \langle j_2(q) \rangle \quad (\text{For Er, } g=6/5 \text{ and } J=15/2).$$

$$j_0(x) = a_1^{j_0} \exp(-a_2^{j_0} x^2) + b_1^{j_0} \exp(-b_2^{j_0} x^2) + c_1^{j_0} \exp(-c_2^{j_0} x^2) + d_1^{j_0}$$

$$j_2(x) = a_1^{j_2} \cdot x^2 \cdot \exp(-a_2^{j_2} x^2) + b_1^{j_2} \cdot x^2 \cdot \exp(-b_2^{j_2} x^2) + c_1^{j_2} \cdot x^2 \cdot \exp(-c_2^{j_2} x^2) + d_1^{j_2} x^2$$

The expressions for  $j_0$  and  $j_2$  are extracted from P. J. Brown's chapter<sup>45</sup> in the same volume as reference 44. The a's and b's coefficients are tabulated<sup>45</sup> for each ion. It can be seen that the data and the theoretical line agree remarkably well suggesting that the Er ions are in a free ion state in concordance with the AC data (we obtained earlier a value of  $9.6 \mu_B$  for the Er ion from the Curie law above  $T_g$ ).

*Figure IV- 24* shows the nuclear and magnetic scattering cross-section at 5K for  $\alpha$ -Er<sub>7</sub>Ni<sub>3</sub> (black) and  $\alpha$ -Tb<sub>7</sub>Ni<sub>3</sub> (red). The first remark that can be made concerns the nuclear part. It is indeed very similar for both samples as might be expected since 1) the two Rare Earths substitute on the same sites and 2) the scattering lengths of Er and Tb are very similar. On the contrary, the magnetic cross-sections are different. First of all, the y scale is considerably lower than above  $T_g$  which suggest that most of the scattering intensity has gone outside the q-range available for this setup on D7. Secondly, the Tb sample shows an pronounced increase in intensity for  $q < 1 \text{ \AA}$ . Both these facts suggest that the scattering is happening at low q. This is corroborated by the unpublished Small Angle Neutron Scattering experiment done by Bewley et al on Random Anisotropy Magnet<sup>46,47</sup>. Qualitatively, as  $J(\text{Er}) > J(\text{Tb})$  and the correlation length  $\xi$  increases as  $(J/D)^2$ , one expects  $\xi(\text{Er}) > \xi(\text{Tb})$  so the scattering should in theory increase at lower q for the Er sample than for the Tb sample which is what the D7 data suggests.



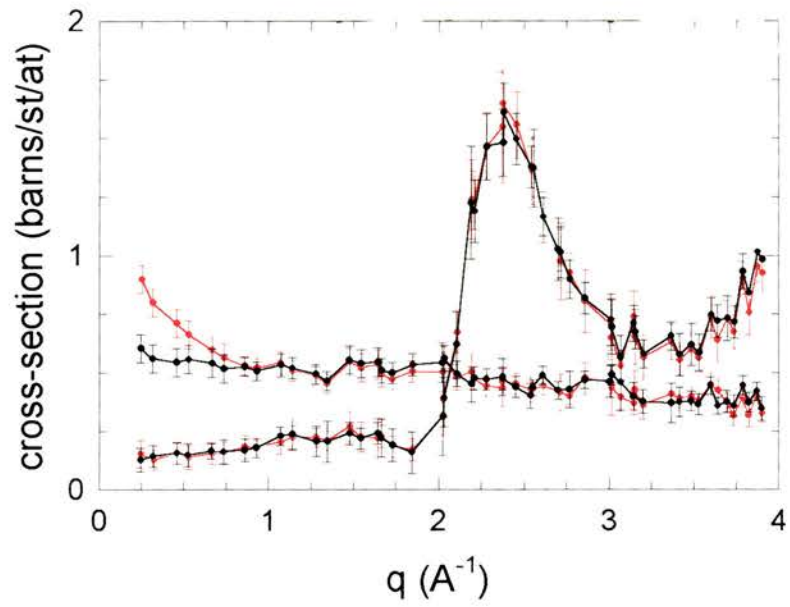


Figure IV- 24 : nuclear and magnetic cross-sections of  $\alpha\text{-Er}_7\text{Ni}_3$  (black) and  $\alpha\text{-Tb}_7\text{Ni}_3$  (red) at 5 K. Note the kink at low  $q$  values for the magnetic contribution in the Tb sample.

## IV.5 Neutron Spin Echo measurements

### IV.5.a The NSE technique

Examining *Figure IV-1* again, it is evident that, because the time window covered by the Neutron Spin Echo (NSE) technique is  $10^{-10}$ - $10^{-7}$ s, this technique is ideally suited for the study of relatively slow relaxation phenomena. The principle of NSE, invented by F. Mezei<sup>48</sup> in 1972, can be understood by considering the Larmor precession of the net spin of a neutron bunch in a magnetic field  $B_0$ . The very basic principles of the method are sketched on *Figure IV-25*.

The Larmor precession is initialised by turning the polarisation into the direction z using a  $\pi/2$  flipper at the point A. Due to the contradictory requirement of a large precession field and a small field in the  $\pi/2$  Mezei coil, Fresnel coils are placed at the end of the precession field solenoids to reduce field inhomogeneity.

The precession angle at a distance L from A is  $\varphi = \gamma LB_0 / v$  where  $\gamma = 2.916$  kHz / Oe is the gyromagnetic ratio of the neutron and v its velocity. If we measure the polarisation along the z-axis, for one neutron we obtain  $\cos \varphi$  but for the whole beam this expression becomes:

$$P_z = \langle \cos \varphi \rangle = \int f(v) \cos\left(\frac{\gamma L_0 B_0}{v}\right) dv \quad \text{Eq. IV-40}$$

where  $f(v)$  is the velocity distribution of the beam. As  $L_0$  increases, the differences between the phases for different v's gets bigger and the Larmor precession gets more and more out of phase. Hence the average  $\langle \cos \varphi \rangle$  tends to zero as shown in the left lower part of *Figure IV-25*. To eliminate the dephasing effect of the velocity distribution  $f(v)$  a field  $B_1$  in the opposite direction of  $B_0$  (in practice,  $B_1$  has the same direction as  $B_0$  in order to avoid field homogeneities and a Mezei  $\pi$  flipper is used instead) is applied so that the neutrons precess in the opposite sense. The total phase for a given neutron (point C of *Figure IV-25*) is then :

$$\varphi = \gamma (B_0 L_0 - B_1 L_1) / v \quad \text{Eq. IV-41}$$

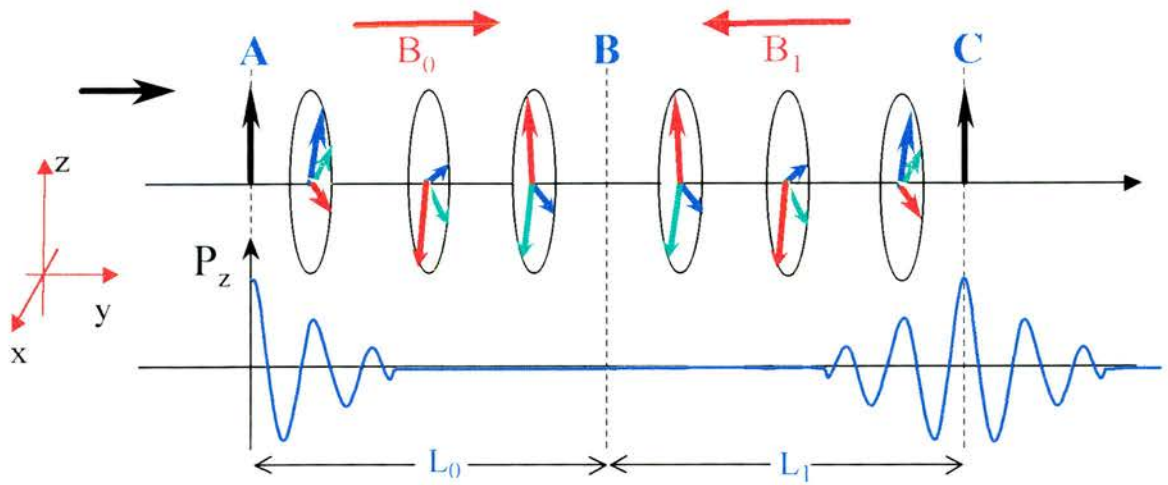


Figure IV- 25 : Schematic of a Neutron Spin Echo experiment

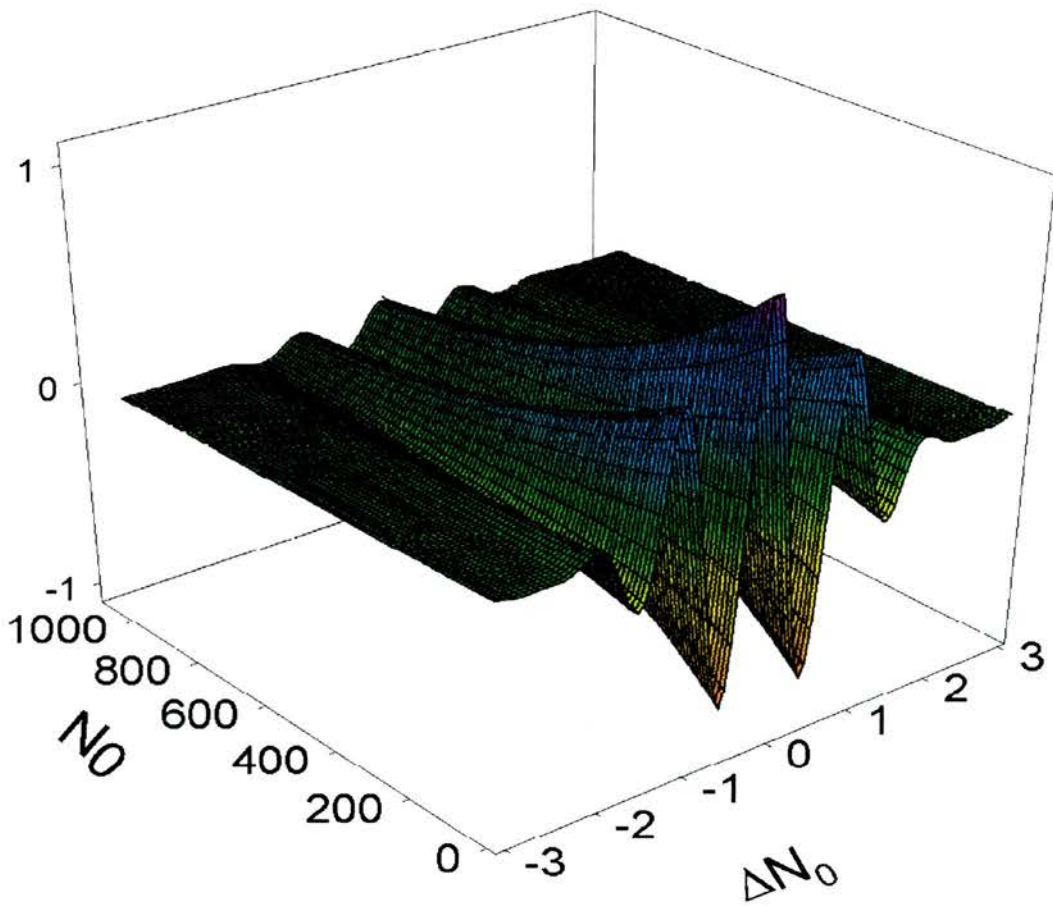


Figure IV- 26 : Neutron Spin Echo signal for a diffuse scatterer showing both asymmetric (varying  $\Delta N_0$ ) and symmetric (varying  $N_0$ ) scans.

If the configuration is symmetric ( $B_0L_0 = B_1L_1$ ), the resulting phase is zero for all  $v$ 's so  $P_z = 1$ ; as shown at the bottom of *Figure IV-25*. The characteristic shape of  $P_z$  around the point C is termed a spin-echo group and  $P_{NSE}$  represents the amplitude of that signal.

When a sample is placed between the two precession magnets, the phase of one neutron at point C is given by :

$$\varphi = \varphi_{in} - \varphi_{out} = \gamma ( L_0B_0/v_0 - L_1B_1/v_1 ) = \varphi(v_0, v_1). \quad Eq. IV-42$$

If the scattering is inelastic, the neutron energy change is

$$\hbar\omega = \frac{1}{2} m(v_0^2 - v_1^2) = \hbar\omega(v_0, v_1) \quad Eq. IV-43$$

It can be shown<sup>49</sup> that for a neutron beam:

$$\varphi - \varphi_{av} = t ( \omega - \omega_{av} ) \quad Eq. IV-44$$

where the subscript "av" implies that  $\varphi$  and  $\omega$  have been calculated for the beam average neutron velocities  $v_{0, av}$  and  $v_{1, av}$ .

The proportionality constant  $t$  in *Eq. IV-44* is :

$$t = \frac{\hbar\gamma L_i B_i}{mv_{i,av}} \quad \text{with } i = 0 \text{ or } 1 \quad Eq. IV-45$$

The neutrons having suffered an energy change  $\omega_{av}$  in the scattering process will produce the same NSE signal as *Figure IV-25* but centred at  $L_1B_1/L_0B_0 \neq 1$ . The sample scattering is characterised by the scattering function  $S(\mathbf{Q}, \omega)$  and the NSE signal is given by :

$$P_{NSE} = P_s \frac{\int S(\mathbf{Q}, \omega) \cos(t(\omega - \omega_{av})) d\omega}{\int S(\mathbf{Q}, \omega) d\omega} \quad Eq. IV-46$$

$P_s$  takes the polarisation-dependence of the scattering process into account. Thus,  $P_{NSE}$  provides a measure of the Fourier transform of  $S(\mathbf{Q}, \omega)$  namely  $S(\mathbf{Q}, t)$  and consequently  $t$  is termed the Fourier time. In fact, *Eq. IV-45* is very approximate because it does not take field inhomogeneity into account and is in practice replaced by a proper Biot and Savart field-integral along the neutron path.

It is also evident that in practice, the lengths  $L_0$  and  $L_1$  are fixed and a NSE group is obtained by varying the number of precessions that the neutrons undergo by slightly varying  $B_1$  with respect to  $B_0$ . Hence a similar plot to *Figure IV-25* can be obtained with  $\Delta N_0$  instead of  $L$  as the abscissa (y- axis). This kind of scan is called an asymmetric spin-echo scan. To obtain useful information about the dynamics of the spins inside the sample,  $S(Q,t)$  need to be determined at different  $t$ , this is achieved by changing the value of  $B_0$  but keeping the ratio  $B_0/B_1$  constant (i.e. at constant  $\Delta N_0$ ) and the literature term for this signal is a symmetric scan. Practically, for each Fourier time chosen, a four point asymmetric scan is performed (four points is enough get the necessary parameters out, including  $P_{NSE}$ ). An illustrative example, inspired from reference <sup>50</sup>, of a symmetric scan and an asymmetric scan is given in *Figure IV-26*.

One of the advantages of the NSE technique is that the broadening due to the resolution function of the instrument can be easily handled. Indeed, the measured  $P_{NSE}$  signal is the product of the  $P_{NSE}$  signal coming from the sample multiplied by the instrumental signal. Hence if we measure the signal for an elastic scatterer for which  $P_s=1$ , the desired quantity  $P_{NSE}$  of the sample is obtained by simply dividing the measured signal for the sample by the measured signal for the elastic scatterer. This is much simpler than the deconvolution required for conventional inelastic scattering techniques. A convenient choice for the elastic scatterer when studying a spin-glass system is the sample itself well below its freezing temperature.

In an isotropic magnetic system such as a paramagnet or a spin glass, the configuration of the spin-echo spectrometer does not include the  $\pi$  flipper just before the sample as it is made redundant by the nature of the magnetic scattering itself. Indeed, the polarisation  $\mathbf{P}'$  of the scattered beam is related to the polarisation of the incoming beam by<sup>49</sup> :

$$\mathbf{P}' = \frac{-\mathbf{q} \cdot (\mathbf{q} \cdot \mathbf{P})}{q^2} \quad \text{Eq. IV- 47}$$

From *Figure IV-27*, if the scattering vector  $\mathbf{q}$  is along the x-axis and  $\mathbf{P}$  is in the (xy) plane ie  $\mathbf{P} = (P_x, P_y, 0)$ , then  $\mathbf{P}'$  is simply the reversed projection of  $\mathbf{P}$  along the x-axis ie  $\mathbf{P}' = (-P_x, 0, 0)$ . From the geometrical construction of *Figure IV-27*, it is easy to see that  $\mathbf{P}'$  (one of the red vectors) can be decomposed into two components (blue vectors), namely  $P_1' = (-P_x/2, P_y/2, 0)$  and  $P_2' = (-P_x/2, -P_y/2, 0)$ .

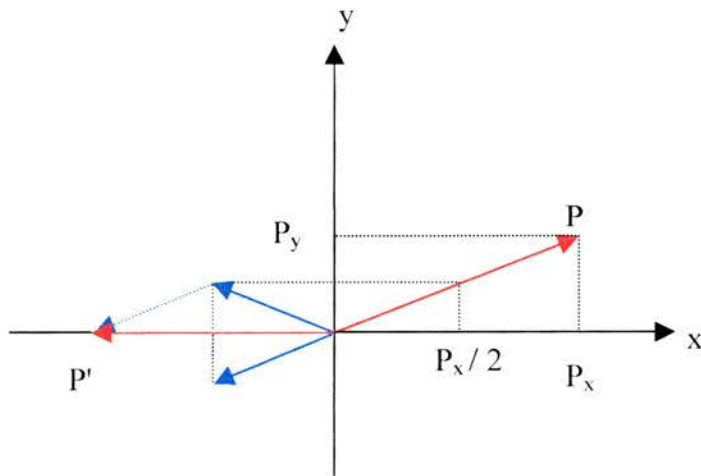


*Figure IV- 27 : schematic diagram of the evolution of the polarisation for an isotropic magnetic sample where the scattering vector  $q$  is along  $x$ .*

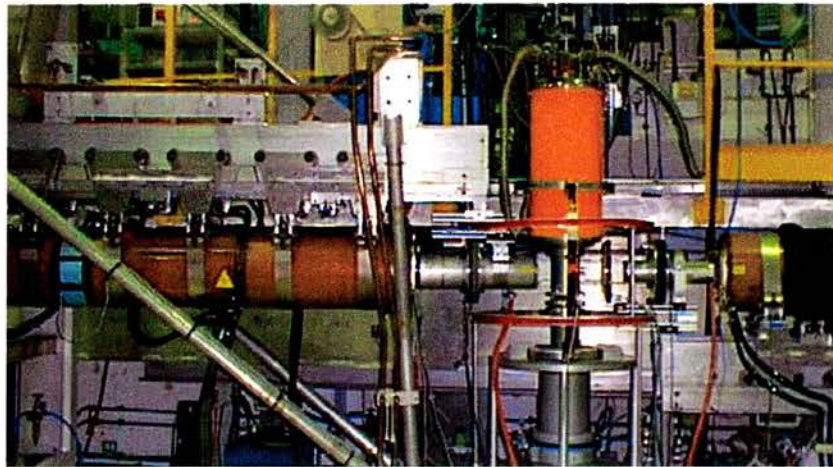


*Figure IV- 28 : the IN11 NSE-spectrometer at the ILL.*



This simply means that half the neutrons, those whose polarisation is being transformed from  $\mathbf{P}$  to  $\mathbf{P}_1'$  undergo a  $\pi$  precession around the y-axis necessary for the spin echo. The phase of the precession angle of the other half of the neutrons is shifted by  $180^\circ$  and the corresponding neutrons do not contribute to the echo signal. This allows the magnetic scattering to be unambiguously separated from the non-magnetic contribution (coherent and incoherent). However, this complete separation has also its drawback : the magnetic scattering is often weaker than its nuclear counterpart as the magnetic cross-sections are often smaller than the nuclear ones and this induces a relatively poor signal to noise ratio. This explains why relaxation studies are easier on polymers and why NSE is so difficult to perform on spin glasses. Indeed, the magnetic contribution from, for instance, CuMn spin glass alloys will only come from a few percents of the sample. To circumvent this problem, a large sample can be used. However, this is not always possible as the absorption will also increase with the mass of the sample.

In order to normalise the echo signals, it is necessary to perform a 3D-polarisation analysis as well as an echo measurement. This is based on the set of six equations IV- 39. The total magnetic intensity  $S(q)$ , integrated over all energy transfers, is then determined as a combination of the  $(x,y,z)_{SF}$  -or  $(x,y,z)_{NSF}$ - intensities. Recalling that the only half of the neutrons contributes to the echo, each echo is normalised for each temperature as:

$$S(q,t) = \frac{\text{Echo}}{S(q)/4} \quad \text{Eq. IV- 48}$$

It is instructive to consider the case of a single relaxation time for the spins. The scattering function  $S(Q,\omega)$  is then a lorentzian namely  $\gamma / ( \gamma^2 + ( \omega - \omega_{av} )^2 )$  and evaluation of the Fourier transform gives  $\exp(-\gamma t)$ . In contrast, when there is a distribution of relaxation times (or equivalently when the distribution of relaxation times is not  $\delta$  Dirac peak centred on  $\tau=1/\gamma$ ), the correlation function is no longer a simple exponential but becomes broadened.

*Figure IV-28* shows the IN11 spin-echo spectrometer at the Institut Laue Langevin, Grenoble, France that has been used to measure the spin correlation function in  $\alpha\text{-Er}_7\text{Ni}_3$  and  $\alpha\text{-Er}_7\text{Fe}_3$ . It shows quite clearly the main precession coils and the flippers.

#### IV.5.b Previous NSE work and related theories on spin glasses

The possibility of measuring the spin-spin correlation function directly is evidently very appealing for direct comparison with theory. Shortly after having developed the Neutron Spin Echo technique, Mezei teamed up with Murani, who had been studying spin glasses which other neutron spectrometers (e.g. back-scattering), to perform a now classic experiment on the canonical spin glass  $\text{CuMn5\%}$ . Their "tour-de-force" experiment was published<sup>51</sup> and provided a huge insight into the peculiar dynamics of spin-glasses. However, there were only 5 or 6 Fourier times measured per temperature and the point corresponding to the shortest time was actually obtained from the 3D-polarisation analysis. The statistics on their data being quite poor, Murani and Mezei did not attempt to fit the correlation function but pointed out that the form of the relaxation in spin glass is strongly non-exponential.

Several functional forms for the time correlation function such as logarithmic decay in 2D Ising system<sup>52</sup> or power law in the famous Kirkpatrick and Sherrington infinite range 3D Ising spin glass<sup>53</sup> have been suggested theoretically. Driven by the analogy between spin glasses and structural glasses, several authors suggested that Kohlrausch relaxation should be observed in spin glasses. Indeed, by that time, the stretched exponential  $\exp(-\omega t)^\beta$  -Eq. IV- 49-, first used by Kohlrausch 150 years ago when he studied the decay of the residual charge on a Leyden jar<sup>54</sup> and rediscovered by Williams and Watts<sup>55</sup> in 1970 had been observed for the slow relaxation processes involving shear, for mechanical relaxation<sup>56</sup> and also for the dielectric relaxation<sup>57</sup> in numerous structural glasses. Two models tackling the problem from different angles were suggested. Ngai et al<sup>58</sup>, following Ngai's cooperative theory for structural glasses that resembles an early version of the mode coupling theory<sup>59</sup> now widely used in the glass community<sup>60</sup>, suggested that the strong coupling between the spin-states and the environment is the cause of the stretched exponential behaviour. A summary of the temperature evolution of the exponent  $\beta$ , the effective  $\tau_p$  and mean  $\langle\tau\rangle$  relaxation times associated with 'fragile' and 'strong' glasses and their spin glass analogues can be found on *Table IV- 4*.

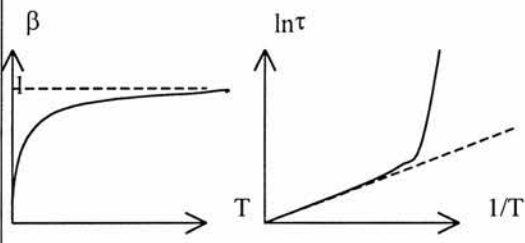
	STRUCTURAL	SPIN GLASS
TYPE A	<input type="checkbox"/> $T \gg T_g$ , $\beta \sim 1$ and $\tau_p = \tau_\infty \exp(E_A/kT)$ ie Arrhenius-like <input type="checkbox"/> $T \rightarrow T_g$ , $\beta$ decreases. $\tau_p$ and $\langle \tau \rangle$ are no longer Arrhenius-like <input type="checkbox"/> Eg : $\text{Ca}_{0.4}\text{K}_{0.6}(\text{NO}_3)$ ie 'fragile' 	<u>CuMn5%</u> , $\text{Eu}_{0.2}\text{Sr}_{0.8}\text{S}$
TYPE B	<input type="checkbox"/> $\tau_p$ Arrhenius even near $T_g$ <input type="checkbox"/> $\beta$ temperature independent <input type="checkbox"/> eg $\text{SiO}_2$ , $\text{GeO}_2$ ie 'strong'	$(\text{Ho}_2\text{O}_3)_{0.08}(\text{B}_2\text{O}_3)_{0.92}$
TYPE C	<input type="checkbox"/> $\tau_p$ non-Arrhenius <input type="checkbox"/> $\beta$ temperature independent <input type="checkbox"/> eg alcohols	?

Table IV - 4 : The Ngai classification.

Palmer et al<sup>61</sup> on the other hand, suggested that Kohlrausch relaxation arises naturally from a hierarchically constrained dynamic model where faster degrees of freedom successively constrain slower ones. The extension to spin glasses quickly followed and stretched exponential behaviour was observed or the relaxation of the remanent magnetisation in spin glasses<sup>62</sup>. In an impressive Monte-Carlo simulation of an Ising spin glass, Ogielski<sup>63</sup> showed that the stretched exponential is adequate for describing the relaxation function above  $T_g$ . However, it should be noted that in Ogielski's paper, above  $T_g$  the stretched exponential is in fact multiplied by a power-law, generally ignored because its exponent is small and below  $T_g$ , only the power-law is required. A very elegant explanation for the occurrence of the stretched exponential in (Ising) spin glasses can be obtained in terms of a random walk in an hypercube<sup>64</sup>. This Ising spin-glass model predicts that the stretched exponent  $\beta$  decreases from 1 at high temperatures to 1/3 at  $T_g$ . Refinement of this theory<sup>65, 66</sup> predicts that the stretched exponential is a direct consequence of the fractal nature of configuration spaces in

complex systems. According to the authors, this is the very reason why Kohlrausch relaxation is so common in nature and thereby gives a physical basis to the stretched exponential, regarded by other authors as no more than a convenient function to explain relaxation data.

Some of the first experiments using the stretched exponential for the relaxation by NSE in spin glasses was performed by Sarkissian<sup>67</sup> on Au-(15%)Fe and later by Sarkissian and Rainford<sup>68</sup> on Pd(5%)Mn. For all temperatures, their data was fitted by a stretched exponential with a single exponent  $\beta=0.6$ . We will discuss their experiments in the light of our own new results later in this chapter. Interestingly, an abundance of NSE data has been taken on ionic<sup>69</sup> or polymer<sup>70</sup> glasses showing stretched exponential behaviour, notable supporting the mode-coupling theory, but relatively little data is available on spin glasses owing to the difficulty of the experiment.

#### **IV.5.c NSE measurements on Random Anisotropy Magnets**

About 5g of amorphous ribbons were packed in an aluminium flat sample holder whose edges were covered by a cadmium frame to mask the bolts and nuts used to close the sample holder. The ensemble sample and sample can was then inserted into an ILL orange cryostat (base temperature 1.5K). Our sample mass was far less than that used by Murani and Mezei in their pioneering experiment<sup>71</sup> but they were measuring a dilute system (5%) with a relatively low value for the Mn moments whereas we had the advantage of studying a very concentrated system (70% of magnetic ions) with a much larger value for the Er moments (more than 10 Bohr magnetons) ensuring a sizeable magnetic cross-section.

The wavelength chosen was 4.64 Å, thereby allowing the Fourier time range [0.006...3.7] ns to be covered. The large detector IN11C that allows the q-dependence to be studied more quickly was not operational at the time of the experiment but the scattering angle  $2\theta$  was varied for some temperatures (angles used : 3°, 5°, 10°, 15° and 20°). By using these  $2\theta$  values coupled with the chosen neutron wavelength, a q-range between 0.07 and 0.5 Å<sup>-1</sup>, all below the first peak of the structure factor<sup>72</sup>, has been probed. The echo signal showed no variation with the scattering angle within experimental errors. Following Murani and Mezei's approach, if we assume little Q-dependence, the intermediate scattering law can be rewritten as  $S(Q,t)=S(t)S'(Q)$ .

Therefore, NSE directly provides information on  $S(t)$ , the time dependent correlation function  $\langle S_i(0)S_i(t) \rangle$ . It should also be noted that the magnetic scattering obtained by polarisation analysis as a linear combination of the (x,y,z) cross sections showed a sharp increase at low angles indicative of ferromagnetic-like interactions.

*Figure IV-29* shows the spin correlation function in the time domain, as obtained directly from the spin echo measurements of  $\alpha$ -Er<sub>7</sub>Fe<sub>3</sub>. On such a plot, a simple exponential falls very rapidly from one to zero, that rapid fall off does not depend on the value of  $\tau$  ( $\tau$  controls the time at which it starts to fall off). To fix ideas, the dashed line of *Figure IV-29* represents a simple exponential with  $\tau = 0.01$ ns and clearly shows that this function is inadequate for our samples. The solid lines represent fits to a stretched exponential function. *Table IV-4* contains the parameters  $\tau$  and  $\beta$  obtained from those fits (for  $T=60$ K, the last points have been left out).

T (K)	14	25	28	32	38	50	60
$\beta$	0.336	0.344	0.357	0.3672	0.4375	0.4642	0.492
$\tau$ (ns)	15027	18.84	3.39	0.556	0.196	0.0342	0.0128

*Table IV-4 :  $\beta$  and  $\tau$  parameters from fitting *Figure IV-29* with Eq. IV- 49*

As previously mentioned, this is not the first time that Kohlrausch behaviour has been observed in NSE data from spin glass samples. Sarkissian and Rainford<sup>68</sup> for instance used this stretched exponential form but, as the authors mentioned in their paper, they could also fit a power law to their data. Their data showed a constant stretched exponent  $\beta = 0.6$  across the whole temperature range. However, in order to fit their data, they introduced a temperature dependent parameter  $\phi^F$  corresponding to a fast fluctuation at times shorter than the experimental window which decreases to zero as  $T$  decreases to zero. There is no mention of what this component might correspond to. For our data, a power law gives a much poorer fit than the stretched exponential and the exponent  $\beta$  varies with temperature, starting from a high value at  $2T_g$  and flattening off to a value of about 1/3 near the transition. This is very similar to the muon depolarisation function obtained by muon spin relaxation in numerous different types of

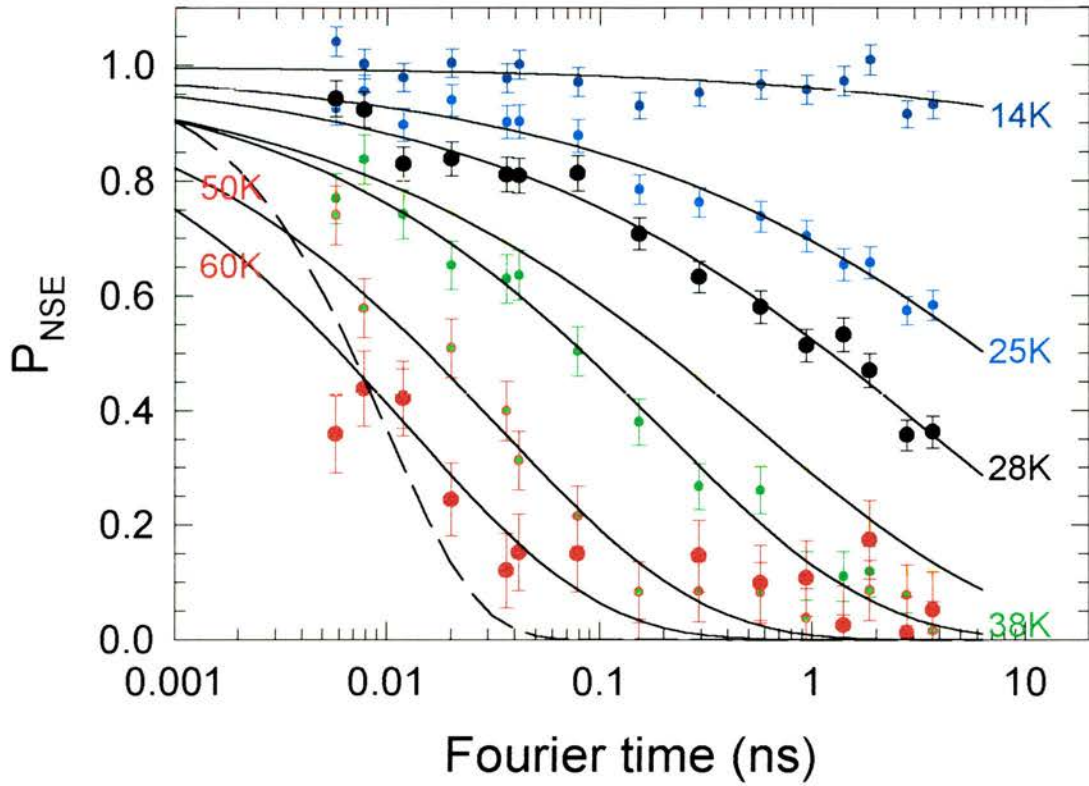


Figure IV- 29 : spin correlation function obtained by NSE for  $\alpha$ -Er<sub>7</sub>Fe<sub>3</sub>. The lines are fits to the stretched exponential function (see text for details)

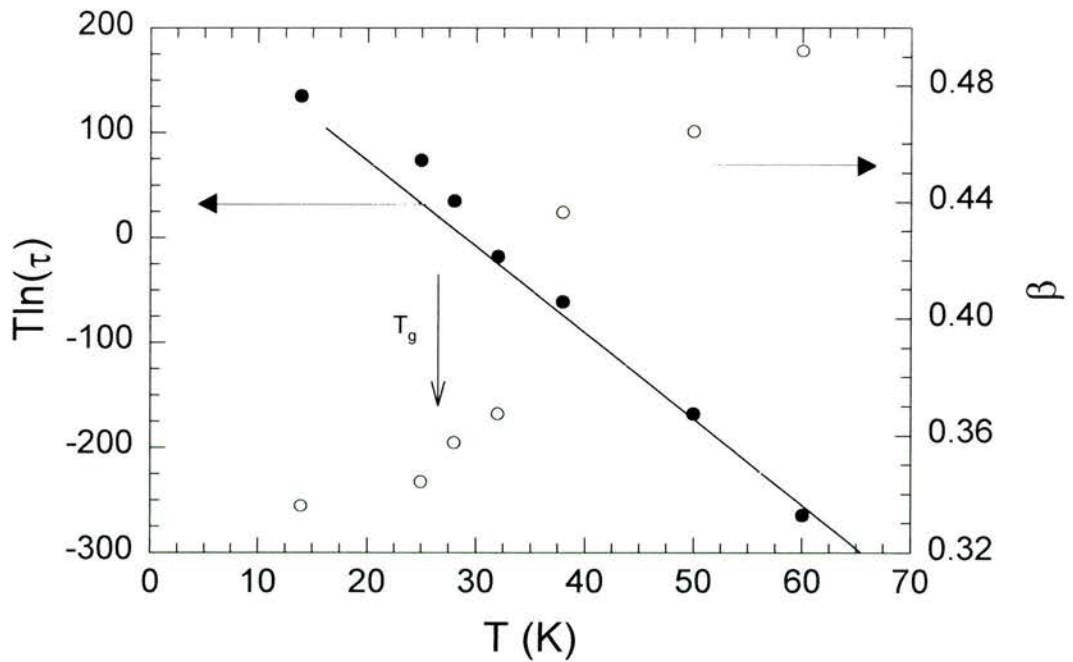


Figure IV - 30 : Temperature evolution of the stretched exponent  $\beta$  and the mean relaxation time  $\tau$  as a function of temperature.



spin glasses<sup>73</sup> (although it is not entirely clear how  $P(t)$  relates to the spin correlation function), so much so that stretched exponential with an exponent  $\beta$  going to a third at the transition has become a signature of spin glass behaviour. The complete "Ogielski form" - stretched exponential multiplied by a power law above  $T_g$  i.e.  $C.t^{-x}.\exp((- \omega t)^\beta)$  and simple power law below  $T_g$  - can also fit our data but the quality of the fits is not significantly improved. We chose to stick with the stretched exponential for the description of our data as it requires only 2 parameters, whereas the Ogielski form needs two extra parameters. Recently, experimentalists have claimed that they have observed the Ogielski form in an Ising spin glass  $Fe_xTiS_2$ <sup>74</sup> and in Au-14%Fe<sup>75</sup> but looking closer at their data, their statistics are not better than ours and they could easily fit their data with a stretched exponential. As a check, I have also scanned the simulations from Ogielski paper and they too can be fitted with a stretched exponential all the way from well above  $T_g$  to below  $T_g$ . It is interesting to note that in Ogielski's article, the  $\beta$  values for the three temperatures very close to but above  $T_g$  have been omitted. When I tried to fit the scanned simulations with the Ogielski form, and the  $\beta$  values were actually increasing for those three temperatures, in contradiction with the suggested 1/3 plateau. With the simpler stretched exponential fit,  $\beta$  was smoothly decreasing from its high temperature value and reached a plateau at  $T_g$  and for the temperature below  $T_g$ . However, my fits of Ogielski's simulation gives a  $\beta$  at and below  $T_g$  well below the 1/3 value. In fact, the low temperature  $\beta$  (0.085) was very close to the value for the power law exponent,  $x$ , obtained by Ogielski (0.065) at  $T_g$  (this  $x$  value decreases further as the temperature is reduced in Ogielski's paper). This value could in principle be compared with the theoretical power exponent, obtained from phase transition theory, depending on standard critical exponents and given by  $x = (d-2+\eta) / 2z$ . This little exercise has proved itself very interesting and probably deserves more attention (it could be worthwhile to simulate Ogielski's data again with state-of-the-art computers to expand the time window and see what functional form could be used).

Mezei et al<sup>76</sup> proposed a different method of analysing their NSE data on the insulating spin-glass  $La_{0.7}Er_{0.3}Al_2$  for  $T > T_g$ . They found that the spin relaxation time  $\tau$  could be described by the Arrhenius law (*Eq. IV- 37*) by assuming that the broad distribution of relaxation time is simply a consequence of a broad distribution of activation energies  $E$ , namely :

$$S(q, t) = E_m^{-1} \int_0^{E_m} \exp[-t / \tau_0 \exp(E / k_B T)] dE \quad \text{Eq. IV- 49}$$

where a constant distribution of E's in the interval (0, E<sub>m</sub>) has been assumed. This model seems to work reasonably well for T > T<sub>g</sub> but fails at lower temperatures. They attributed that failure to the onset of strong ferromagnetic short range order : the approximation of a constant distribution of energies therefore ceases to be valid.

By analogy with Ngai's model for structural glasses<sup>59</sup>, Ngai et al<sup>58</sup> suggested that the relaxation of a spin glass is a stretched exponential whose stretched exponent is a function of T, H and thermal and magnetic history. Far above T<sub>f</sub>, β is equal to unity and the relaxation follows an Arrhenius behaviour. As T approaches T<sub>f</sub>, the distribution g(τ) broadens as well as the mean relaxation time <τ> departs from Arrhenius behaviour. Interestingly, when this model is applied to the magnetic susceptibility with a constant β=0.3 for all T, a frequency dependent peak that resembles that of the (Ho<sub>2</sub>O<sub>3</sub>)<sub>0.08</sub>(B<sub>2</sub>O<sub>3</sub>)<sub>0.92</sub> spin-glass is obtained. This spin-glass is classified, again by analogy with structural glasses, as a "type B" spin glass because β is independent of T and T<sub>f</sub> varies with ν according to the Arrhenius law. If applied to a "type A" spin-glass where β varies with temperature, magnetic susceptibility curves resembling experimental ones can be obtained and the frequency dependence of T<sub>f</sub> becomes Vogel-Fulcher like (Eq. IV-38). This reinforces the idea that the key to the understanding of the spin glass state lies in the dynamics.

Another strong argument for the distribution of relaxation times model is provided by a muon spin relaxation study<sup>77</sup> of the RAM systems. Indeed, both α-Dy<sub>1</sub>Y<sub>6</sub>Ni<sub>3</sub> and α-Gd<sub>1</sub>Y<sub>6</sub>Ni<sub>3</sub> show spin-glass like transition around 6K from ac-susceptibility data. Gd being a s-state ion (see §II), this alloy can be regarded as a true spin glass whereas the Dy compound is a RAM. By contrast with the similarity in the ac data, the muon data is strikingly different : the muon depolarisation can be fitted to a stretched exponential for both samples but for the Dy system, β approaches 1/3 and the depolarisation rate diverges at 10T<sub>g</sub> whereas for the Gd, these characteristics happen at T<sub>g</sub>. Models based on random walks in a hypercube imply that β approaches a 1/3 at the transition even if λ is beyond the instrumental window which is clearly not the case for the Dy compound. Interestingly, a simple model where the muon depolarisation function is obtained from the integration of the distribution of depolarisation rates over

all the muon sites gives a stretched exponential, whatever shape the distribution has, providing it is wide enough. This simulation shows a  $\beta$  going below 1/3 but only for incredibly broad distributions for which the muon response would appear static. It is possible that the limiting value of 1/3 for the stretched exponent  $\beta$  observed experimentally could arise from the time-window limitation of the technique : when the relaxation time goes beyond that time window,  $\beta$  can no longer evolve. This "time-window limitation" (TWL) model is an attractive solution in the light of muon spin relaxation data for the very dilute spin-glasses<sup>78</sup> (eg Au-1%Fe) and superparamagnet (eg.<sup>79</sup> Cu-2%Co). In the limit of fast fluctuations, the Uemura function (a stretched exponential with a fixed  $\beta$  value of 1/2, which is reminiscent of the type A spin-glass defined by Ngai), found to fit muon spin relaxation data for can be used. The TWL model proposed earlier could be a quite attractive solution for simulation studies as well, as one could associate a time window defined by the Monte Carlo time-step.

*Figure IV-30* shows the evolution of the mean relaxation time  $\tau$  as a function of temperature. The striking feature is that it continues to evolve below the freezing temperature  $T_g$ . This evolution is neither Arrhenius (the plot is a 'modified' Arrhenius plot where the abscissa is T and not 1/T) or Vogel-Fulcher like but two regimes can be clearly distinguished : above  $T_g$ , the relaxation times evolve a lot slower than below  $T_g$ .

Finally, one of the challenges in spin-glass dynamics is to tie up the results from different techniques (eg. NSE,  $\mu$ SR, ac susceptibility) in order to study the relaxation over as wide a range as possible. However, this very often requires some manipulation of the data and the results are to be taken with precaution. I have tried to simulate the correlation function at times relevant to the spin echo window using the distribution obtained from AC susceptibility but it did not give results along the line of the measured spin echo signal (the simulated echo signal was much flatter than the experimental one). This is hardly surprising if we consider that in order to get a spin echo signal significantly changing in the ns range, the distribution itself has to change significantly in that range and according to the ac susceptibility measurements, apart from a very narrow temperature range, the distributions obtained were very flat in this time range. It should be noted however that the AC susceptibility measures at  $q=0$  whereas our NSE data was taken at a well defined  $q$  (similarly, the  $\mu$ SR represents a sum over the Brillouin zone).

## IV.6 Conclusions and perspectives

In this chapter, the spin correlation function in a spin-glass type system has been showed to follow closely and conclusively the Kohlrausch function for the first time. However, several questions still remain. As better NSE data are now within our reach, there could be a dilemma between "simple" stretched exponential form and the Ogielski form. One way of testing which function better fits the data could be achieved by using a dilute RAM (eg a few % Er) to see whether the temperature evolution of  $\beta$  is really typical of concentrated systems and more dilute systems show a constant  $\beta$ . As mentioned earlier, NSE experiments on glassy magnets are more difficult as the dilution increases because of the associated reduction in the magnetic scattering but 1) it is possible to counterbalance this effect by using a bigger sample and 2) recent improvements in the instrument design (the new IN11C detector would allow the angle dependence to be studied more rapidly, higher flux on IN15) would also improve statistics. Another interesting test, which we have put through for a proposal round at the ILL, would be to study the differences between  $(\text{Dy}_{0.6}\text{Y}_{0.4})\text{Mn}_2$  and  $(\text{Dy}_{0.6}\text{Y}_{0.4})\text{Al}_2$ . In the former compound, the interactions are predominantly antiferromagnetic whereas for the latter case they are ferromagnetic and authors<sup>80</sup> have claimed that they represent a crystalline equivalent of RAM. Both compounds show a spin glass like behaviour. Muon spin relaxation measurements on the Mn compound show the typical Ogielski dependence<sup>81</sup> ( $\beta$  decreasing to 1/3 at  $T_g$ ). Although Dy has a relatively high absorption cross-section for neutrons, the sizeable Dy moments and their high concentrations should ensure that a significant cross-section will be achieved. Furthermore, as these alloys can be obtained by argon arc melting rather than melt-spinning, it is easier to produce bigger quantities of sample.

## References for chapter IV

---

- <sup>1</sup> F Hund, *Linienspektren und periodisches System des Elemente* (Julius Springer, Berlin, 1927)
- <sup>2</sup> See for instance, C. Cohen Tannoudji, Bernard Diu, Franck Laloë, *Mécanique Quantique*, Wiley (1987)
- <sup>3</sup> M. A. Ruderman and C. Kittel, *Phys. Rev.* **96** (1954) 99  
T. Kasuya, *Prog. Theor. Phys.* **16** (1956) 45, 58  
K. Yosida, *Phys. Rev.* **106** (1957) 893
- <sup>4</sup> R.W. Cochrane, R. Harris & M.J. Zuckermann, *Phys. Reports* **48** (1978) 1
- <sup>5</sup> R. Harris, M. Plischke & M.J. Zuckermann, *Phys. Rev. Lett.* **31**(1972) 1562
- <sup>6</sup> Sellmer and Nafis, *J. Appl. Phys.* **57** (1985) 3584
- <sup>7</sup> J.R. De Almeida and D.J. Thouless, *J. Phys.* **A11** (1978) 983
- <sup>8</sup> B. Dieny and B. Barbara, *Phys. Rev. Lett.* **57** (1986) 1169
- <sup>9</sup> See for instance, A. Herpin, *Théorie du magnétisme* or reference 10 below. The original paper giving the calculations of N for a general ellipsoid is J. A. Osborn, *Phys. Rev.* **67** (1945) 351
- <sup>10</sup> H. Zijlstra, *Experimental Methods in Magnetism* (North-Holland, Amsterdam, 1967)
- <sup>11</sup> T. Kaneyoshi, *Amorphous Magnetism* (CRC Press)
- <sup>12</sup> ESR and susceptibility measurements on CuMn alloys are first reported in J. Owen et al, *Phys. Rev.* **102** (1956), 1501. However, the authors interpreted their results in terms of an antiferromagnetic transition. Later measurements on CuFe and AuFe by J.L. Tholence and R. Tournier, *J. Phys. (Paris)* **32** (1971) C1-211, were interpreted by a theory from L. Néel, *Physique des Basses Températures* (1961, Gordon and Breach) in which a continuous freezing of the spins takes place, in agreement with the absence of a sharp transition in the susceptibility. It was not until the now classic papers V. Cannella, J.A. Mydosh and J.I. Budnick, *J. Appl. Phys* **42** (1971) 1689 and V. Cannella and J. A. Mydosh, *Phys. Rev. B* **6** (1972) 4220 on AuFe that a sharp cusp was observed. These later measurements were performed in a small ac field in contrast to the previous ones where a non negligible dc field was used.
- <sup>13</sup> D.J. Sellmyer and S. Nafis, *J. Appl. Phys.* **57** (1985) 3584
- <sup>14</sup> R.I. Bewley and R. Cywinski, *Phys. Rev. B* **54** (1996) 1
- <sup>15</sup> R. I. Bewley, PhD thesis (Reading, 1994)
- <sup>16</sup> K.H.J. Buschow, *J. Magn. Magn. Mat.* **21** (1980) 97
- <sup>17</sup> A. Lienard and J.P. Rebouillat, *J. Appl. Phys* **49** (1979) 1680
- <sup>18</sup> R.I. Bewley, S.H. Kilcoyne and R. Cywinski, *J. Magn. Magn. Mat.* **104-107** (1992) 1133
- <sup>19</sup> A.C. Hannon, A.C. Wright and R.N. Sinclair, *Mater. Sci. Eng A* **134** (1991) 883
- <sup>20</sup> J. L. Tholence, *Solid State Comm.* **35** (1980) 113
- <sup>21</sup> D. Dekker et al, *Phys. Rev. Letters* **61** (1988) 1780
- <sup>22</sup> J. L. Tholence in "Magnetic susceptibility of superconductors and other spin systems" (Plenum Press, 1991) ed. R. A. Hein, T. L. Francavilla and D. H. Liebenberg.
- <sup>23</sup> L. Lundgren, P. Svedlindh and O. Beckman, *J. Magn. Magn. Mat.* **25**(1981) 33
- <sup>24</sup> P. Debye, *Polar molecules* (Chemical catalogue company, New York, 1929)
- <sup>25</sup> D. Hüser et al, *J. Phys. C* **19** (1986) 3697
- <sup>26</sup> K.S. Cole and R. H. Cole, *J. Chem. Phys.* **9**(1941) 341
- <sup>27</sup> C. Dekker et al, *Phys. Rev. B* **40** (1989) 11243
- <sup>28</sup> A. Chelkowski, *Dielectric physics*.
- <sup>29</sup> P.R. Bevington, *Data reduction and error analysis for the Physical Sciences* (McGraw-Hill, 1969)
- <sup>30</sup> J.J. Baalbergen et al, *J. de Physique* **C8** (1988) 1065
- <sup>31</sup> R.I. Bewley and R. Cywinski, *J. Magn. Magn. Mat.* **140-144** (1995) 869
- <sup>32</sup> J. Filippi et al, *J. Magn. Magn. Mat.* **104-107** (1992) 165
- <sup>33</sup> R. Fuos and J.G. Kirkwood, *J. Am. Chem. Soc.* **63** (1941) 385
- <sup>34</sup> For a review, see for instance, C.Y. Huang, *J. Magn. Magn. Mat.* **51** (1985) 1-74
- <sup>35</sup> F. Holtzberg et al, *J. Appl. Phys.* **53** (1982) 2229
- <sup>36</sup> J. L. Tholence, *J. Appl. Phys.* **50** (1979) 7310
- <sup>37</sup> H. Vogel, *Phys. Z.* **22** (1921) 645
- <sup>38</sup> G.S. Fulcher, *J. Am. Ceram. Soc.* **8** (1925) 339
- <sup>39</sup> S. Strickman and E. P. Wohlfarth, *Phys. Letters* **85A** (1981) 467
- <sup>40</sup> J. L. Dorman et al, *J. Magn. Magn. Mat* **35** (1983) 117
- <sup>41</sup> C.A. Angell, *J. Non-Cryst. Sol.* **102** (1988) 205
- <sup>42</sup> <http://www.ill.fr/YellowBook/D7>
- <sup>43</sup> O. Schärpf and H. Capellmann, *Phys. Stat. Sol.* **A135** (1993) 359



- 
- <sup>44</sup> International Tables of Crystallography, Vol. C, p513, (D. Reidel Publ. Company, Ed. T. Hahn, 1985)  
<sup>45</sup> International Tables of Crystallography, Vol. C, p391, (D. Reidel Publ. Company, Ed. T. Hahn, 1985)  
<sup>46</sup> R.I. Bewley, J.R. Stewart and R. Cywinski, ILL Report 5-32-523  
<sup>47</sup> R. Cywinski, private communication  
<sup>48</sup> F. Mezei, Z. Physik **255** 146 (1972)  
<sup>49</sup> F. Mezei in "Neutron Spin Echo", Lecture notes in Physics n° 128, edited by F. Mezei (Springer-Verlag, 1979)  
<sup>50</sup> J. B. Hayter and J. Penfold, Z. Physik B **35** (1979) 199  
<sup>51</sup> A. Murani and F. Mezei, J. Magn. Magn. Mat **14** (1979) 211-213  
<sup>52</sup> K. Binder and K. Schröder, Phys. Rev. B **14** (1976) 2142  
<sup>53</sup> S. Kirkpatrick and D. Sherrington, Phys. Rev. B **17** (1978) 4304  
<sup>54</sup> R. Kohlrausch, Ann. Phys. Lpz. **12** (1847) 393 and Pogg. Ann. Phys. Chem. **91** (1854) 179  
<sup>55</sup> G. Williams and D.C. Watts, Trans. Faraday Soc. **66** (1970) 80  
<sup>56</sup> R. Weiler, R. Bose and P.B. Macedo, J. Chem. Phys. **53** (1970) 1258  
<sup>57</sup> A.K. Jonscher, Nature **267** (1977) 673  
<sup>58</sup> K.L. Ngai, A.K. Rajagopal and C.Y. Huang, J. Appl. Phys. **55** (1984) 1714  
<sup>59</sup> K.L. Ngai, Comments Solid State Phys. **9** (1979) 127 and *ibid*, **9** (1980) 141  
<sup>60</sup> L. Götze and W. Sjögren, Rep. Prog. Phys. **55** (1992) 241  
<sup>61</sup> R.G. Palmer, D.L. Stein, E. Abrahams and P.W. Anderson, Phys. Rev. Letters **53** (1984) 958  
<sup>62</sup> R.V. Chamberlin, G. Mozurkewich and R. Orbach, Phys. Rev. Letters **52** (1984) 211  
<sup>63</sup> A.T. Ogielski, Phys. Rev. B **32** (1985) 7384  
<sup>64</sup> I.A. Campbell and L. Bernardi, Phys. Rev B **50** (1994) 12643 and *ibid* **52** (1995) R9819  
<sup>65</sup> N. Lemke and I.A. Campbell, Physica A **230** (1996) 554-562  
<sup>66</sup> P. Jund, R. Jullien and I.A. Campbell, arXiv:cond-mat/0011494 29 Nov 2000  
<sup>67</sup> B.V.B. Sarkissian, J. Phys : Condens. Matter **2** (1990) 7873  
<sup>68</sup> B.V.B. Sarkissian and B. D. Rainford, Solid State Communications **78** (1991) 185  
<sup>69</sup> F. Mezei, V. Knaak and B. Farago, Phys. Rev. Letters **58** (1987) 571  
<sup>70</sup> B. Frick and B. Farago, Phys. Rev. Letters **61** (1988) 2465  
<sup>71</sup> A. Murani, private communication  
<sup>72</sup> D.A. Keen, R.I. Bewley, R. Cywinski and R.L. McGreevy, Phys. Rev. B **54** (1996) 1036  
L. Karlsson, A. Wannberg, R.L. McGreevy and D.A. Keen, *ibid* **61** (2000) 487  
<sup>73</sup> I.A. Campbell, S.H. Kilcoyne, R. Cywinski et al, Phys. Rev. Letters **72** (1994) 1291  
<sup>74</sup> F. Gulener, PhD thesis, Orsay University, France  
<sup>75</sup> C. Pappas et al, to be published  
<sup>76</sup> F. Mezei, A.P. Murani and J.L. Tholence, Solid State Commun. **45** (1983) 411  
<sup>77</sup> R.I. Bewley et al, ISIS report and R. Cywinski, private communication.  
<sup>78</sup> Y.J. Uemura et al, Phys. Rev. Letters **45** (1980) 583  
Y.J. Uemura et al, Phys. Rev. B **31** (1985) 546  
<sup>79</sup> R.I. Bewley and R. Cywinski, Phys. Rev. B **58** (1998) 11544  
<sup>80</sup> Gering, Salamon, del Moral and Arnoudas, Phys. Rev. B **41** (1990) 9134  
<sup>81</sup> M.T.F. Telling, R. Cywinski and C. Ritter, J. Magn. Magn. Mat **177-181** (1998) 1480



# **Chapter V : Synthesis and characterisation of novel Rare Earth-Transition Metal phases by crystallisation of amorphous precursors.**

## **V.1. Introduction**

The Rare Earth - Transition Metal (RE-TM) alloys have attracted a huge amount of interest for a few decades<sup>1</sup>, principally due to their technological interest, most notably as high-density permanent magnets but also as magnetic storage media and as giant magnetoresistive materials<sup>2</sup>. Indeed, in most rare earth compounds, the magnetocrystalline anisotropy is high which is one of the possible ways of producing high coercivity magnets and carefully prepared nucleation-type SmCo<sub>5</sub> or pinning-type Sm<sub>2</sub>Co<sub>17</sub> magnets can achieve coercivity of several teslas. However, due to the cost of both Sm and Co, extensive research in the RE<sub>2</sub>Fe<sub>17</sub> compounds, which, unfortunately, all had low ordering temperatures, has led to the more widely used Nd<sub>2</sub>Fe<sub>14</sub>B based magnets. In addition to their technological applications, the RE-TM alloys also offer an ideal test-bed for theories on magnetic properties of intermetallics. The availability of a fairly large number of possible phases, obtained by varying the alloy composition, combined with the possibility of substituting one RE by another allow both the magnetic exchange and the anisotropy to be mapped. To illustrate this statement, let us briefly consider the RMn<sub>2</sub> system for which the Mn-Mn nearest neighbour distance is very close to the threshold value of 2.7 Å below which the Mn moments delocalise. Substitution of Y by a magnetic RE such as Dy or Ho allows this instability region to be studied and a change from spontaneous Mn moments to moments induced by the RE ions has been observed<sup>3</sup>.

As a consequence of the technological and theoretical interest in the RE-TM, the equilibrium phase diagrams associated with these alloys are considered very well known and the only questions that remain opened concern site selectivity or interstitial substitution which can give rise to very interesting magnetic properties (see for instance

H substitution in  $Y\text{Mn}_2$  or  $\text{TbMn}_2$ )<sup>4</sup>. In fact, there has not been a discovery of an entirely new binary alloy for a long time. As an example of such an equilibrium phase diagram, the Y-Fe alloy is presented in *Figure V- 5* and will be discussed in details later. However, it is extremely important to emphasise the fact the conditions under which these so-called equilibrium phase diagrams are generated are in fact far from equilibrium. Indeed, the phase diagrams are generally obtained by annealing at given temperatures and subsequently quenching the binary mixes before analysing the phases formed by, for example, X-rays. Therefore, this procedure relies entirely on the hope that the phases and phase proportions obtained after quenching are the same as the ones formed at the annealing temperatures. This technique is therefore very likely to miss out any metastable phases that could have formed and ideally one would like to perform an in-situ study to obtain the 'true' equilibrium phase diagram. This can however be very hard to achieve in practice. In principle, one could use the high flux available on an X-ray instrument but, as noted in chapter II, X-rays are unfortunately primarily sensitive to the surface of the ribbons where small crystalline impurities are most likely to appear. This chapter will report novel ways of creating new alloys by in-situ kinetic neutron diffraction on amorphous precursors. This method has been proved previously successful in making high quality superconducting Bi-Sr-Ca-Cu-O<sup>5</sup> or nanocrystalline Fe-Nb-Cu-Si-B<sup>6</sup> but has not been used to re-examine phase diagrams of binary alloys. It should also be noted that diffraction patterns also contains information about the microstructure of the alloys studied which is crucial in the design of, for instance, nanocrystalline magnets.

## **V.2. The D20 and D2B spectrometers at the ILL**

Due to the nature of the experiment, it is evident that the real time mapping of the true equilibrium phase diagram requires either very large samples or a high intensity instrument. The 2-axis diffractometer D20 at the ILL is a high-intensity, medium resolution instrument, ideal for experiments requiring a precise measure of the intensity (e.g. for disordered systems such as liquids or amorphous solids; or for very weak magnetic systems) or many very shorts measurements (for mapping phase transitions as function of temperature, pressure) or the use of very small samples (some experiments have been conducted on samples of only a few milligrams). A picture and a schematic<sup>7</sup>

of D20 can be found on *Figures V-1 and V-2* respectively. The flux of thermal neutrons on D20 varies between  $1.5$  and  $6.0 \times 10^7$  n.cm<sup>-2</sup>.s<sup>-1</sup> depending on which of the three available wavelengths (0.82, 1.3 and 2.4Å) has been chosen. Such a flux allowed us to obtain refinable data on samples of about 2 to 3g. An impressive  $2\theta$  coverage of  $160^\circ$  is achieved by 1600 cells, filled by <sup>3</sup>He and CF<sub>4</sub>, and the detection system is made of microstrips which allows a small distance between the anode and the cathode (170µm) and thereby a fast evacuation of the cations and very high count rates ( $5 \times 10^4$  counts/cell/s). The efficiency of each cell is calibrated at the beginning of each cycle by running a Vanadium or a plexiglass sample.

The very high flux on D20 makes this instrument extremely valuable for watching the phases forming as they are created in beam. However, the full characterisation of novel structures generally requires a much better resolution than that offered by D20. The other instrument that has been used for the characterisation of the phases formed by crystallisation of amorphous precursors is D2B. This high-resolution two-axis diffractometer is located in the reactor hall of the ILL, next to D20, and possesses 64 <sup>3</sup>He counting tubes spaced at  $2.5^\circ$  intervals. A diffraction pattern is typically obtained after 100 steps of  $0.025^\circ$  in  $2\theta$  thereby giving a very good resolution. The flux available is at least an order of magnitude smaller than that of D20. A picture and a diagram of the D2B instrument<sup>8</sup> are presented on *Figures V-3 and V-4* respectively. Evidently, due to the need of moving the tubes step by step to obtain a complete diffraction pattern and the relatively smaller flux, this experimental setup is rather useless for studying relatively fast processes that are irreversible such as those involved in the crystallisation. The sample used during our investigation was therefore obtained by watching the crystallisation in-situ in a fast-counting instrument, such as D20, and quenching at the desired temperature.



Figure V- 1 : Picture of the D20 instrument showing the impressive PSD detector bank covering a very wide range of  $2\theta$  angles.

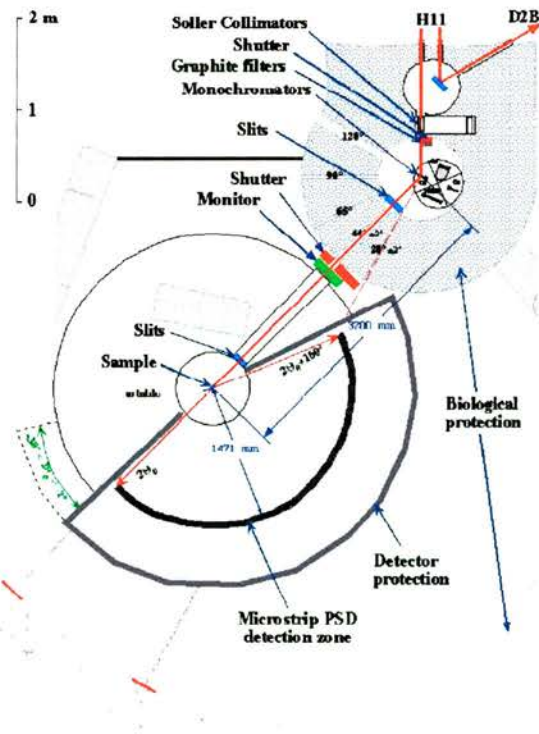


Figure V- 2 : Schematic of D20



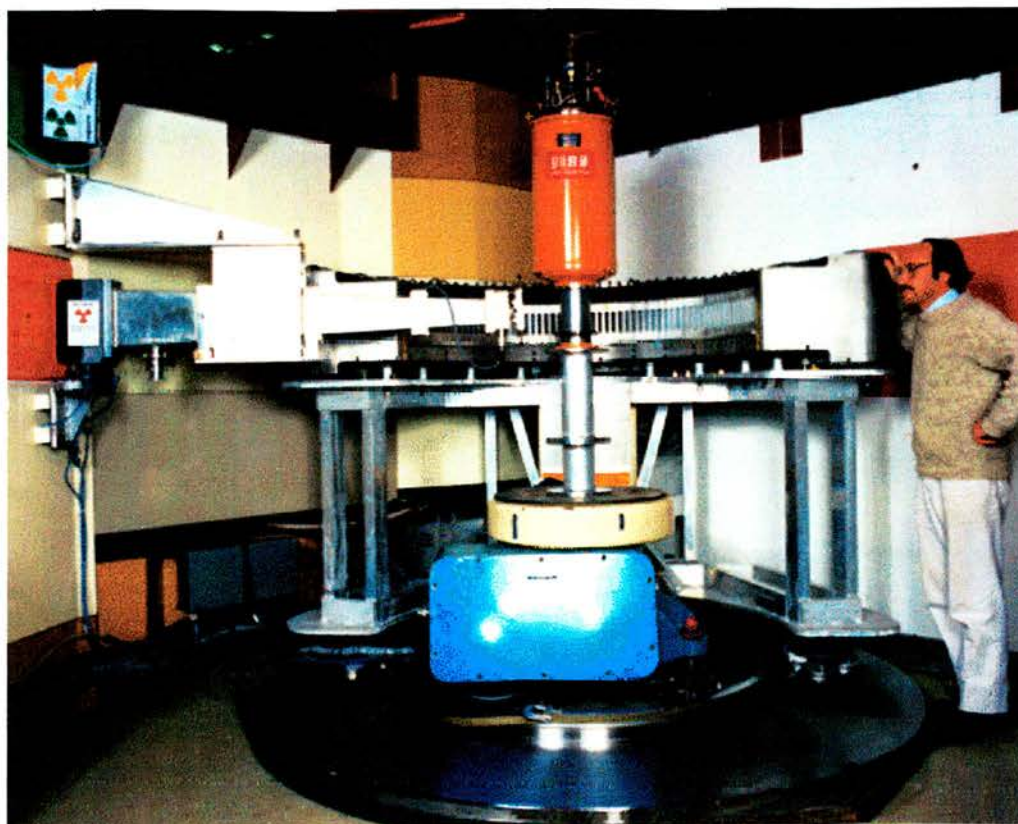


Figure V- 3 : The D2B spectrometer at the ILL

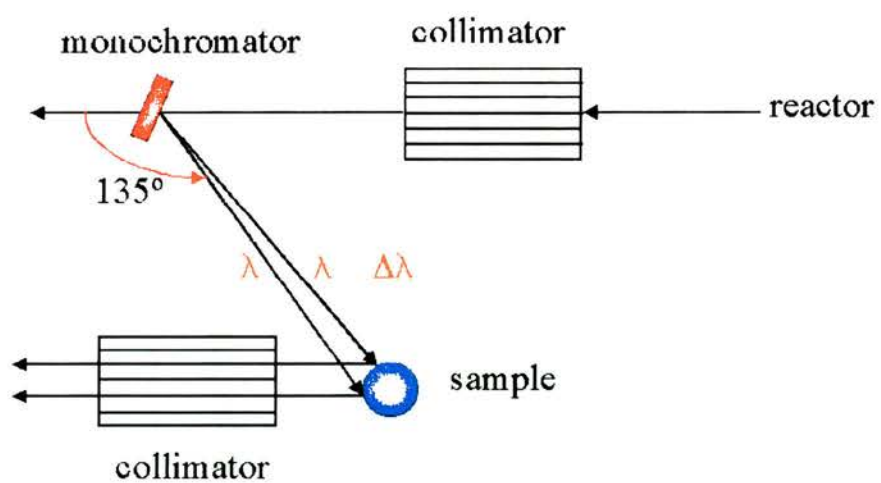


Figure V- 4 : Schematic of the D2B instrument

### **V.3. Crystallisation of amorphous $Y_{67}Fe_{33}$ : a novel YFe phase.**

#### **V.3.a. Previous studies on the Y-Fe system**

The YFe phase diagram is presented on *Figure V-5* and shows the existence of several tie-lines corresponding to the formation of the well-known  $YFe_2$ ,  $YFe_3$ ,  $YFe_4$  and  $YFe_9$  alloys. Crystallisation of  $Y_{66}Fe_{34}$  amorphous ribbons has been first carried out on splat-cooled samples by Tenhover<sup>9</sup> in 1981 by a combination of  $^{57}Fe$  Mössbauer, X-ray diffraction, high temperature resistivity and Differential Scanning Calorimetry (DSC) techniques. He concluded that the crystallisation in this amorphous alloy is a two stage process : at first, Y forms in an Fe-rich amorphous matrix; then, formation of  $YFe_2$  occurs at the detriment of the amorphous matrix that gradually disappears, until the whole sample is fully crystalline. On the other hand, Croat<sup>10</sup> studied melt-spun  $Y_{1-x}Fe_x$  ribbons with  $0.4 < x < 0.79$  using DSC and x-ray diffraction. His DSC measurements indicated that while the Fe rich alloys with  $x > 0.6$  crystallise directly into the appropriate metallic phase, the Y rich alloys with  $x = 0.4, 0.45$  and  $0.5$  exhibit a multi-stage crystallisation process with the formation of an intermediate metastable phase. Croat was able to further investigate this metastable phase by collecting X-ray diffraction patterns from samples whose crystallisation was stopped at the appropriate temperatures, chosen while running the DSC, and cooled to room temperature. However, he made no attempt in trying to characterise the structure or the magnetic properties of that new phase.

#### **V.3.b. Neutron study of the crystallisation processes in $\alpha$ - $Y_{67}Fe_{33}$**

All the samples were prepared in St Andrews by the melt-spinning method described in chapter II. About 3g of sample were sealed in a vanadium can and placed in a furnace mounted on the D20 diffractometer. The good quality of the amorphous ribbons can be checked on *Figure V- 6* which shows only very small crystalline Y impurities. Neutron diffraction patterns were collected on D20 with an incident wavelength of  $2.4 \text{ \AA}$ , every four minutes while the furnace temperature was ramped smoothly from  $230^\circ \text{ C}$  to  $510^\circ \text{ C}$  at a rate of  $40^\circ \text{ C}$  per hour. The resulting neutron thermogram is shown in *Figure V- 7*, where it can be seen that partial crystallisation of the sample first occurs by the formation of the elemental Y hexagonal closed packed phase at approximately  $300^\circ \text{ C}$ , with the Fe atoms segregating to form an Fe rich amorphous phase. The formation of the Y phase is accompanied by a pronounced



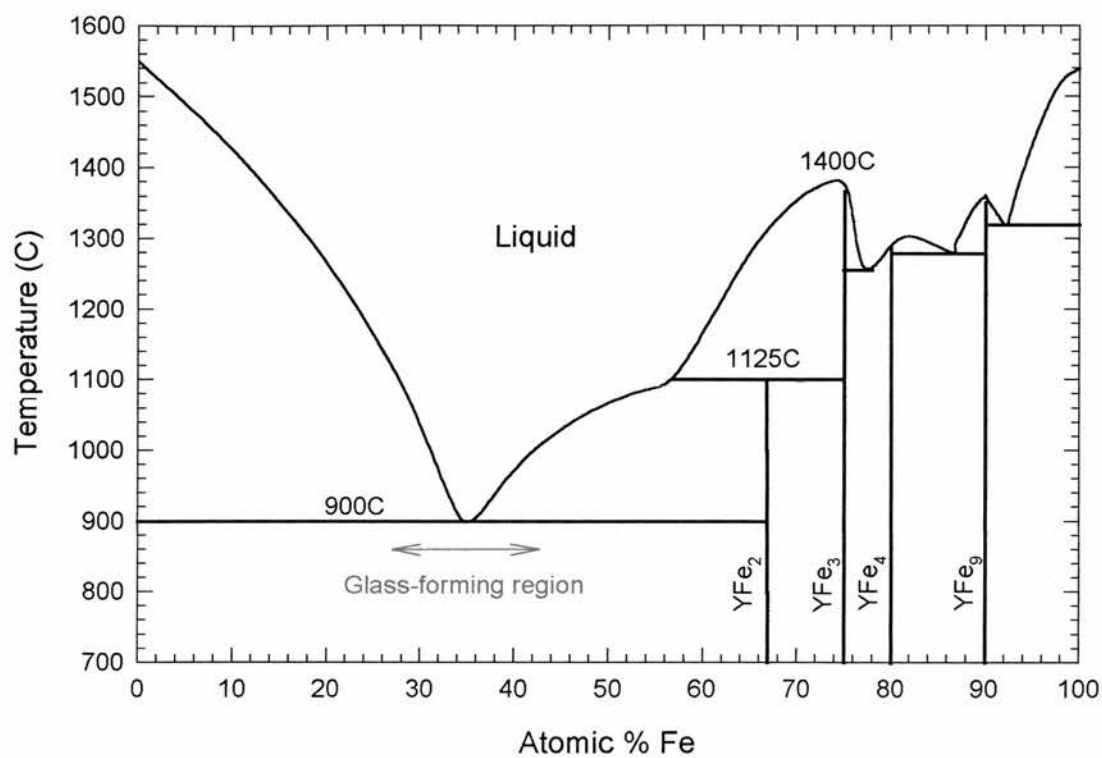


Figure V- 5 : Y-Fe phase diagram

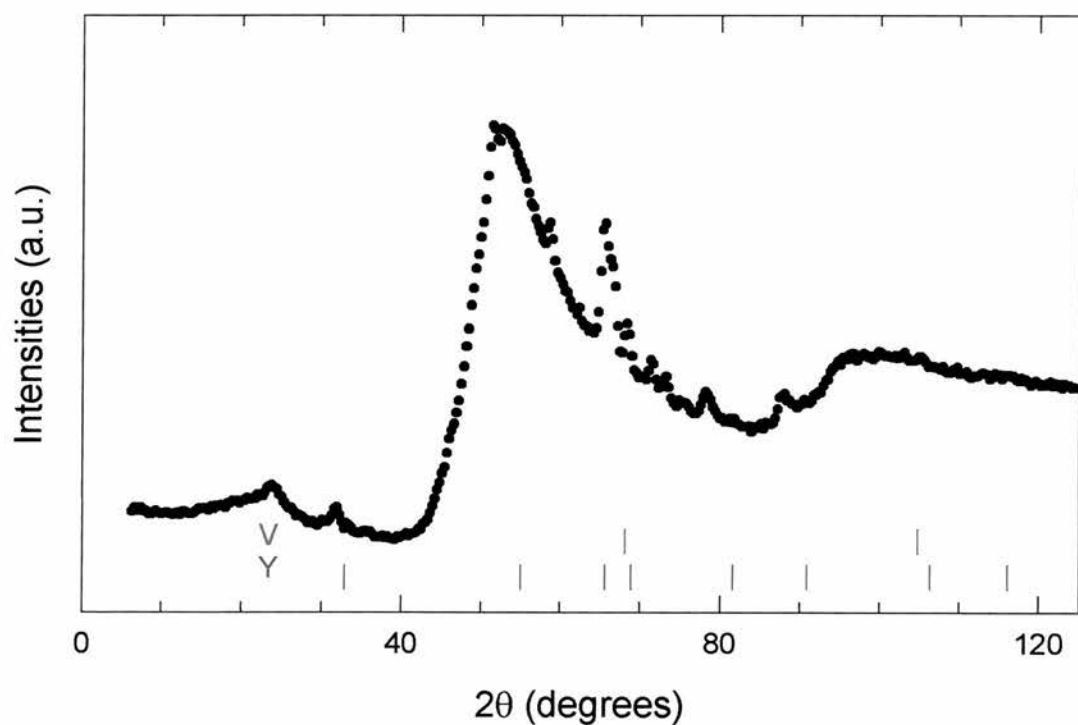


Figure V- 6 : Amorphous  $Y_{67}Fe_{33}$  at  $220^{\circ}C$  measured on D20 in a vanadium can. This plot is a section through Figure V- 7 and shows that the crystalline Y impurities are extremely small.

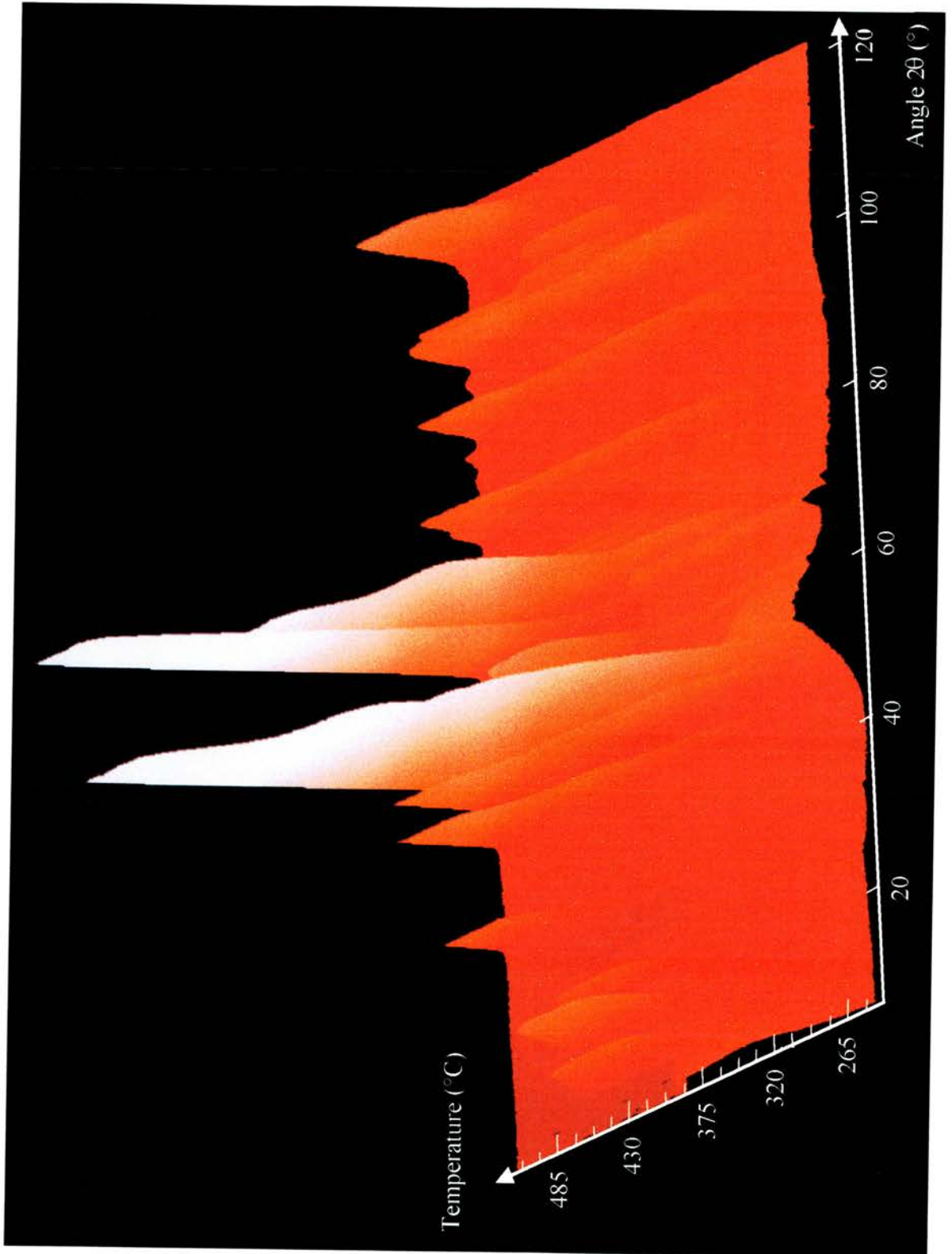


Figure V- 7 : Crystallisation of  $\alpha\text{-Y}_{67}\text{Fe}_{33}$  at the steady rate of  $40^\circ\text{C}/\text{hour}$ .

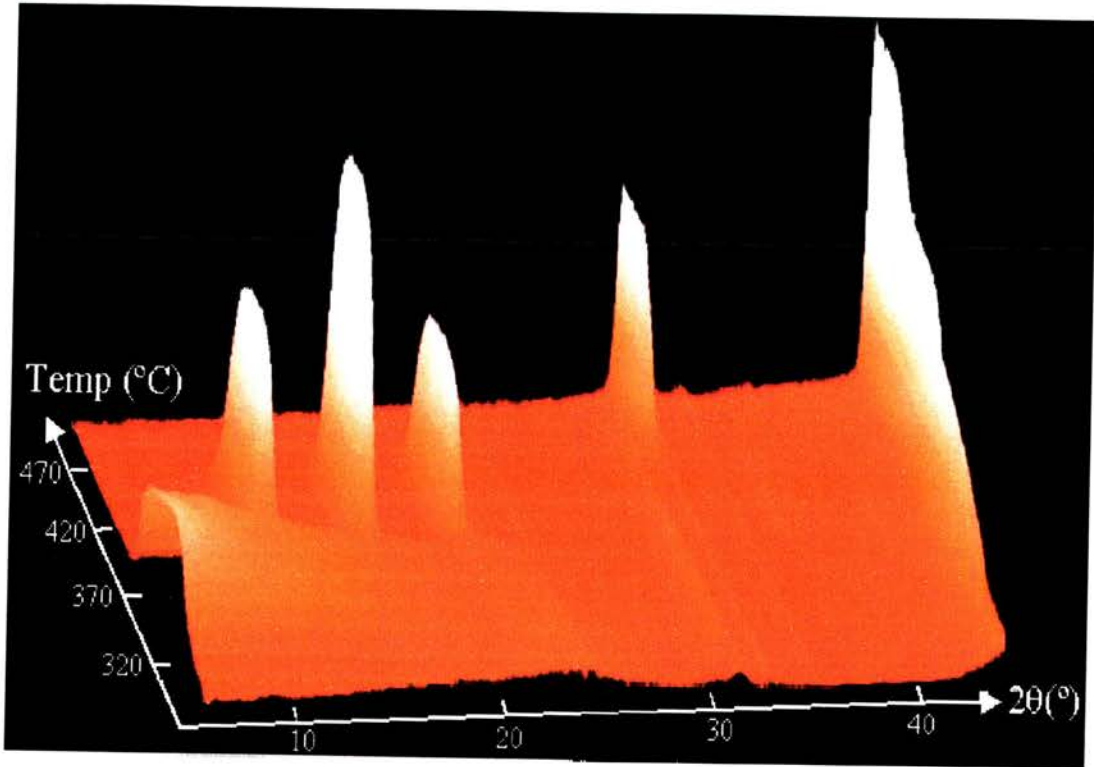
increase in the scattering at low angles (see *Figure V-8*). At 390° C, both the amorphous contribution to the diffraction pattern and the low angle scattering abruptly decrease, thereby testifying that the entire sample has suddenly crystallised. At the same temperature, the appearance of new Bragg peaks, not associated with any previously known phases, signifies the formation of an intermediate phase which coexists with the Y matrix to about 450° C. At this temperature, the intensity of the Bragg peaks associated with this intermediate phase rapidly decreases. This is accompanied by a further increase in the intensity of the Y peaks, and the well-known cubic C15 Laves phase YFe<sub>2</sub> emerges. The final crystallisation product is therefore YFe<sub>2</sub> coexisting in equilibrium with crystalline elemental Y. It is easier to see the formation and transformation of the different phases on the side view of the low angle region 5° < 2θ < 50° (*Figure V-9*). The most salient features are the temperature dependence of the different stages of the formation of elemental Y, the narrowness of the temperature range over which the intermediate phase forms and the formation of YFe<sub>2</sub>. In the following paragraphs, the nature of each of these phases will be discussed in more detail.

#### *V.3.b.1. Low angle region*

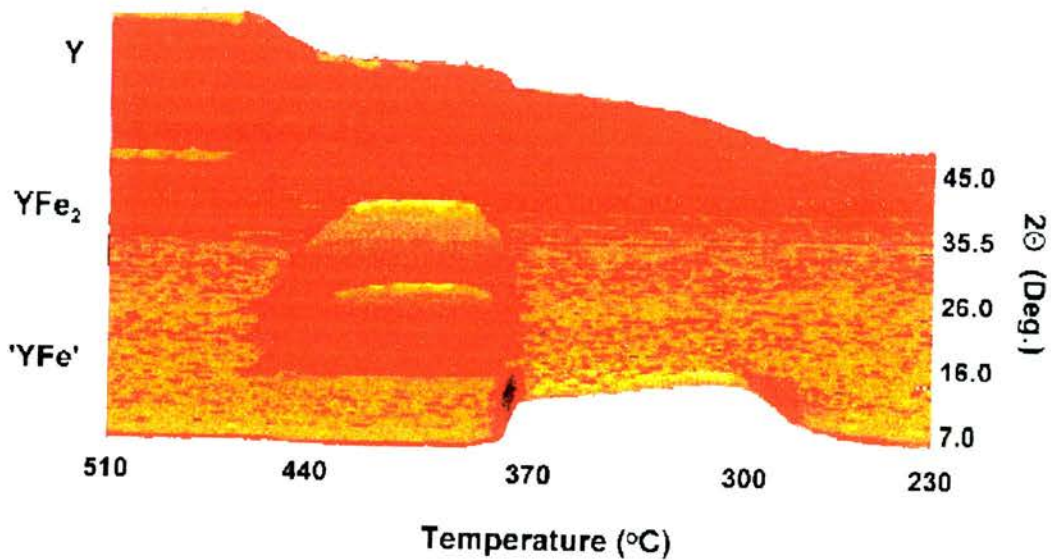
A dramatic increase in the low angle scattering is clearly seen on both *Figures V-8 and V-9*. This scattering first appears at about 275°C, and rapidly reaches a plateau at 310°C, around where the first Y Bragg peaks start to appear, then decreases slowly until at 375°C, the whole sample crystallises. It seems therefore reasonable to assume that this low angle scattering is associated with microcrystallites of Y in the Fe-rich amorphous matrix.

#### *V.3.b.2. Formation and evolution of the Y phase*

As can be seen from the thermogram, the first Bragg peaks appear at about 300°C. A Rietveld refinement of a diffraction pattern obtained at 327° C using FullProf<sup>11</sup> confirms the presence of an elemental HCP Y phase (space group P6<sub>3</sub>/mmc, with a=3.6501 Å, c=5.771 Å, α=β=90° and γ=120°). From the top of *Figure V-10*, where the intensity of the Y(100) Bragg peak has been plotted as a function of temperature, four distinct regions can be distinguished. Below 300° C, no crystallization has taken place, and the intensity at the position of the Y (100) reflection is due to scattering from the amorphous material. The Y Bragg peaks begin to appear at



Figures V- 8 (above) and V- 9 (below) : Low angle scattering of the crystallisation process in  $\alpha\text{-Y}_{67}\text{Fe}_{33}$ . Front and side views. Note the narrow range of temperatures of which the intermediate phase exists.



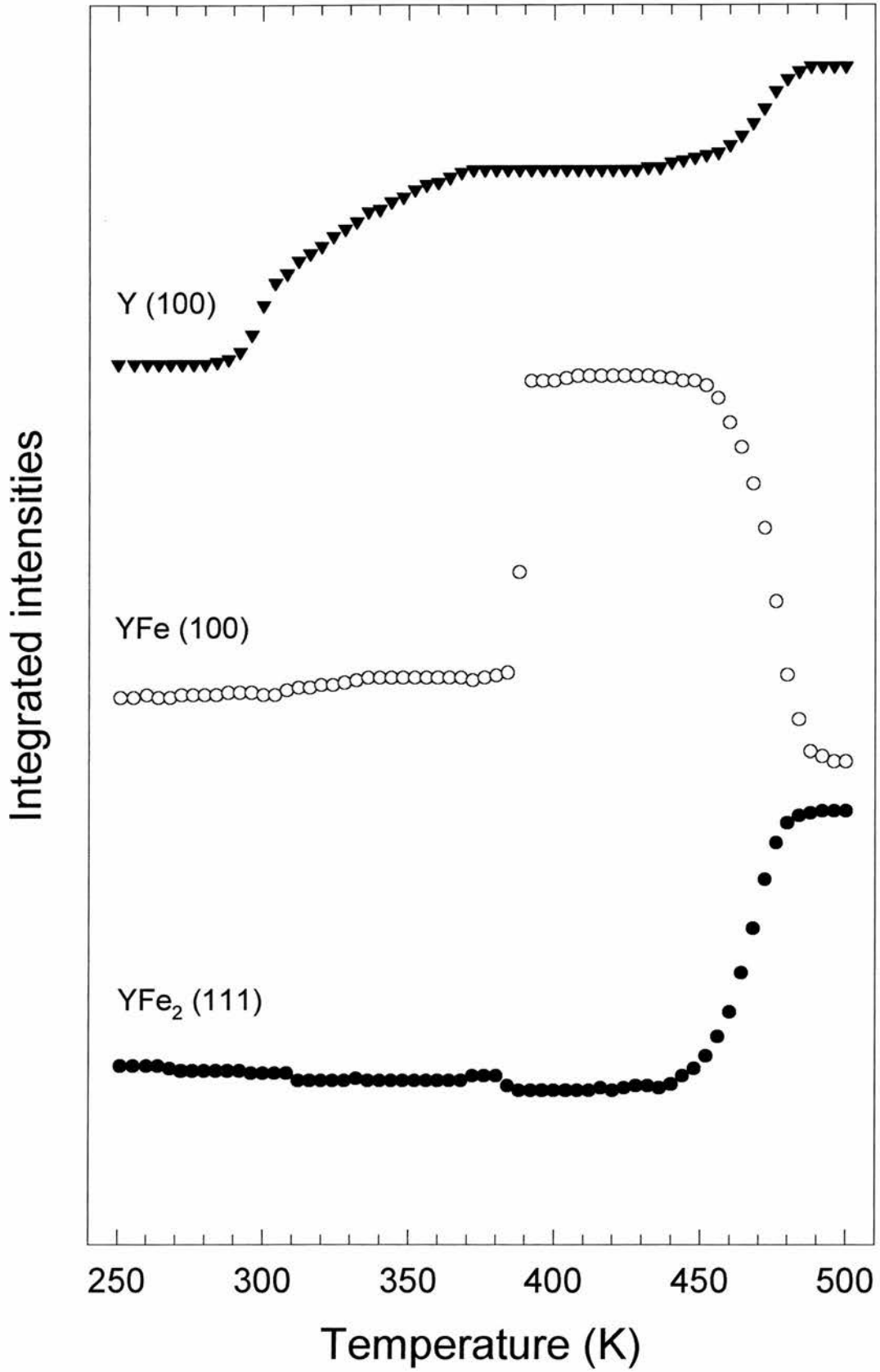


Figure V- 10 : evolution of the Y (100), 'YFe' (100) and YFe<sub>2</sub> (111) peaks as the temperature is ramped from 250 to 500°C at 40°C/hour.



approximately 300° C and their intensities rise steadily as the temperature increases to 375° C. However, in the narrow temperature range between 375° C and 390° C, a sudden crystallisation of the sample. This process is accompanied by the sudden disappearance of the low angle scattering and the appearance of the intermediate Y–Fe phase. The intensity of the Y Bragg peaks remains more or less constant while this new phase exists. When this phase no longer exists (at about 450°C), there is a third and final increase in intensity of the Y (100) peak as the YFe<sub>2</sub> phase is formed in coexistence with the pure Y phase.

As might be expected, the Y Bragg peaks sharpen considerably during the annealing process, with a dramatic decrease in the FWHM occurring at ~375° C, the temperature at which the whole sample crystallises. The dimension of the Y grains can be deduced from the FWHM of the Bragg peaks by using the well-known the Scherrer formula<sup>12</sup> :

$$\delta = \frac{0.9\lambda}{B \cos \theta} \quad \text{Eq. V- 1}$$

In this expression,  $\delta$  is particle size in Å,  $\lambda$  is the neutron wavelength (2.4 Å in this experiment),  $\theta$  is half the scattering angle and B is related to the experimental FWHM of a Bragg peak in radians. Indeed, in order to relate  $\delta$  to the 'real' size of the Y grains, it is necessary to evaluate the resolution of the instrument. This is generally achieved by collecting a diffraction pattern from a standard. The standard chosen for this experiment was an Yttrium-Iron garnet (YIG, Y<sub>3</sub>Fe<sub>5</sub>O<sub>12</sub>, space group : Ia3d, lattice constants : a=b=c=12.38 Å, atomic positions : Fe(0,0,0) and (0.375,0,0.25), Y(0.125,0,0.25) and O(0,0,0.15) ) provided by the local contacts on D20. The 'true' FWHM of a Bragg peak B is then simply related to the FWHM B<sub>YIG</sub> obtained from the YIG run and to the experimental FWHM of a Bragg peak from the sample, B<sub>S</sub> , by the deconvolution expression :

$$B^2 = B_S^2 - B_{YIG}^2 \quad \text{Eq. V- 2}$$



The size of the Y grains determined from *Eq. V-1 and Eq. V-2* is shown as a function of temperature in *Figure V-11* which clearly shows the evolution of the Y phase. At first, Y grains of  $\sim 170$  Å appear at  $\sim 310^\circ$  C, and remain to  $\sim 350^\circ$  C. Above  $350^\circ$  C, these grains grow steadily, reaching  $\sim 800$  Å at  $450^\circ$  C. At higher temperatures, grain growth is extremely rapid and by  $\sim 475^\circ$  C the determination of the grain size is limited by the resolution of the instrument.

### *V.3.b.3. Intermediate phase*

At  $390^\circ$  C, new Bragg peaks, which cannot be identified with any of the known YFe alloys (or with elemental Y or Fe), appear and then disappear at  $450^\circ$  C when the YFe<sub>2</sub> phase is formed. From the intensity of the pure Y peaks and the intensity of the Y and YFe<sub>2</sub> peaks in the final phase and from the composition of the precursor material (Y<sub>67</sub>Fe<sub>33</sub>), the chemical composition of the intermediate phase seems to be close to stoichiometric YFe. It is worthwhile noting that such a phase is entirely absent from all published phase diagrams of the well known Y–Fe system, but seems to be related to the phase observed by Croat<sup>10</sup>. Careful examination of *Figures V-9 and V-10* shows that this new phase is stable only over a range of about  $40^\circ$ C which could well explain the absence of this intermediate phase from the phase diagrams. I have produced several crystalline ingots of YFe by argon arc melting Y and Fe and subsequently annealed the ingots at several different temperatures but unfortunately, the result was a two phase sample : a mixture of YFe<sub>2</sub> and Y as suggested from the phase diagram, *Figure V-5*. Clearly, the formation of the YFe phase requires the intimate atomic mixing of constituents afforded by the amorphous precursor in order to form. However, it is possible to stabilise this phase at room temperature, where it coexists with elemental Y, by rapidly cooling the sample from  $375^\circ$  C. The best way to make sure that the phases existing at room temperatures are the same as those observed at high temperature, is to carry out the crystallisation and subsequent rapid cooling in the neutron beam, and to collect diffraction patterns during the cooling process.

*Figure V-12* shows the high resolution neutron diffraction pattern collected on D2B at ambient temperature from a sample of crystalline Y and Y–Fe. Confirmation that the phase has not transformed during the quenching process is obtained by comparing the data collected on D2B to the diffraction pattern collected at  $420^\circ$  C on D20. Therefore, any structural information obtained from our room temperature, high resolution data relates to the phase which exists at high temperatures. The solid black

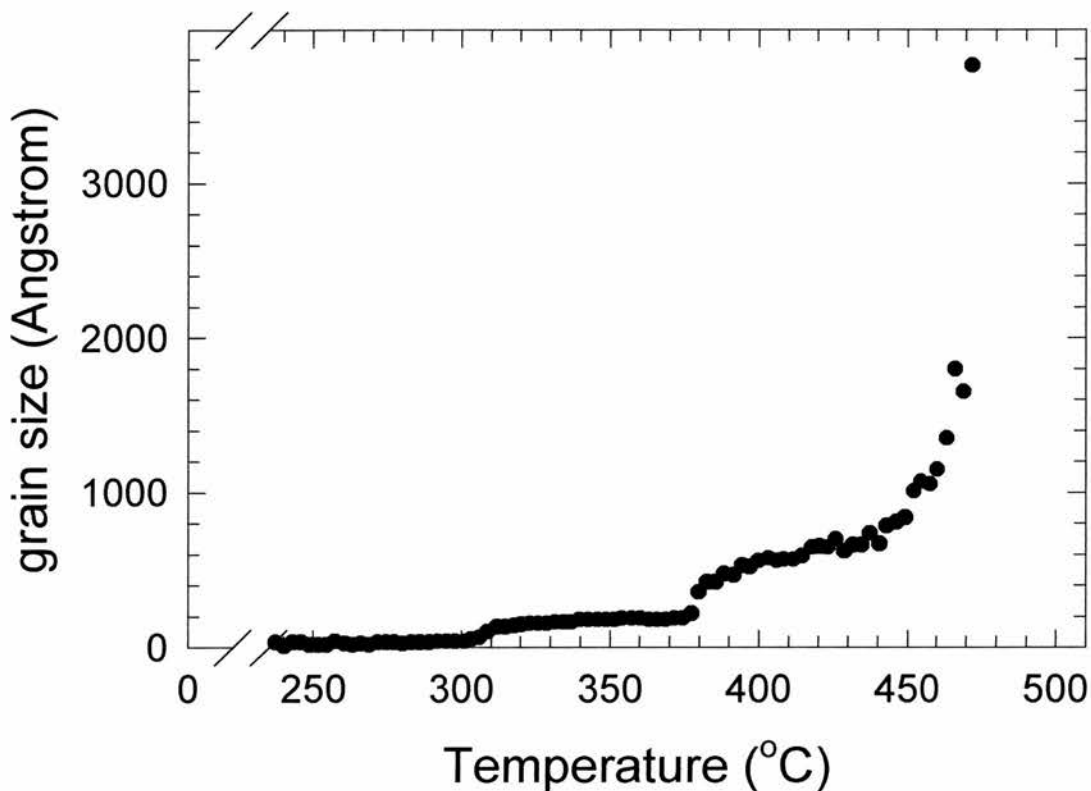


Figure V- 11 : Y grain size as a function of furnace temperature, determined from the (100) peak as described by the Scherrer formula (requires YIG standard)

Phase 1 : elemental Y (Rietveld refinement)	Phase 2 : Y-Fe (Profile matching)
Space group : P 6 <sub>3</sub> /m m c	Space group : P 6 <sub>3</sub> /m m c
a = 3.6417 (2) Å	a = 12.8903 (7) Å
c = 5.7383 (5) Å	c = 11.7015 (9) Å
α = β = 90° γ=120°	α = β = 90° γ=120°
V = 65.9037 (6) Å <sup>3</sup>	V = 1683.781 (1) Å <sup>3</sup>
Bragg R-factor 3.95	Bragg R-factor = 0.291
R <sub>f</sub> factor = 2.03	R <sub>f</sub> factor = 0.264

Table V- 1 : Results of a two-phase refinement of the diffraction pattern shown in Figure V- 12. The parameters for the Y phase were determined using a full Rietveld refinement of the data. Those for the YFe phase were determined using the pattern matching option in FullProf (atomic positions are not refined).

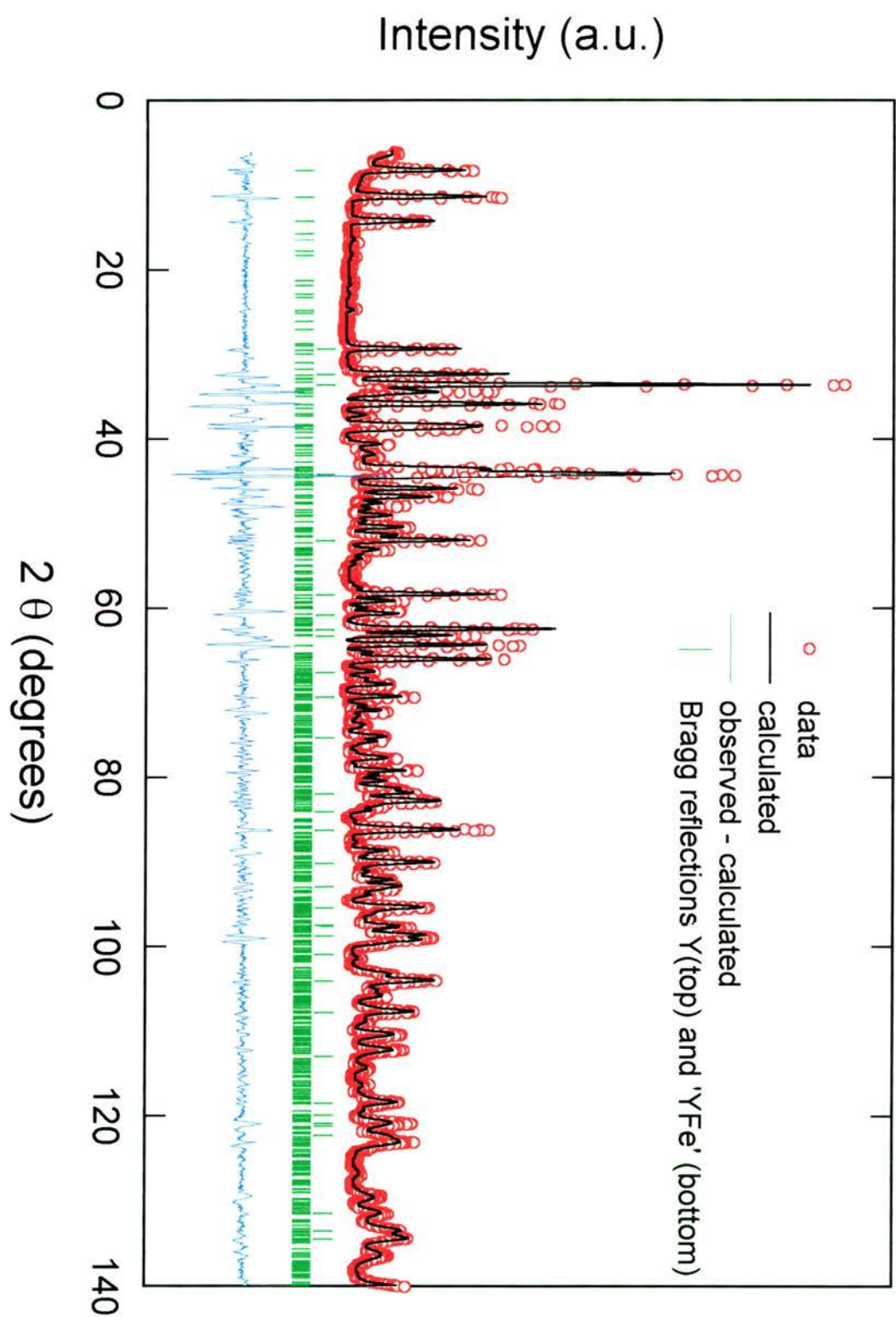


Figure V- 12 : Two phases Rietveld refinement for the Y and the intermediate 'YFe' phase. (D2B data).

line in *Figure V- 12* shows the result of a two-phase Rietveld refinement using FullProf<sup>11</sup>. An *ab initio* description of the YFe phase is obtained using the pattern matching option and the crystal structure of the Y phase is obtained from a full Rietveld refinement of the spectrum. From this *ab initio* structural method, the YFe phase crystallises with the hexagonal space group  $P 6_3/m m c$  with an unusually large cell dimensions of  $a = 12.8893(7) \text{ \AA}$  and  $c = 11.7006(9) \text{ \AA}$ , giving a cell volume of  $1683.781(1) \text{ \AA}^3$ . The large values for the unit cell are not surprising as the diffraction pattern associated with the intermediate phase shows three peaks at fairly low angles (between  $12^\circ$  and  $22^\circ$ ). The best fit of the Y spectrum is found using a hexagonal cell, space group  $P 6_3/m m c$ , with the Y atoms sitting on the  $(1/3, 2/3, 1/4)$  position. The details of the cell parameters can be found in *Table V- 1* and are in good agreement with the reported values<sup>13</sup> of  $a = 3.647 \text{ \AA}$  and  $c = 5.728 \text{ \AA}$ . As yet, the exact atomic positions of the Y and Fe atoms in this structure have not been determined, although it is clear that a cell of this volume will contain a large number of atoms. I have tried to use the simulated annealing option of Fullprof to guess the atomic positions but, due to the large number of atoms, the results are not too convincing, although they are in qualitative agreement with the obtained Patterson pattern. However, by examining the Fe–Fe and Y–Fe distances in other Y–Fe phases ( $\sim 2.6 \text{ \AA}$  and  $\sim 3.5 \text{ \AA}$  respectively) and assuming a density of  $7 \text{ g.cm}^{-3}$  (density measurements have been attempted on this material but the accuracy was quite poor due to the fact that the ribbons have got a large surface/volume ratio and do not wet very well with the solvent used for the measurement) a structure containing 90–100 atoms/unit cell can be proposed.

By applying the Scherrer equation (*Eq. V- 1*) to the Y–Fe reflections between  $2\theta = 12^\circ$  and  $22^\circ$  the grain size of the new Y-Fe phase can be determined. As soon as the Y–Fe phase crystallises, grains of  $250 \pm 11 \text{ \AA}$  are formed immediately. These grains do not grow as the temperature increases, but their size remains constant until  $460^\circ \text{ C}$ , when the phase disappears.

#### V.3.b.4. Final phases : Y and YFe<sub>2</sub>

At about 445° C, the Bragg peaks associated with the intermediate phase begin to decrease in intensity (see *Figure V- 10*), and peaks associated with the final crystallisation product, the well-known C15 Laves phase YFe<sub>2</sub>, begin to appear. This C15 phase co-exists with elemental Y at all temperatures. The diffraction pattern collected on D20 from the final material at 490° C is shown in *Figure V- 13*. Apart from a small peak at  $2\theta \sim 59^\circ$ , no Bragg peaks other than those associated with either Y or YFe<sub>2</sub> are observed. The best two-phase Rietveld refinement of the data is obtained with one phase of elemental Y, as described in the previous paragraph, and a second phase of cubic YFe<sub>2</sub>, space group Fd3m with  $a = 7.416(3) \text{ \AA}$  (the atomic positions are : Y(0,0,0) and Fe(0.625,0.625,0.625) ). The results of the Rietveld refinement are shown as the solid black line in *Figure V- 13* and the accompanying parameters are listed in *Table V- 2*.

The understanding of the kinetics of a reaction is absolutely crucial for the design of new magnetic materials. Indeed, if the kinetics are known, one can in principle stop the crystallisation at a chosen temperature to select a certain grain size and thereby effectively tailor the magnetic properties for a specific application (for example, one could obtain monodomain magnetic particles embedded in a non magnetic matrix and tune the grain size to match a preferred transition temperature). In order to study the kinetics of this crystallisation process, a sample of about 3g of  $\alpha\text{-Y}_{67}\text{Fe}_{33}$  was placed in a vanadium can and loaded into a furnace that was heated as quickly as possible to 450°C. The temperature was then kept constant and neutron diffraction patterns were collected every four minutes. The intensity of the (111) YFe<sub>2</sub> peak has been integrated over a narrow angular range around its  $2\theta$  position and plotted as a function of time on *Figure V- 14*. The most widely used analysis of growth kinetics is the Kolmogorov-Johnson-Mehl-Avrami (KJMA) approach<sup>14,15,16</sup>. The KJMA theory is based on a phenomenological and stochastic kinetic model of a first order phase transformation. The model assumes that an untransformed specimen at time 0, evolves by following a given stochastic rate of creation of point nuclei that are randomly distributed in the remaining untransformed space. A grain is assumed to grow radially at a given constant rate from the moment of creation of each nucleus until impingement with other growing grains when it ceases to grow.

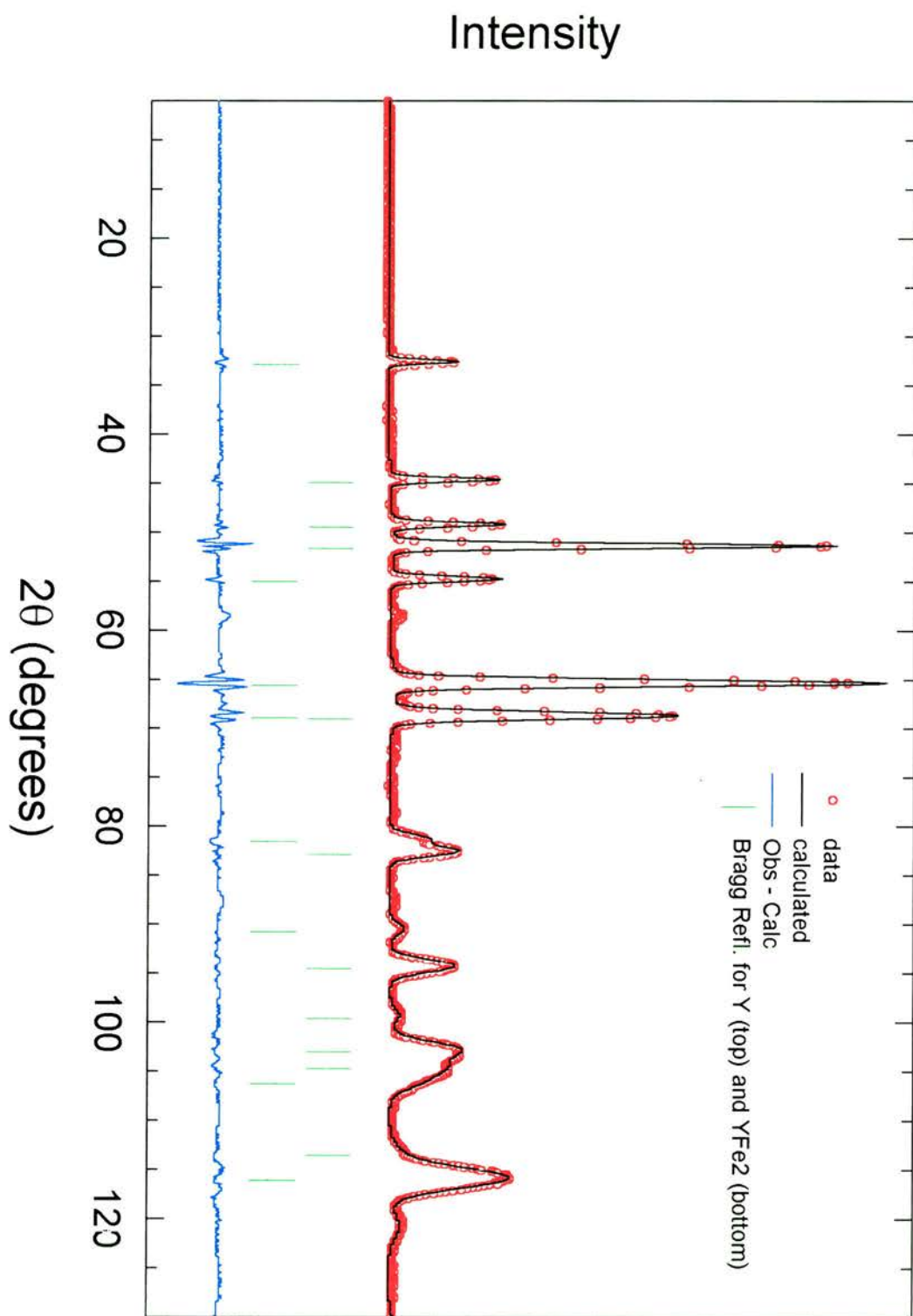


Figure V- 13 : Two phases Rietveld refinement for the final phases Y and YFe<sub>2</sub> (pattern collected on D20 for  $T > 450^\circ\text{C}$ ).



Phase 1 : elemental Y (Rietveld refinement)	Phase 2 : YFe <sub>2</sub> (Rietveld refinement)
Space group : P 6 <sub>3</sub> /m m c	Space group : F d 3 m
a = 3.659 (1) Å	a = 7.416 (3) Å
c = 5.791 (4) Å	
$\alpha = \beta = 90^\circ$ $\gamma = 120^\circ$	$\alpha = \beta = \gamma = 90^\circ$
V = 67.14 (4) Å <sup>3</sup>	V = 407.858 (2) Å <sup>3</sup>
Bragg R-factor 2.50	Bragg R-factor = 3.99
R <sub>f</sub> factor = 2.37	R <sub>f</sub> factor = 2.32

Table V- 2 : Results of a two-phase refinement of the diffraction pattern shown in Figure V- 13. The parameters for the two phases (Y and YFe<sub>2</sub>) were determined using a full Rietveld refinement of the data collected on D20.

Exponent n	Type of growth
n = 1	homogeneous
1 ≤ n < 2	dendritic (one dimensional)
2 ≤ n < 3	plate-like (two dimensional)
3 ≤ n < 4	three dimensional

Table V- 3 : Relationship between the exponent of the KJMA equation and the type of growth process.

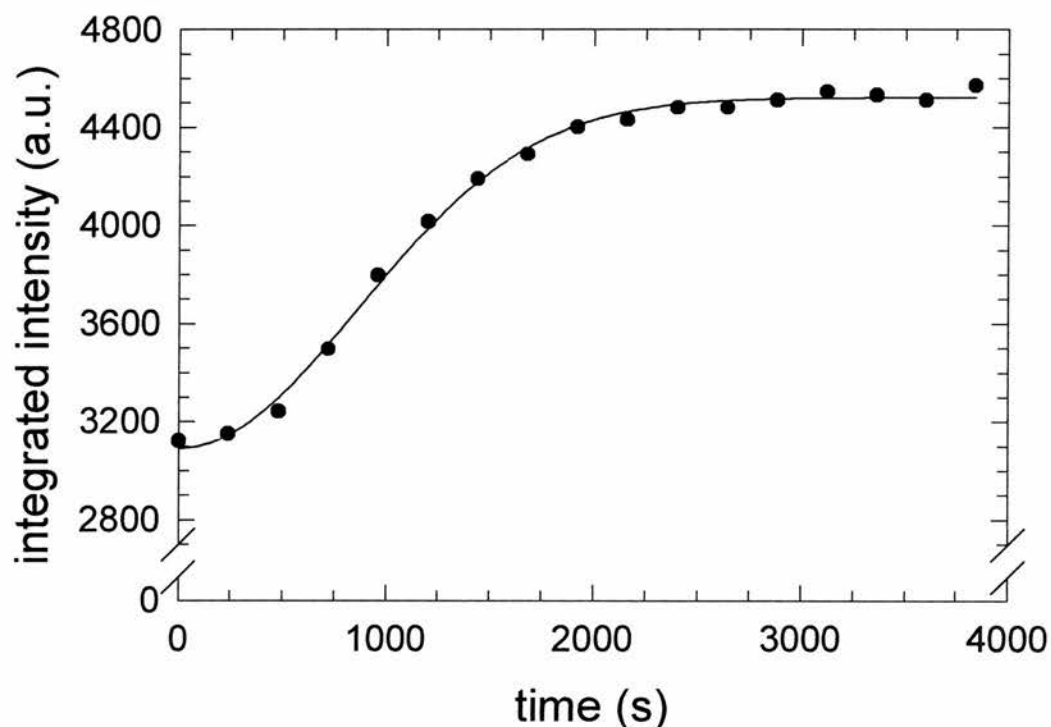


Figure V- 14 : Intensity of the (111) YFe<sub>2</sub> Bragg peak as a function of time. The line is a fit to the KJMA equation as described in the text.

At time  $t$ , the radius of a grain that nucleated at time  $\tau$  is :

$$R(t, \tau) = \int_{\tau}^t V(t') dt' \quad \text{Eq. V- 3}$$

Assuming nucleation has occurred in the space-time  $(\mathbf{x}, t)$  - where  $\mathbf{x}=(x,y,z)$  in 3 dimensions -, we can define  $\Omega_c$  the set of all points and earlier times  $(\mathbf{x}', \tau)$  that caused this transformation. If the radius  $R$  is greater than the distance between  $\mathbf{x}$  and  $\mathbf{x}'$  the points  $\mathbf{x}$  transform before the time  $t$ . In other words,  $\Omega_c$  is a time-cone where nuclei outside it never grow into it, whose equation is :

$$|R(t, \tau)|^2 + |\mathbf{x}' - \mathbf{x}|^2 \geq 0 \quad \text{Eq. V- 4}$$

It is then possible to introduce the geometry of the growth, by calculating the time arrival  $t(\mathbf{x})$  of a moving surface at point  $\mathbf{x}$  for each specific geometry.

The number of nuclei  $\langle N_c \rangle$  in the time cone is simply given by the integration of the nucleation rate over  $\Omega_c$ . Assuming a constant nucleation rate  $\alpha$  gives :

$$N_c = \frac{\alpha B t}{d + 1} \quad \text{Eq V- 5}$$

where  $B=2Vt$ ,  $\pi V^2 t^2$  and  $4\pi V^3 t^3/3$  for 1, 2 and 3 dimensional growth respectively. If the nucleation events are stochastically independent, Poisson statistics can be applied and the probability that  $\mathbf{x}$  is untransformed at time  $t$  is given by :

$$P(t) = e^{-\langle N_c \rangle} \quad \text{Eq. V- 6}$$

Further refinements to the theory include its generalisation to finite specimens, and anisotropic nucleation rate for which the well-known KJMA equation is obtained. The phase fraction of the crystallised phase is :

$$F = F_0 \left( 1 - e^{-(t/\tau_c)^n} \right) \quad \text{Eq. V- 7}$$

where  $\tau_c$  is a time constant characteristic of the phase transformation under study and  $n$  is an exponent related to the dimensionality of the growth of the nucleated region as described in *Table V- 3*. The integrated intensity of the (111)  $\text{YFe}_2$  peak in *Figure V- 14* has been fitted to *Eq. V- 7* (plus a background) and the resulting fit is plotted as a

line. The extracted exponent  $n$  is  $2.0 \pm 0.15$  and the time constant is  $1200 \pm 25$  s. According to *Table V- 3*, a value of 2 is indicative of a 2D-like growth which is perhaps not too surprising when considering that the samples under study are ribbons. Indeed, the quenching process might induce some preferential strain along the longest direction of the ribbons. This is corroborated by a Small Angle Neutron Scattering experiment we performed on the LOQ instrument at ISIS to study the particle size and particle size distribution of the Y nanocrystallites during the initial crystallisation in the Y-Fe system. *Figure V- 15* shows the increase in the SANS for amorphous  $Y_{67}Fe_{33}$  at  $295^\circ C$  (where only Y is growing) for several annealing times. SANS arises from fluctuations in the scattering length density and provides structural and magnetic information on a scale of a few Å to  $5000\text{Å}$ . These fluctuations can originate from defects such as voids, from different combination of atoms (e.g. presence of different phases as in our case) or from a difference in the magnetic scattering length. The first step in analysing SANS data is to use the well-known Guinier<sup>17</sup> plot ( $\log(\text{SANS})$  vs  $q^2$ , where  $q$  is the scattering vector). In the YFe sample under study, such a plot does not give the expected straight line over a wide  $q$ -range. However, the Guinier approximation assumes a low inhomogeneity concentration and is only valid in the limited  $q$ -range up to  $qR_g \sim 1.5$  where  $R_g$  is the radius of gyration of the inhomogeneities (the shape of the inhomogeneities is ignored). Another well used SANS plot is based on the Porod approximation<sup>18</sup>, valid for large  $qR_g$  values ( $>2.5$ ), where the cross-section falls off as  $1/q^4$  and the scattering is proportional to the surface of the inhomogeneities (whose shapes are again ignored). More complete analysis using the program FISH<sup>19</sup> has been carried out and reveals that the resulting crystallites are discs of radii  $300\text{Å}$  and thickness  $30\text{Å}$  (*Figure V- 16*). It is not unreasonable to suggest that this shape can be the result of the crystallite morphology (Y is hcp and therefore forms platelets). The influence of sample preparation on the final nanocrystalline material has been observed in amorphous Fe-Cu-Nb-Si-B (due to its excellent soft-magnetic properties<sup>20</sup>, this alloy has been studied in great detail) prepared by planar flow casting<sup>21</sup>. By preparing several alloys for which the quenching rate during the flow casting procedure has been varied, and subsequently annealing the samples, the authors of ref. 21 showed that the beginning of the nanocrystallisation is deeply affected by the initial degree of disorder : the samples prepared with a slower quench rate crystallise earlier. They associated this effect with the presence of very small crystallites in the slower quench rate samples which act as nucleation centres.

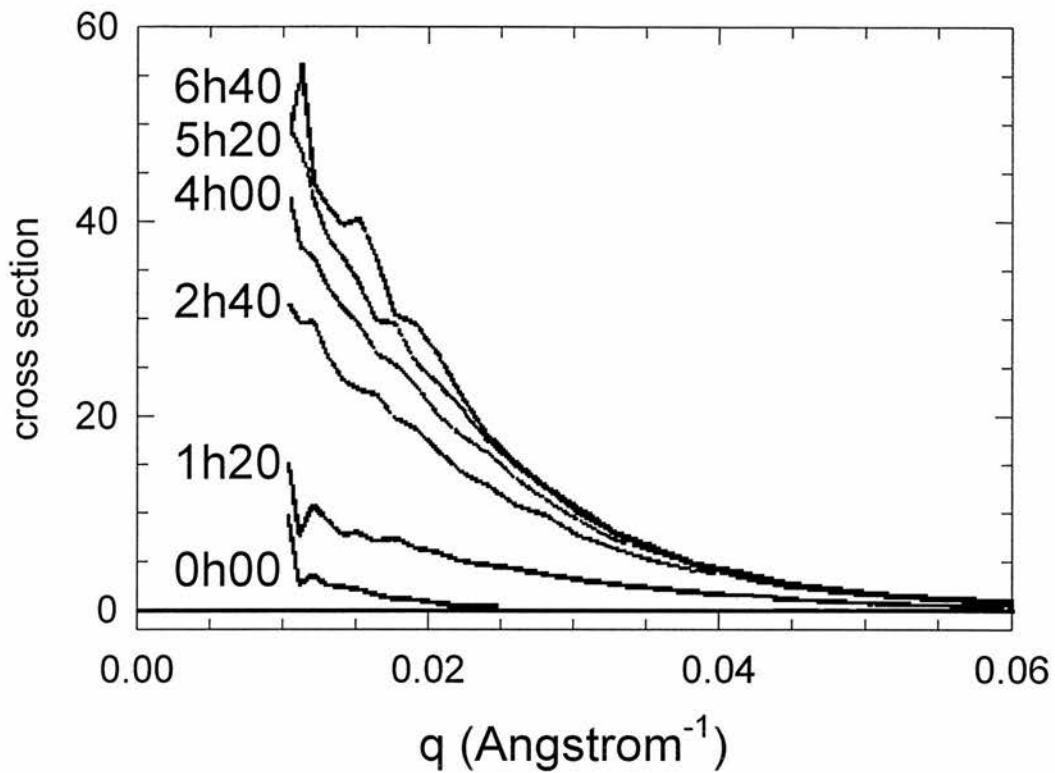


Figure V- 15 : Small Angle Neutron Scattering for  $\alpha$ - $Y_{67}Fe_{33}$  held at  $295^{\circ}C$  for different times.

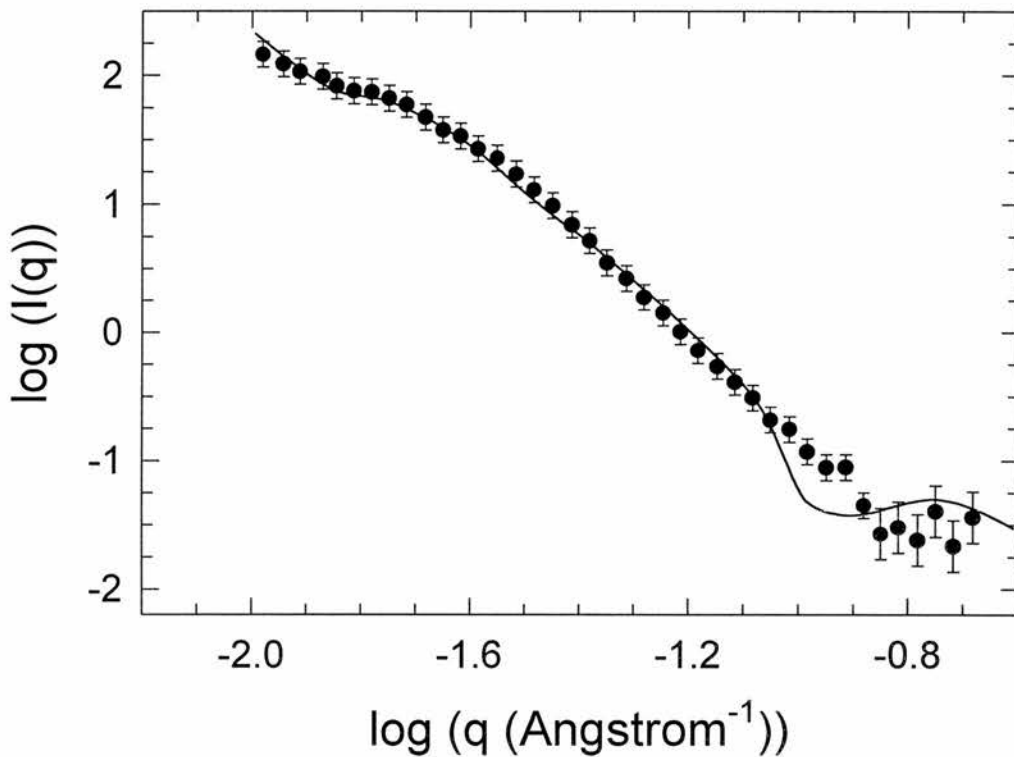


Figure V- 16 : log-log plot of the SANS data for an annealing of 6h40 at  $295^{\circ}C$ . The line is a fit to a model with disk-shaped crystallites using the FISH program, as described in the text, The resulting parameters are :  $300\text{\AA}$  for the radii and  $30\text{\AA}$  for the thickness.

### V.3.c. Magnetic study of the new intermetallic Y-Fe alloy

In the previous paragraph, it has been shown that an Y-Fe compound with entirely new structure can be produced by careful control of the crystallisation processes of an amorphous precursor. In the Y-Fe crystalline phase diagram, several phases are reported to be magnetic. The most-iron rich magnetic YFe phase is the body-centered tetragonal  $YFe_{12}$ . Interestingly, this phase does not exist as a pure compound but is stabilised, in an iron rich form, by the addition of other transition metals such as Cr, Mo, Ti or V<sup>22</sup> whereas the previously known compounds  $YFe_{12-x}Al_x$  and  $YFe_{12-x}Mn_x$  can only exist at a low Fe concentrations<sup>23</sup> ( $x > 0.4$ ). These TM-doped compounds exhibit ferro-, ferri- or antiferro-magnetic behaviour. The next alloy obtained by increasing the Y content is the rhombohedral  $Y_2Fe_{17}$ , which exhibits a ferromagnetic transition at about 300 K<sup>24</sup>. By reducing the Fe concentration even further, the next stable alloy is the  $YFe_3$  which possesses a Curie temperature of 580K<sup>25</sup>. Finally, the most Y-rich compound studied, before the Y-Fe phase obtained by the annealing of amorphous precursor, is the Laves phase  $YFe_2$  with a ferromagnetic transition in the bulk compound at 570 K<sup>25</sup>.

The magnetic properties of the new Y-Fe phase obtained with the procedure described in the previous paragraphs have been studied by a combination of magnetisation using a Vibrating Sample Magnetometer (VSM), AC susceptibility, Mössbauer, Muon Spin Relaxation ( $\mu$ SR) and Neutron Scattering experiments.

#### *V.3.c.1. DC and AC susceptibility measurements*

For the VSM and AC susceptibility measurements, two samples were analysed. One of the samples was quenched at the beginning of the formation of the new phase (sample 1) whereas the other one (sample 2) was heated slightly longer and therefore quenched towards the end of crystallisation of the intermediate phase. Neutron diffraction on both samples confirmed the presence of a mixture of Y and the intermediate phase without any sign of  $YFe_2$ . Nevertheless, it should be noted that neutron diffraction would not be sensitive to a few percent of an impurity phase such as  $YFe_2$ . *Figure V- 17* shows the magnetisation of sample 1 as measured in the 12T Oxford Instrument VSM described in chapter II. This measurement was carried out in an applied field of 100 Oe for two different magnetic histories : in one procedure, the sample was cooled in zero field and once the minimum temperature was attained, the 100 Oe field was applied (Zero Field Cooled or ZFC) and the magnetisation of the sample was

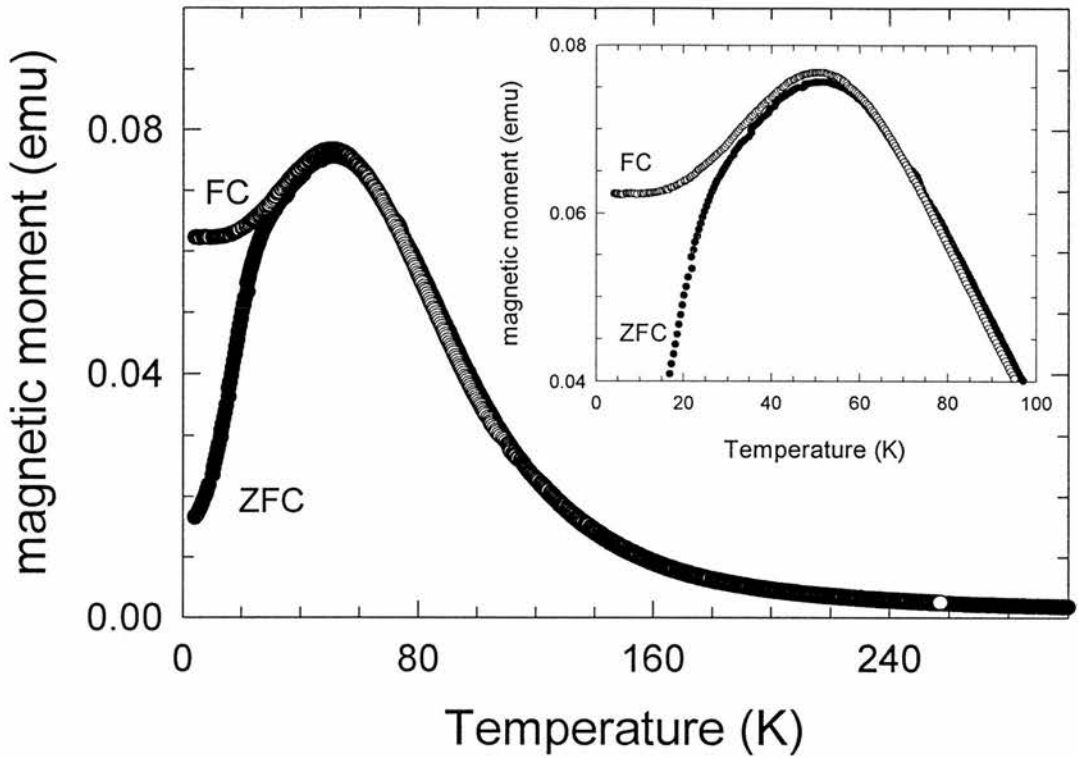


Figure V- 17 : Magnetic moment versus temperature for sample 1. The part near the peak is expanded in the insert for clarity.

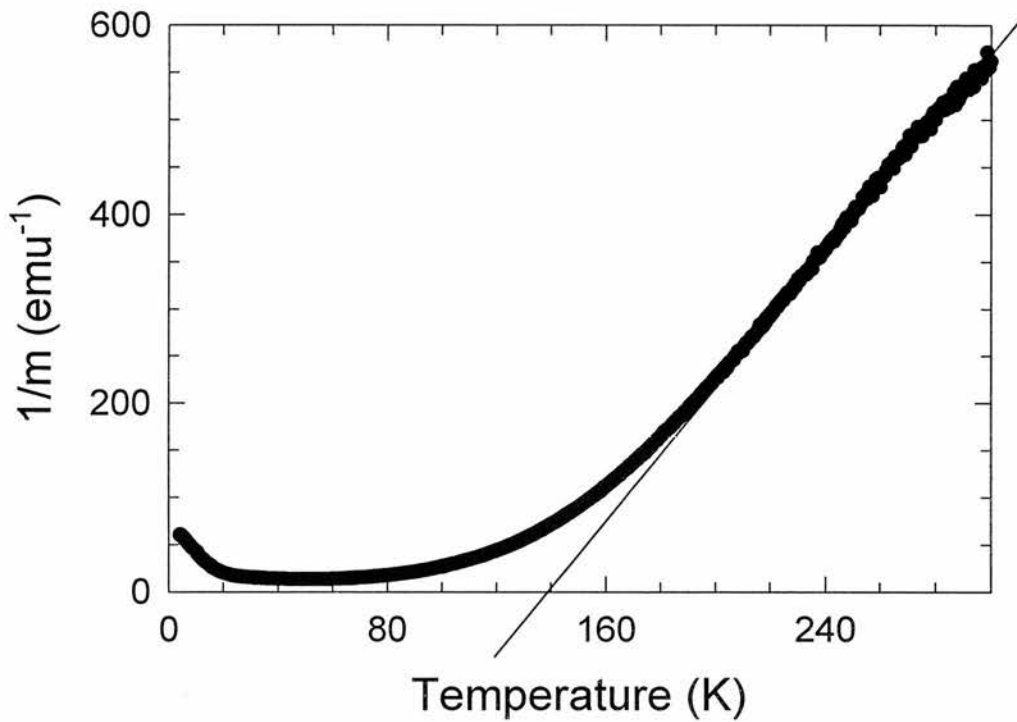


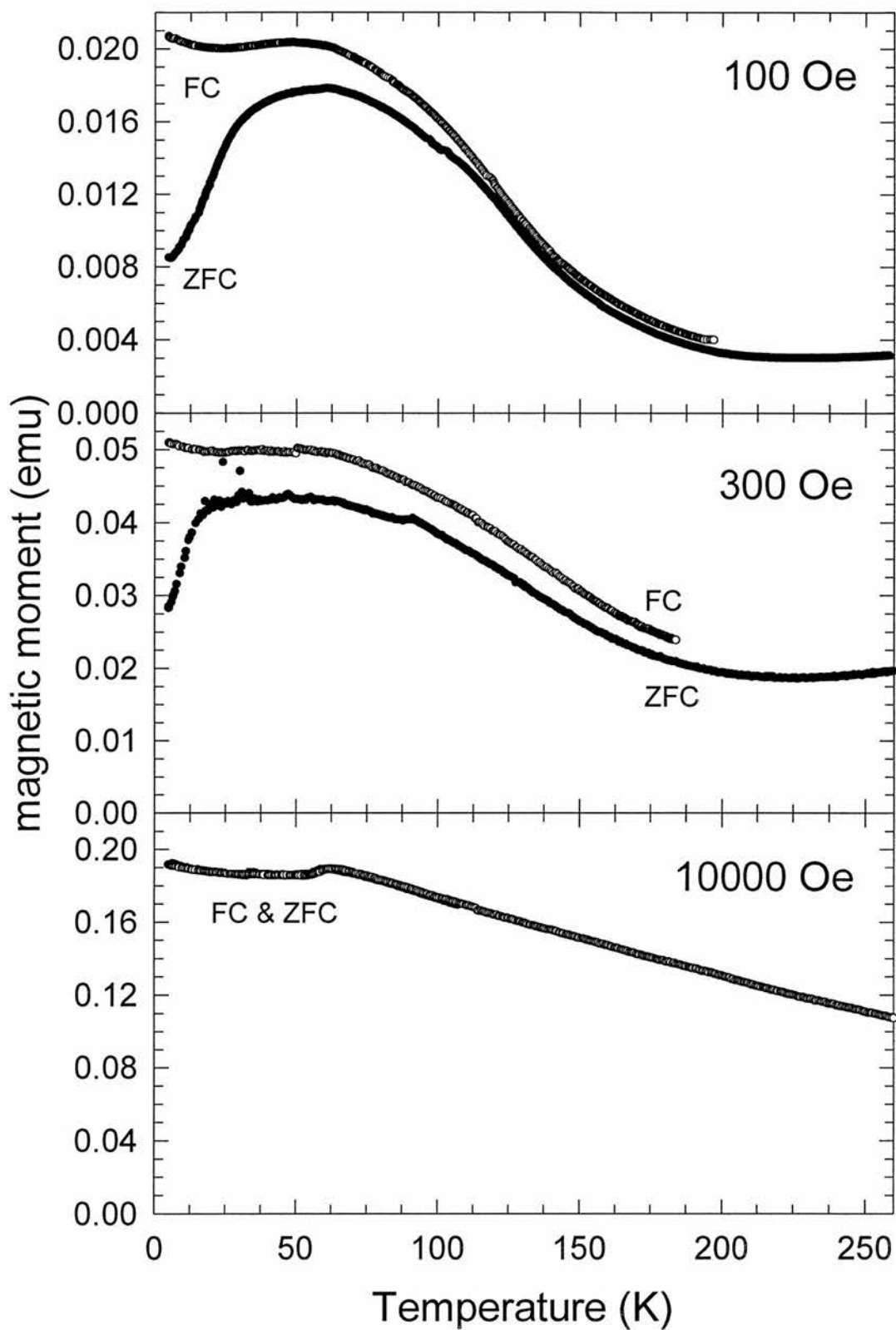
Figure V- 18 : inverse magnetic moment versus temperature for sample 1. The positive intercept on the temperature axis suggests ferromagnetic correlations.



recorded as the temperature was increased, whereas in the other case, the sample was cooled down in the 100 Oe applied field and the magnetisation was measured on warming (Field Cooled or FC). The most striking features of *Figure V- 17* are the presence of a broad peak at about 52 K and the joining of the two curves for temperatures higher than 60 K. This behaviour is generally associated with a spin glass or micromagnetic transition. However, as will be shown later, neutron diffraction of the intermediate phase below 60K reveals the presence of a Bragg peak thereby clearly suggesting that this intermediate phase exhibits long-range magnetic order. To help clarify this apparent disagreement, it is worth pointing out that the presence of a broad peak in the thermal variation of the magnetisation has been observed in other complicated magnetic systems such as the helimagnets<sup>26</sup>  $\text{TmMn}_6\text{Ge}_{6-x}\text{Ga}_x$ . Furthermore, the occurrence of a difference between the ZFC and FC curves can be simply explained by the presence of domains. Recently, differences between ZFC and FC in the complicated system  $\text{TbNi}_5$  system<sup>27</sup> where a helimagnetic behaviour is present between 16.5K and 23K and in the helimagnetic epitaxial Nd/Y superlattice have been reported<sup>28</sup>. The later authors, for comparison with the superlattice sample and a previous report of a susceptibility peak in a NdY alloy<sup>29</sup> at roughly the same temperature, have also produced an MBE grown  $\text{Nd}_{0.62}\text{Y}_{0.38}$  alloy but have unfortunately shown the ZFC curve only.

Plotting the inverse of the magnetisation of sample 1 against the temperature and extrapolating the linear high temperature Curie-like part to zero gives a positive value (about 140K), indicative of ferromagnetic interactions (see *Figure V- 18*). The small contribution of the Y (Pauli paramagnetic) has been neglected.

The thermal variation of the magnetisation obtained on sample 2, for fields comparable to the measuring field for sample 1, shows similar behaviour with the presence of a peak slightly above 50K and the splitting of the ZFC and FC curves (see *Figures V- 19*). As the measuring field is increased, it is interesting to note that this difference between ZFC and FC curves at temperature lower than 55 K no longer exists. In a simple magnetic system, this generally means that domains are present and do not respond equally to the magnetic field until a threshold field where they are all aligned. This would not be too surprising considering the sample preparation involved. However, the facts that the difference between the ZFC and the FC curves persists well above the peak temperature and that the magnetisation seems to increase very slightly above 200K for the two smallest fields is harder to explain. This could mean that some



Figures V- 19 : Magnetic moment versus temperature for sample 2 at three different measuring fields: 70, 300 and 10000 Oe. Note the disappearance of the difference between ZFC and FC curves for the highest field.

complicated magnetism remains above the peak temperature or that, although the sample is "neutron clean" (typically less than 5% impurity), some  $\text{YFe}_2$  particles are present. Due to this peculiar behaviour, the inverse magnetisation versus temperature plot are ill defined and therefore not included. Indeed, it is impossible to know what the magnetisation will do at higher temperatures (out of the VSM temperature range) and a proper subtraction of the contribution from the impurity phase (if present) is consequently out of reach.

In order to further investigate the magnetic properties of the intermediate  $\text{YFe}$  phase by DC magnetisation, hysteresis loops at fixed temperatures have also been collected. *Figures V- 20 and V- 23* show some of these loops for a few selected temperatures for sample 1 and sample 2 respectively. The first noticeable characteristic is the non-saturation of the high field magnetisation. This is generally associated with an itinerant magnetism. For the samples under consideration, this would however be biased as there is some Pauli paramagnetic Y definitely present in both samples which could well contribute to the major part of the slope of magnetisation versus applied field data at high fields. The presence of hysteretic behaviour in both samples can however be clearly assigned to the new  $\text{YFe}$  phase (see for instance *Figure V- 22*). The values of the remanence decrease smoothly between 0.06 emu at 5K and 0.025 emu at 60K; this is followed by a broad bump at 180 K before finally decreasing to reach a value of 0.02 emu at 300K. On the other hand, coercivity presents an ill-defined minimum at around 60K. Interestingly, this hysteretic behaviour persists, albeit decreasing in amplitude, at high temperatures for both samples. By closer examination of *Figures V- 20 and V- 23*, it is possible to notice that the slope at high magnetic applied fields is higher for temperatures just below 60K. By fitting the high field magnetisation to a straight line for all the isotherms on sample 1 and plotting the linear coefficient versus temperature, *Figure V- 21* is obtained and clearly shows a peak at 58 K.

A convenient way of presenting magnetic data is the so-called Arrott plot<sup>30</sup> where the magnetisation squared is plotted against the applied field divided by the magnetisation. This plot is particularly useful for weak itinerant ferromagnets (the archetype being <sup>31, 32</sup>  $\text{ZrZn}_2$ ) where it is used for determining the transition temperatures with precision. The basic idea behind such a plot is that, for a ferromagnet, the use of a generalised molecular field model leads to a component of the internal field  $H$  proportional to the third power of the magnetisation  $M$  (the leading term is linear). Thus a plot of  $M^2$  versus  $H/M$  for various temperatures consists of parallel isotherms and the

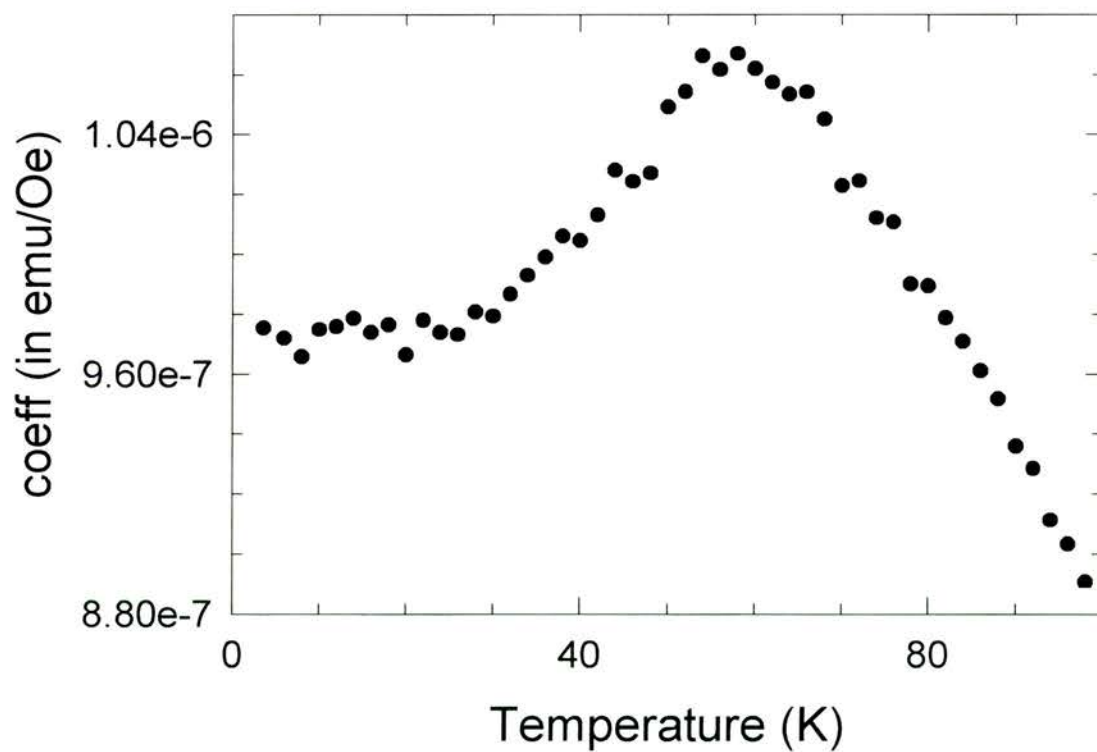
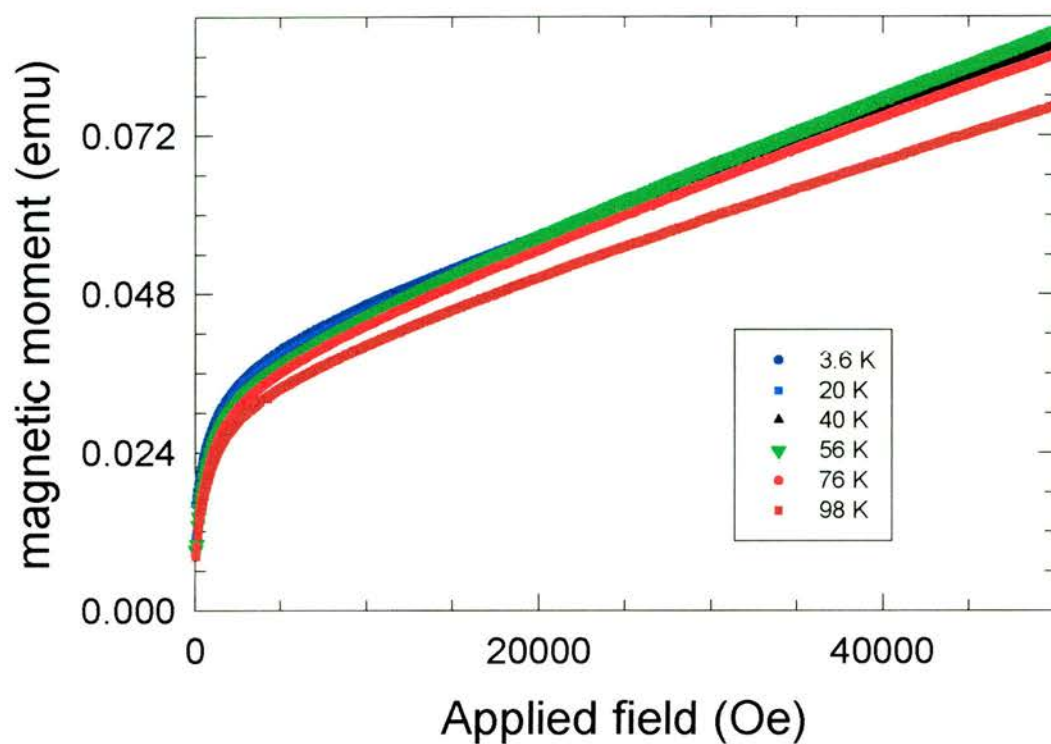


Figure V- 20 (top) : 5T magnetisation curves for sample 1.

Figure V- 21 (bottom) : linear coefficient of the high field magnetisation versus applied field curve.

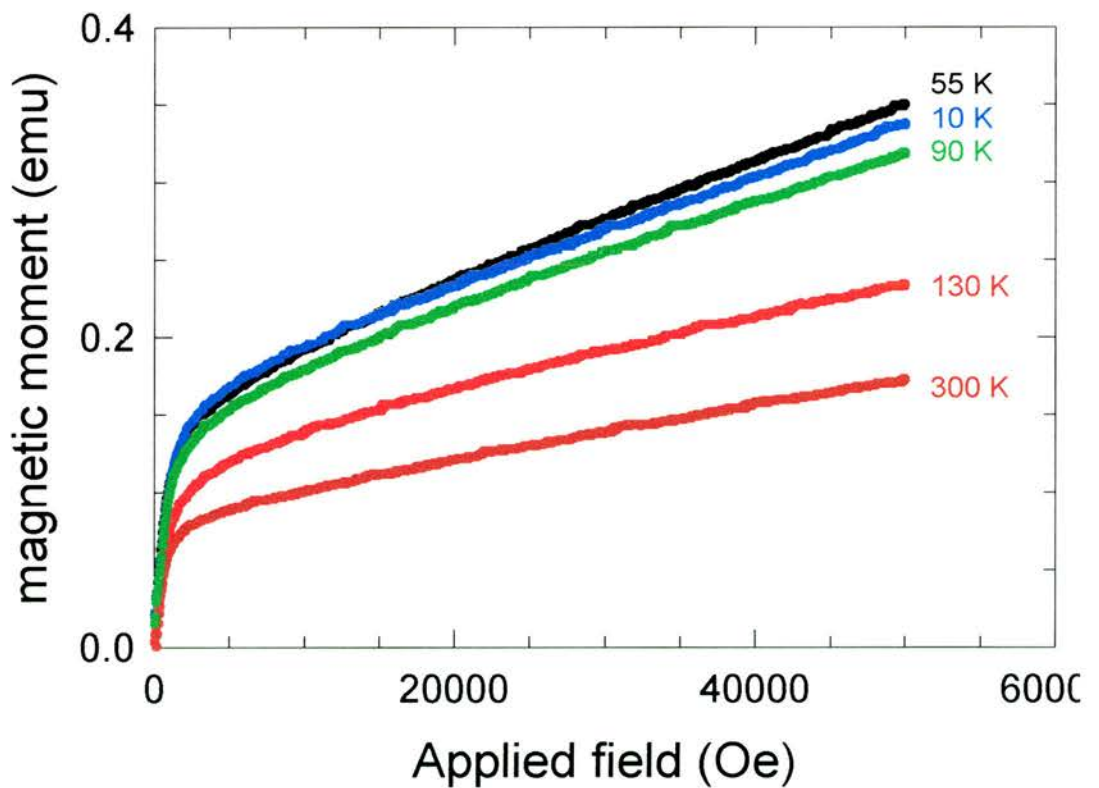
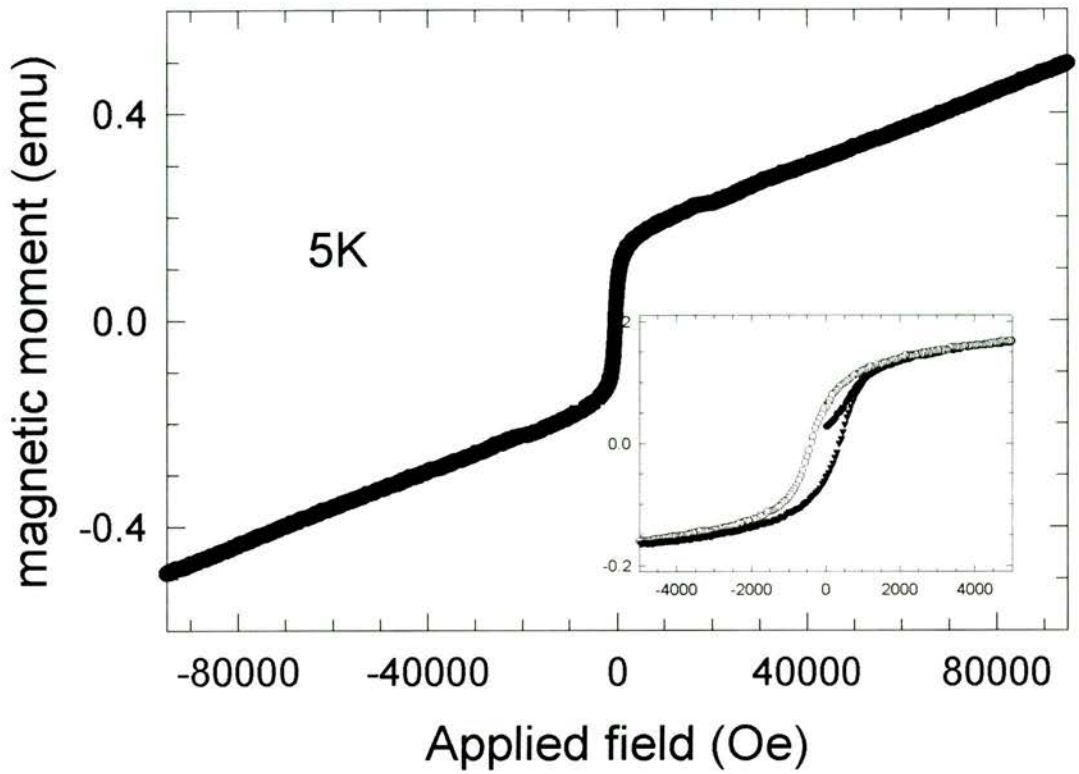


Figure V- 22 (top) : 10 T loop at 5 K for sample 2. The insert shows more clearly the hysteretic behaviour.

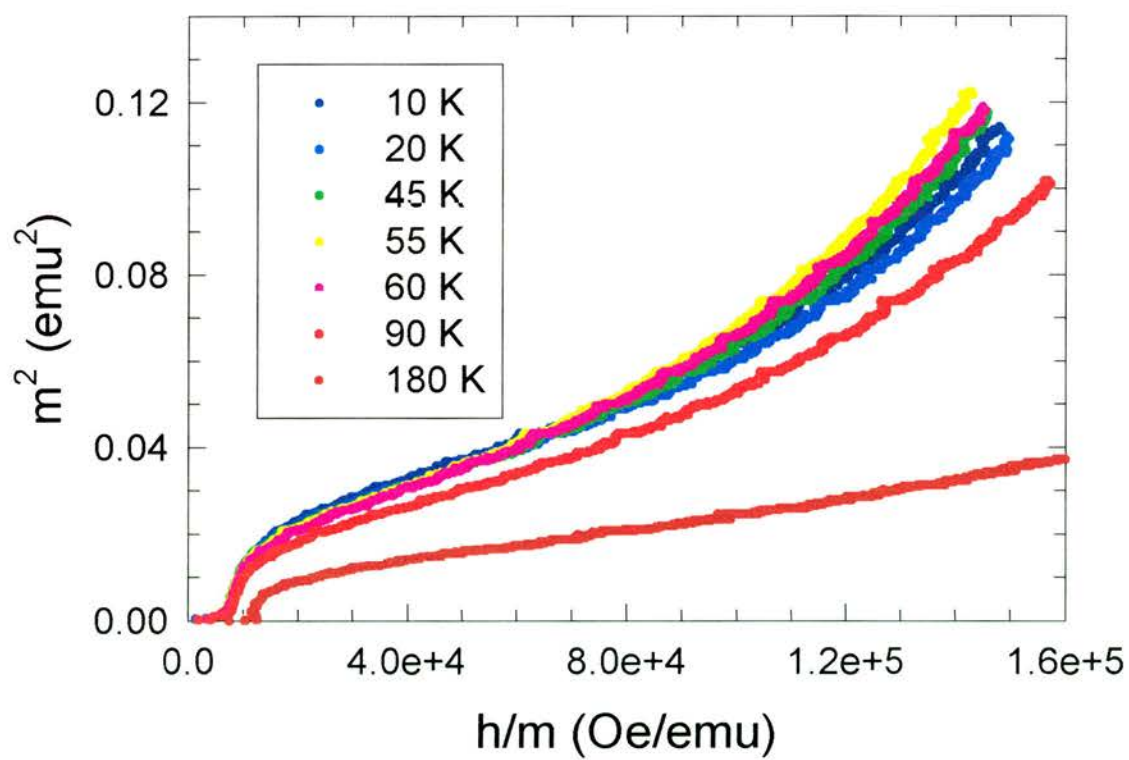
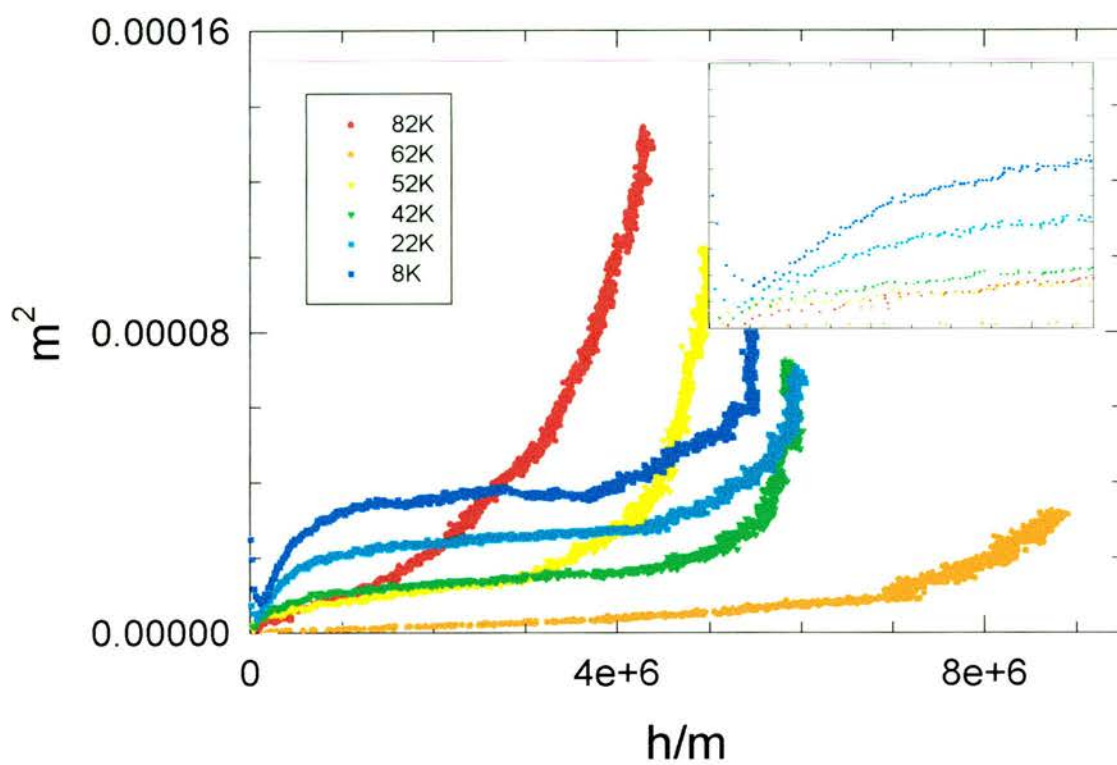
Figure V- 23 (bottom): 5 T loops for sample 2 at  $T = 10, 55, 90, 130$  and 300 K.



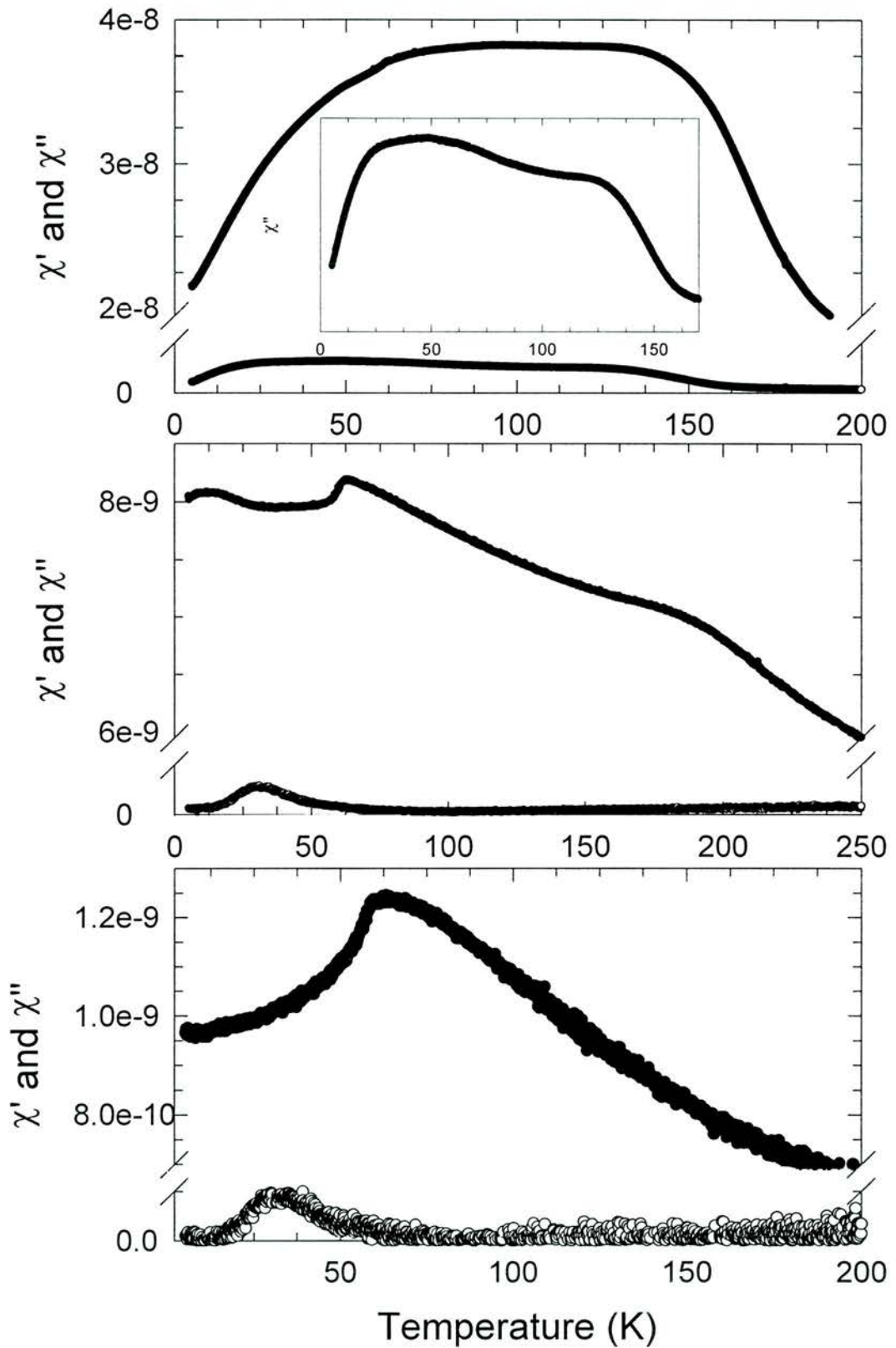
isotherm passing through the origin is the one corresponding to the transition (Curie) temperature. In contrast, for antiferromagnets, the isotherms never pass through the origin. The Arrott plots on sample 1 and sample 2 are presented on *Figures V- 24* and *V- 25* respectively. Both plots clearly show a cross-over between two regimes at around 55 K, consistent with the moment versus temperature data. There are however some differences between the plots. For sample 1, the isotherms below 50K present a positive initial curvature, whereas around 50K, this curvature is nearly zero (nearly a straight line) and above 60K, it becomes negative. This is not strikingly different from a ferromagnet. By zooming on the low H/M region, a strange dependence below T=20K is also seen : inside a narrow field range, the  $M^2$  vs H/M curve increases as the field is lowered. This could correspond to a reentrant phase. For sample 2, the isotherms all have positive curvature but the zero seems displaced. Nonetheless, the isotherm reaching the maximum value is still that corresponding to 55K.

The AC susceptibility has also been used to study the magnetic properties of the new intermediate phase. For both sample 1 (*Figures V- 26*) and sample 2 (*Figures V- 27*), the temperature dependence of the real part  $\chi'$  of the AC susceptibility, in a small AC field of 1 Oe and in zero applied DC field shows a peak at 90 K, very far from the value obtained by DC magnetisation. The peak is considerably broader in sample 1 than in sample 2. Furthermore, this peak is quite strongly frequency dependent (*Figures V- 27*) and therefore suggests a spin glass-like transition. A common feature in both samples is the presence of a broad shoulder at about 130K on the real part of the susceptibility. On the contrary, the temperature dependence of the imaginary component of the susceptibility is dependent on which sample has been measured : for sample 1,  $\chi''$  slowly increases with temperature, peaks just above 50K (see insert of *Figure V- 26*) then slowly decreases with temperature until 125K where it presents a little plateau and finally drops above 150 K whereas for sample 2 it only peaks at around 85K (*Figure V- 27*). The difference between sample 1 and sample 2 also include a shoulder on the real part of the susceptibility at about 55K for sample 1. These results are surprising in the light of the DC magnetisation experiments described above. However, AC susceptibility with different DC applied fields superimposed on the top of the smaller AC field has also been used for comparison and the results clearly show transition temperatures of the order of 55 - 60 K and a much smaller (or a complete disappearance for big enough fields) frequency dependence of the susceptibility whatever the sample. As the DC field

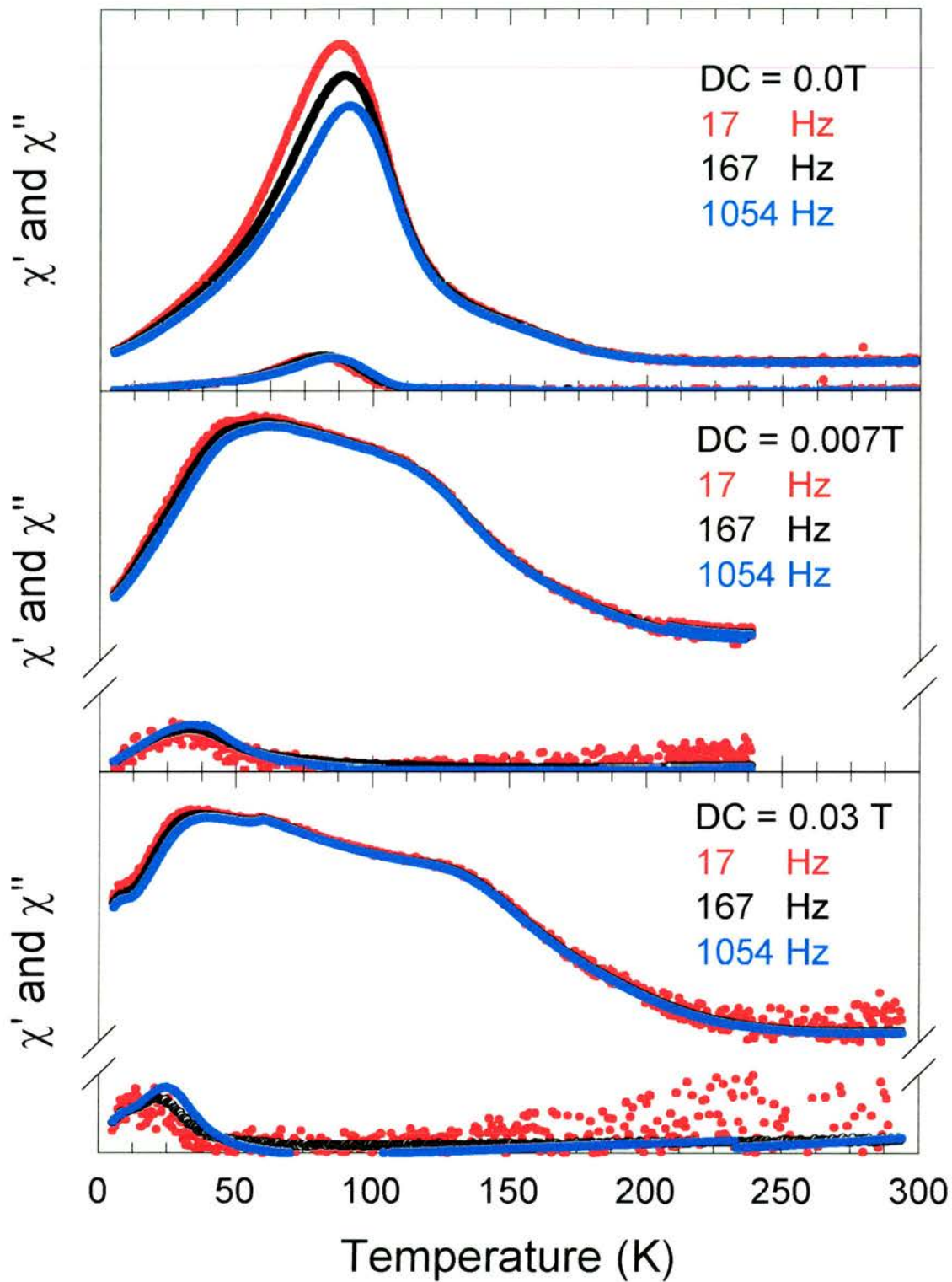




Figures V- 24 (top) and V- 25 (bottom) Arrott plots for sample 1 and sample 2.



Figures V- 26 : Real and imaginary components of the AC susceptibility for sample 1. The characteristics of the measuring AC field are : 1 Oe and 330 Hz. The applied DC field is from top to bottom : 0, 0.1T and 1T.



Figures V- 27 : Real and imaginary components of the AC susceptibility for sample 2. The measuring AC field has an amplitude of 1 Oe and three different frequencies are used : 17, 167 and 1054 Hz. The applied DC field is from top to bottom : 0, 0.007T and 0.03T (to compare with the DC magnetisation).



is increased, the AC signal becomes smaller and it becomes more difficult to detect. At present, it is difficult to comment on the presence of a peak in the imaginary component  $\chi''$  of the susceptibility at 30 - 40 K because it could either be associated with the sample or be intrinsic to the AC susceptometer (similar behaviour has been seen in other samples when the detected signal becomes small and it is possibly due to the resistivity anomaly in the copper coils at these temperatures).

To sum up the results so far, the magnetic transition in the new YFe phase seems to be very complex in nature : in zero field, the AC susceptibility reveals a spin-glass like transition occurring at about 90K whereas even a small applied field is enough to drive the system into a magnetic order below 55K, consistent with the DC magnetisation data. Furthermore, there is evidence for contamination of the sample by small amounts of YFe<sub>2</sub>.

### *V.3.c.2. Mössbauer results*

Mössbauer spectra were collected at several temperatures on sample 1 between 5K and 100K using the conventional constant acceleration described in chapter II. Four such spectra collected at 5, 50, 60 and 100 K are plotted on *Figure V- 28*. As usual, the velocities are calibrated by running a natural iron foil at room temperature. The low temperature spectra show the presence of sextets, characteristics of a magnetic ordering on the Fe sites and have been fitted using the program Recoil<sup>33</sup>. A reasonable fit to the data could be obtained with a model including three different magnetic hyperfine fields but the number of sites could be increased to four with an equally good fit. On the other hand, attempts with fewer sites than three decreased significantly the quality of the fit. It seems therefore logical to present the fits with the smallest number of refined parameters ie the one with three sites. The evolution of the hyperfine splitting of the three sites is presented on *Figure V- 29*. The hyperfine splittings appear sharply and all at once between 60K and 55K, consistent with the magnetisation data described earlier. It therefore suggests that, at least on a local scale, there is an ordering of the Fe moments below 55 K. For completeness, it should be noted that if four sites are included, they are two pairs of magnetic hyperfine splittings : one with hyperfine fields of the order of 12T and one in the order of 7T at low temperatures. Fitting the High temperature spectra required the presence of two doublets signifying the presence of two different Fe environments.

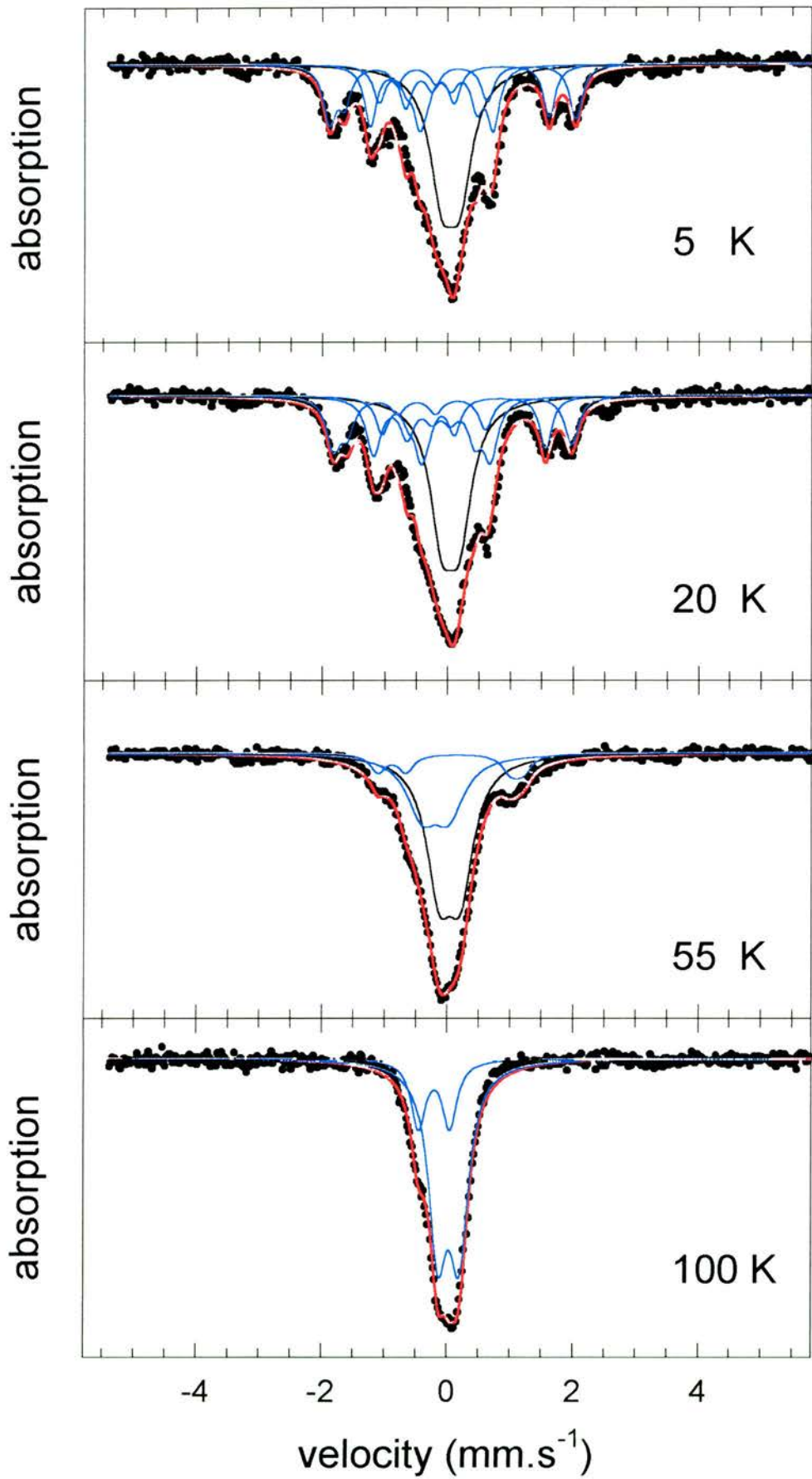


Figure V- 28 : Mössbauer spectra for the new YFe phase from 5K to 100K.

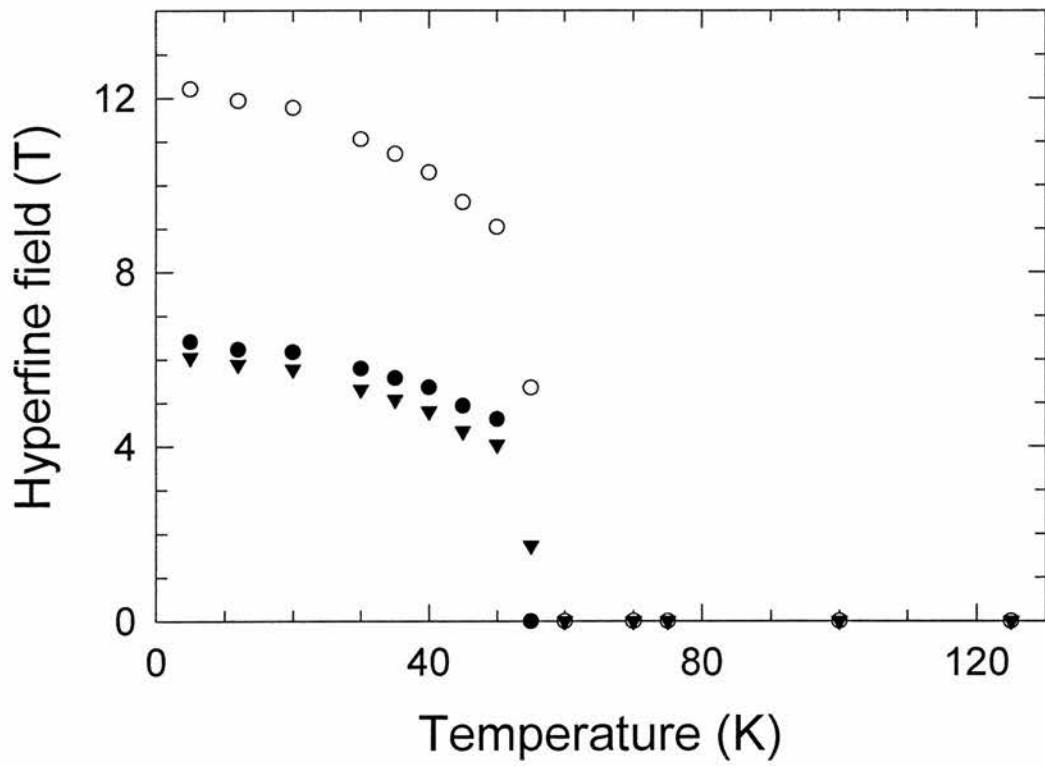


Figure V- 29 : hyperfine fields parameters from the fit of the data to three magnetic sextets.



### V.3.c.3. Muon spin relaxation

Muon spin relaxation ( $\mu$ SR) is a powerful technique with which to study spin relaxation processes in solids, as described in chapter III. Approximately 3g of materials were placed in a sample holder consisting of a plate where a disk of 25mm diameter and 2mm thickness has been cut out and sealed with a mylar film. The sample was then mounted onto a Closed Circuit Refrigerator (CCR) in the MuSR spectrometer at the ISIS pulsed muon and neutron facility at the Rutherford Appleton Laboratory (Oxfordshire). The temperature range available in the CCR is 10K - 300 K.

The time independent background was determined by mounting  $\text{Fe}_2\text{O}_3$  (haematite) at the sample position and performing a transverse field measurement at ambient temperature. The muons implanted into the sample holder rotate at the Larmor frequency of 1.7MHz appropriate to a 2mT (or 20 G hence the name T20 for this type of run) transverse field and their depolarisation rate is negligible. Randomly oriented antiferromagnetic domains depolarise 2/3 of the muons localising in the haematite much faster than the first available time-bins on MuSR, representing the component of the muon polarisation transverse to the domain magnetisation. The remaining 1/3 component of the muon polarisation parallel to the domain magnetisation is lightly depolarised due to the presence of water in the haematite. The resulting asymmetry plot is shown in *Figure V- 30*, where the solid line is a least squares fit of the data to the equation

$$P(t) = a_{bg} \cos(2\pi\gamma_{\mu}Bt) \exp(-\lambda_{SH}t) + a_H \exp(-\lambda_Ht), \quad \text{Eq. V- 8}$$

where,  $a_{bg}$  is the background asymmetry, B is the applied transverse field,  $\lambda_{SH}$  is the small depolarisation rate of muons thermalised in the sample holder,  $a_H$  is the 1/3 asymmetry component of the muons thermalised in the haematite and  $\lambda_H$  is the depolarisation rate of the 1/3 component due to the presence of water in the haematite. The background asymmetry was found to be of the order of  $a_{bg} = 0.073$  and has been kept constant during the data analysis. The reason why the signal is not centred on zero is that the correction factor  $\alpha$  has been calculated for the actual sample thickness and this run was obtained by putting  $\text{Fe}_2\text{O}_3$  in front of the mylar film thereby increasing considerably the thickness. Indeed, the correction factor  $\alpha$ , correcting for difference in detector efficiencies, was calculated from another T20 run on the sample itself collected at 300K. *Figure V- 31* shows the T20 data along with a fit. The obtained  $\alpha$  value was 1.24 and has been kept throughout the whole data analysis.

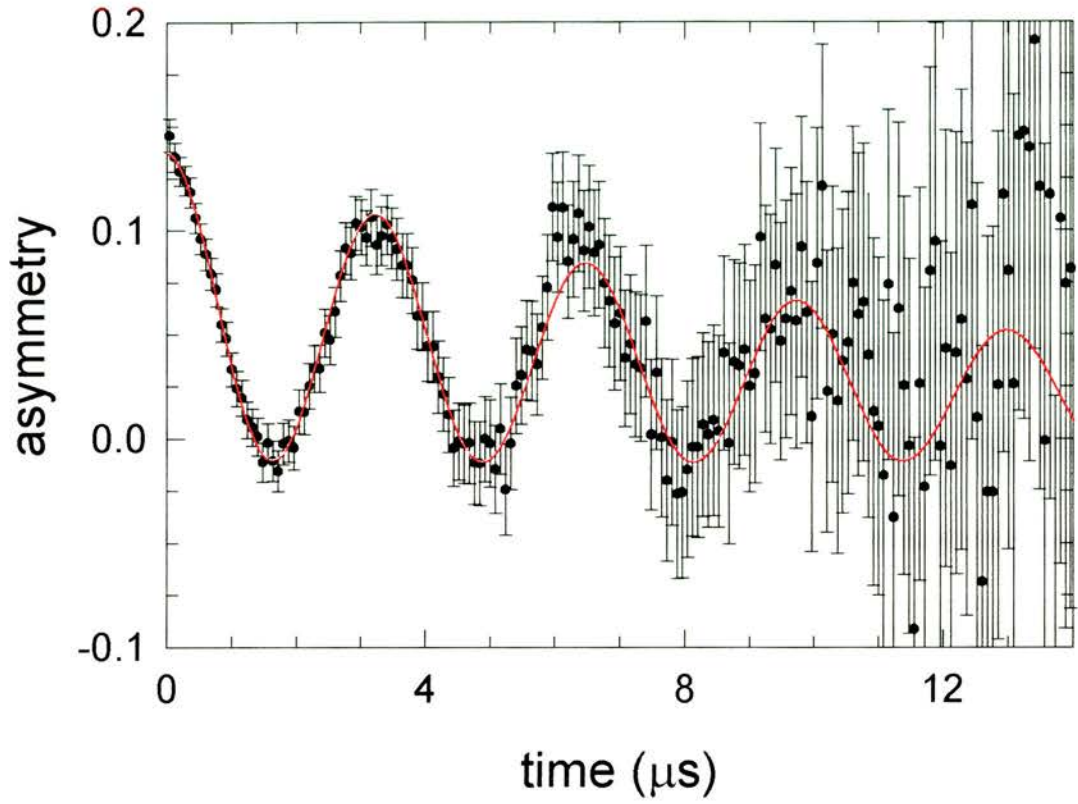


Figure V- 30 : T20 run with haematite covering the sample.

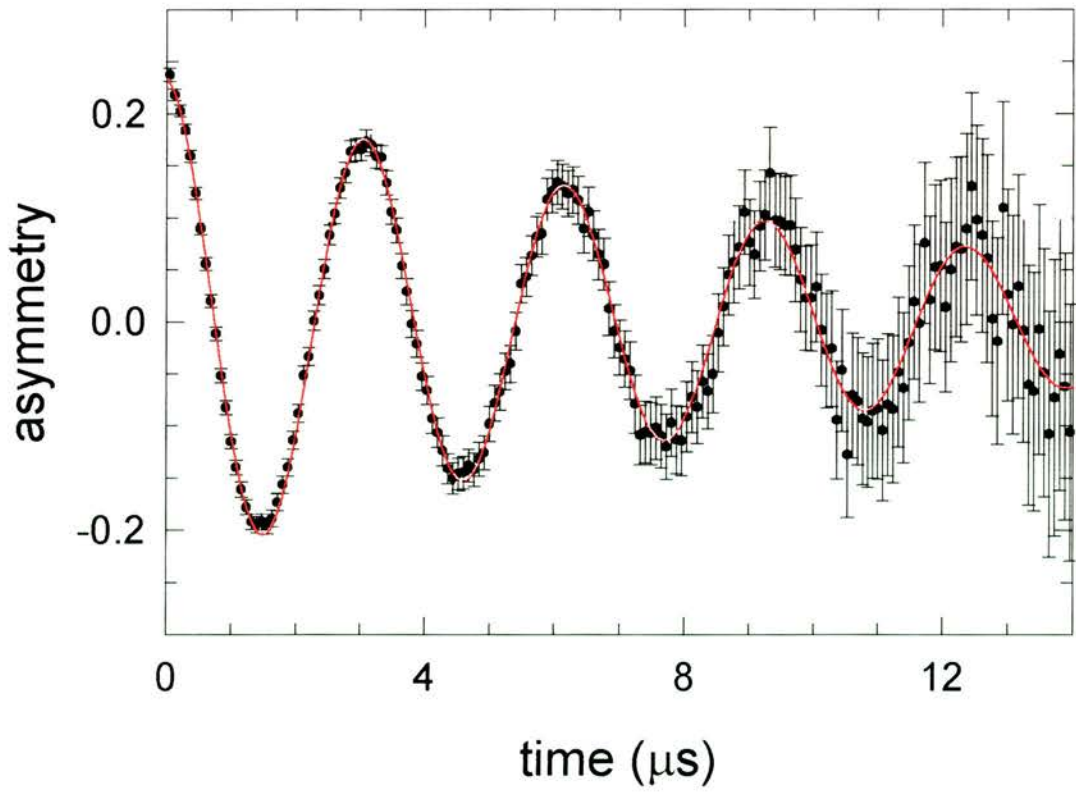


Figure V- 31 : T20 run with the sample in the CCR.

*Figures V- 32 and V- 33* show  $\mu$ SR spectra collected on a sample of the new YFe phase for a few selected temperatures (40K, 50K, 55K, 62 K and 200K) with no field applied parallel to the muon beam polarisation (i.e. no longitudinal field). The abscissa on the main graphs present the time range 0-10  $\mu$ s bunched in bins of 5 data points for clarity whereas the inserts focus on the 0-1  $\mu$ s region with no grouping of data points. It can be seen that the difference between the 200 K and the 60 K spectra is quite small although some dynamics can be observed but a spectacular change appears just below 60K coinciding with the transition observed in Dc magnetisation, AC susceptibility measurements in an applied field and Mössbauer spectroscopy. The close inspection of the short time regime, show on the inserts of *Figures V-32 and V-33*, clearly indicates the presence of rapidly depolarising "wiggles". Coherent oscillations are generally associated with the onset of magnetic order<sup>34</sup>. Because the sample contains two phases (Y and the new intermediate phase YFe), the expression for the depolarisation function must contain at least as many terms.

Y on its own<sup>35</sup> has been previously studied by  $\mu$ SR and it was proved that as far as the muon spectra are concerned, pure yttrium possesses neither electronic nor nuclear spin. However, this does not imply that in our sample, the Y will not experience any depolarisation. For instance, in superparamagnetic heterogeneous  $\text{Cu}_{98}\text{Co}_2$ , the muons landing in the Cu experience the fields created by the Co clusters<sup>36</sup> (whereas those landing in the ferromagnetic Co clusters depolarise so rapidly that they cannot be seen by pulsed  $\mu$ SR).

Above the transition temperature, the data could be well described by the equation :

$$P(t) = a_1 e^{-\lambda_1 t} + a_2 e^{-\lambda_2 t} + a_{bg} \quad \text{Eq. V- 9}$$

Using this functional form assumes that the muon depolarisation function is due to fluctuating atomic spins in the fast fluctuation limit. Whereas below the transition temperature, the data could be fitted by :

$$P(t) = a_1 \cos(\omega t) e^{-(\sigma t)^2} + a_2 e^{-\lambda t} + a_{bg} \quad \text{Eq. V- 10}$$

The second part of the equation refers to the Y phase whereas the first part is associated with muons landing in the new YFe phase. For a multi-domain polycrystalline ordered magnet, the expression should have included another exponential term with an initial asymmetry  $a_1'$  corresponding to the dynamic fluctuations of the longitudinal field



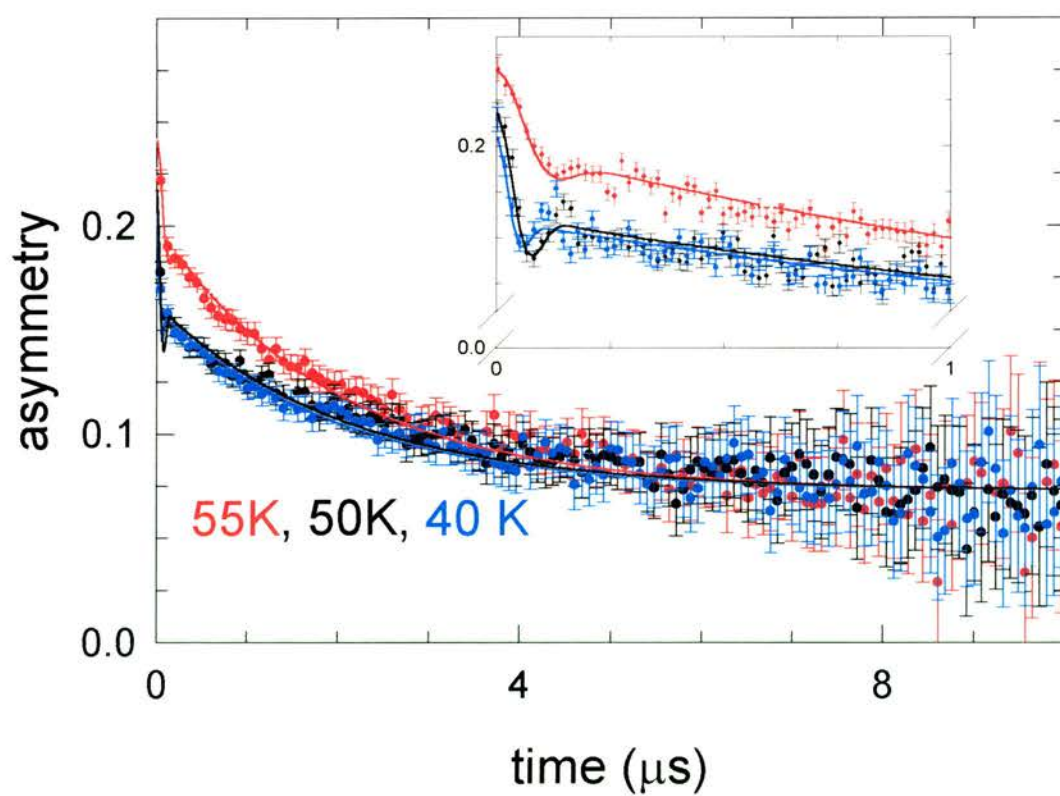
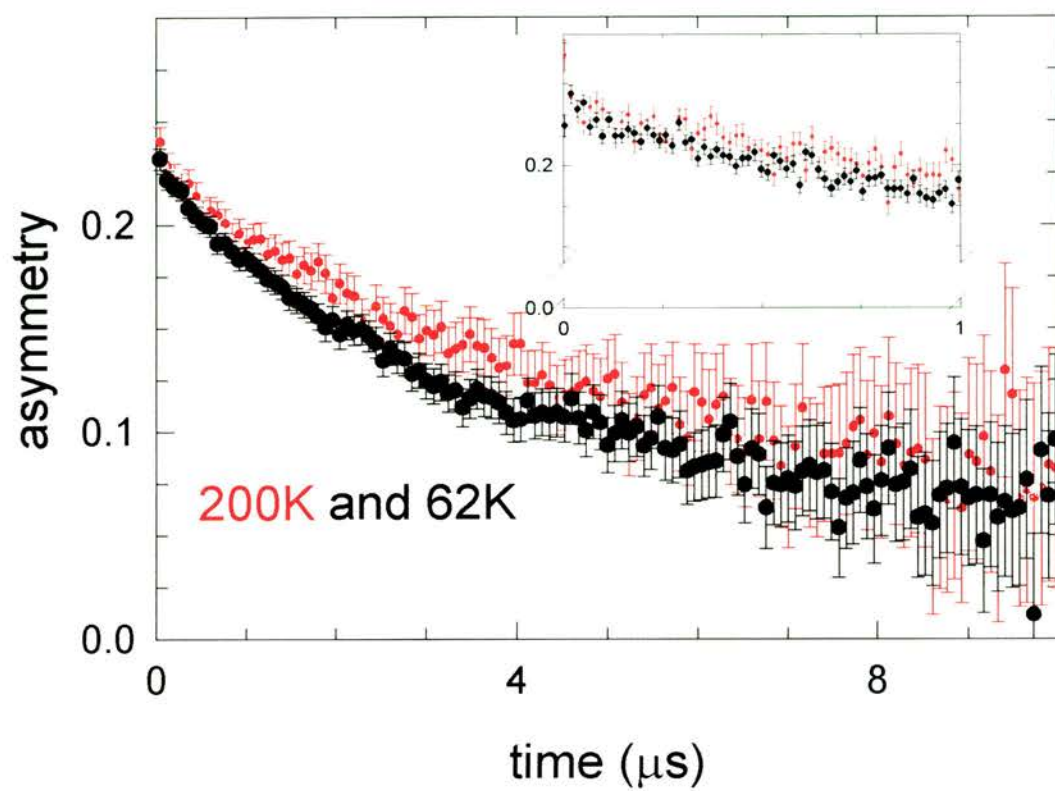


Figure V- 32 (top) and V- 33 (bottom) : ZF  $\mu\text{SR}$  spectra for five selected temperatures. The inserts show a zoom in the small time region.

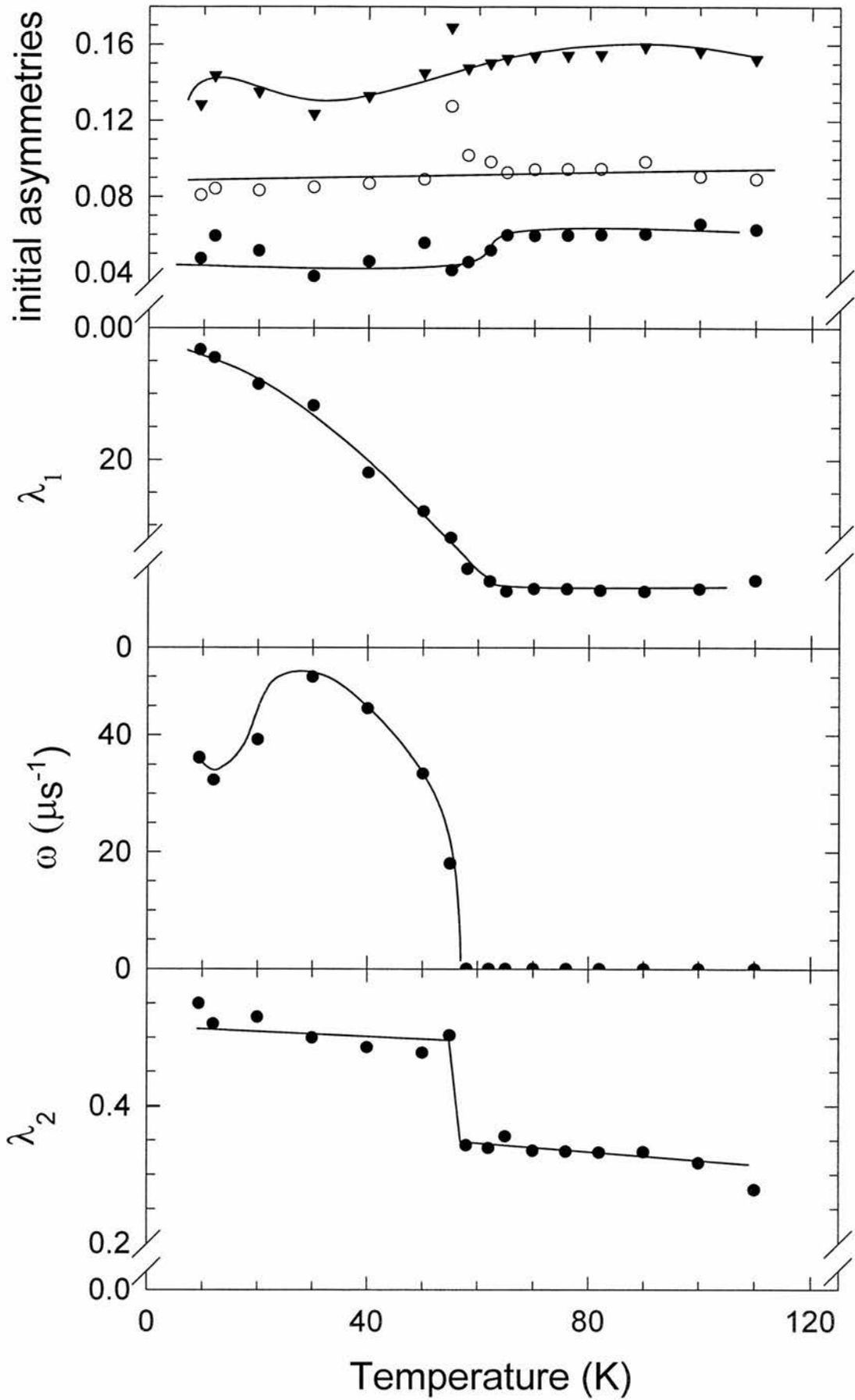


Figure V- 34 : temperature evolution of the fitting parameters described in the text.

component with an initial asymmetry equal to a 1/3 of that of the YFe phase ( $a_1'=1/2a_1$ ). However, this did not improve the fits and was not finally included.

The fits to the data for the five selected temperatures are shown as solid lines on *Figures V-32 and V-33*. The temperature dependence of the relevant parameters is plotted on *Figure V- 34*. The main advantage of the pulsed  $\mu$ SR technique is that the background is small, allowing data collection over several muon lifetimes (typically 16 $\mu$ s). This allows even small depolarisation rates to be measured. However, the muon pulse width imposes an upper limit to the muon spin relaxation rates that can be extracted from the data. This is rather unfortunate for this sample as it implies that the most interesting part of the time evolution is contained within the few first points only and it is therefore hard to fit with great precision (if the internal field is even higher, like in haematite for instance, the only signature of magnetic order is a drop of the initial asymmetry to 1/3 of its initial value) A better study could in principle be achieved at a continuous muon source like the Paul Scherrer Institute. Having pointed out that the fits may not be entirely reliable, it is nonetheless interesting to notice that the frequency of the oscillations presents a maximum around 25K, a temperature coinciding with an anomaly in the DC magnetisation data. The total initial asymmetry arising from the sample was approximately constant at 0.15 throughout the whole temperature range. One component is about 0.09 whereas the other one is roughly 0.06 although we expect the sample to be 50% Y and 50% YFe. This slight difference could be due to the fact that the muons thermalising in Y or in the interface Y/Fe experience similar fields. Near the actual transition temperature, the fits tend to overestimate the initial asymmetry. There is also a step-like increase of the relaxation rate of the second component at the transition temperature.

#### *V.3.c.4. neutron scattering results*

In order to provide useful information on the magnetic ground state of new YFe phase, a neutron scattering experiment has been conducted. So far, the local Mössbauer and  $\mu$ SR probes have both shown that a magnetic transition occurs between 50K and 60K, consistent with the macroscopic DC magnetisation and AC susceptibility (in a DC applied field) measurements. Thanks to the magnetic moment of the neutron, a Neutron scattering experiment can provide unique insights into the type of magnetic ordering. For instance, the nuclear Bragg peaks of a ferromagnet present extra intensity when the



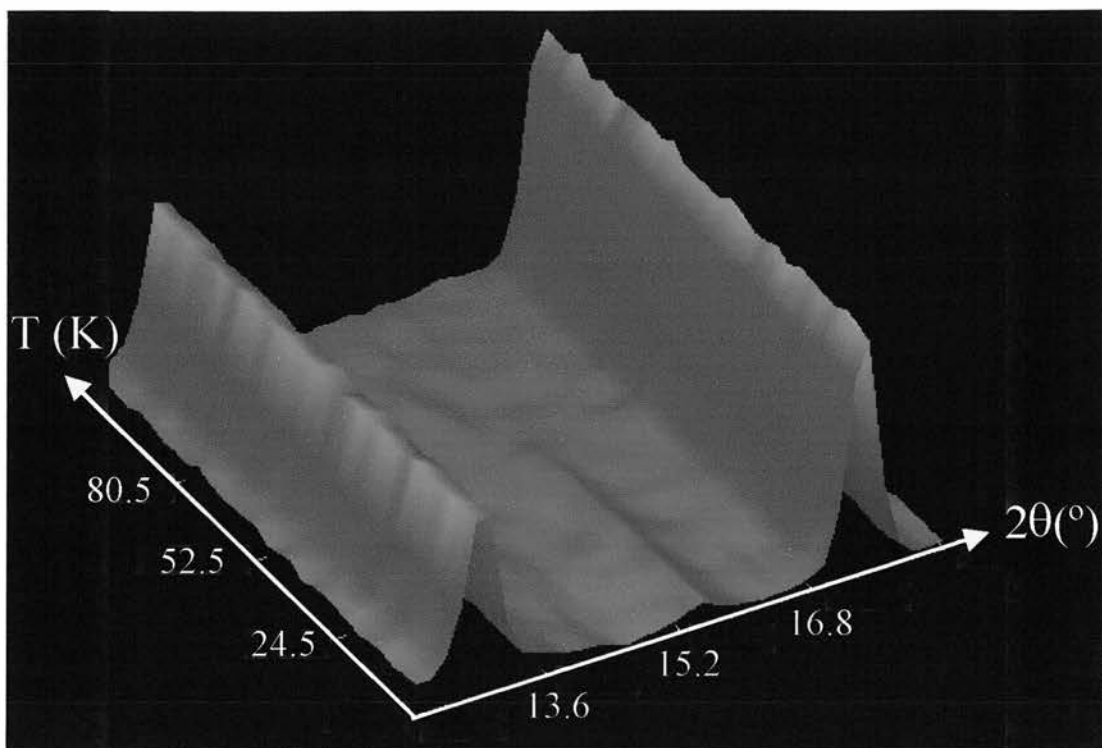


Figure V- 35 : neutron thermogram in the temperature range 5K - 100 K of the new YFe phase for  $2\theta$  between  $12^\circ$  and  $20^\circ$ .

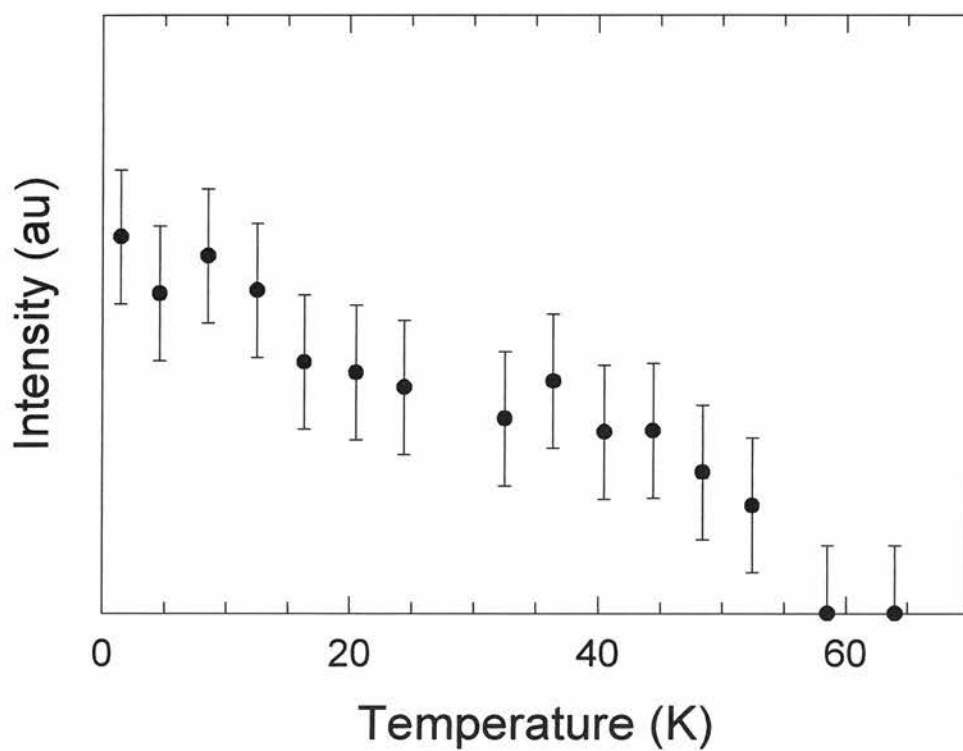
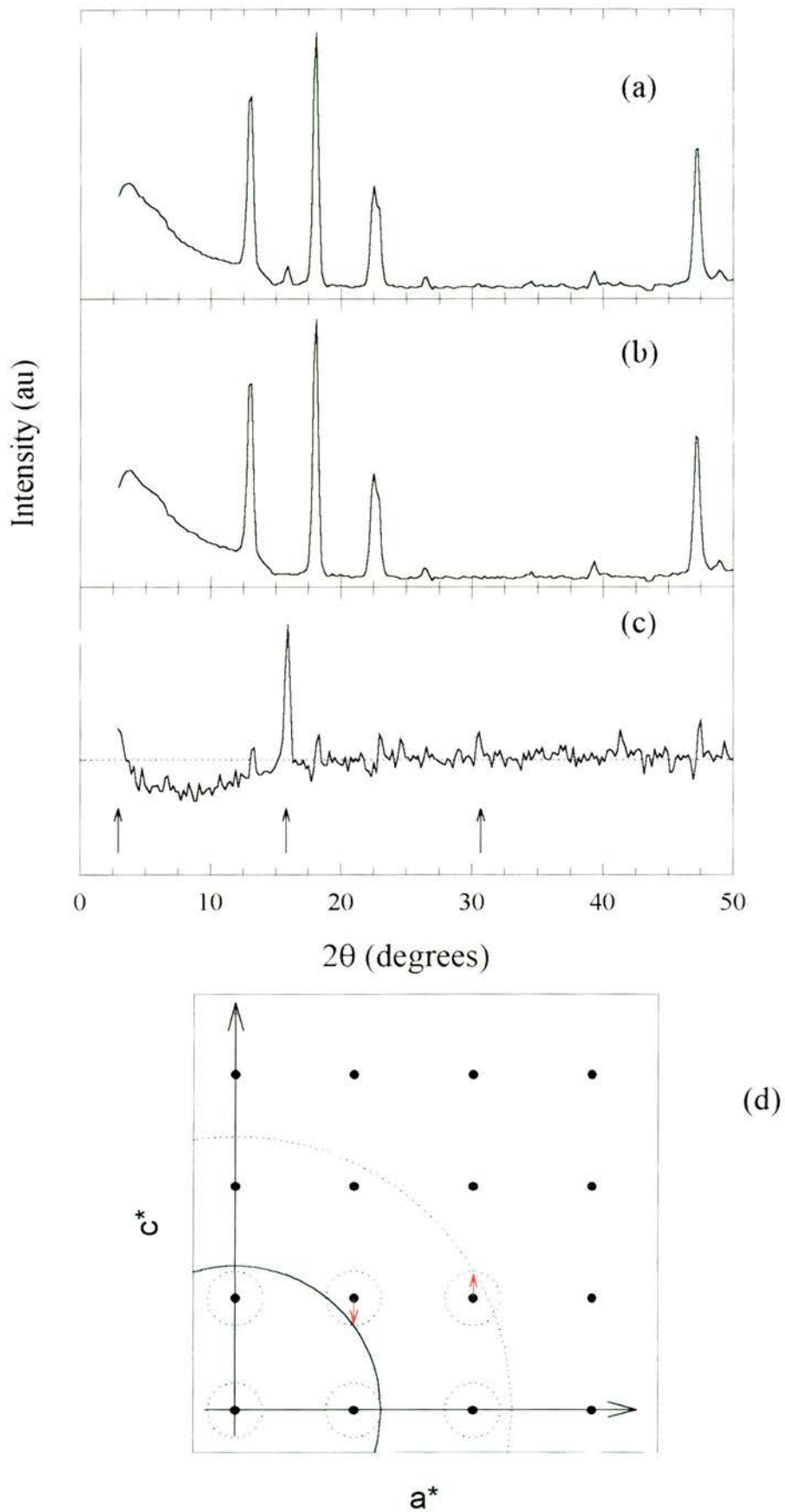


Figure V- 36 : Temperature evolution of the integrated intensity of the most visible extra magnetic peak at  $16^\circ$ .

sample is cooled through the Curie temperature. On the contrary, if additional Bragg peaks appear when a sample is cooled below a transition temperature it implies that the magnetic cell is bigger than the nuclear one and therefore suggest an antiferromagnetic, ferrimagnetic or helicoïdal magnetic order, depending on the position of the extra peaks. It should be noted that neutron will only show diffraction peak if long-range magnetic order is present and will not show any sharp features in the presence of some local order such as in spin-glass systems.

It seemed therefore extremely useful to study the new intermediate YFe phase by neutron scattering. Approximately 3g of material were loaded into a vanadium can and mounted into an Orange cryostat on D1B. *Figure V- 35* shows a neutron thermogram of a section of  $2\theta$  range available on D1B collected between 5K and 100K. There is a faint extra peak appearing just below 58K and present down to the lowest temperatures. Unfortunately, this is the only striking peak in the whole  $2\theta$  range making the entanglement of the magnetic structure extremely difficult. This peak is best seen on *Figures V- 37* where the scattering intensities at (a) 75K and (b) 5K are shown. From the difference pattern (*Figure V- 37 (c)*), the position of the peak is determined to be  $2\theta = 16^\circ$ , which is not consistent with a simple antiferromagnet. The first step in determining a magnetic structure consists of plotting the reciprocal space and drawing spheres whose radii are consistent with the  $2\theta$  position of the magnetic peaks<sup>37</sup>. This procedure is relatively straightforward if the magnetic peaks can be seen clearly. Furthermore, the absence of a peak between zero and the peak corresponding to the first nuclear reflection - the (100) - in the allowed  $2\theta$  range makes the magnetic structure solving even more complicated. Indeed, there is no simple way of determining the magnetic structure if there is no peak in the Brillouin zone centred on the origin. In order to try and see if there was a simple solution to the magnetic structure of the new YFe alloy, this simple method has been tested on several reciprocal planes and the most sensible result can be found on *Figure V- 37 (d)*. It suggests an incommensurate phase with wave vector  $\mathbf{k}$  (0, 0, 0.23). However, it must be stressed that this result should be taken with extreme reserve as 1) it was achieved by assuming peaks where the scattered intensity was just above the background level and 2) if this was true, other peaks should be present but cannot be conclusively (if at all) observed on *Figure V- 37 (c)*. The integrated intensity of the clear additional peak at  $16^\circ$  is presented on *Figure V- 36* where a small plateau at around 25K can be observed.



Figures V- 37 : Diffraction pattern of the new YFe phase at (a) 1.5K and (b) 75 K and (c) difference. The arrows represent the  $2\theta$  values chosen for (d), the most sensible magnetic structure.

### V.3.c.5. Discussions

All the experimental techniques used seem to confirm that the new YFe phase exhibits a magnetic transition at about 58K, the only exception being the zero field AC susceptibility but the transition at 58K reappears if a small DC field is superimposed. For comparison purposes, it is very instructive to recapitulate previous work done on amorphous YFe compounds. These alloys are notorious to possess widely different transition temperatures depending on the sample preparation. For instance,  $\alpha$ -YFe<sub>2</sub> prepared by dc- sputtering<sup>38</sup> is non magnetic down to 3.5K but exhibit strong short range ferromagnetic order and Mössbauer measurements on the same sample<sup>39</sup> found a spin glass-like transition at 58K. Other  $\alpha$ - Y<sub>x</sub>Fe<sub>1-x</sub> samples made by sputtering also show a paramagnetic to spin glass transition<sup>40</sup>. On the other hand, samples made either by melt spinning<sup>10,41</sup> or by electron beam co-evaporation<sup>42</sup> tend to show a transition from a paramagnetic to a ferromagnetic state at much higher temperatures (around 250K). This suggests that local chemical ordering plays an absolutely crucial role in the magnetic ground state in these amorphous alloys. This fact has been recognised by theorists who, in order to simulate quantitatively the magnetic phase diagram of YFe had to introduce a atomic short range order parameter<sup>43</sup>. Experimentally, re-entrant spin glass behaviour has been observed in a weak magnetic field in Fe-rich Y<sub>x</sub>Fe<sub>1-x</sub> alloys<sup>44</sup> and it was later shown that the re-entrant phase was stabilised by annealing<sup>45</sup>.

Some of the characteristics in the  $\alpha$ - Y<sub>x</sub>Fe<sub>1-x</sub> alloys, such as the stabilisation of a magnetic phase by an applied field, a transition temperature of 58K (in the  $\alpha$ -YFe<sub>2</sub> prepared by dc- sputtering), bear resemblance with the new recrystallised YFe phase. At first, this can appear disturbing but the cell parameters suggest a large number of atoms and the local arrangement of the amorphous structure can be very similar to that of the new crystalline alloy. Indeed, EXAFS studies have revealed that the amorphous structure of amorphous Zr<sub>x</sub>Fe<sub>1-x</sub> alloys is a mixture of clusters with comparable coordinations to the different crystalline ZrFe compounds<sup>46</sup>. One other possibility for explaining similar magnetic data would have been that some amorphous YFe remains during the crystallisation process, even after the appearance of the new intermediate phase, which would be difficult to detect by neutron diffraction if in small quantities. However, this can be ruled out as the muon response clearly shows that a major part of the sample is affected by the transition and the low temperature neutron diffraction results indicate that the magnetic order at 58K is long-range in nature. Several theory

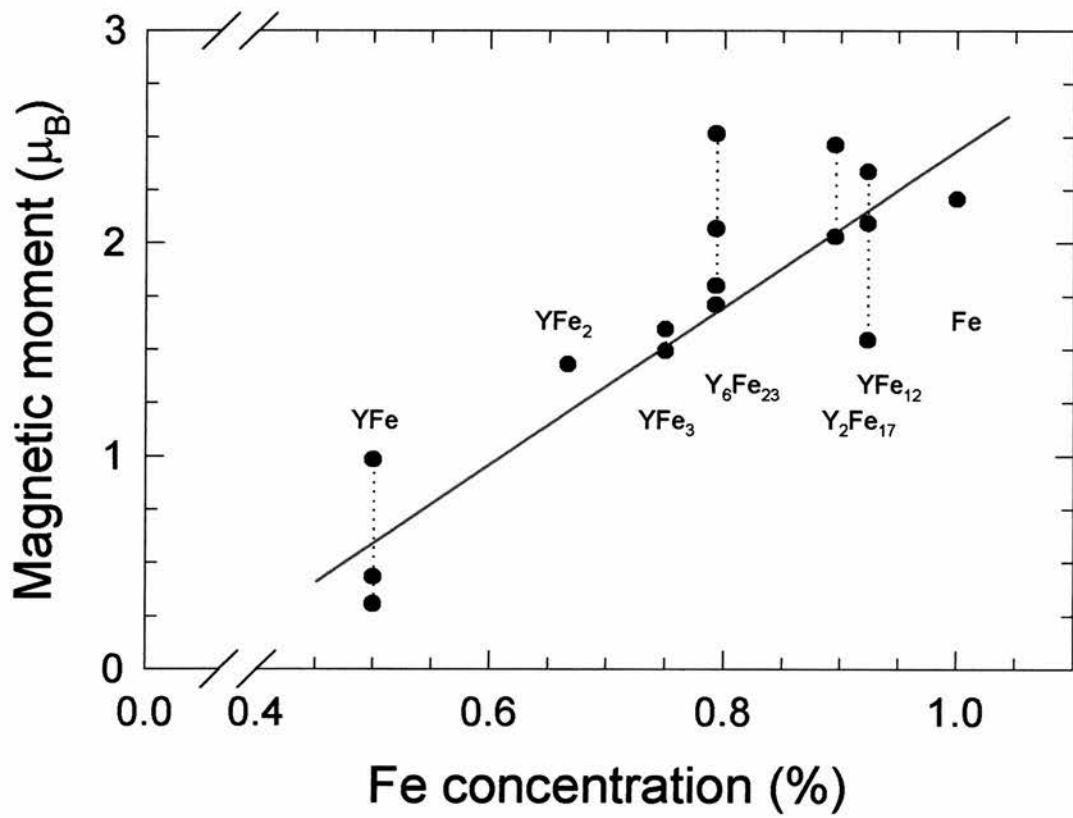


Figure V-38 : Iron magnetic moments calculated from the Mössbauer hyperfine fields for the previously known YFe phases (from Coehoorn<sup>47</sup>) and for the new YFe phase.

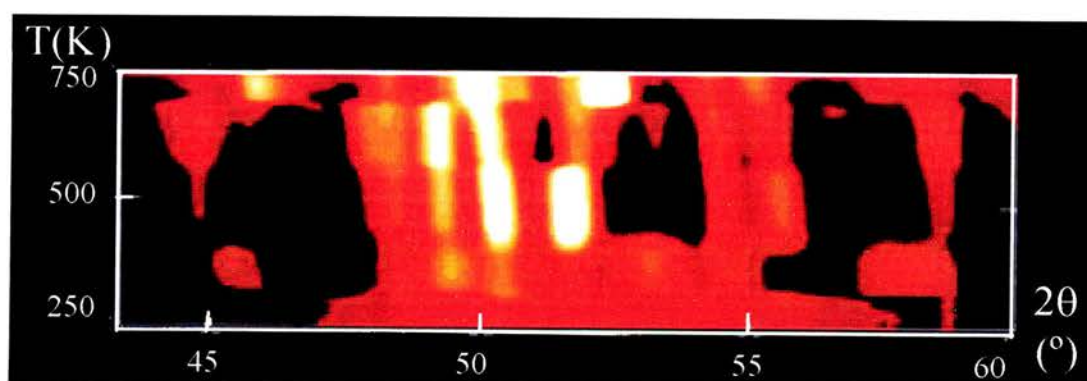
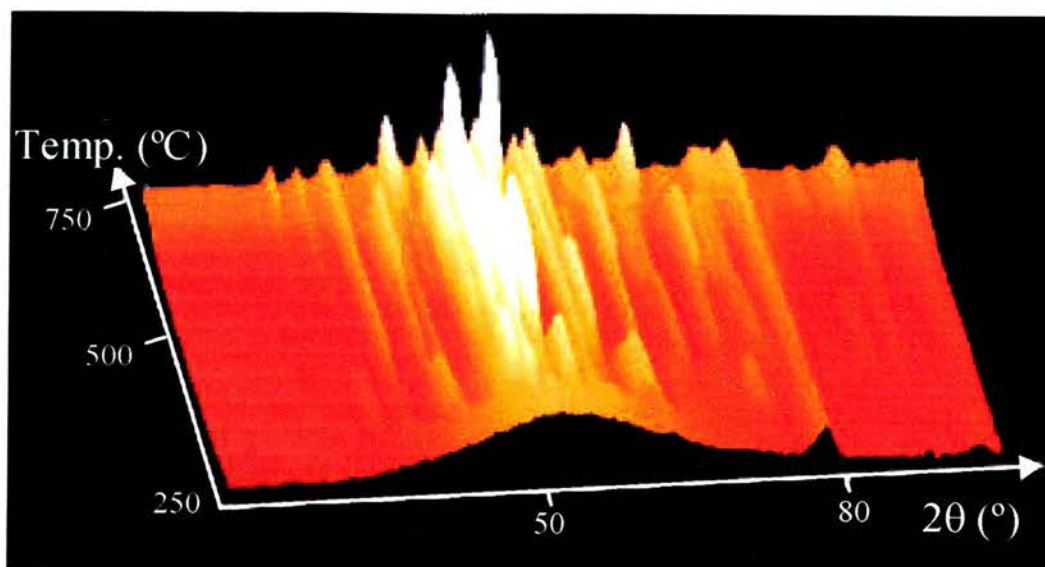
papers have tried to explain the electronic structure and the magnetic properties of the YFe compounds from ab-initio band structure calculations<sup>47</sup>, or in terms of local environment parameters such as the Voronoi polyhedron and the hybridisation of a given atom with its neighbours<sup>48</sup>. It would be enlightening to perform such calculations for the new YFe phase. Indeed, the moment per iron atom obtained from Mössbauer spectroscopy is about  $1\mu_B$  and seems to fit reasonably well with the general trend observed in the YFe compounds<sup>48</sup> (see *Figure V- 38*). Another recent theory paper based on a molecular dynamics approach to itinerant magnetism, devised to predict the magnetic state in  $\gamma$ -Fe, also suggests that complicated helical structures for certain ratio of d-electron number and Fe-Fe distances.

#### V.4. Crystallisation study of other RE-TM amorphous alloys

Two other amorphous alloys, namely  $Y_{67}Co_{33}$  and  $Er_{67}Fe_{33}$  have been recrystallised by the same method on D20 for direct comparison with the YFe alloy. About 3g of each sample was loaded into a vanadium can and mounted onto a furnace and then inserted in the D20 beamline as for the YFe study. The crystallisation processes in YCo are much more complex with the appearance of 5 distinct phases, some of which might be magnetic. The final phase itself seems to be a mixture of three phases. Attempts to characterise the phases by Rietveld refinement have proven difficult due to the fairly poor resolution on D20 and would benefit immensely from D2B data sets, if each of the intermediate phase can be quenched as in the YFe system. A neutron thermogram of the YCo system for the whole  $2\theta$  covered by D20 and a zoom at the  $2\theta$  range  $45^\circ - 60^\circ$  showing the occurrence of all the different phases more clearly are presented on *Figures V- 39*.

The crystallisation processes in the ErFe system are much closer to those in the YFe system. *Figure V- 40* shows a neutron thermogram of  $\alpha$ - $Er_{67}Fe_{33}$  for which a diffraction pattern was collected over the angular range  $2\theta = 5^\circ$  to  $135^\circ$  every four minutes while the sample was being heated up smoothly from  $250^\circ C$  to  $720^\circ C$  at a ramp rate of  $1^\circ C/min$ . Similarly to the YFe system, the final phase is a mixture of crystalline Er and  $ErFe_2$  phases. A two phase Rietveld refinement obtained by using Fullprof can be found on *Figure V- 41*. The space groups and the lattice parameters obtained are fully consistent with reported values<sup>13</sup> for Er ( $P 6_3 / m m c$ ,  $a = 3.54(1) \text{ \AA}$ ,  $c = 5.61(2) \text{ \AA}$ ,





Figures V- 39 (top) : Neutron thermogram for the crystallisation of  $\alpha\text{-Y}_{67}\text{Co}_{33}$  obtained on D20 ( $\lambda=2.4 \text{ \AA}$ ). The furnace was ramped at  $1^\circ\text{C} / \text{min}$  and data was collected every four minutes.

(bottom) : enlargement of the  $2\theta = 45^\circ - 60^\circ$  region showing the phases more clearly.

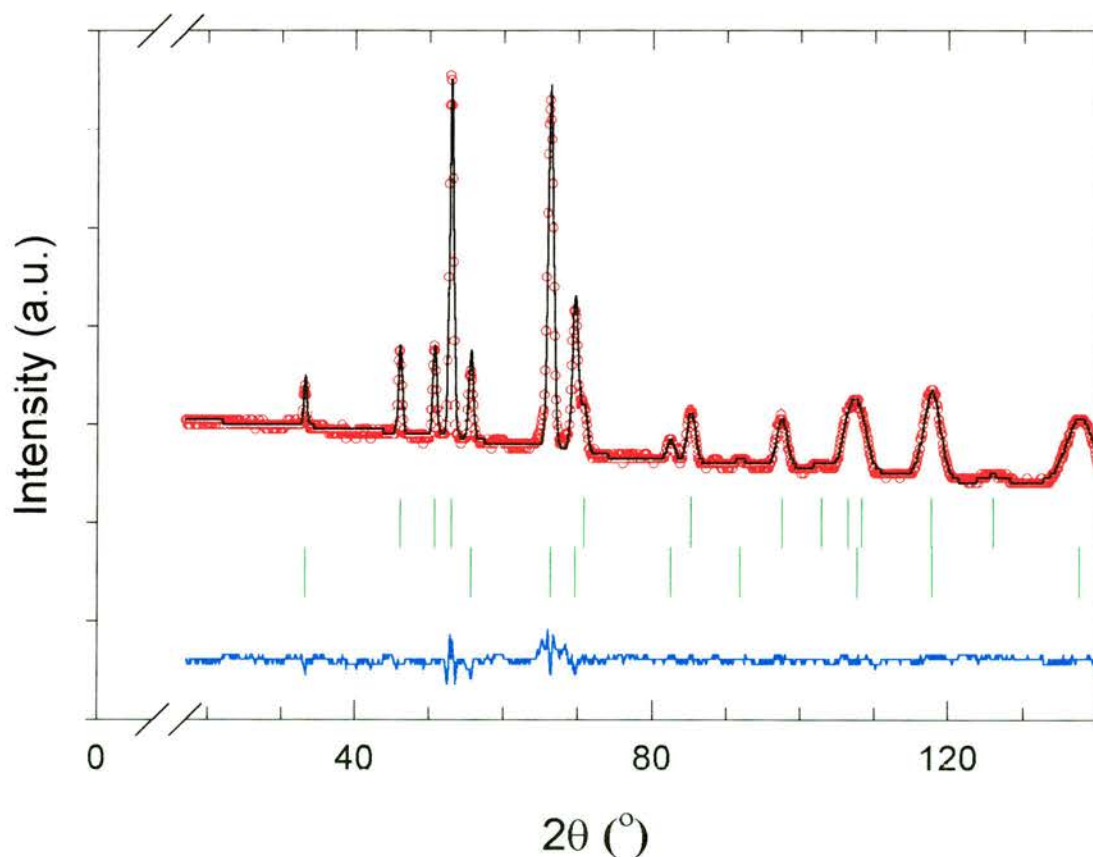
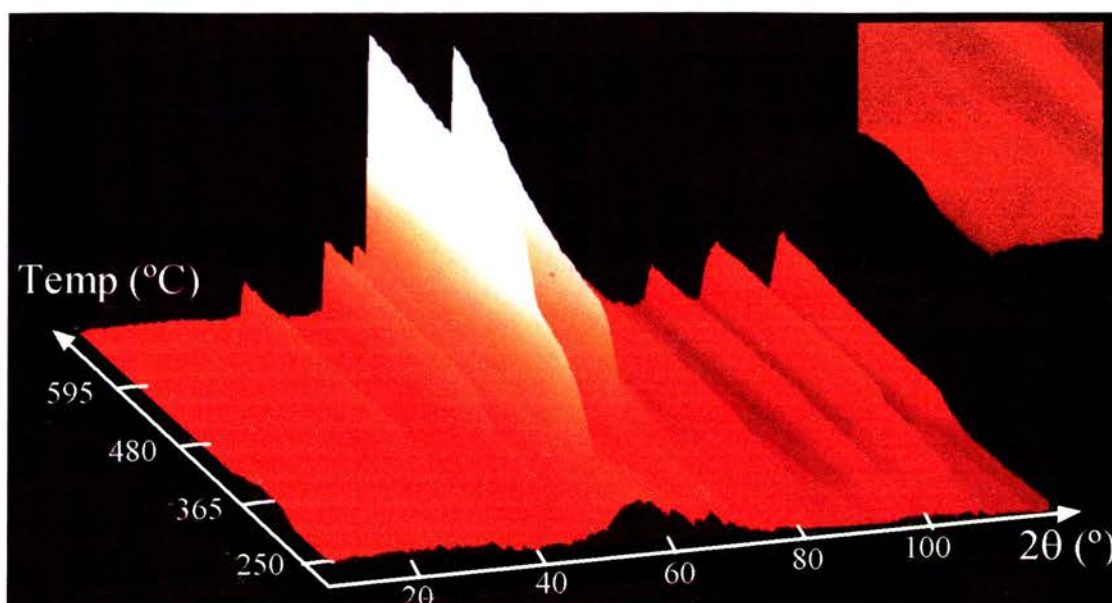


Figure V- 40 (top) : Neutron thermogram of the crystallisation of  $\alpha\text{-Er}_{67}\text{Fe}_{33}$ . The data were obtained by collecting spectra every four minutes while ramping at  $1^\circ\text{C} / \text{min}$  on D20 ( $\lambda = 2.4 \text{ \AA}$ ). Insert : enlargement of the low angle region of the ErFe thermogram (Figure V- 40). Three small peaks, very similar to the YFe ones can be observed.

Figure V- 41 (bottom) : Rietveld refinement of the final phases (Er and  $\text{ErFe}_2$ ).

$\gamma = 120^\circ$ , Er atomic co-ordinates :  $1/3, 2/3, 1/4$  ) and  $\text{ErFe}_2$  (F d 3 m,  $a = 7.28(1) \text{ \AA}$ , Er atomic co-ordinates :  $1/8, 1/8, 1/8$ , Fe atomic co-ordinates :  $1/2, 1/2, 1/2$ ). However, contrary to the YFe case, the small angle region does not show the massive increase followed by an abrupt drop when the sample starts to crystallise : there is some small angle scattering but it is much less pronounced. Furthermore, the plateau present between  $390^\circ\text{C}$  and  $450^\circ\text{C}$  in the temperature evolution of the Y (100) peak (*Figure V-10*) is present in the temperature evolution of the Er (100) peak as well, as shown on *Figure V-42 (a)* but it is much narrower (between  $340^\circ\text{C}$  and  $360^\circ\text{C}$ ).

Although it is not seen as clearly as in the YFe case, the newly discovered structure is also present in the ErFe system. To see the three characteristic peaks at low angles associated with the large unit cell clearly, it is necessary to zoom on the  $2\theta$  range  $10^\circ - 25^\circ$ , as shown on the insert of *Figure V-40*. At first, the faintness of the peaks characteristic of the new RE-TM phase seems quite odd, as Er and Y have similar scattering length and the starting composition of the amorphous alloys and the final phases are the same. This is however explained by the temperature evolution of the  $\text{ErFe}_2$  (111) peak -*Figure V-42 (b)*-. In contrast to the YFe case, the crystallisation of the ErFe system is characterised by the formation of  $\text{ErFe}_2$  nanoparticles early in the process. The  $\text{ErFe}_2$  peaks are very wide, indicating very small particles, but nonetheless present. This implies that some Fe is being taken out of the ErFe amorphous matrix to form  $\text{ErFe}_2$  at an earlier stage, thereby reducing the amount of Fe available for the formation of the new phase. The temperature evolution of the new ErFe phase is shown on *Figure V-42 (c)* where it can be seen clearly that the new phase appears at roughly  $300^\circ\text{C}$  and disappears at around  $400^\circ\text{C}$ , temperatures somewhat lower than in the YFe case. This  $100^\circ\text{C}$  range over which the new ErFe phase exists is much wider than the range over which the Er presents a plateau, in opposition to the YFe case where the new YFe phase appearance coincides with a plateau in the Y crystallisation (*Figure V-10*). The different crystallisation processes between the YFe and the ErFe systems could be due to different amorphous alloy microstructure, different segregation of the TM or RE or different kinetics in the crystallisation of the two new phases. In the later case, the ramp rate used could be crucial to the preparation of the new ErFe phase.

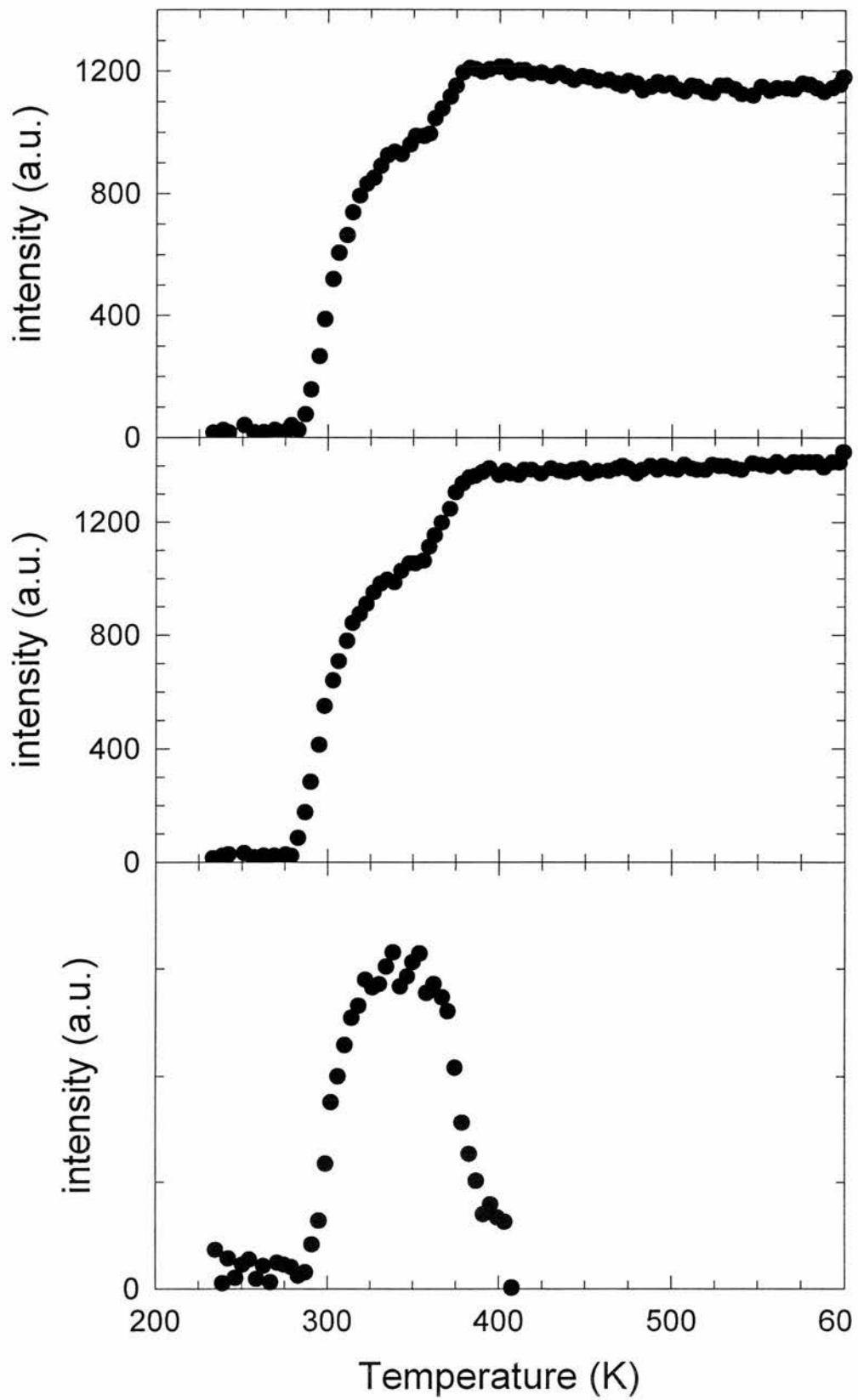


Figure V- 42 : Temperature evolution of the integrated intensities of (a) the (100) Y , (b) the (111) YFe<sub>2</sub> , and (c) (100) intermediate phase peaks.

## V.5. Conclusions and further work

The work on the crystallisation of RE-TM by neutron scattering has proven very fruitful. It has been possible to show that the crystallisation processes and kinetics (the Avrami time constant for instance) can be monitored on fast counting instruments such as D20. It appears that the known phases are obtained at a much lower temperature by crystallising amorphous samples than by conventional melting. This can be due to the intimate mixing of the elements in the amorphous phase. The complete monitoring of the phase diagrams opens the door to the tailoring of the magnetic properties by simply stopping the crystallisation at the right time and temperature. This can be very important in more complex systems of technological relevance. The pseudo-binary (DyTb)-Fe alloy could be an extremely interesting candidate as the  $(\text{Tb}_{0.27}\text{Dy}_{0.73})\text{Fe}_2$  is otherwise known as<sup>49</sup> Terfenol-d and is commercially used for its large magnetostriction ( $\text{TbFe}_2$  has the highest known room temperature magnetostriction<sup>50</sup>) combined with its low magnetocrystalline anisotropy energy and high sensitivity to external magnetic fields. If prepared by sputtering, alloys near the terfenol composition exhibit Curie temperature of the order of  $400^\circ\text{C}$  which represents a disadvantage for practical applications<sup>51</sup>. However, it has been shown that crystallising the amorphous films significantly increase the Curie temperature (about  $600\text{K}$ )<sup>52</sup> and that a small addition of Zr reduces the coercive field<sup>53</sup>. As the magnetostrictive properties are controlled by the microstructure, a detailed analysis of the processes by neutron scattering could prove extremely useful.

Another example can be taken in the superconducting magnet technology. Indeed, most commercial superconducting magnets are made of NbSn alloys (generally around the  $\text{Nb}_3\text{Sn}$  composition). The NbSn phase diagram is extremely complex and poorly understood. Consequently, the recipe for making good wires is not reliable and magnets of poor quality (phases or microstructure not exactly right) can be made. As the making of NbSn wires involve surrounding the NbSn alloy by Cu, the non-neutron methods such as X-rays or transmission electron microscopy, used so far have failed to address this problem and the only test for the manufacturer is to build the magnet, cool it down and test it, which results in a substantial amount of money being wasted in case the wires are faulty. Following the success of the investigation of the binary RE-TM alloys, it is hoped that beamtime will be given for the study of these phase diagrams.



On the other hand, new YFe and ErFe (and possibly YCo) phases have been discovered using the crystallisation of amorphous precursors method. It should be stressed that no new RE-TM had been discovered for some time before this study. The only compound that was possible to stabilise (i.e. the most studied one) showed very interesting magnetic properties with transition to a complex long range magnetic order below 58 K. The properties of intermetallics containing Fe have received intensive theoretical treatment and if these theories are consistent, they should be able to explain the properties of every new alloy. Up to now, the lowest obtainable Fe concentration in the YFe system was 67% but this percentage has now been lowered to about 50 % and should therefore arouse considerable interest for the theorists. As this phase is present in the YFe and ErFe, it can be expected in the other RE-Fe alloys. A simple extrapolation of a theory paper<sup>47</sup> explaining the evolution of the iron magnetic moment as a function of the Fe concentration is presented on *Figure V- 38* with the new phase added. Ideally, single phase samples of these new compounds should be obtained either by sputtering or by ball milling ( $\alpha$ -YFe<sub>2</sub> has recently been obtained by this method<sup>54</sup>) and subsequent annealing.

Another interesting test-bed provided by these experiments is that of the crystallisation processes themselves, especially in the light of the microstructure calculation by recent Monte Carlo simulation of nucleation and growth kinetics<sup>55</sup>. Particular interest should be given to the small angle region where massive increase just before the crystallisation has been observed. This could well be associated with phase separation and deserves more attention.



## References for Chapter V

- <sup>1</sup> For an early review on intermetallic Rare-Earth compounds, see K.N.R. Taylor, *Advances in Physics* **20** (1971) 551.
- <sup>2</sup> F.E. Stanley, M. Perez, C.H. Marrows, S. Langridge & B.J. Hickey, *Europhys. Letters* **49** (2000)528
- <sup>3</sup> C. Ritter, R. Cywinski, S.H. Kilcoyne, S. Mondal and B.D. Rainford, *Phys. Rev. B* **50** (1994) 9894
- <sup>4</sup> I.N. Goncharenko, I. Mirebeau, A.V. Irodova and E. Suard, *Phys. Rev. B* **59** (1999) 9324
- <sup>5</sup> C.J. Boardman, S.H. Kilcoyne and R. Cywinski, *Physica B* **180-181** (1992) 426
- <sup>6</sup> L. Fernandez Barquin et al, *J. Phys.: Condens. Matter* **10** (1998) 5027
- <sup>7</sup> <http://www.ill.fr/YellowBook/D20>
- <sup>8</sup> <http://www.ill.fr/YellowBook/D2B>
- <sup>9</sup> M. Tenhover, *J. Phys F : Met. Phys* **11** (1981) 2697
- <sup>10</sup> J.J. Croat, *J. Appl. Phys.* **53** (1982) 6932
- <sup>11</sup> J. Rodriguez-Carvajal, *Physica B* **192** (1993) 55 and <http://www-llb.cea.fr/fullweb/winplotr> for the Fullprof2k version.
- <sup>12</sup> B.D. Cullity, *Elements of X-ray Diffraction* (1956) Reading MA: Addison-Wesley and *International tables of crystallography*, Volume B.
- <sup>13</sup> *Metals and Alloys Index* (1992) JCPDS-ICDD
- <sup>14</sup> A. N. Kolmogorov, *Bull. Acad. Sci. USSR, Phys. Ser.* **1** (1937) 355
- <sup>15</sup> W. A. Johnson and P.A. Mehl, *Trans. Am. Inst. Min. Metall. Eng.* **135**(1939) 416
- <sup>16</sup> M. Avrami, *J. Chem. Phys* **7** (1939) 1103, *ibid* **8** (1940) 212 and *ibid* **9** (1941) 177
- <sup>17</sup> A. Guinier, *Comptes rendus de l' Académie des Sciences* **204** (1937) 115 and *ibid* **206** (1938) 1374
- <sup>18</sup> G. Porod, *Kolloid Z.*, **124** (1951) 83
- <sup>19</sup> R.K. Heenan, the "FISH" (data fitting program) manual, RAL report 89-129 (revised 01/09/97)
- <sup>20</sup> Y. Yoshizawa, S. Oguma & K. Yamauchi, *J. Appl. Phys.* **64** (1988) 6044
- <sup>21</sup> M. Garcia del Muro, R. Zquiak and X. Batlle, *J. Magn. Magn. Mat.* **171** (1997) 315
- <sup>22</sup> D.B. de Mooij and K.H.J. Buschow, *J. Less-Common Metals* **136** (1988) 207
- <sup>23</sup> Y.C. Yang et al, *J. Appl. Phys.* **52** (1981) 2077
- <sup>24</sup> H. Fujii et al, *J. Alloys and Compd.* **219** (1995) 10
- <sup>25</sup> J.P. Gavignan, *Physica B* **149** (1988) 345
- <sup>26</sup> G. Venturini, A Verniere and B. Malaman, *J. Alloys Compd.* **319** (2001) 50
- <sup>27</sup> V.M.T.S. Barthem & al, *J. Magn. Magn. Mat.* **208** (2000) 97
- <sup>28</sup> B.A. Everitt et al, *Phys. Rev. B* **56** (1997) 5452
- <sup>29</sup> B. Sharif and B.R. Coles, *J. Less-Common Metals* **62** (1978) 295
- <sup>30</sup> A. Arrott, *Phys. Rev.* **108** (1957) 1394
- <sup>31</sup> B.T. Matthias & R.M. Bozorth, *Phys. Rev.* **109** (1958) 604
- <sup>32</sup> S. Ogawa & N. Sakamoto, *J. Phys. Soc. Japan* **22** (1967) 1214
- <sup>33</sup> K. Lagarec & D.G. Rancourt, *Recoil, Mössbauer spectral analysis software*, Univ. of Ottawa (1998)
- <sup>34</sup> Y.J. Uemura in "Muon Science : Muons in physics, chemistry and materials", edited by S.L. Lee, S. H. Kilcoyne and R. Cywinski, SUSSP and Institute of Physics Publications, 1999.
- <sup>35</sup> S.M. Bennington et al, *Muon studies in Solid Sate Physics*, IOP short meetings (1988), p 81, edited by S.J. Cox
- <sup>36</sup> R.I. Bewley and R. Cywinski, *Phys. Rev. B* **58** (1998) 11544
- <sup>37</sup> J. Rossat-Mignod, *Methods of Experimental Physics*, Vol 23, Part C, Chapter 19.
- <sup>38</sup> J.J. Rhyne, J.H. Shelleng and N.C. Koon, *Phys. Rev. B* **10** (1974) 4672
- <sup>39</sup> D.W. Forester, N.C. Koon, J.J. Rhyne & J.H. Shelleng, *J. Appl. Phys.* **50** (1979) 7336
- <sup>40</sup> J.M.D. Coey et al, *J. Phys. F* **11** (1981) 2707
- <sup>41</sup> S. Ishio et al, *J. Magn. Magn. Mater.* **60** (1986) 236
- <sup>42</sup> J.W.M. Biesterbos, M. Brouha and A.G. Dirks, *Physica* **86-88B** (1977) 770
- <sup>43</sup> Y. Kakehashi and M. Yu, *Zeit. Phys. B* **101** (1996) 487
- <sup>44</sup> A. Fujita et al, *J. Phys. : Cond. Matter* **5** (1993) 3003
- <sup>45</sup> T. Suzuki et al, *J. Phys. : Cond. Matter* **6** (1994) 5741
- <sup>46</sup> H. Terauchi et al, *J. Phys. Soc. Jpn* **52** (1983) 3454
- <sup>47</sup> R. Coehoorn, *Phys. Rev. B* **39** (1989) 13072
- <sup>48</sup> R.F. Sabiryanov and S.S. Jaswal, *Phys. Rev. B* **57** (1998) 7767
- <sup>49</sup> A. E. Clark, *Proceedings of the 19<sup>th</sup> Conference in Magnetism and Magnetic Materials*, AIP, 1974
- <sup>50</sup> A. E. Clark and H. S. Belson, *Phys. Rev. B* **5** (1972) 3642
- <sup>51</sup> F. Schwatz et al, *J. Appl. Phys.* **76** (1994) 5380
- <sup>52</sup> K. Ried et al, *Phys. Stat. Sol. A* **167** (1998) 195

- 
- <sup>53</sup> B. Winsek et al, J. Alloys & Compounds **283** (1999) 78  
<sup>54</sup> C. Larica et al, J. Alloys & Compounds **274** (1998) 23  
<sup>55</sup> D. Crespo and T. Pradell, Phys. Rev. B **54** (1996) 3101

# Chapter VI : Study of the superconducting properties of amorphous Zr-TM

## VI.1. Introduction

In an attempt to study the influence of extreme disorder on the superconducting properties of simple metals, Buckel and Hilsch<sup>1</sup> conducted intensive systematic studies of amorphous metals obtained by quenching metallic vapours onto a cryogenically cooled substrate. They were able to show that these amorphous films have higher superconducting transition temperatures than their crystalline counterparts and that, for instance, amorphous Bi is a superconductor below 6K whereas crystalline Bi is a non-superconducting semi-metal<sup>2</sup>. The first observation of superconductivity in a metallic glass prepared by quenching from the melt (i.e. "bulk" sample) is due to Johnson et al<sup>3</sup> in a LaAu alloy. More recently, Samwer and Lohneysen<sup>4</sup> have showed that superconductivity exists in the  $\alpha$ -Zr<sub>x</sub>Cu<sub>100-x</sub> system and the superconducting transition temperatures vary between 0.3K for x=40 to 3.2K for x=75. Altounian and Strom-Olsen<sup>5</sup> have studied in great details the  $\alpha$ -ZrTM (which TM = Cu, Ni, Fe, and Co) system for which they demonstrated the importance of the spin fluctuations. This is perhaps not surprising as the high density of states necessary for superconductivity is also favourable to the formation of spin fluctuations. The pressure dependence of the spin fluctuations in amorphous Zr<sub>75</sub>Ni<sub>25</sub> and Zr<sub>75</sub>Fe<sub>25</sub> was studied by Hamed et al<sup>6</sup> ( $T_c$  increases with increasing pressure) and analysed within the McMillan<sup>7</sup> framework. Spin fluctuations were thought to act as pair breakers and therefore inhibit superconductivity<sup>8</sup> until the recent theory of antiferromagnetic spin-fluctuation driven superconductivity in exotic superconductors<sup>9</sup> (heavy fermions, HTc and organic superconductors), based on the Moriya's Self Consistent Renormalisation (SCR)<sup>10</sup> theory of magnetism. According to this SCR treatment, the relevant parameter for determining the energy scale of the pairing mechanism is the energy width  $T_0$  of the dynamical spin fluctuations and an observed linear dependence between  $T_c$  and  $T_0$  is derived. Historically,  $\mu$ SR has played a very important role in identifying the condensation mechanisms. For instance, the so-called Uemura plot<sup>11</sup> where the superconducting transition  $T_c$  is plotted versus the Fermi

temperature  $T_F$ , extracted from  $\mu$ SR data, tends to favour a Bose-Einstein (BE) like rather than a BCS mechanism. Moreover, a similar ratio of the experimental  $T_c/T_B$  and the predicted  $T_c/T_0$  suggests that the spin fluctuations considered in the SCR theory could account for a real space local pairing of the superconducting carriers, leading to a BE condensation<sup>12</sup>. In the light of these recent results in unconventional superconductors, a  $\mu$ SR study of a completely different system, the amorphous ZrTM, where the importance of spin fluctuations has been recognised, seemed very appropriate. This chapter will be devoted to such a study. More specifically, the ZrFe system will be looked into more details as, if pressure is replaced by Zr concentration, its phase diagram<sup>13</sup> (see *Figure VI- 1*) is not dissimilar to systems such as CePd<sub>2</sub>Si<sub>2</sub> and CeIn<sub>3</sub>, antiferromagnetic at ambient pressure but superconducting at around 20 kbars, for which a strong coupling was attributed to dynamical spin fluctuations near magnetic instabilities<sup>14</sup>. It should be noted that the amorphous ZrFe system has not been studied for temperatures lower than 1.8K and it is not known exactly how close the ferromagnetic and superconducting part of the phase diagram are. More recently, superconductivity on the border of itinerant magnetism has been observed in the heavy fermion<sup>15</sup> UGe<sub>2</sub> and in textbook itinerant ferromagnet<sup>16</sup> ZrZn<sub>2</sub>. Remarkably, a similar phase diagram where the oxygen doping replaces the Pressure in the x-axis can be drawn for high-temperature superconductors and has led some authors to suggest a magnetic coupling.

## **VI.2. A brief review on superconductivity**

In 1911, a few years after having been the first person to liquefy helium thereby opening the field of low temperature research, Kamerlingh Onnes<sup>17</sup> observed that the electrical resistivity of mercury suddenly drops to zero below a certain transition temperature  $T_c$ . This constituted the first observation of superconductivity, a phenomenon which, as we shall described later, exhibits properties far richer than just perfect conductivity.

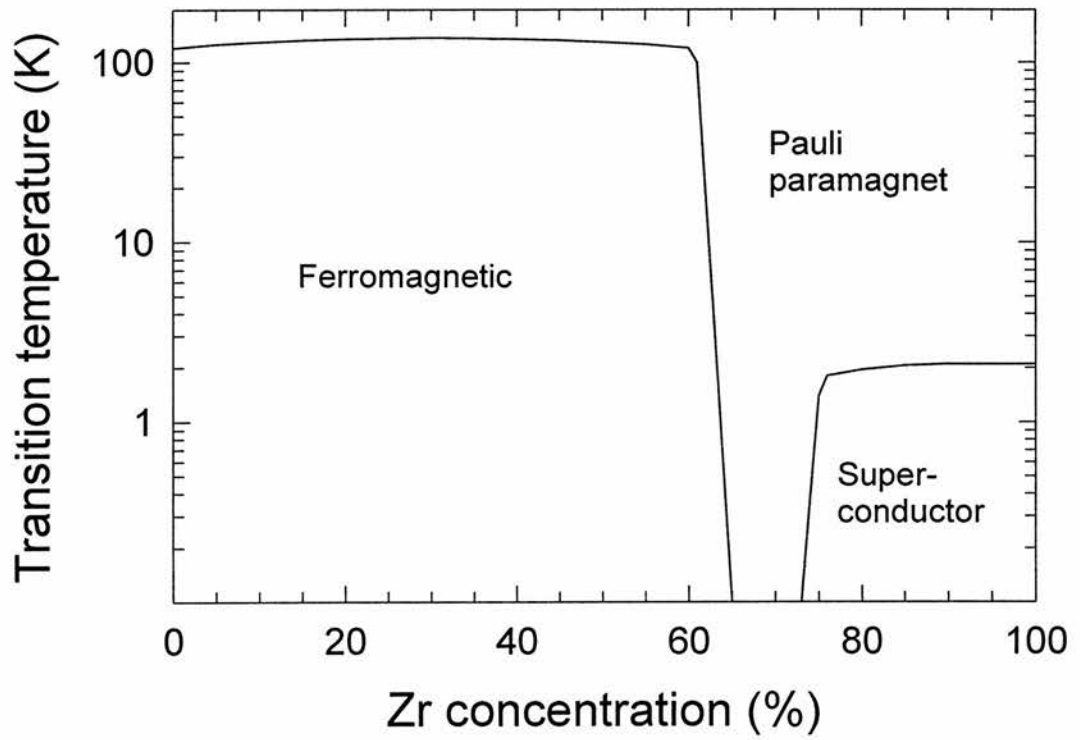


Figure VI- 1 : phase diagram for amorphous Zr-Fe from reference 1.

### VI.2.a. Meissner effect and the two types of superconductivity

Meissner and Ochsenfeld<sup>18</sup> showed that when a metal in its normal state is put into a magnetic field and then cooled below its transition temperature, the magnetic flux is expelled from the sample. Hence, we have  $B = H_a + 4\pi M = 0$  where  $H_a$  is the applied field. In other words, a superconductor exhibits perfect diamagnetism as its magnetic susceptibility is given by :

$$\chi = \frac{\partial M}{\partial H} = -\frac{1}{4\pi} \quad \text{Eq. VI- 1}$$

This behaviour does not result solely from perfect conductivity for which, using Maxwell's equation  $\partial \mathbf{B} / \partial t = -\mathbf{c} \text{curl} \mathbf{E}$  and recognising that the electric field  $\mathbf{E}$  is null inside a perfect conductor, only  $\partial \mathbf{B} / \partial t$  is expected to be equal to zero.

From the Meissner-Ochsenfeld experiment, the magnetisation curve expected for a superconductor is that of *Figure VI- 2* and the sample is called a type-I superconductor. By contrast, other materials show a different magnetisation curve where above a certain field  $H_{c1}$  they do not behave like a perfect diamagnet but they still conserve their electrical properties, they are in the mixed state and above the critical field  $H_{c2}$  the superconductivity disappears (see *Figure VI- 3*). These materials are termed type-II superconductors and are often transition metals or alloys having a shorter electronic mean-free path. As we shall see later, between  $H_{c1}$  and  $H_{c2}$ , the flux penetrates the sample in the form of a lattice of flux lines each carrying a flux  $\phi_0 = 2.07 \times 10^{-15} \text{ T.m}^2$ .

### VI.2.b. The Two-fluid model

As an analogy with the superfluidity<sup>19</sup> in  $\text{He}^{\text{II}}$ , it is possible to describe a superconductor as two fluids : one consisting of normal electrons and the other one of superconducting electrons. This phenomenological model was introduced in 1934 by Gorter and Casimir<sup>20</sup> but is however not really correct as, contrarily to the superfluidity case, the normal fluid can be scattered by impurities or lattice defects. If we chose  $x$  to be the ratio between the normal electrons to the total number of electrons,  $-\beta$  to be the condensation energy for  $x=1$  and  $\gamma T^2/2$  the normal free electron energy, the free energy can be written as :

$$F(x, T) = -\frac{x^{1/2} \gamma T^2}{2} - (1-x)\beta \quad \text{Eq. VI- 2}$$



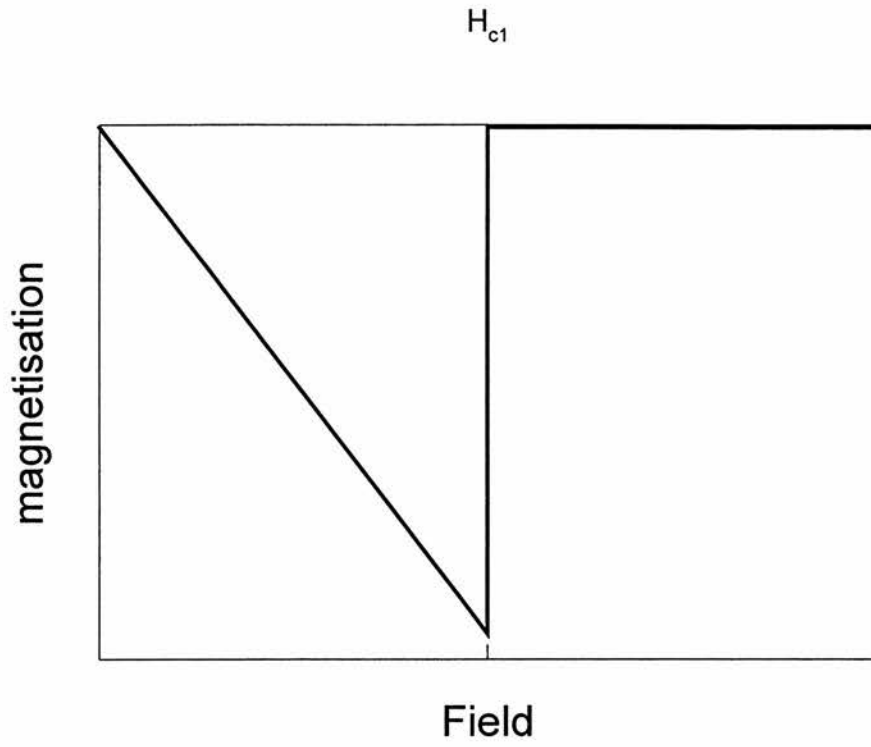


Figure VI - 2 : magnetisation curve of a type I superconductor.

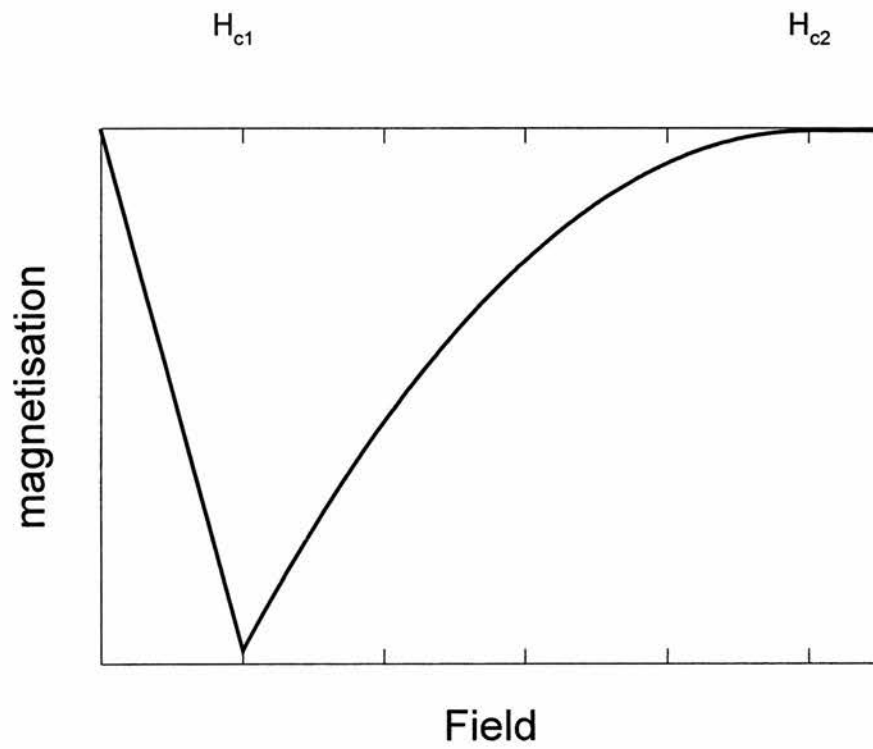


Figure VI- 3 : magnetisation curve for a type II superconductor.

Minimising  $F$  with respect to  $x$  and defining  $T_c = 4\beta/\gamma$  gives :

$$x = \left[ \frac{T}{T_c} \right]^4 \quad \text{Eq. VI- 3}$$

from which the temperature dependence of the superelectron density can be derived :

$$n_s(T) = n_s(0) \left( 1 - \left[ \frac{T}{T_c} \right]^4 \right) \quad \text{Eq. VI- 4}$$

The extension of the two-fluid model that is used consists simply in replacing the power 4 by some power  $n$ .

### VI.2.c. Pinning and critical state

One important experimental aspect of the superconductivity is the pinning of the flux lines by structural defects. Indeed, for a practical application such as the fabrication of a high field magnet, the superconductor must not only have a high critical field (type II) but must also be able to carry a high current in that field without resistance. However, in a defect-free type II superconductor, the Lorentz force acting on the flux lines due to the presence of a magnetic field and a current causes the flux lines to move transverse to the current. This movement induces an electric field parallel to the applied current and effectively acts as a resistive voltage. This implies that power is dissipated. If, on the other hand, there are some "pins" in the material that can prevent the flux lines to move due to the Lorentz force and stay fixed to certain locations, power dissipation will not occur. The most obvious choice for such a pinning mechanism is the existence of spatial inhomogeneities in the material such as impurities, inclusions, voids, grain boundaries, etc... These pins being normal, the Flux Line Lattice will have a lower energy if the cores are sitting on these defects. To be efficient, these pins need to have a volume of the order of  $\xi^3$ . The presence of pinning in superconductors also explains the existence of hysteresis in the experimental magnetisation curves (see *Figure VI- 4*) : on increasing the field strength from zero, there is no sudden entry of flux at  $H_{c1}$  and similarly, on reducing the field from a value above  $H_{c2}$ , some fluxons get trapped in the superconductor.

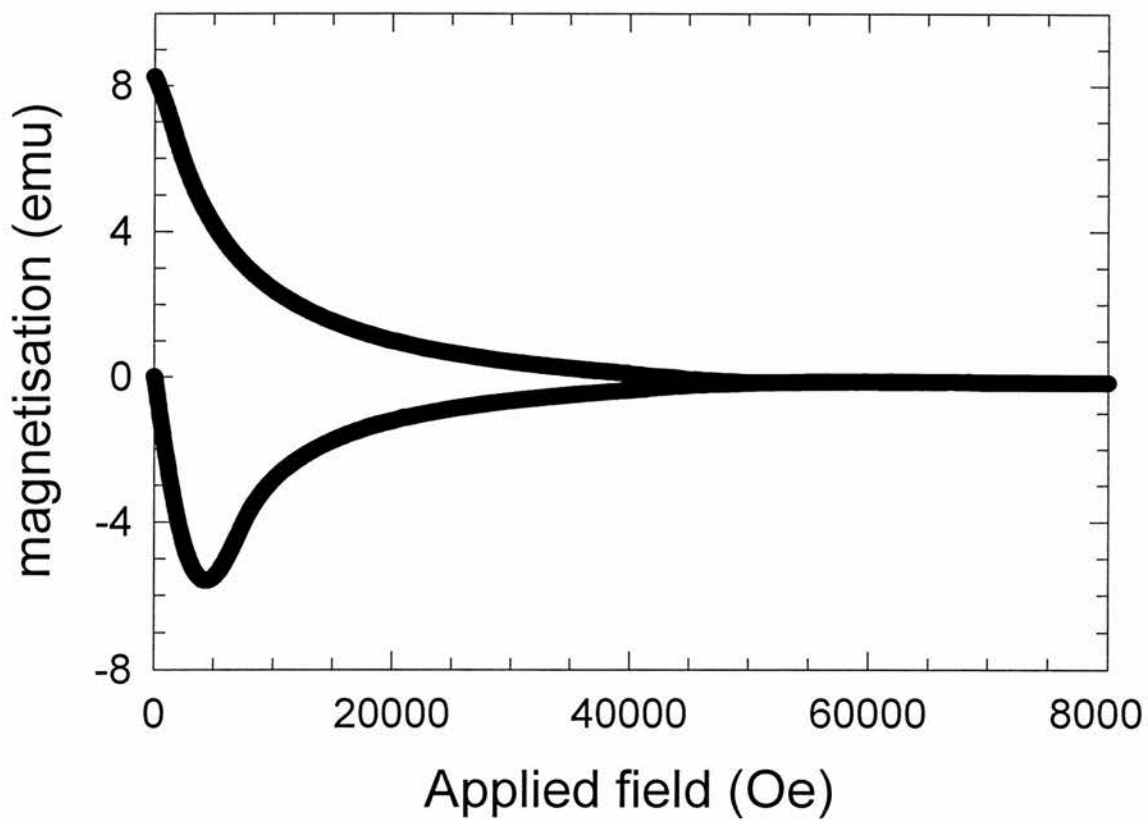


Figure VI- 4 : Experimental magnetisation curve for a  $Zr_2(RhFe)$  alloy showing the presence of strong hysteresis.

In 1962, Bean<sup>21</sup> developed a simple model based on a strong pinning to qualitatively explain the magnetisation curves in a superconductor. He assumed that as the field is increased above  $H_{c1}$ , the flux does not penetrate uniformly inside the superconductor but that, instead, the flux density profiles are straight lines of slope  $4\pi J_c/c$  where  $J_c$  is the critical current. Using this model, it is possible to relate the width  $\Delta M = M_{\uparrow} - M_{\downarrow}$  of the magnetisation to the value of the critical current. For a cylindrical sample,  $J_c = 3\Delta M / 2R$  and for a spherical sample,  $J_c = 16 \Delta M / 3\pi\mu_0 d$  ( $R$  = radius of the cylinder,  $d$  = diameter of the sphere).

#### VI.2.d. Ginzburg-Landau equations and London model

In 1950, Ginzburg and Landau (GL) developed a phenomenological theory of superconductivity<sup>22</sup> that was able to account for the two different types of superconductivity. Their theory is based around the concept of Landau phase transition theory and the complex order parameter  $\psi(x)$  chosen was a macroscopic wave-function describing the superconducting electrons. As  $\psi(x)$  is a complex quantity, it possesses an amplitude and a phase. The free energy density in a presence of a magnetic field  $\mathbf{B}$  can be written as:

$$F_s = F_n + a |\psi|^2 + b |\psi|^4 + (1/2m^*) |-i\hbar\nabla\psi + (e^* \mathbf{A}\psi/c)|^2 + B^2/8\pi \quad \text{Eq. VI-5}$$

where  $m^*$  and  $e^*$  are the effective mass and charge of the particles described by  $\psi$  and  $\mathbf{A}$  is the vector potential.

By convention, GL chose the normalisation  $|\psi|^2 = n_s^* = n_s / 2$ . Experiments<sup>23</sup> impose  $m^* = 2m$  and  $e^* = 2e$ . In other words,  $\psi$  describes the pair of electrons. As we shall see later, Bardeen-Cooper-Schrieffer<sup>24</sup> proposed in 1957 a microscopic theory in which the normal state (all the electronic states are occupied inside the Fermi surface and none outside) becomes unstable under an attractive interaction between electrons forming Cooper pairs ( $k_{\uparrow}, -k_{\downarrow}$ ) hence confirming the GL phenomenological approach. It should be noted that although the isotopic effect<sup>25</sup> ( $M^{\alpha}T_c$  constant for different isotopes with  $\alpha$  generally equals to 1/2) strongly suggests that the electron-phonon interaction is responsible for the attractive interaction between electrons, in principle, any attractive interaction could lead to the formation of Cooper pairs.

In an uniform external field, the Gibbs function is given by :

$$\int d^3x \left[ F_s - \frac{1}{4\pi} \mathbf{B} \cdot \mathbf{H} \right] = \int d^3x G_s \quad \text{Eq. VI- 6}$$

and must be stationary with respect to the variations of the order parameter and of the vector potential  $\mathbf{A}$  such that  $\mathbf{curl} \mathbf{A}(x) = \mathbf{B}(x)$ .

The minimisation of the  $G_s$  with respect to  $\psi^*$  gives the first GL equation :

$$\frac{1}{2m^*} \left( -i\hbar\nabla + \frac{e^* \mathbf{A}}{c} \right)^2 \psi + a\psi + b|\psi|^2\psi = 0 \quad \text{Eq. VI- 7}$$

whereas with respect to  $\mathbf{A}$  it gives the second GL equation :

$$\frac{c}{4\pi} \mathbf{curl} \mathbf{B} = -\frac{e^* \hbar}{2m^* i} \left( \psi^* \nabla \psi - \psi \nabla \psi^* \right) - \frac{(e^*)^2}{m^* c} |\psi|^2 \mathbf{A} = \mathbf{j} \quad \text{Eq. VI- 8}$$

which is the quantum mechanical expression of a current of particles described by a wave-function  $\psi$ . Studying the solutions for some limit cases of the GL equations enables us to introduce the two main parameters of a superconductor : its coherence length and its magnetic penetration depth and to distinguish between the two type of superconductivity.

In zero applied field,  $\mathbf{A} = \mathbf{0}$  and therefore  $\nabla \mathbf{A} = 0$  and we obtain  $\psi = 0$  (normal state) or  $|\psi|^2 = -a/b$  (superconducting state). By considering an 1D geometry where  $\psi$  varies but  $\mathbf{B} = 0$ , the GL equations give with  $f(z) = \psi(z) / |\psi_\infty|$  where  $|\psi_\infty| = (|a|/b)^{1/2}$  :

$$-\frac{\hbar^2}{2m^* |a|} \frac{d^2 f}{dz^2} - f + f^3 = 0 \quad \text{or simply}$$

$$\frac{d^2 f}{dz^2} = -\frac{1}{\xi^2} f(1 - f^2) \quad \text{with} \quad \xi^2 = \frac{\hbar^2}{2m^* |a(T)|} \quad \text{Eq. VI- 9}$$

$\xi$  is called the coherence length and is a measure of the length scale of the variations of  $\psi$  i.e. the spatial variations of  $\psi$  are restricted to a region  $|z| \approx \xi$ . In other words,  $\xi$  represents the distance on which  $\psi$  varies from its maximum value to zero.

By applying a magnetic field but considering the order parameter to be uniform i.e.  $\psi = \psi_\infty$  the second GL equation reduces to

$$\frac{c}{4\pi} \mathbf{curl} \mathbf{B} = -\frac{(e^*)^2}{m^* c} |\psi|^2 \mathbf{A}(x) = \mathbf{j}(x) \quad \text{Eq. VI- 10}$$

The magnetic penetration depth  $\lambda$  can now be deduced via :

$$(4\pi/c)\mathbf{j} = \mathbf{curl} \mathbf{B} = \mathbf{curl} \mathbf{curl} \mathbf{A} = (-1/\lambda^2) \mathbf{A} \quad \text{Eq. VI- 11}$$

This is equivalent to the London electro-dynamical treatment<sup>26</sup> that will be explained in more details later and we obtain :

$$\lambda = -\frac{(e^*)^2}{m^* c} |\psi|^2 = -\frac{(e^*)^2}{m^* c} n_s^* \quad \text{Eq. VI- 12}$$

It now becomes evident that the GL ratio  $\kappa = \lambda / \xi$  represents a good way of determining whether a superconductor is a type-I or a type-II. Indeed, if  $\kappa \leq 1/\sqrt{2}$  the superconductor is of type-I whereas if  $\kappa > 1/\sqrt{2}$  it is of type-II (see *Figure VI- 5*).

From now on, type-II superconductivity will be the main focus of interest since the samples studied are of this type. For a type-II superconductor, the order parameter can go to zero over a length smaller than the penetration depth, this suggests that there should be some inclusion of normal phase in the mixed state. Alternatively, the existence of the mixed state can be justified as a result of the negative total surface energy, favourable to the inclusion of small normal regions (to maximise the interface normal/superconducting thereby minimising the energy) due to the fact that the positive magnetic contribution increases less rapidly, as a function of distance, than the negative electron ordering contribution. Abrikosov<sup>27</sup> discovered a periodic solution of the GL equations which consists of a lattice of parallel flux lines each carrying a quantum of flux  $\phi_0 = h/2e = 2.07 \times 10^{-15} \text{ Tm}^2$ . The cores of these vortex have a length of  $\xi$  and are in the normal state ( $|\psi| = 0$ ) and the field extends to the superconducting region over a length of  $\lambda$ .  $\xi$  and  $\lambda$  can be estimated by the values of  $H_{c1}$  and  $H_{c2}$  via the relations<sup>28</sup> :

$$H_{c1} = \frac{\phi_0}{4\pi\lambda^2} (\ln \kappa + 0.5) \quad \text{and} \quad H_{c2} = \frac{\phi_0}{2\pi\xi^2} \quad \text{Eq. VI- 13}$$

At this point, we will introduce the modified London equation<sup>29, 30</sup>. As part of my PhD project, I wrote a program enabling the field inside a type-II superconductor to be mapped and the subsequent field distribution to be calculated. Although the amorphous samples I prepared in St-Andrews are isotropic type-II superconductors, the theory presented here accounts for the anisotropy since it is very easy to go back to the anisotropic case by setting the parameters introduced below to certain values (namely  $\Gamma=1$  and  $\theta=0$ ). The London theory can be regarded as a good approximation for high- $\kappa$  superconductors provided  $H_{c1} \ll H \ll H_{c2}$ .



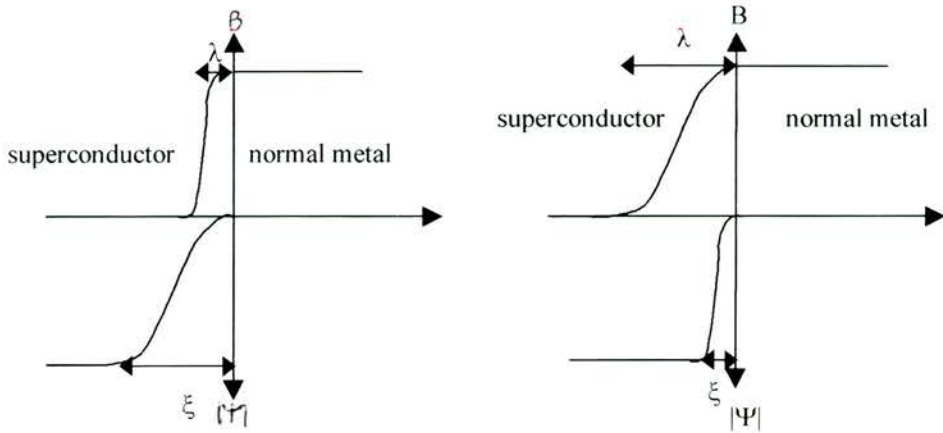


Figure VI- 5 : Variation of the order parameter  $|\psi|$  and the magnetic field  $B$  at the interface superconductor-normal metal for a type-I (left) and a type-II (right) superconductor.

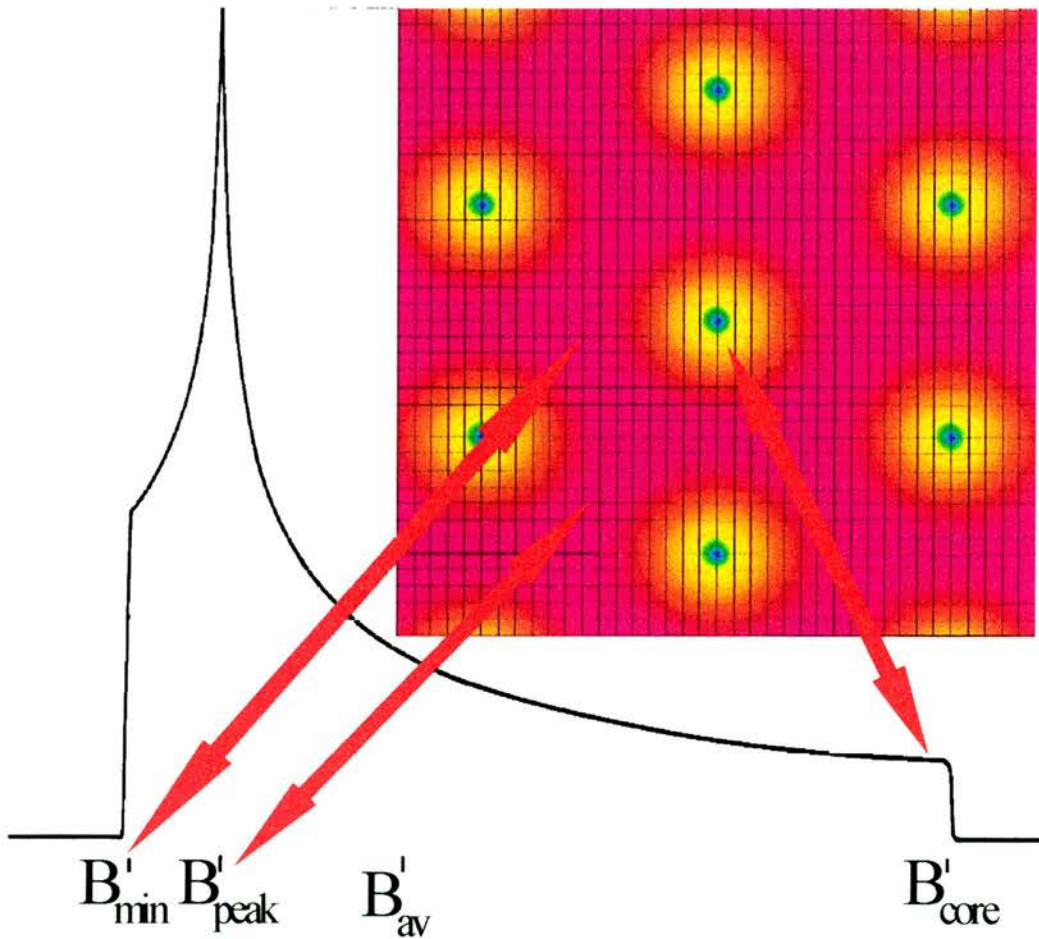


Figure VI- 6 : Calculated field profile for a hexagonal Flux Line Lattice (insert) and the associated field distribution.

The starting point is to write the free energy density (energy density of the magnetic field + kinetic energy) and minimise it with respect to the variations in the magnetic field. As the high- $\kappa$  limit implies a rapid variation of the order parameter from one to zero inside the region core (the superconducting carrier density  $n_s$  is zero at the centre of the core), it is possible to model the core by introducing a  $\delta$  source term. In anisotropic uniaxial superconductors such as  $\text{YBa}_2\text{Cu}_3\text{O}_{7-\delta}$ , measurements show that the superconducting currents flow easily parallel to the a-b directions ( $\text{CuO}_2$  planes) but with more difficulty along the c-axis. Therefore, two different London penetration depths and consequently two different effective masses ( $m_x=m_y=m_1$  and  $m_z=m_3$ ) of the superconducting particle can be defined. It is also useful to introduce the angle  $\theta$  between the c-axis and the average field  $B$ , the average mass  $m_{\text{av}} = (m_1^2 m_3)^{1/3}$  and the anisotropy parameter  $\Gamma = m_3/m_1$ .

The minimisation of the London equation gives <sup>31</sup>:

$$\begin{aligned} b_x - \lambda^2 \left( m_{zz} \nabla_{xy}^2 b_x - m_{xz} \frac{\partial^2 b_z}{\partial y^2} \right) &= 0 \\ b_y - \lambda^2 \left( m_{zz} \nabla_{xy}^2 b_y - m_{xz} \frac{\partial^2 b_z}{\partial x \partial y} \right) &= 0 \\ b_z - \lambda^2 \left( m_1 \frac{\partial^2 b_x}{\partial x^2} + m_{xx} \frac{\partial^2 b_z}{\partial y^2} - m_{xz} \nabla_{xy}^2 b_x \right) &= \phi_0 \sum_{\nu} \delta(\mathbf{r} - \mathbf{r}_{\nu}) \end{aligned} \quad \text{Eqs. VI- 14}$$

where  $m_{xx} = m_1 \cos^2 \theta + m_3 \sin^2 \theta$ ,  $m_{xy} = m_{yz} = 0$ ,  $m_{zz} = m_1 \sin^2 \theta + m_3 \cos^2 \theta$ ,  $m_{yy} = m_1$ ,  $m_{xz} = (m_1 - m_3) \sin \theta \cos \theta$ ,  $\lambda^2 = m_{\text{av}} c^2 / 4\pi n_s e^2$ ,  $\nabla_{xy}^2 = \partial^2 / \partial x^2 + \partial^2 / \partial y^2$  and  $\mathbf{r}_{\nu}$  are vectors to the vortices in the (x,y) plane.

The periodicity of the lattice enables us to expand the field in the Fourier series :

$$\mathbf{b}(\mathbf{r}) = \sum_{\mathbf{G}} \mathbf{b}(\mathbf{G}) \exp(i\mathbf{G} \cdot \mathbf{r}) \quad \text{Eq. VI- 15}$$

and reciprocally 
$$\mathbf{b}(\mathbf{G}) = \frac{B}{\phi_0} \int \mathbf{b}(\mathbf{r}) \exp(-i\mathbf{G} \cdot \mathbf{r}) d^2 \mathbf{r} \quad \text{Eq. VI- 16}$$

where the integral is taken over one FLL unit cell.

The equations for the field become :

$$\begin{aligned} b_x(\mathbf{G}) &= B\lambda^2 m_{xz} G_y^2 / d \\ b_y(\mathbf{G}) &= -B\lambda^2 m_{xz} G_x G_y / d \\ b_z(\mathbf{G}) &= B(1 + \lambda^2 m_{zz} G^2) / d \end{aligned} \quad \text{Eq VI- 17}$$

with  $d = (1 + \lambda^2 m_1 G_x^2 + \lambda^2 m_{xx} G_y^2)(1 + \lambda^2 m_{zz} G^2) - \lambda^4 m_{xz}^2 G^2 G_y^2$ .

The basis vectors of the primitive cell can be written as :

$$\mathbf{a}_1 = \left( \frac{2\phi_0}{B} \right)^{1/2} \left( \frac{m_{zz}}{3m_3} \right)^{1/4} \hat{\mathbf{x}} \quad \text{and} \quad \mathbf{a}_2 = \frac{a_1}{2} \left[ \hat{\mathbf{x}} + \left( \frac{3m_3}{m_{zz}} \right)^{1/2} \hat{\mathbf{y}} \right] \quad \text{Eq. VI- 18}$$

They describe triangles which become equilateral for  $\theta = 0$ .

The reciprocal lattice vectors corresponding to the cell ( $\mathbf{a}_1, \mathbf{a}_2$ ) are :

$$\begin{aligned} G_x &= \pi \left( \frac{2B}{\phi_0} \right)^{1/2} \left( \frac{3m_3}{m_{zz}} \right)^{1/4} n \\ \text{and } G_y &= \pi \left( \frac{2B}{\phi_0} \right)^{1/2} \left( \frac{m_{zz}}{3m_3} \right)^{1/4} (2m - n) \end{aligned} \quad \text{Eqs. VI- 19}$$

with  $m, n = 0, \pm 1, \pm 2, \dots$

Hence the inputs of the program are  $\Gamma$  (thus  $m_1$  and  $m_3$ ),  $\lambda$  and  $\theta$ . The mass tensor  $m_{\alpha\beta}$  and the field in reciprocal space are calculated and a Fourier transform is performed to obtain the field in real space. The field distribution is obtained by building a histogram and further precision is obtained by extrapolating the field between the points in real space via the bilinear interpolation process<sup>32</sup>.

The insert of *Figure VI- 6* is a map of the field inside an isotropic type-II superconductor for a 400G applied field and a penetration depth of 600nm obtained by the program. The field distribution is plotted on the same figure. As observed, the distribution is by no means symmetric and a gaussian distribution cannot be assumed. The maximum field ( $B_{\text{cores}}$ ) is obviously at the centre of the cores, the minimum field  $B_{\text{min}}$  corresponds to the centre of a triangle formed by three flux lines and the most probable field  $B_{\text{peak}}$  corresponds to the middle point between two flux lines. It should be noted that the program has also been tested in the anisotropic mode where, as expected<sup>33</sup>, peaks close (or at) to zero appear in the  $n(b_x)$  and  $n(b_y)$  distributions and two peaks instead of one can be seen in the  $n(b_z)$  distribution (unfortunately, these two peaks

are very close to one another and get smeared out by instrumental broadening and/or pinning. Some experiments suggest their existence<sup>34</sup> but to my knowledge no conclusive data have been published).

This London model can be refined by theory to take into account cases where the magnetic field gets close to  $B_{c2}$ . This  $b=B/B_{c2}$ , where  $B$  is the applied field, correction introduces an  $\exp(-\xi^2 G^2/2(1-b))/(1+G^2\lambda^2/(1-b))$  term in *Eq. VI- 15*. It should be noted that this core correction is isotropic and would require modifications for the anisotropic case).

However, in a polycrystalline material, the distribution has to be integrated over all angles via the equation :  $n(b_z) = \int_{\theta_{\min}}^{\theta_{\max}} n_{\text{perf}}(b_z, \theta) \sin \theta d\theta$  and the resulting distribution becomes smeared out and looks more symmetric<sup>35</sup>. Consequently, a simple gaussian is sometimes used for analysing  $\mu$ SR data<sup>36</sup> (see discussion in Chapter III).

### **VI.2.e. Microscopic theory of Bardeen-Copper-Schrieffer**

In 1957, more than forty years after Kamerlingh Onnes' experimental discovery<sup>17</sup>, Bardeen, Cooper and Schrieffer<sup>24</sup> were the first to propose a theory which successfully explained the microscopic mechanisms involved in the phenomenon of superconductivity. The basic idea behind the BCS theory is the following : the ground state in the normal state (all the electronic states inside the Fermi sphere are occupied and empty outside) becomes unstable with respect to a electron pairing ( $\mathbf{k}\uparrow, -\mathbf{k}\downarrow$ ) due to the presence of an attractive interaction between electrons. The resulting binding energy separates the excited states from the ground state by an energy gap and most of the thermodynamic and magnetic properties are consequences of the existence of this gap. The isotope effect shows the importance of the electron-phonon interaction and Fröhlich<sup>37</sup> was the first to propose an attractive interaction between electrons driven by the electron-phonon interaction. A simplistic picture very often used to describe this interaction is : an electron interacts with a positively charged lattice (ions) and distort this lattice. Due to the inertia of the ions, this distortion remains after the passage of the electron and can attract another electron. A schematic of the interaction where an electron emits a virtual phonon that is absorbed by a second electron can be found on *Figure VI- 7*. It should be noted that it only involves a *virtual* phonon, this is very important as it implies that this interaction can persist to very low temperatures where

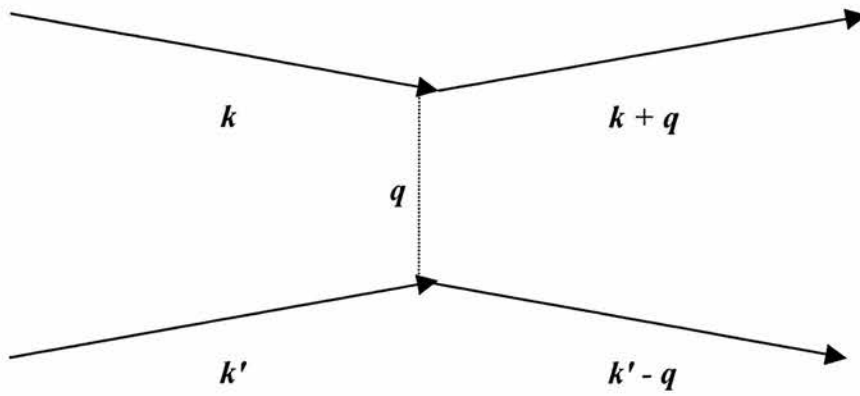


Figure VI- 7 : the attraction between electrons due to the Fröhlich interaction.

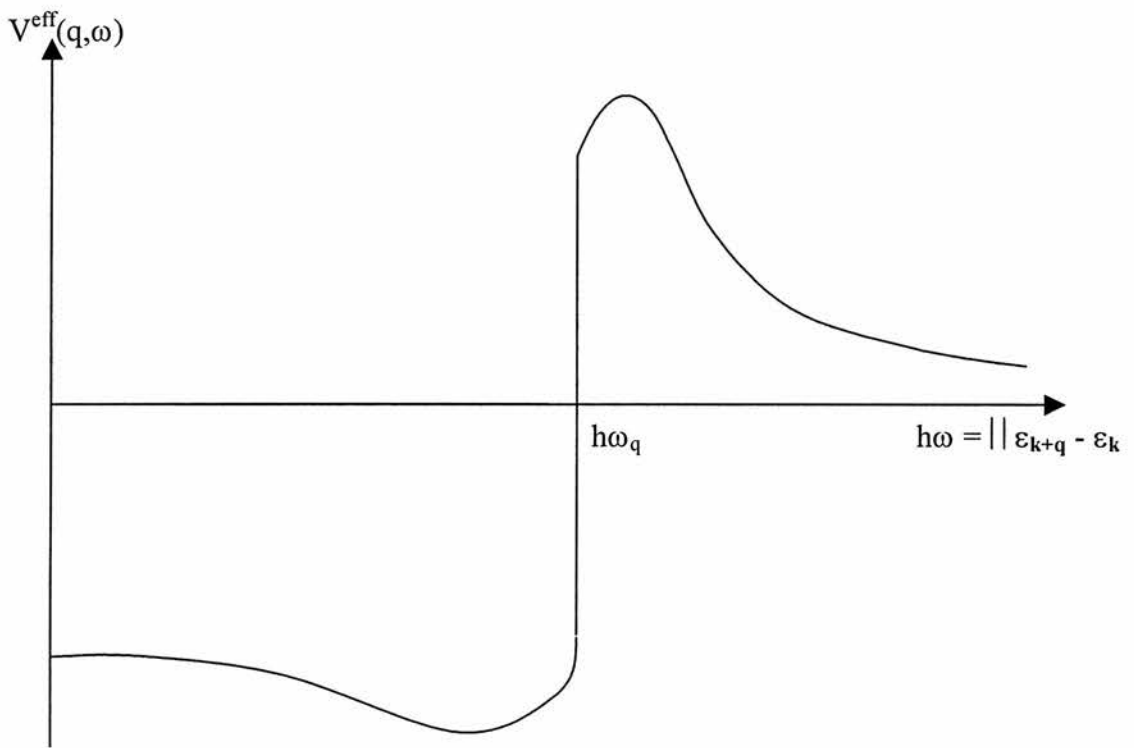


Figure VI- 8 : frequency dependence of the effective interaction in the jellium model.

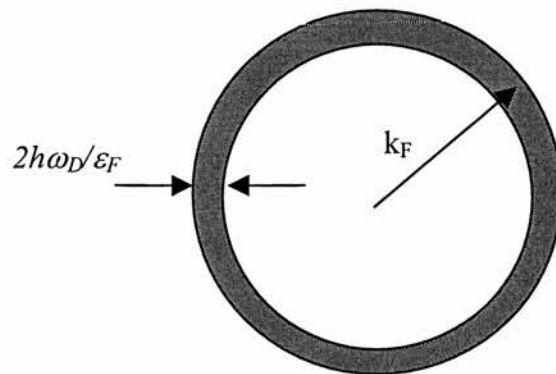


Figure VI- 9 : shell of integration for the BCS Hamiltonian

no phonons can be excited thermally. Briefly, the Fourier transform of the Coulomb interaction  $4\pi e^2/q^2$  is screened by the interaction between two electrons and by the ions and can be written, for two electrons of wavevectors  $\mathbf{k}$  and  $\mathbf{k}'$  and energies  $\epsilon_{\mathbf{k}}$  and  $\epsilon_{\mathbf{k}'}$  as<sup>38</sup> :

$$V_{\mathbf{k},\mathbf{k}'}^{\text{eff}} = \frac{4\pi e^2}{q^2 + q_0^2} \left[ 1 + \frac{\omega(\mathbf{q})}{\omega^2 - \omega(\mathbf{q})^2} \right] \quad \text{Eq. VI- 20}$$

where  $\omega(\mathbf{q})$  is the phonon frequency,  $\mathbf{q} = \mathbf{k} - \mathbf{k}'$ ,  $\omega = (\epsilon_{\mathbf{k}} - \epsilon_{\mathbf{k}'})/h$  and the term between brackets is due to the movement of the ions. As the upper limit for the phonon frequency is of the order of the Debye frequency  $\omega_D$ , the phonon correction is small when the energies of the two electrons differ by more than  $h\omega_D$ . Typically,  $\epsilon_F/h\omega_D$  is of the order of  $10^2$ - $10^3$  which means that only the electrons with very similar energies will be affected. However, when the difference in energy is less than  $h\omega_D$ , the phonon contribution effectively introduces an attraction between electrons (see *Figure VI- 8*).

More specifically, the electron-phonon interaction can be written as<sup>39</sup> :

$$H_{\text{ep}} = i \sum_{\mathbf{k},\mathbf{q}} g_{\mathbf{q}} c_{\mathbf{k}+\mathbf{q}}^+ c_{\mathbf{k}} (a_{\mathbf{q}} - a_{-\mathbf{q}}^+) \quad \text{Eq. VI- 21}$$

where  $c$  and  $c^+$  (resp.  $a$  and  $a^+$ ) are fermions (resp. bosons) operators and  $g_{\mathbf{q}}$  is a coupling constant that will be assumed to be real and independent of  $\mathbf{q}$  in the following.

The total Hamiltonian can then be written as :

$$H = \sum_{\mathbf{k}} \epsilon_{\mathbf{k}} c_{\mathbf{k}}^+ c_{\mathbf{k}} + \sum_{\mathbf{q}} \omega(\mathbf{q}) a_{\mathbf{q}}^+ a_{\mathbf{q}} + i \sum_{\mathbf{k},\mathbf{q}} g_{\mathbf{q}} c_{\mathbf{k}+\mathbf{q}}^+ c_{\mathbf{k}} (a_{\mathbf{q}} - a_{-\mathbf{q}}^+) \quad \text{Eq. VI- 22}$$

BCS used a simplified version of this Hamiltonian by replacing the effective interaction by :  $V(\mathbf{q},\omega) = -V/2$  for  $\epsilon_F - h\omega_D < \epsilon_{\mathbf{k}}$  and  $\epsilon_{\mathbf{k}\pm\mathbf{q}} < \epsilon_F + h\omega_D$  and null otherwise. In other words, the attraction between two electrons is constant and attractive if  $\mathbf{k}$  and  $\mathbf{k}' \pm \mathbf{q}$  are in a shell of width  $2h\omega_D/\epsilon_F$  (see *Figure VI- 9*). The Hamiltonian becomes :

$$H_{\text{BCS}} = \sum_{\mathbf{k},\sigma} \epsilon_{\mathbf{k}} c_{\mathbf{k}\sigma}^+ c_{\mathbf{k}\sigma} - \frac{V}{2\Omega} \sum_{\mathbf{k},\mathbf{k}',\mathbf{q},\sigma,\sigma'} c_{\mathbf{k}+\mathbf{q},\sigma}^+ c_{\mathbf{k}\sigma} c_{\mathbf{k}'-\mathbf{q},\sigma'}^+ c_{\mathbf{k}',\sigma'} \quad \text{Eq. VI- 23}$$

where the energies are labelled with respect to the Fermi level.

In a paper published one year before the BCS theory, Cooper<sup>40</sup> showed that two electrons interacting through an attractive potential in the Fermi sea, can form a bound state  $(k_0\uparrow, -k_0\downarrow)$  whose energy is negative. Consequently, this state induces an instability of the Fermi surface. Using the same Cooper pair, it can be shown that the



same instability of the normal state exists for the BCS Hamiltonian (Eq. VI- 20). This is however not satisfactory as it only considers two electrons and neglects the interactions between pairs : the proper theory requires a N-body treatment. However, the complete BCS Hamiltonian involves a large number of nearly degenerate configurations, some of which do not possess negative elements for the interaction. Guided by the Cooper pair problem, BCS chose a  $\mathbf{k} + \mathbf{k}' = 0$  and  $S = 0$  pairing mechanism for which the matrix elements of the interaction are always negative. The Hamiltonian can then be reduced to the sub-space where the states are occupied only by pairs ( $\mathbf{k}\uparrow, -\mathbf{k}\downarrow$ ). More explicitly :

$$H_{\text{red}}^{\text{BCS}} = \sum_{\mathbf{k},\sigma} \varepsilon_{\mathbf{k}} n_{\mathbf{k},\sigma} - \frac{V}{\Omega} \sum_{\mathbf{k},\mathbf{k}'} c_{\mathbf{k}\uparrow}^{\dagger} c_{-\mathbf{k}\downarrow}^{\dagger} c_{-\mathbf{k}\downarrow} c_{\mathbf{k}\uparrow} \quad \text{Eq. VI- 24}$$

where  $n_{\mathbf{k},\sigma}$  is the occupation number of the state  $\mathbf{k},\sigma$ .

It should be noted that the pair was chosen in a s-state ( $L=0, S=0$ ) but that nothing in principle forbids a more exotic  $L=1, 2 \dots$  pairing although most calculations show that the singlet state has the biggest bound energy. Furthermore, as the BCS Hamiltonian does not contain explicitly the electron-phonon interaction but a rather crude approximation, it is possible to imagine mechanisms other than the electron-phonon coupling to be responsible for the attraction between electrons and therefore for the superconductivity. It seems however that an exchange of quasi-boson (this could be a magnon, a paramagnon, a plasmon, an exciton...) between the two electrons is required. BCS were able to show that their Hamiltonian was consistent with the observed properties of superconductors using a variational method but an easier way of obtaining the same result was later given by Bogoliubov<sup>41</sup> and will be used in the following. The equations of motion for  $c_{\mathbf{k}}^{\dagger}$  and  $c_{-\mathbf{k}}$  can be written as :

$$\begin{aligned} i \frac{d}{dt} c_{\mathbf{k}}^{\dagger} &= -\varepsilon_{\mathbf{k}} c_{\mathbf{k}}^{\dagger} + c_{-\mathbf{k}} \frac{V}{\Omega} \sum_{\mathbf{k}'} c_{\mathbf{k}'}^{\dagger} c_{-\mathbf{k}'}^{\dagger} \\ i \frac{d}{dt} c_{-\mathbf{k}} &= -\varepsilon_{\mathbf{k}} c_{-\mathbf{k}} + c_{\mathbf{k}}^{\dagger} \frac{V}{\Omega} \sum_{\mathbf{k}'} c_{-\mathbf{k}'} c_{\mathbf{k}'} \end{aligned} \quad \text{Eqs. VI- 25}$$

A mean field approximation resulting in replacing the three fermion operators terms by a one fermion operator term multiplied by an average of the two other ones.

An order parameter  $\Delta$  is defined by :

$$\Delta = \frac{V}{\Omega} \sum_{\mathbf{k}'} \langle c_{\mathbf{k}'}^{\dagger} c_{-\mathbf{k}'}^{\dagger} \rangle = \frac{V}{\Omega} \sum_{\mathbf{k}'} \langle c_{-\mathbf{k}'} c_{\mathbf{k}'} \rangle \quad \text{Eq. VI- 26}$$

Equations VI- 25 then become linearised and can be written as :

$$i \frac{d}{dt} c_k^+ = - \varepsilon_k c_k^+ + \Delta c_{-k}$$

$$i \frac{d}{dt} c_k = - \varepsilon_k c_k + \Delta c_{-k}^+$$

Choosing  $\gamma_{-k} = u_k c_{-k} + v_k c_k^+$  (the so-called Bogoliubov transformation) with the normalisation  $u_k^2 + v_k^2 = 1$  and  $i \frac{d}{dt} \gamma_{-k} = E \gamma_{-k}$ , gives the solution is  $E^2(k) = \varepsilon_k^2 + \Delta^2$  and the eigenvectors are defined by :

$$\Delta^2 (u_k^2 - v_k^2) = 2 \varepsilon_k \Delta u_k v_k$$

By posing  $u_k = \sin(\theta_k)$  and  $v_k = \cos(\theta_k)$  we obtain :  $\tan 2\theta_k = -\Delta / \varepsilon_k$  and the self-consistent relation :

$$\Delta = \frac{V}{\Omega} \sum_{k'} \frac{\Delta}{2\sqrt{\varepsilon_k^2 + \Delta^2}} \quad \text{Eq. VI- 27}$$

At finite temperature, the average over the fundamental in Eq. VI- 23 can be replaced by a thermodynamic average ie  $\langle c_{-k} c_k \rangle = u_k v_k (1 - 2f(E_k))$  where  $f(E_k)$  is the Fermi-Dirac distribution ( $1 / (\exp(\beta E_k) + 1)$ ) and the gap becomes :

$$\Delta = \frac{V}{\Omega} \sum_{k'} \frac{\Delta}{2E_k} [1 - 2f(E_k)] \quad \text{Eq. VI- 28}$$

If the sum over k-space is transformed into an integral in energy up to  $\hbar\omega_D$ , it is possible to obtain :  $\Delta(0) / k_B T_C = \pi / \gamma = 1.76$ .

By calculating the free energy in the superconducting state, it can be shown that the specific heat at low temperature varies as  $\exp(-\Delta_0/k_B T)$  and that the jump of the specific heat at the transition is given by  $(C_s - C_n)/C_n = 1.43$ . Both results agree reasonably with experiments on the common superconductors<sup>42</sup>.

The success of the BCS theory and its prediction that, due to the strength of the electron-phonon interaction, the phenomenon of superconductivity is limited to 25K meant that for a period of 20 years, research on superconductivity slowed down considerably. Nonetheless, in the hope of finding a non-s wave superconductivity, heavy fermions<sup>43</sup> and organic<sup>44</sup> systems were investigated during that dark age period. However, the renewal of the field of superconductivity was only achieved in 1986 when a critical temperature of 40K was observed by Bednorz and Müller<sup>45</sup>, who received the Nobel Prize a year later, in  $\text{La}_{2-x}\text{Sr}_x\text{CuO}_4$ . In parallel to the discovery of perovskites with even higher transition temperatures (most famously 95K<sup>46</sup> in  $\text{YBa}_2\text{Cu}_3\text{O}_{7-\delta}$  and

115K<sup>47</sup> in Bi<sub>2</sub>Sr<sub>2</sub>Ca<sub>2</sub>Cu<sub>3</sub>O<sub>10</sub>), theorists have suggested many possible origins for this high-temperature superconductivity (HTS). Even 15 years after the experimental discovery of the HTS, there is still a very active debate as to which phenomenon is responsible for it.

#### **VI.2.f. local pairing superconductivity and Uemura classification**

As this thesis is experimental rather than theoretical, a complete review of all the current theories will not be attempted (good reviews can be found in references 48 and 49). This paragraph will merely try to present some ideas behind the local pairing mechanism and put them into perspective with the  $\mu$ SR technique.

The most striking feature to local pairing superconductivity is its implication that the electron pair can remain above the superconducting transition temperature,  $T_c$ , in contrast with the BCS theory. This is because the pairs can be in a disordered state where superconductivity cannot exist but other cooperative phenomena such as a charge density wave are allowed. Below  $T_c$ , the pairs are ordered and superconductivity prevails whereas at sufficiently high temperatures, the pairs break up and the normal electronic behaviour is predicted. The transition from normal electrons to disordered pairs is accompanied by the existence of a gap.

The mechanisms invoked for the couplings are numerous : from a strong electron coupling (local deformation of the lattice causing the formation of a polaron or even a bi-polaron) to an electronic coupling where the electrons are coupled to an electronic subsystem resulting in a screening of the coulomb repulsion, similar to that of *Eq. VI- 20*, or even a exciton or a plasmon.

The discovery of the high  $T_c$  superconductors<sup>45</sup> shortly followed by those of the buckminster fullerenes<sup>50</sup> and the nickel borocarbides<sup>51</sup> added to the list of already existing non conventional superconductors such as the Chevrel phases<sup>52</sup>, where superconductivity and magnetic order coexist, the organic superconductors<sup>44</sup> where p-wave superconductivity was suspected or the heavy fermion systems<sup>43</sup>. At the time of their discovery, these superconductors were all branded "new" or "exotic" and a more consistent pattern to identify whether each one of these families truly constituted a new class was needed. By studying the systematics in HTc superconductors using muon spectroscopy, Uemura et al<sup>53</sup> noticed the existence of a linear relation between  $T_c$  and the muon relaxation rate  $\sigma(T \rightarrow 0)$ . This has profound implications as the muon

depolarisation rate is related to the inverse penetration depth  $\lambda$  and thereby to the effective electron mass  $m^*$  and the superconducting carrier density  $n_s$  by the relation :

$$\sigma(T \rightarrow 0) \propto \frac{1}{\lambda(0)^2} = \frac{4\pi r_e m_e n_s}{m^*} \frac{1}{1 + \xi/l_e} \quad \text{Eq. VI- 29}$$

where  $r_e$  is the classical radius of the electron (2.82 fm),  $l_e$  is the electron mean free path and  $\xi$  the superconducting coherence length. Within the clean limit ( $\xi/l_e \ll 1$ ), the relationship becomes :

$$\sigma(T \rightarrow 0) \propto \frac{n_s}{m^*} \quad \text{Eq. VI- 30}$$

The observed linear dependence between  $T_c$  and  $\sigma(0)$  thus implies a linear correlation between  $T_c$  and  $n_s/m^*$  which is not consistent with weak coupling BCS theory ( $T_c \propto \omega_D$  and as  $n_s$  is structureless on the scale of  $\hbar\omega_D$ ,  $T_c$  is not related to  $n_s$ ).

To further analyse the significance of Eq. VI- 30, it is necessary to introduce the quasi-2d character of the High  $T_c$  cuprates. Indeed, for a 2d electron gas, the Fermi energy  $E_F$  is simply :

$$E_F = k_B T_F = (\hbar^2 \pi) n_{s,2d} / m^* \quad \text{Eq VI- 31}$$

Where  $T_F$  is the Fermi temperature and  $n_{s,2d}$  is the carrier concentration within the CuO planes. For 3d system, the relation between  $T_F$  and  $n_s/m^*$  is not linear but if the Sommerfeld constant  $\gamma$  of the material is known, it is still possible to derive the Fermi energy from muon measurements. The combination of :

$$k_B T_F = (\hbar^2 / 2)(3\pi^2 n_s)^{2/3} / m^* \quad \text{and} \quad \gamma = \left(\frac{\pi}{3}\right)^{2/3} \frac{k_B^2 m^* n_e^{1/3}}{\hbar^2} \quad \text{Eqs. VI- 32}$$

where  $n_e$  is the carrier density which can be assumed to be equal to  $n_s$  at  $T=0$ , gives :

$$k_B T_F \propto \sigma(0)^{3/4} \gamma^{-1/4} \quad \text{Eq VI- 33}$$

From muon measurements, it is therefore possible to plot  $T_c$  versus  $T_F$  for all systems and such a systematical study reveals that all the "unconventional" superconductors such as the cuprate, the heavy fermion, the organic, the Chevrel, and the fullerene superconductors follow a similar trend with  $1/100 < T_c/T_F < 1/10$  in contrast with all the conventional BCS superconductors for which  $T_c/T_F < 1/1000$ . Such a plot, now referred to as the Uemura plot<sup>11,12</sup>, is shown on *Figure VI- 10*.

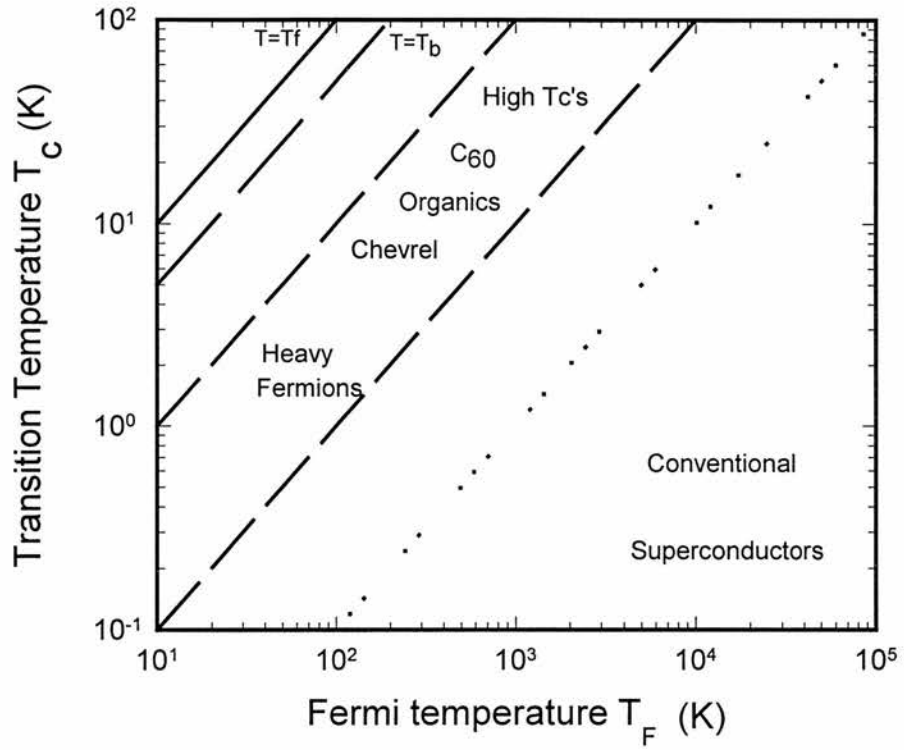


Figure VI- 10 : the Uemura plot.

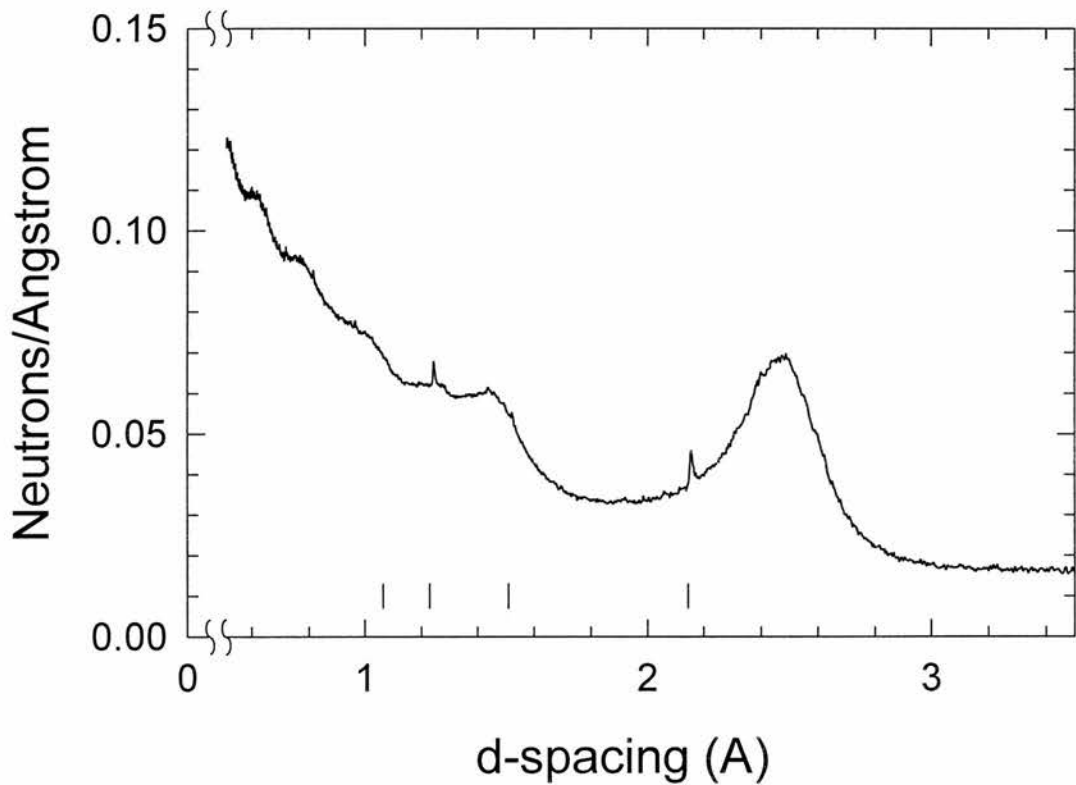


Figure VI- 11 :  $\alpha$ -  $Zr_{76}Fe_{24}$  in a vanadium can measured on LAD. The ticks correspond to vanadium peaks.

### **VI.3. Superconducting properties of $\alpha$ - ZrTM (TM = Co, Fe, Ni, Rh and Cu) by conventional methods.**

#### **VI.3.a. structural characterisation**

The amorphous  $\alpha$ -Zr<sub>76</sub>TM<sub>76</sub> (TM = Fe, Cu, Co, Rh, Ni) and  $\alpha$ -Zr<sub>80</sub>Fe<sub>20</sub> samples were prepared using the melt-spinning method described in §II.4. The resulting ribbons could be bent to an angle of 180° without breaking which is a good sign for amorphicity. As discussed in Chapter II, X-rays probe only the surface of the ribbons where the crystalline impurities are most likely to form. Consequently, neutron scattering is the method of choice to probe the bulk of the amorphous ribbons. However, as neutron beam-time is virtually impossible to get for sample testing only, not all the samples could be neutron tested. However, two samples were inserted in a neutron beam in between other experiments : neutron diffraction patterns were collected on  $\alpha$ -Zr<sub>76</sub>Fe<sub>24</sub> with good statistics on LAD at ISIS (collection time : 8h) and with poorer statistics (collection time : 20 mins) on  $\alpha$ -Zr<sub>76</sub>Ni<sub>24</sub> on D1B at the ILL. In light of the results obtained on  $\alpha$ -Zr<sub>76</sub>Fe<sub>24</sub> (*Figure VI- 11*) and  $\alpha$ -Zr<sub>76</sub>Ni<sub>24</sub> (*Figure VI- 12*), and with the knowledge that  $\alpha$ -Zr<sub>76</sub>Fe<sub>24</sub> was by far the harder sample to spin, we can be confident that all the ribbons obtained are good amorphous samples.

#### **VI.3.b. magnetic characterisation**

When it was possible, the magnetic properties of the amorphous superconductors prepared in St Andrews were also investigated in St Andrews. Unfortunately, the low values of transition temperature  $T_c$  for several alloys<sup>5</sup> (see *Table VI- 1*) rendered the magnetic measurements impossible on our VSM, which cannot access temperatures below 3.6K. The temperature control of the continuous flow cryostat of the VSM is poor at those temperatures and attempts to change the temperature in order to measure the ZFC-FC curves were not very successful (see *Figure VI- 13*). On the contrary, it was easier to perform measurements where the field was changing while the temperature remained constant. This was however not very useful as any  $H_{c1}$  or  $H_{c2}$  determination requires the temperature to be as close to zero as possible. As a consequence of the VSM drawbacks for the magnetic study of  $\alpha$ - Zr<sub>76</sub>Co<sub>24</sub>, I went to the Service de Physique de l' Etat Condensé at the Commissariat à l' Energie Atomique in Saclay,



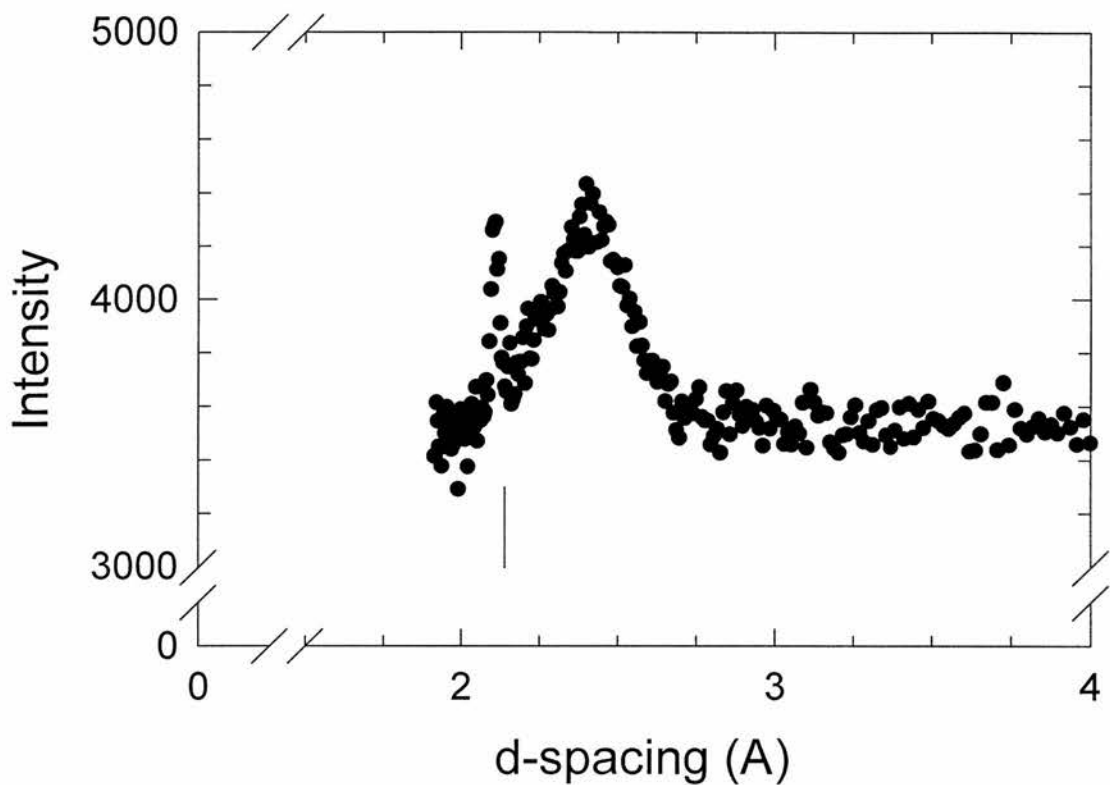


Figure VI- 12 :  $\alpha$ -Zr<sub>76</sub>Ni<sub>24</sub> in a vanadium can measured on DIB. The tick corresponds to a vanadium peak.

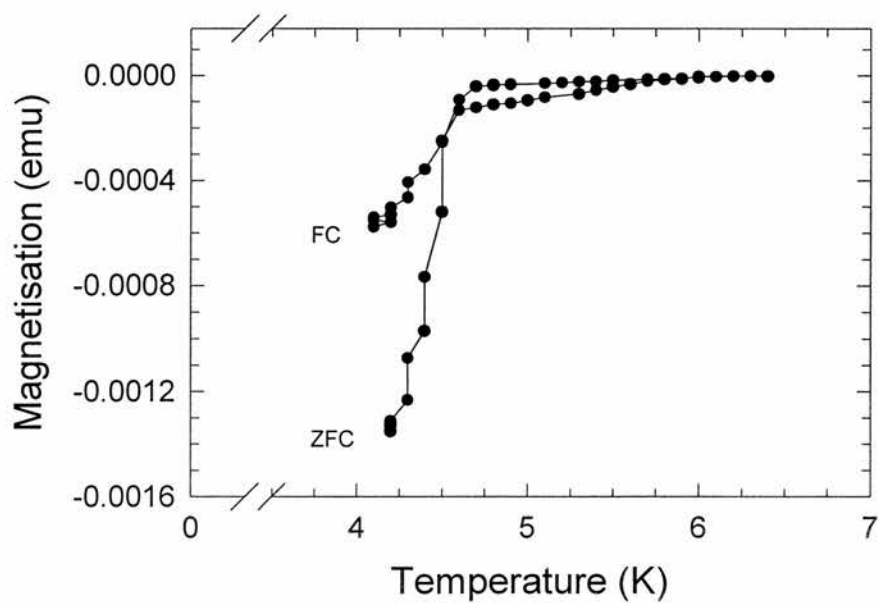


Figure VI- 13 : ZFC-FC curves for  $\alpha$ -Zr<sub>76</sub>Rh<sub>24</sub> obtained in the VSM.

Alloy	Zr <sub>76</sub> Fe <sub>24</sub>	Zr <sub>80</sub> Fe <sub>20</sub>	Zr <sub>76</sub> Ni <sub>24</sub>	Zr <sub>76</sub> Co <sub>24</sub>	Zr <sub>76</sub> Cu <sub>24</sub>	Zr <sub>76</sub> Rh <sub>24</sub>
$T_c$	2.0K	3.3K	3.6K	3.7K	3.2K	4.5K

Table VI- 1 : superconducting transition temperatures for  $\alpha$ -Zr-TM.

France to use a SQUID. Similarly, for the heat capacity measurements, I went to Oxford Instruments Superconductivity in Tubney Woods, Oxfordshire.

### *VI.3.b.1. DC magnetisation measurements*

Several pieces of  $\alpha$ -Zr<sub>76</sub>Co<sub>24</sub> ribbons of approximately 3mm in lengths were stuck together with some vacuum grease and placed in a straw which was then inserted in the SQUID magnet. In order to study the effect of the demagnetising factor N on the long and thin amorphous ribbons, two geometries were used : the shortest length of ribbons (about 20  $\mu$ m) along the direction of the field (large N) or perpendicular to it (N~0). This also allows the pinning in both directions to be probed. For each geometry, a sample was cooled in zero field and once at the base temperature of the SQUID, a field of 10 Oe was applied (Zero Field Cooled or ZFC) and the temperature was raised slowly while data was being collected. Once warmed up above T<sub>c</sub>, the sample was cooled in the same field (Field Cooled or FC) and data was collected on warming. *Figure VI- 14* and *Figure VI- 15* show the temperature evolution of the ZFC-FC magnetisation for the perpendicular and parallel geometry. It can be seen that the transition occurs at roughly the same point, consistent with the literature, but that the transition is quite broad.

The magnetic hysteresis loops show a profound difference between the parallel and the perpendicular configuration. Indeed, as shown by *Figure VI- 16*, some pinning is present for the perpendicular geometry whereas it appears much weaker in the parallel direction (*Figure VI- 17*). On both figures, the values of the magnetisation are small which implies a small J<sub>c</sub> and hence low pinning. For completeness, these figures should also be compared with a loop obtained on the VSM at St Andrews in the perpendicular configuration (see *Figure VI- 18*) for the lowest possible achievable temperature (3.6K) which shows virtually no pinning. The weak pinning is perhaps simply due to the fact that the amorphous matrix shows no defect on the length scale of  $\xi$ . Furthermore, one of the most important properties of amorphous metals for industrial use is their non-rusting properties due to the absence of grain boundaries. In other words, we might have a very homogenous superconductor whose flux lattice is weakly pinned by, for instance, surface pinning. The pinning in  $\alpha$ -Zr<sub>76</sub>Co<sub>24</sub> will be discussed in more details in the light of the muon results.

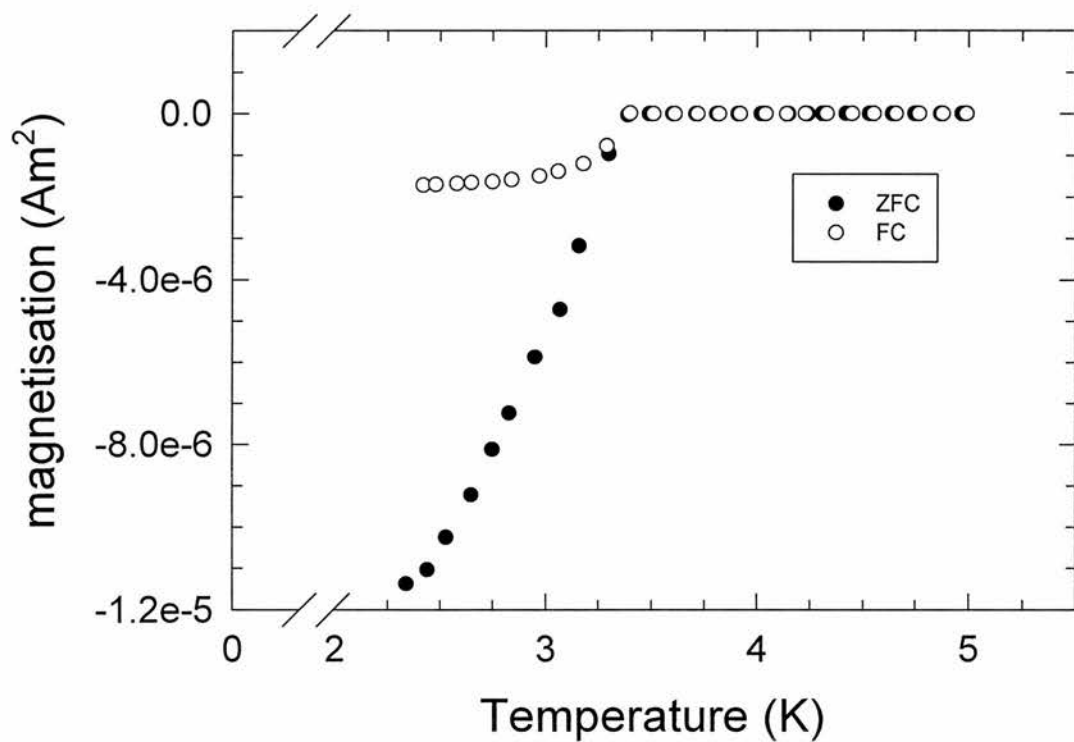
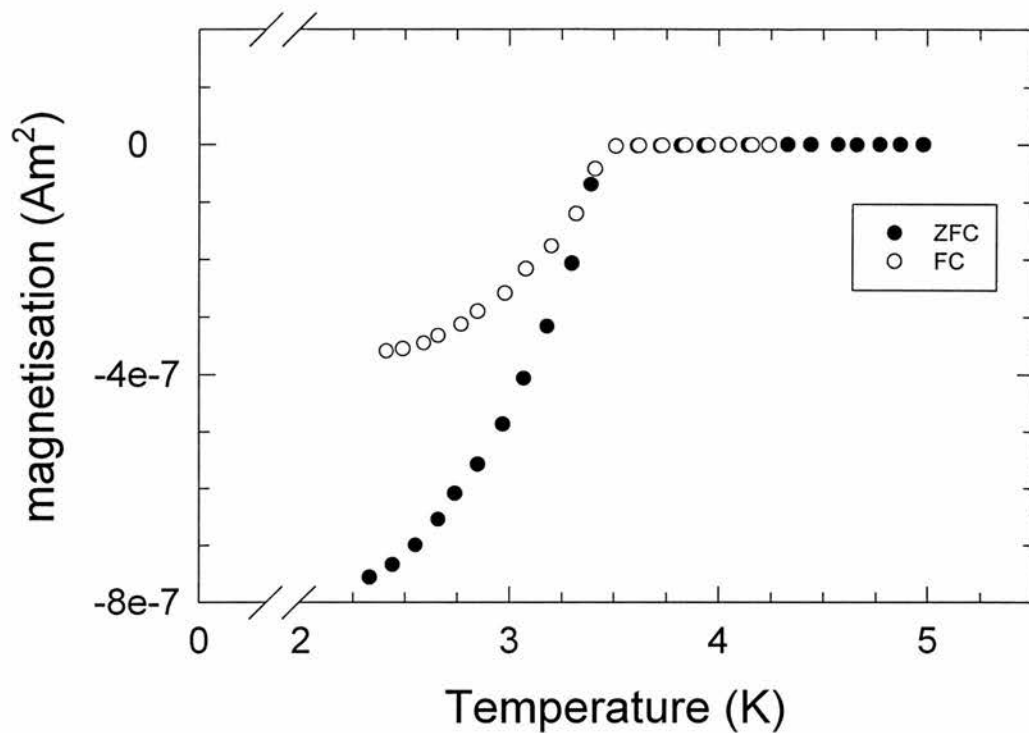


Figure VI- 14(top) and VI- 15 (bottom): Temperature evolution of the magnetisation for  $\alpha$ -Zr<sub>76</sub>Co<sub>24</sub> in the perpendicular and in the parallel geometry respectively.

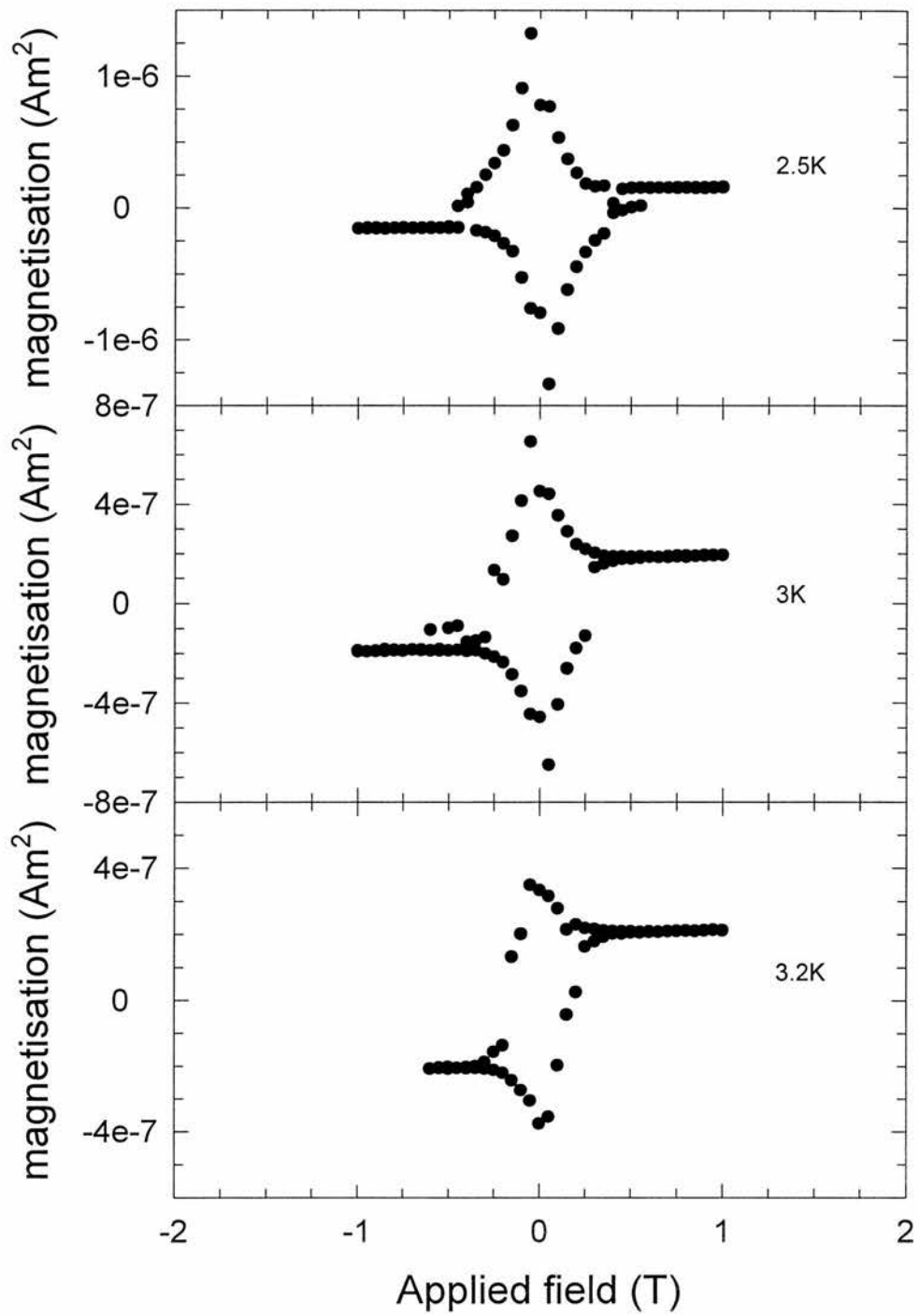


Figure VI- 16: Magnetic hysteresis loops for three different temperatures(2.5K, 3.0K and 3.2K) for  $\alpha$ - Zr<sub>76</sub>Co<sub>24</sub> in the perpendicular direction.

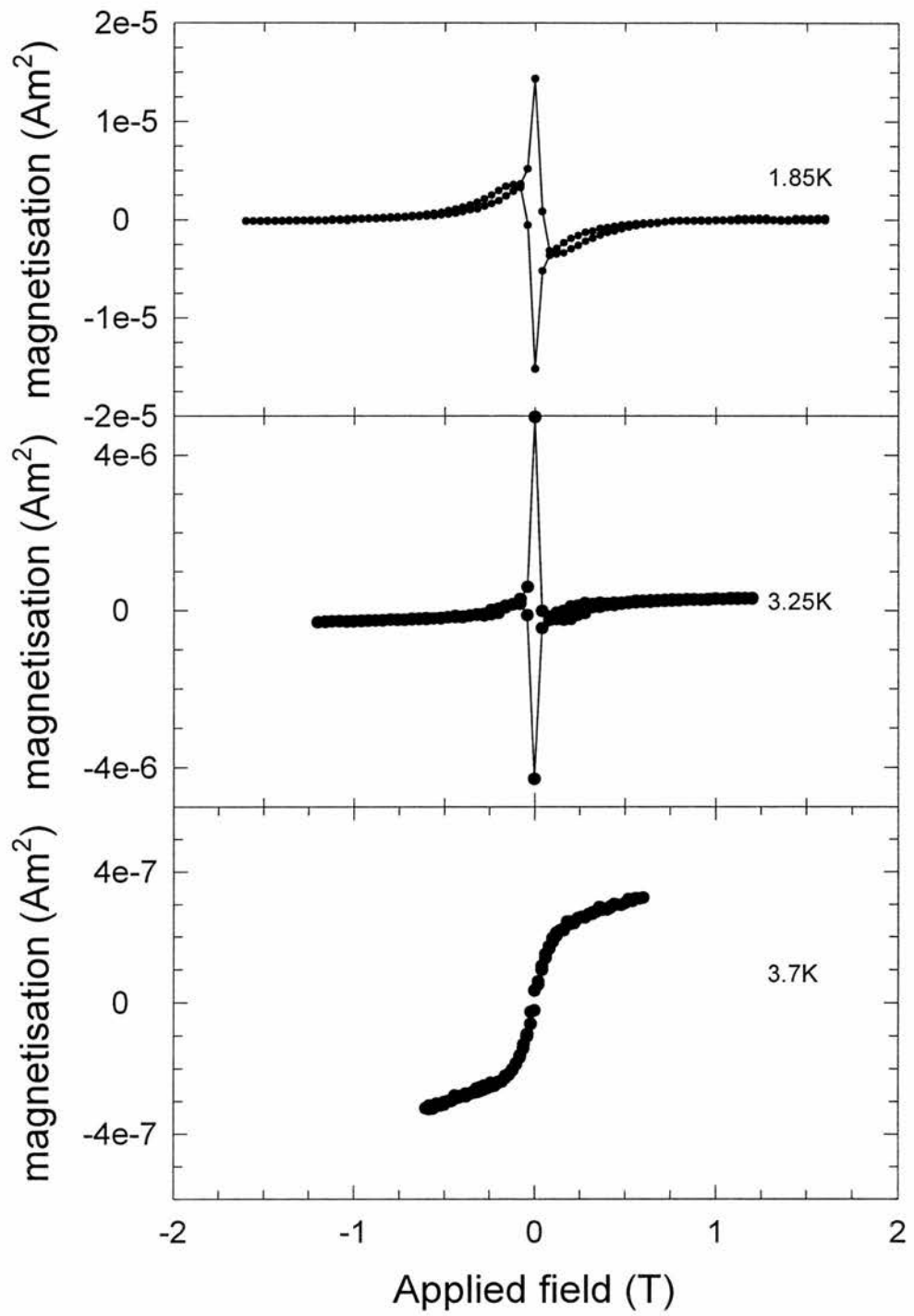


Figure VI- 17: Magnetic hysteresis loops for three different temperatures(1.85K, 3.25K and 3.7K) for  $\alpha$ -Zr<sub>76</sub>Co<sub>24</sub> in the parallel direction.

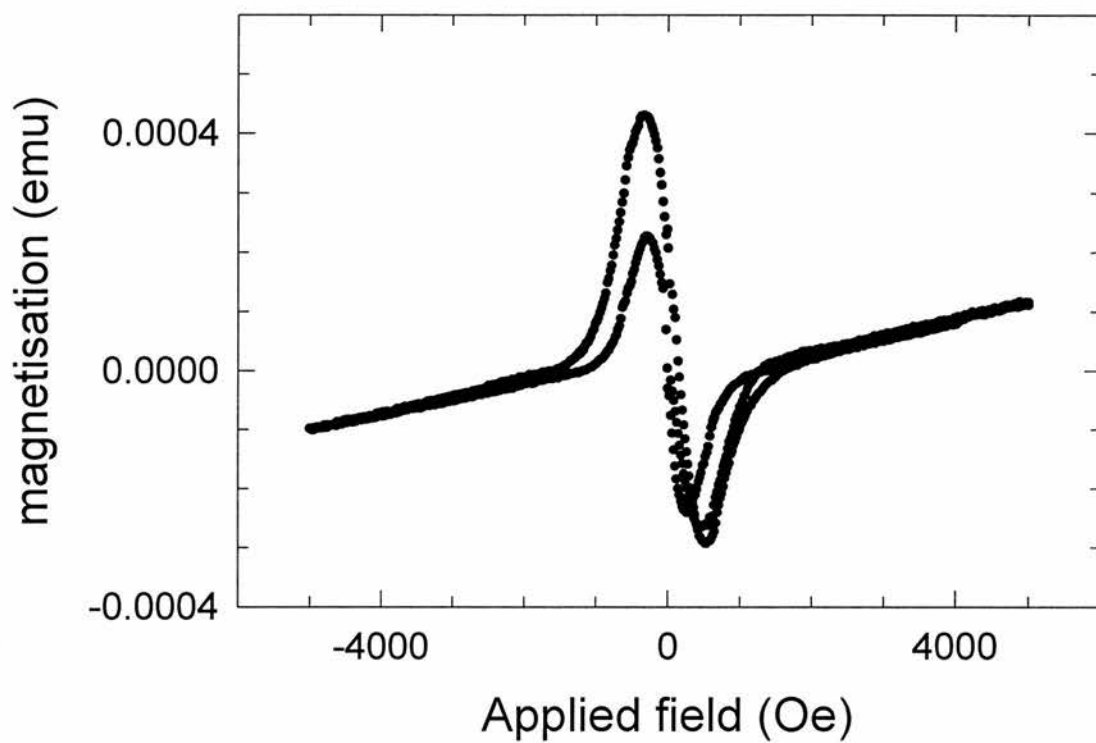


Figure VI- 18 : Magnetic hysteresis loops obtained by the VSM at around 3.6K for  $\alpha$ - $Zr_{76}Co_{24}$  in the perpendicular direction.



### VI.3.b.2. Heat capacity measurements

A few milligrams of sample (generally two pieces) were stuck on the HCR chip by Wakefield grease as described in Chapter II. A prototype  $^3\text{He}$  insert of the MagLab<sup>EXA</sup> was used to reach a base temperature of 0.3K on the  $\alpha\text{-Zr}_{76}\text{Fe}_{24}$  but not for the  $\alpha\text{-Zr}_{76}\text{Ni}_{24}$  system as the transition temperature is high enough to be achieved by simply pumping on the He bath. *Figures VI- 19* and *VI- 21* show the heat capacity measured for  $\alpha\text{-Zr}_{76}\text{Fe}_{24}$  and  $\alpha\text{-Zr}_{76}\text{Ni}_{24}$  respectively. In order to compare the Sommerfeld constant  $\gamma$  with published values<sup>54</sup>, a plot of  $C/T$  versus  $T^2$  is presented on *Figure VI- 20* and *VI- 22* for each sample. The extrapolation of this plot to zero temperature gives the Sommerfeld constant and the results agree well with the published data. However, for  $\alpha\text{-Zr}_{76}\text{Ni}_{24}$ , the jump at the specific heat is about 0.85 for  $\alpha\text{-Zr}_{76}\text{Ni}_{24}$  and 1.2 for  $\text{Zr}_{76}\text{Fe}_{24}$  i.e. not very close to the BCS value of 1.43.

## VI.4. $\mu\text{SR}$ study of $\alpha\text{-Zr}_{76}\text{TM}_{24}$ .

The amorphous samples were mounted according to the procedure described in Chapter III. The resulting time spectra (a typical example on  $\text{Zr}_{76}\text{Fe}_{24}$  can be found on *Figure VI- 23*) were either fitted directly in the time domain to a gaussian or fed to the Maximum Entropy (ME) routine to obtain the most uniform field distribution without assumption on the form of the distribution. The ME method was preferred to a Fourier Transform because aberrations can occur by simply Fourier transforming the data due to the fact that the time window available is only finite. By examining the lineshape of the field distribution (*Figure VI- 24*) obtained from *Figure VI- 23* by the ME method, an asymmetry is clearly seen as expected for a Flux line lattice (FLL) and it is therefore not really appropriate to use a gaussian to fit the data. Of particular interest is the long tail at high fields due to regions of the lattice close to the vortex cores. It should be noted that the lineshapes from superconductors are in most cases symmetric due to the fact that most experiments are done on powders<sup>28</sup> for which the combination of a polycrystalline average, a broadening from a range of demagnetisation factors and random pinning processes smooth the asymmetric lineshape so much that it can be fitted to a gaussian. In fact, asymmetric lineshapes from  $\mu\text{SR}$  measurements have only been observed using high quality single-crystals<sup>55</sup>. The line through the data (*Figure VI- 24*) is a simulation using a magnetic penetration depth  $\lambda = 475$  nm and a coherence length  $\xi = 42$  nm (as a

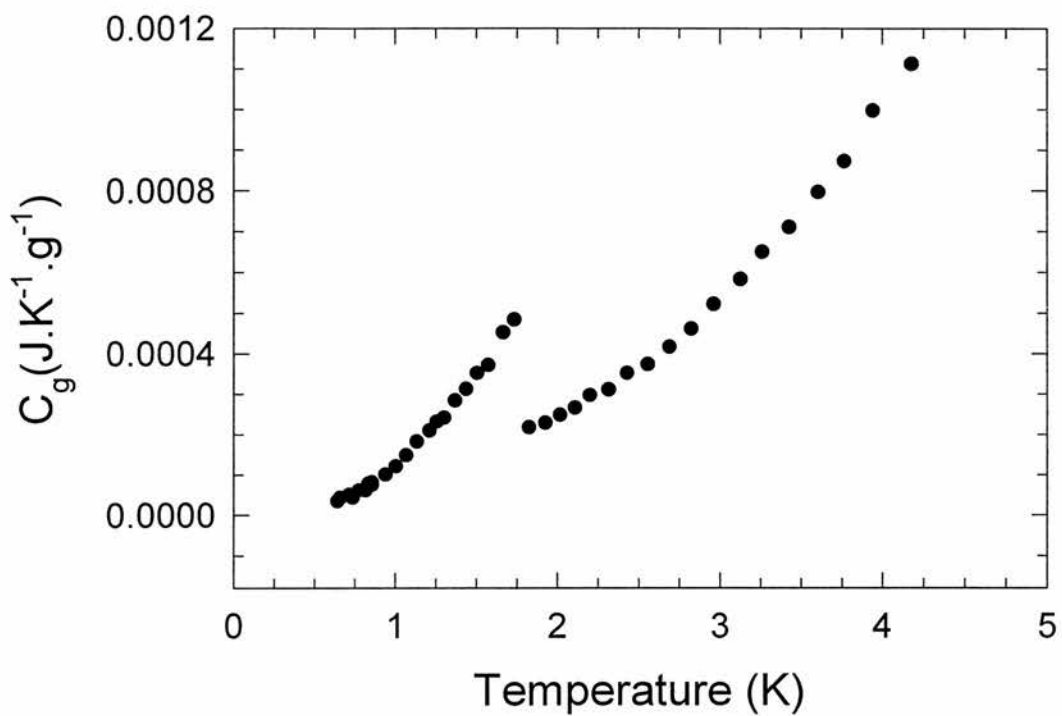


Figure VI- 19 : heat capacity for  $\alpha$ -  $\text{Zr}_{76}\text{Fe}_{24}$ .

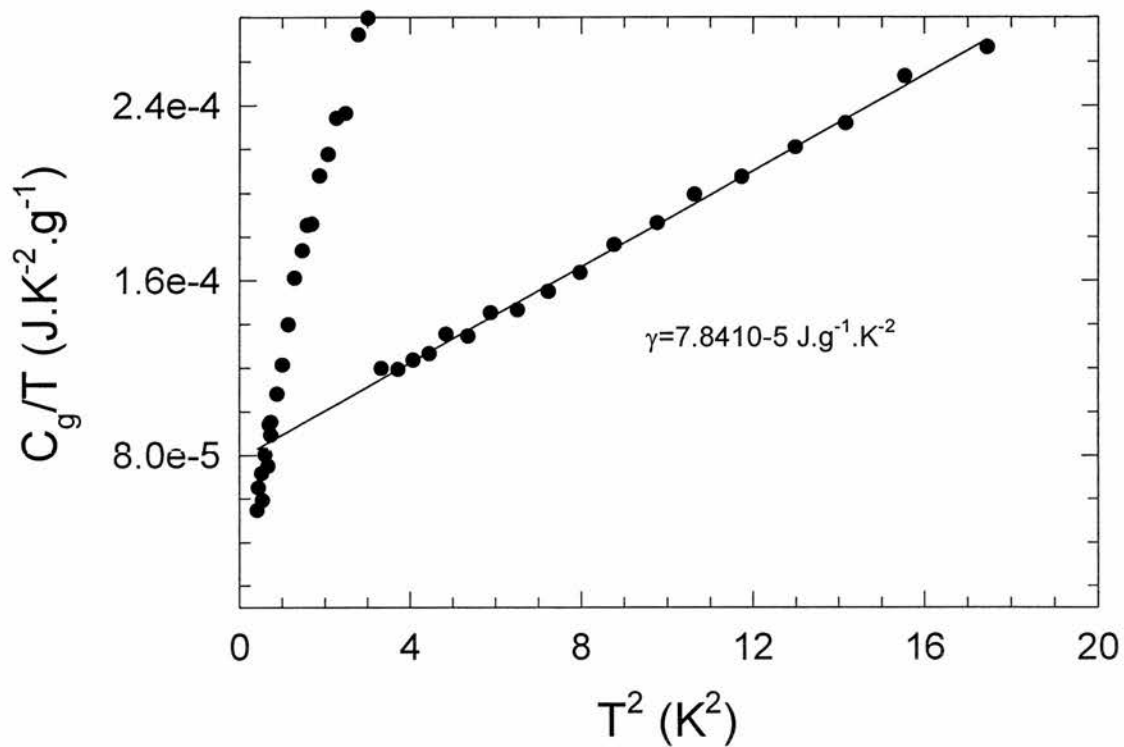


Figure VI- 20 :  $C/T$  vs  $T^2$  plot for heat capacity of  $\alpha$ -  $\text{Zr}_{76}\text{Fe}_{24}$ .

2D Graph 5

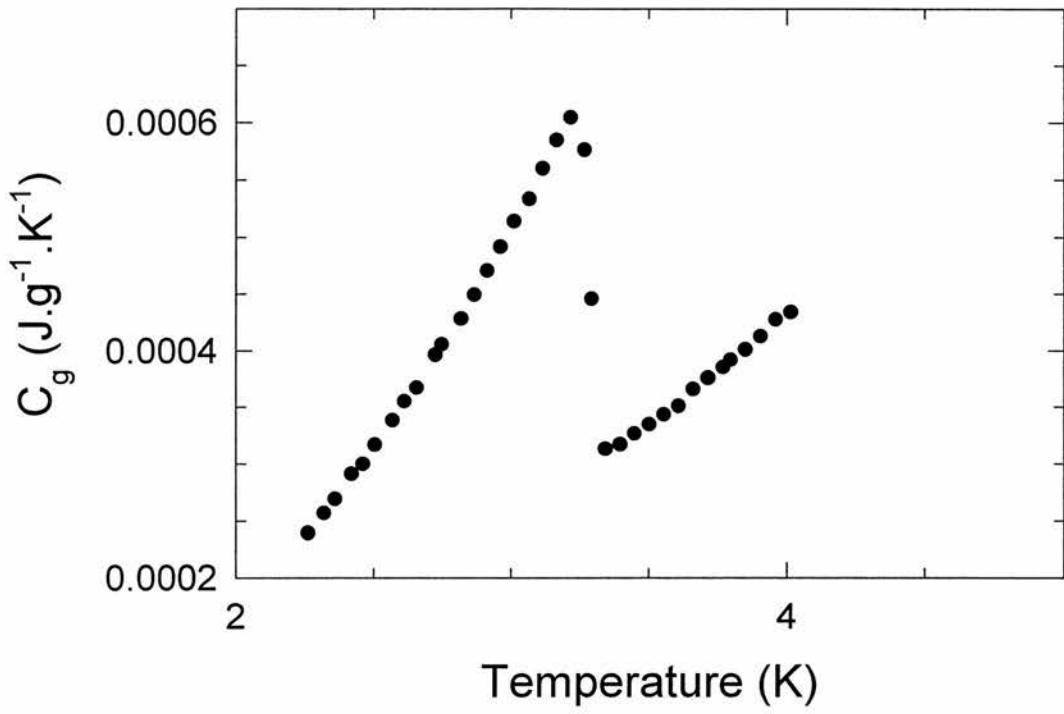


Figure VI- 21 : heat capacity for  $\alpha\text{-Zr}_{76}\text{Ni}_{24}$ .

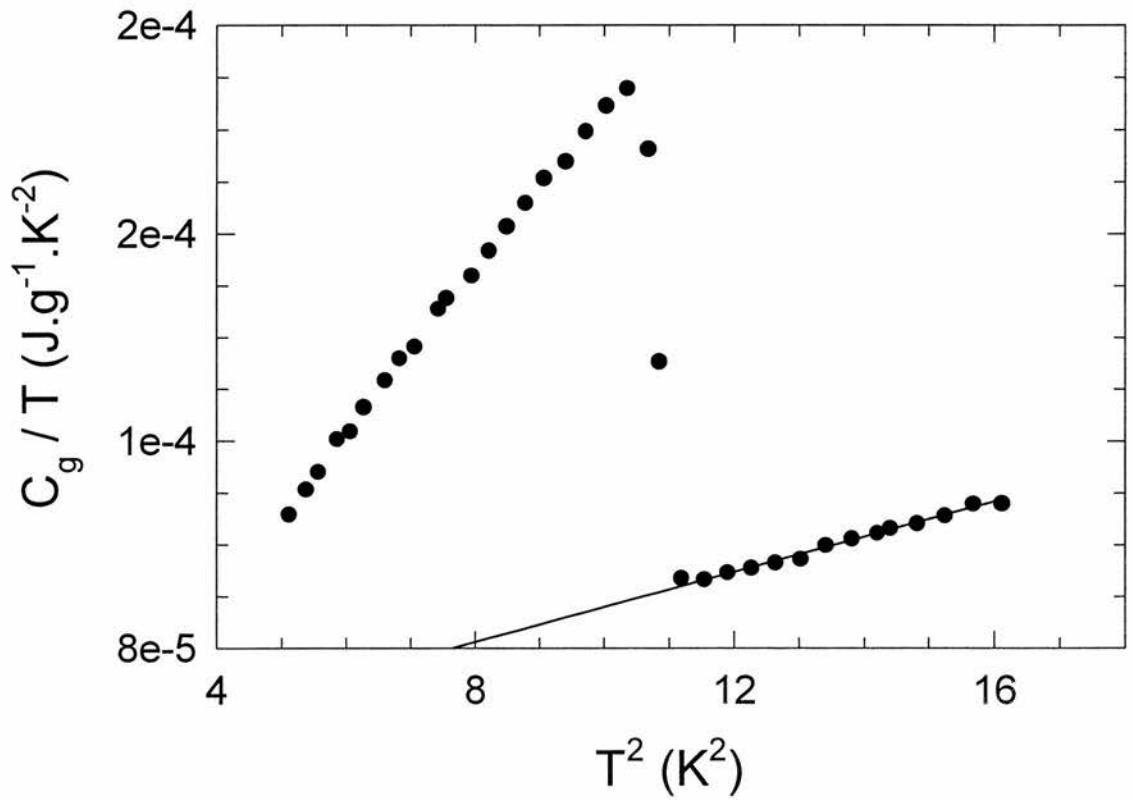


Figure VI- 22 :  $C/T$  vs  $T^2$  plot for heat capacity of  $\alpha\text{-Zr}_{76}\text{Ni}_{24}$ .

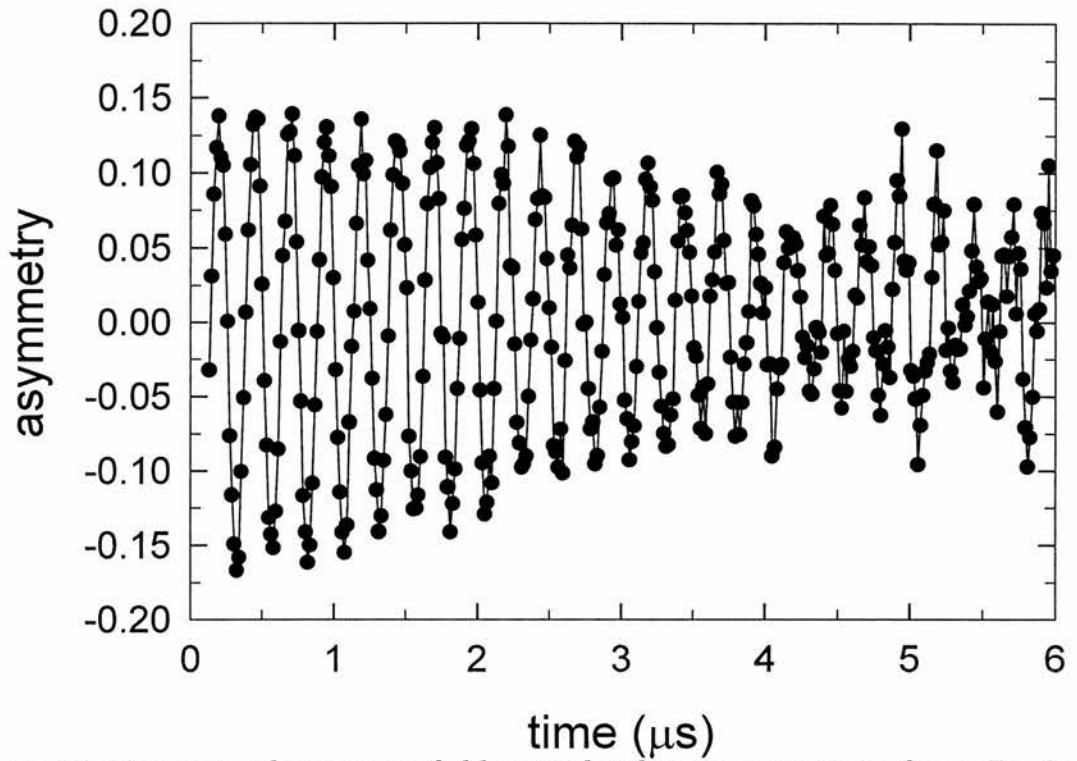


Figure VI- 23 : a typical transverse field muon depolarisation spectrum for  $\alpha$ -  $Zr_{76}Fe_{24}$  at 50 mK and 300G.

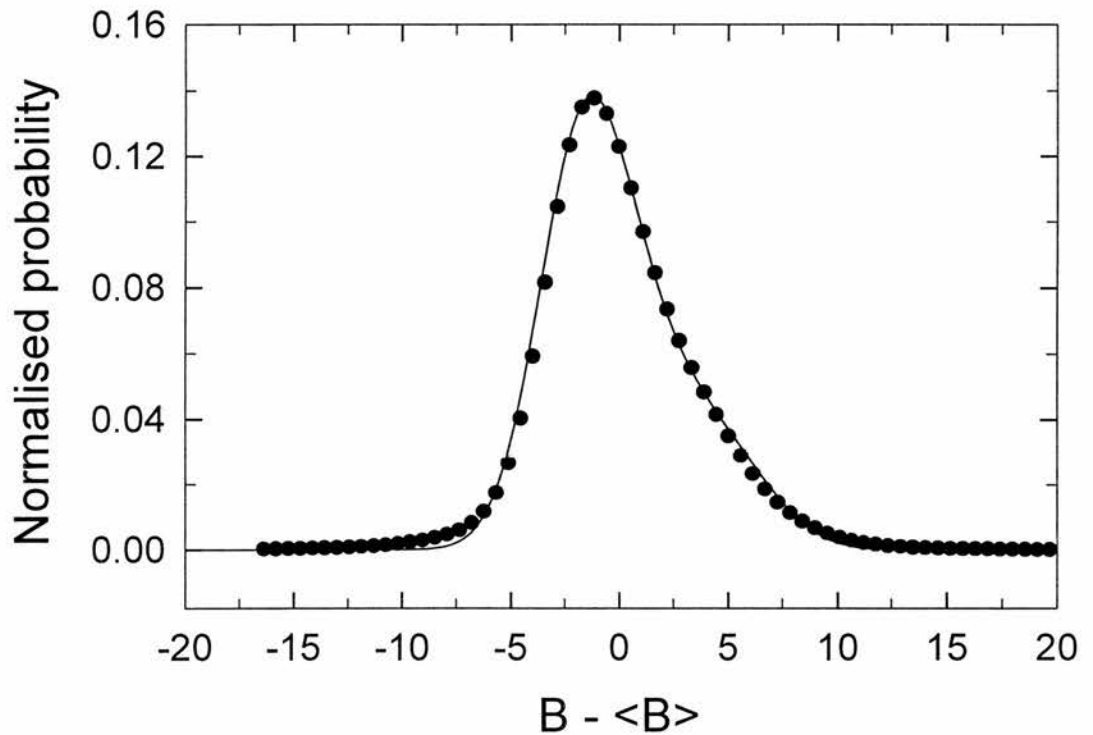


Figure VI- 24 : the field distribution obtained from Figure VI- 23 by the ME method. The distribution has been normalised and shifted by the average field. The line is explained in the text.

check,  $\kappa > 11$  so it is correct to use the London model) using my program. This field distribution for a perfect lattice is then convoluted with a gaussian of width 2.3 G (to simulate broadening due to pinning or dipolar moments or even instrumental resolution) by using a simple integration algorithm. This convolution routine was tested on performing it on two gaussians of width  $w_1$  and  $w_2$  and checking that the resulting width was  $(w_1^2 + w_2^2)^{1/2}$ . The model used seems to represent the data particularly well, apart from at the edges of the field distribution. However, the normal state itself is not really a gaussian either (it seems to be better represented by a gaussian convoluted with a lorentzian which could come from muon diffusivity<sup>56</sup>, although not very likely at these temperatures, or dipolar broadening). It should be stressed that the high value of  $\lambda$  (one of the longest measured on  $\mu$ SR) implies that the distribution is very narrow and renders the experiment and data analysis more difficult. Luckily, as the samples were mounted very carefully, there is no background signal (which would manifest itself as a peak at the applied field) preventing the extraction of the relevant moments (the second and the third) of the field distribution from the data. Furthermore, as most samples show a very similar behaviour (with similar  $\lambda$ ), it was thought best to avoid repetition and similar data on each one of the  $\alpha$ -Zr<sub>76</sub>TM<sub>24</sub> series are not shown. The results are compiled in *Table VI- 2*. The perfection of the FLL can be estimated through the expression<sup>57</sup> :

$$\beta = \frac{B_{\text{saddle}} - \langle B \rangle}{\langle \Delta B^2 \rangle^{1/2}} \quad \text{Eq. VI- 34}$$

For a perfect lattice,  $\beta$  should be about 0.6. For  $\alpha$ - Zr<sub>76</sub>Co<sub>24</sub>,  $\beta$  is estimated to be 0.53 which is pretty close to the expected value. However, the estimation of  $\beta$  is difficult because the lineshape is so narrow. Another important parameter is the so-called asymmetry parameter  $\alpha$  :

$$\alpha = \frac{\sqrt[3]{\langle \Delta B^3 \rangle}}{\sqrt{\langle \Delta B^2 \rangle}} \quad \text{Eq. VI- 35}$$

Due to the tail at high fields in the field distribution due to a FLL,  $\alpha$  is generally positive. However, if melting of the FLL occurs, the shape of the lineshape becomes such that a bigger weighting of the fields lower than the average fields occurs and  $\alpha$  becomes negative. Consequently,  $\mu$ SR, via the variations of  $\alpha$ , has been used to study the melting transition<sup>55</sup> in the high temperature superconductor BSSCO. Interestingly, the temperature evolution of  $\alpha$  in  $\alpha$ -Zr<sub>76</sub>Co<sub>24</sub> follows the same pattern as in the high

T<sub>c</sub>'s:  $\alpha$  changes sign slightly below the transition temperature (see *Figure VI- 25*) but a shift between the lineshape at temperatures between the point where  $\alpha$  is negative and T<sub>c</sub> and the applied field still remains. This behaviour is not unexpected as DC magnetisation measurements previously showed that the pinning can be very low in these amorphous alloys. A major difference when comparing the temperature evolution of  $\alpha$  in Zr<sub>76</sub>Co<sub>24</sub> and that of BSSCO is that the range over which  $\alpha$  is negative is considerably smaller for the amorphous alloys. The presence of melting is perhaps not too surprising as the melting field at a temperature T is proportional<sup>58</sup> to  $\lambda^{-4}$  (for high T<sub>c</sub>'s, the anisotropy  $\gamma$  is included, and the melting field is further reduced as  $\gamma^{-2}$ ). Also, the Larkin-Ovchinnikov theory of collective pinning<sup>59</sup> has been used for both the high T<sub>c</sub>'s such as Rb<sub>a2</sub>Cu<sub>3</sub>O<sub>7.8</sub><sup>60</sup> and the amorphous superconductors<sup>61</sup>. Interestingly, if pins are introduced by heat treating the sample (see *Figure VI- 26*), the melting occurs at lower temperatures (see *Figure VI- 25*), but so does T<sub>c</sub>, indicating that these pins are not efficient in making the FLL more rigid. Unfortunately, it was not possible to work out the size of the pins from the neutron data, to see if they were bigger than  $\xi$ .

From the second moment of the distribution and the equation

$$\sqrt{\langle \Delta B^2 \rangle} = B_0 \sqrt{\sum_{n,m} \frac{\exp(-\xi^2 G_{n,m}^2)}{(1 + G_{n,m}^2 \lambda^2 / (1 - b))^2}} \quad \text{Eq. VI- 36}$$

where  $b = B_0/B_{c2}$ , the values of  $\lambda = 460\text{nm}$  and  $\xi = 29\text{nm}$  are obtained for  $\alpha$ -Zr<sub>76</sub>Fe<sub>24</sub> (see *Figure VI- 27*) which are very close to the values obtained by simulating the FLL and convoluting it with a gaussian. This equation is only valid within the London model and therefore concerns high  $\kappa$  value superconductors which is definitely the case here ( $\kappa \approx 16$ ). The temperature dependence of the second moment can be described by the two fluid- model :

$$\sqrt{\langle \Delta B^2 \rangle} = \sqrt{\langle \Delta B^2(0) \rangle \left( 1 - \left( \frac{T}{T_c} \right)^N \right)} \quad \text{Eq. VI-37}$$

and N is found to be 2.9 for  $\alpha$ - Zr<sub>76</sub>Fe<sub>24</sub> (see *Figure VI- 28*). The values of N for different samples are reported in *Table VI- 2*.



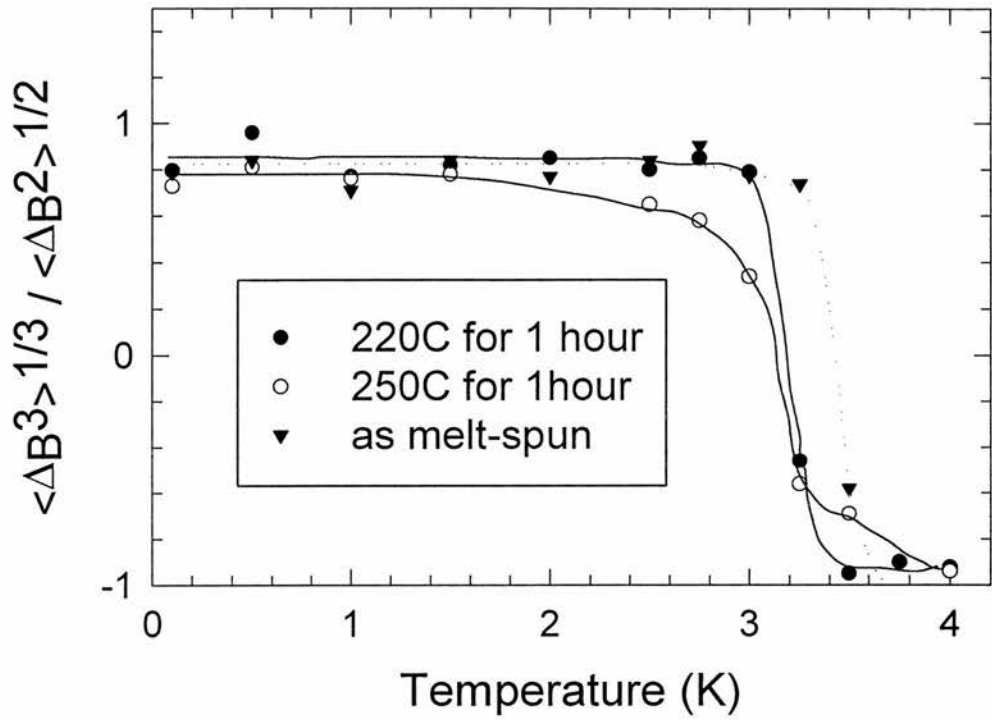


Figure VI- 25 : evolution of the asymmetry parameter as a function of temperature for different heat treatments on  $\alpha\text{-Zr}_{76}\text{Co}_{24}$ .

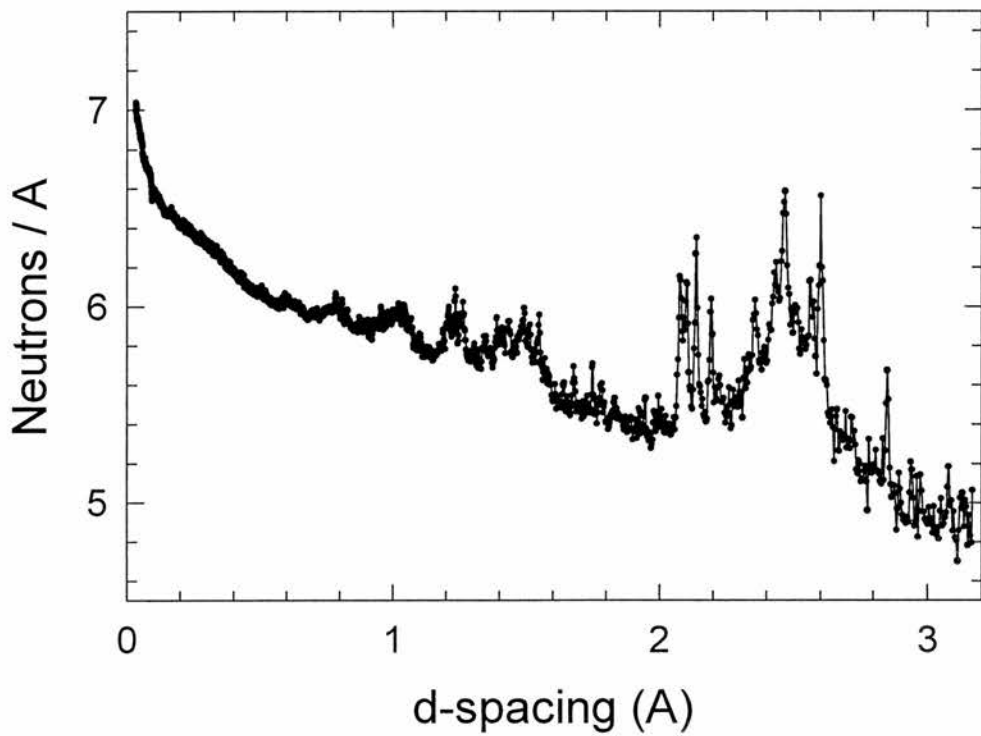


Figure VI- 26:  $\alpha\text{-Zr}_{76}\text{Co}_{24}$  annealed at 220°C to introduce pins. A few Zr Bragg peaks are just starting to appear.

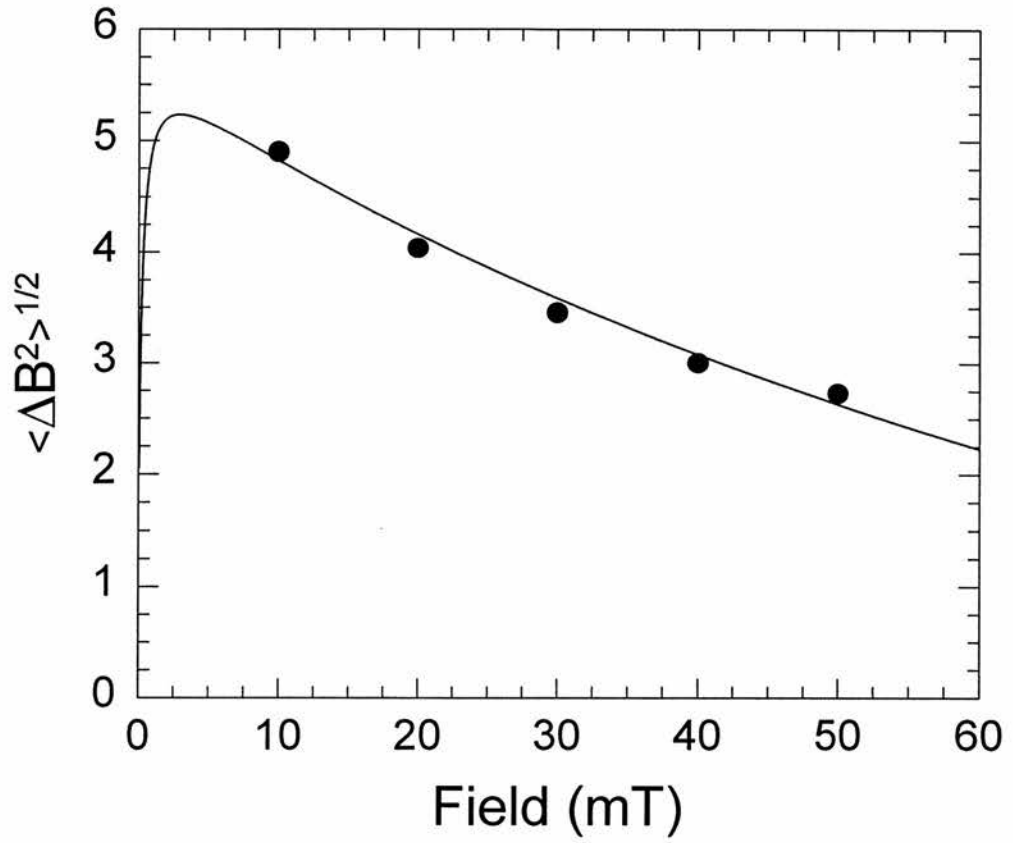


Figure VI- 27 : field dependence of  $\langle \Delta B^2 \rangle^{1/2}$  for  $\alpha\text{-Zr}_{76}\text{Fe}_{24}$  at 50 mK.

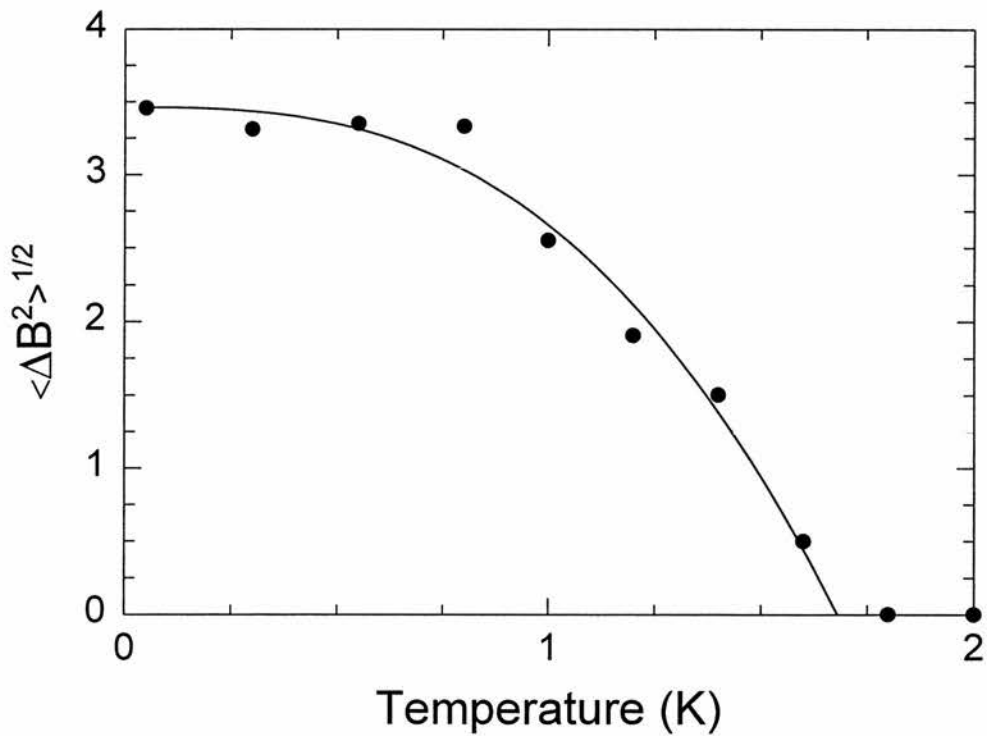


Figure VI- 28 : Temperature dependence of  $\langle \Delta B^2 \rangle^{1/2}$  for  $\alpha\text{-Zr}_{76}\text{Fe}_{24}$  in 30 mT.

Finally, *Figure VI- 29* presents an Uemura plot, where  $T_c$  is plotted versus the Fermi Temperature  $T_F$  obtained from a combination of the  $\mu$ SR determination of  $\lambda$  and from the specific heat measurement through the formulae :

$$\lambda(0) = \left[ \frac{m^*/m_e}{4\pi m_s r_e} \left( 1 + \frac{\xi}{l_e} \right) \right]^{1/2} \quad \text{Eq. VI- 38}$$

$$\gamma = \left( \frac{\pi}{3} \right)^{2/3} \frac{k_B m^* n_e^{2/3}}{\hbar^2} \quad \text{Eq. VI- 39}$$

where the mean free path  $l_e$  (small for amorphous alloys) is estimated from resistivity measurements :

$$l_e = \frac{0.18\pi^2 k_B \hbar}{\rho \gamma \xi_0 e^2 T_c} \quad \text{Eq. VI- 40}$$

In such a plot, the amorphous  $Zr_{76}TM_{24}$  are all on the verge of conventional and unconventional superconductors, contrarily to the crystalline  $Zr_2TM$  for which a linear evolution from the "conventional" to the "exotic" region was observed as TM changed from Fe to Rh<sup>62</sup>.

## VI.5. Conclusions and further work

Using the muon spin rotation technique, we were able to demonstrate the existence of a well defined flux lattice in an amorphous superconductor. To my knowledge, this is the first observation of this kind using any other technique (eg. Bitter decoration). Although the FLL seems perfect using  $\mu$ SR, an attempt to see a FLL using Small Angle Neutron Scattering failed to see a well defined lattice but could only detect a very weak Debye-Scherrer like cone at the right  $q$  values for the three different applied fields chosen during the experiment<sup>63</sup> ( $q = 2\pi(2B/3\phi_0)^{1/2}$ ). This is partly due to the high value of the penetration depth as the SANS intensity changes as  $\lambda^{-4}$ . For YBCO,  $\lambda$  is three times smaller than for  $\alpha$ -  $Zr_{76}Co_{24}$ . and SANS experiments on YBCO already require long counting times (for Nb, a good spectrum can be obtained in a matter of minutes!). Also the lowest temperature available was only about 1/2  $T_c$  and for the geometry used (field parallel to the shortest distance of the ribbons), it means that the lattice is quite soft. It could be useful to redo that experiment in a more appropriate

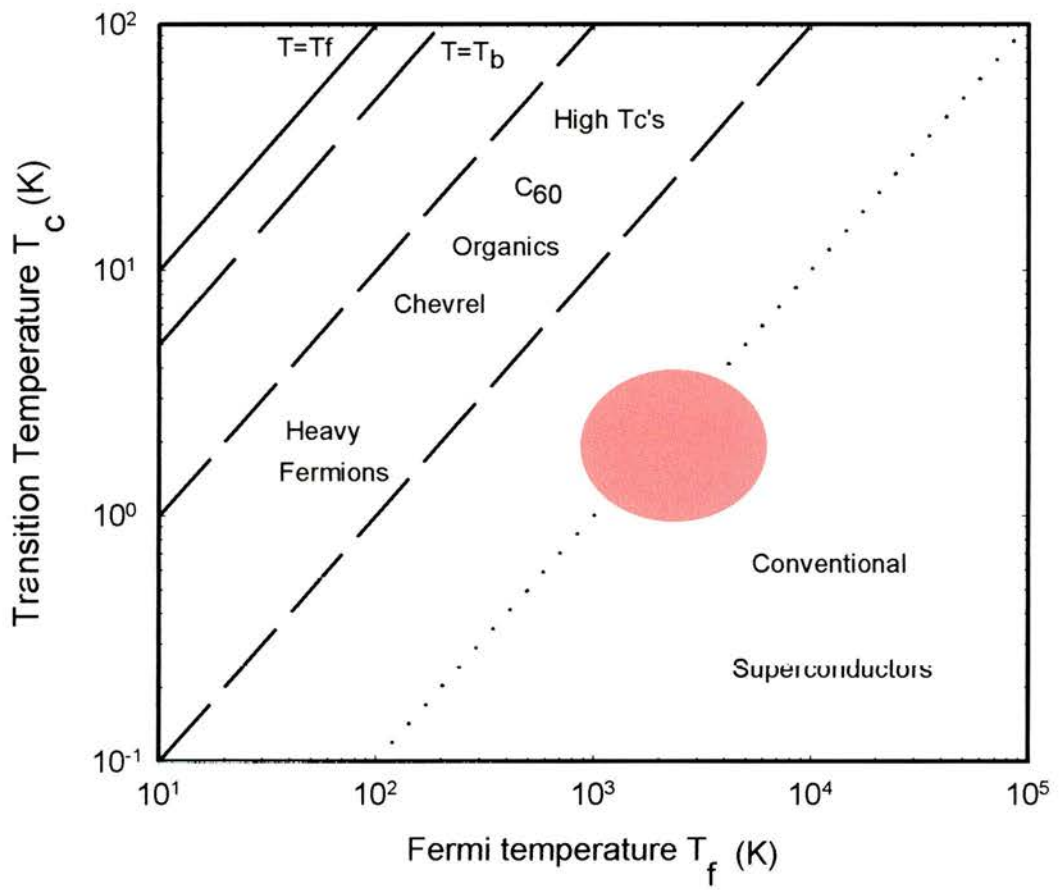


Figure VI- 29 : the Uemura plot with the amorphous  $Zr_{76}TM_{24}$  as a red point.

geometry and at lower temperature (in a dilution fridge rather than in a cryostat). Another possible explanation for the observed SANS signals could be that the lattice is very well defined on the muon length scale but disordered in the more macroscopic level probed by SANS. A picture of different domains of well defined FLL would then emerge.

Using the Uemura classification scheme, it was shown that the amorphous ZrTM alloys sit near the boundary between conventional and exotic superconductors. This observation, coupled with the well-known importance of the pressure on the superconductivity in these alloys suggest then spin fluctuation might play a role in establishing the superconductivity. These spin fluctuations could be probed by a series of inelastic neutron scattering experiments in a similar way to the work on high Tc's<sup>64</sup>.

## References for chapter VI

- <sup>1</sup> W. Buckel and R. Hilsch, *Z. Phys.*, **138** (1954) 109
- <sup>2</sup> W. Buckel and R. Hilsch, *Z. Phys.*, **146** (1956) 27
- <sup>3</sup> W.L. Johnson, S.J. Poon and P. Duwez, *Phys. Rev. B* **11** (1975) 150
- <sup>4</sup> K. Samwer and H.V. Lohneysen, *Phys. Rev. B* **26** (1982) 107
- <sup>5</sup> Z. Altounian and J.O. Strom-Olsen, *Phys. Rev. B* **27**(1983) 4149
- <sup>6</sup> F. Hamed et al, *Phys. Rev. B* **43** (1991) 3649
- <sup>7</sup> W.L. McMillan, *Phys. Rev.* **167** (1967) 331
- <sup>8</sup> P.B. Allen and B. Mitrovic, in *Solid State Physics*, edited by H. Ehrenreich, F. Seitz and D. Turnbull (Academic, New York, 1982)
- <sup>9</sup> S. Nakamura, T. Moriya and K. Ueda, *J. Phys. Soc. Japan* **65** (1996) 4026
- <sup>10</sup> T. Moriya and A. Kawabata, *J. Phys. Soc. Japan* **34** (1973) 639
- <sup>11</sup> Y. J. Uemura et al, *Phys. Rev. Lett.* **66** (1991) 2665
- <sup>12</sup> Y. J. Uemura, *Hyp. Int.* **105** (1997) 35  
Y. J. Uemura and R. Cywinski in *Muon Science : Muons in Physics, Chemistry and Materials*, (1999) NATO/SUSSP51 Summer School (Editors : S.L. Lee, S.H. Kilcoyne and R. Cywinski), Institute of Physics Publishing
- <sup>13</sup> E. Batalla, Z. Altounian and J.O. Strom-Olsen, *Phys. Rev. B* **31**(1985) 577
- <sup>14</sup> N. D. Mathur et al, *Nature* **394** (1998) 39
- <sup>15</sup> S. S. Saxena, *Journal of Mag. & Mag. Mat.*, **226-230** (2001) 45
- <sup>16</sup> C. Pfleiderer et al, *Nature* **412**(2001) 58
- <sup>17</sup> H. Kamerlingh. Onnes, *Leiden Comm* 120b,122b, 124c (1911)
- <sup>18</sup> W. Meissner and R. Ochsenfeld, *Naturwiss.* **21** (1933) 787
- <sup>19</sup> L. Tisza, *Nature* **141** (1938) 913
- <sup>20</sup> C.J. Gorter and H.B.G. Casimir, *Physica* **1** (1934) 306  
*Phys. Z.* **35** (1934) 963  
*Z. Tech. Phys.* **15** (1934) 539
- <sup>21</sup> C.P. Bean, *Phys. Rev. Letters* **8** (1962) 250
- <sup>22</sup> V.L. Ginzburg and L.D. Landau, *JETP* **20** (1950) 1064
- <sup>23</sup> J.E. Zimmerman and J.E. Mercerau, *Phys. Rev. Lett.* **14** (1965) 887
- <sup>24</sup> J. Bardeen, L.N. Cooper and J.R. Schrieffer, *Phys. Rev.* **108** (1957) 1175
- <sup>25</sup> F. London and H. London, *Proc. Roy. Soc. (London)* **A149** (1955) 71
- <sup>26</sup> E. Maxwell, *Phys. Rev.* **78** (1950) 477
- <sup>27</sup> A.A. Abrikosov, *Zh. Eksp. Teor. Fiz.* **32** (1957) 32
- <sup>28</sup> E.H. Brandt, *Rep. Prog. Phys.* **58** (1995) 1465
- <sup>29</sup> S.L. Thiemann et al, *Phys. Rev. B* **39** (1989) 11407
- <sup>30</sup> L.J. Campbell et al, *Phys. Rev. B* **38** (1988) 2439
- <sup>31</sup> S.L. Thiemann, Z. Radovic and V.G. Kogan, *Phys. Rev. B* **39** (1989) 11406
- <sup>32</sup> W.H. Press et al, *Numerical Recipes in Fortran* (Cambridge), p97
- <sup>33</sup> A.J. Greer and W.J. Kossler, *Low Magnetic Fields in Anisotropic Superconductors*, Springer 1995
- <sup>34</sup> S.L. Lee, private communication
- <sup>35</sup> E.H. Brandt, *J. of Low Temp. Phys.* **73** (1988) 355  
E.H. Brandt and A. Seeger, *Advances in Physics* **35** (1986) 189
- <sup>36</sup> B. Pumpkin et al, *Phys. Rev. B* **42** (1990) 8019
- <sup>37</sup> H. Fröhlich, *Phys. Rev.* **79** (1950) 845
- <sup>38</sup> P.G. de Gennes, *Superconductivity of metals and alloys* (Benjamin) 1966
- <sup>39</sup> M. Héritier, *Cours de D.E.A. de Physique des Solides*, Orsay
- <sup>40</sup> L. Cooper, *Phys. Rev.* **104** (1956) 1189
- <sup>41</sup> N.N. Bogoliubov, *Nuovo Cimento* **7** (1958) 794
- <sup>42</sup> R.D. Parks, *Superconductivity*, Volume I (M. Dekker, New York) 1969
- <sup>43</sup> G.R. Stewart, *Rev. Mod. Phys.* **56** (1984) 755  
G.P. Meisner et al, *Phys. Rev. Letters* **53** (1984) 1829
- <sup>44</sup> D. Jérôme et al, M. Ribault, A. Mazaud and K. Bechgaard, *J. Phys. Lettres* **41** (1980) L95
- <sup>45</sup> J.G. Bednorz and K.A. Müller, *Z. Phys. B* **84** (1986) 189
- <sup>46</sup> M.K. Wu et al, *Phys. Rev. Letters* **58** (1987) 908
- <sup>47</sup> H. Maeda et al, *Jap. J. Appl. Phys.* **27** (1988) L209
- <sup>48</sup> J.P. Carbotte, *Reviews of Modern Physics* **62** (1990) 1027
- <sup>49</sup> R. Micnas, J. Ranninger and S. Robaszkiewicz, *Reviews of Modern Physics* **62** (1990) 113



- 
- <sup>50</sup> K. Tanigaki et al., *Nature* **352**, (1991) 222  
<sup>51</sup> R. Cava et al, *Nature* **367** (1994) 252  
<sup>52</sup> R. Chevrel, M. Sergent and J. Pringent, *J. Solid State Chem.* **3** (1971) 515  
<sup>53</sup> Y.J. Uemura et al, *Phys. Rev. Letters* **62** (1989) 2317  
<sup>54</sup> J.P. Xanthakis, R.L. Jacob, E. Babic, *J. of Phys F : Metal Phys.* **16** (1986) 323  
<sup>55</sup> S.L. Lee et al, *Phys. Rev. Letters* **71** (1993) 3862  
<sup>56</sup> E.H. Brandt and A. Seeger, *Adv. in Phys.* **35** (1986) 189  
<sup>57</sup> A.D. Sidorenko, V.P. Smilga and V.L. Fesenko, *Hyp. Int.* **63** (1990) 49  
C.M. Aegerter and S.L. Lee, *Appl. Magn. Reson.* **13** (1997) 75  
<sup>58</sup> M. Tinkham, *Introduction to Superconductivity*, Mc Graw-Hill  
<sup>59</sup> A.L. Larkin and Y.N. Ovchinnikov, *J. of Low Temp. Phys.* **34** (1979) 409  
<sup>60</sup> C.G. Perkins and A.D. Caplin, *Phys. Rev. B* **54** (1996) 12511  
<sup>61</sup> P.H. Kes and C.C. Tsuei, *Phys. Rev. B* **28** (1983) 5126  
R. Wördenweber et al, *J. of Low Temp. Phys.* **70** (1988) 253  
<sup>62</sup> A.D. Hiller, PhD thesis, St Andrews (1999)  
<sup>63</sup> P. Manuel, A.D. Hillier and S.H. Kilcoyne, *Physica B* **276-278** (2000) 818  
<sup>64</sup> P. Dai et al, *Science* **284** (1999) 1344

## Chapter VII : Conclusions and perspectives

Conclusions have been made and further studies have been proposed in each chapter as the relevant data were presented. Therefore, this chapter will provide a brief summary of all the results and suggest some possible future work.

The spin correlation function in a random anisotropy system has been showed to follow closely and conclusively the Kohlrausch function for the first time. However, several questions still remain. Better statistics on NSE data tend to show that, for spin glass systems, the Ogielski form seems to fit the spin autocorrelation function better than the stretched exponential<sup>1</sup>. This suggests that the spin glass and the random anisotropy systems could indeed belong to two distinct universality classes. A NSE experiment on a dilute RAM (eg a few % Er) could be useful to determine whether the temperature evolution of  $\beta$  is really typical of concentrated systems and more dilute systems show a constant  $\beta$ . Another possibility for explaining the different trends in spin glass and random anisotropy systems is the difference in the interactions. The magnetic properties of random anisotropy magnets, derive from the presence of a *local, single ion* magnetic anisotropy axis which varies randomly from site to site whereas the interaction responsible for the spin glass behaviour is more long range.

From the work on the crystallisation of amorphous precursors RE-TM, it has been possible to show that the crystallisation processes and kinetics (the Avrami time constant for instance) can be monitored on fast counting instruments such as D20. This opens great perspectives for technological applications such as the tailoring of the magnetic properties by simply stopping the crystallisation at the right time and temperature. An obvious candidate for such a study would be the pseudo-binary (DyTb)-Fe alloy as the  $(\text{Tb}_{0.27}\text{Dy}_{0.73})\text{Fe}_2$  is otherwise known as<sup>2</sup> Terfenol-d and is commercially used for its large magnetostriction combined with its low magnetocrystalline anisotropy energy and high sensitivity to external magnetic fields. Since the magnetostrictive properties are controlled by the microstructure, a detailed analysis of the processes by neutron scattering could prove extremely useful. However, the most exciting results from the crystallisation of amorphous RE-TM, is the discovery of new YFe and ErFe (and possibly YCo) phases. The only compound that was possible

to stabilise (YFe) had very interesting magnetic properties with transition to a complex long range magnetic order below 58 K. This could prove very useful for theorists as it expands the composition range previously known. Ideally, single phase samples of these new compounds should be obtained and work is currently underway to try and make it by sputtering.

Using the muon spin rotation technique, the existence of a well defined flux lattice in an amorphous superconductor was conclusively proven. To my knowledge, this is the first observation of this kind using any other technique (eg. Bitter decoration). Similarities with the high temperature (single crystal) superconductors such as the pinning mechanisms might revive the interest in such systems. Using the Uemura classification scheme<sup>3</sup>, it was shown that the amorphous ZrTM alloys sit near the boundary between conventional and exotic superconductors. This observation, coupled with the observed pressure effects on the superconductivity in these alloys, suggest that spin fluctuations might play a role in establishing the superconductivity. These spin fluctuations could be probed by a series of inelastic neutron scattering experiments in a similar way to the work on high Tc's<sup>4</sup>.

---

<sup>1</sup> C. Pappas, private communication

<sup>2</sup> A. E. Clark, Proceedings of the 19<sup>th</sup> Conference in Magnetism and Magnetic Materials, AIP, 1974

<sup>3</sup> Y.J. Uemura, Hyp. Int **105** (1997) 1169

<sup>4</sup> P. Dai et al, Science **284** (1999) 1344